

High Velocity Impact Fracture

by

Xiaoqing Teng

B.S., Naval Architecture, Shanghai Jiao Tong University (1994)
M.S., Structural Mechanics, Shanghai Jiao Tong University (1997)

Submitted to the Department of Ocean Engineering
in partial fulfillment of the requirements for the degree of

Doctor of Philosophy in Applied Mechanics

at the

MASSACHUSETTS INSTITUTE OF TECHNOLOGY

February 2005

© Massachusetts Institute of Technology 2005. All rights reserved.

Author
Department of Ocean Engineering
December 2, 2004

Certified by
Tomasz Wierzbicki
Professor of Applied Mechanics
Thesis Supervisor

Accepted by
Michael S. Triantafyllou
Chairman, Department Committee on Graduate Students

High Velocity Impact Fracture

by

Xiaoqing Teng

Submitted to the Department of Ocean Engineering
on December 2, 2004, in partial fulfillment of the
requirements for the degree of
Doctor of Philosophy in Applied Mechanics

Abstract

An in-depth understanding of dynamic ductile fracture is one of the most important steps to improve the survivability of critical structures such as the lost Twin Towers. In the present thesis, the macroscopic fracture modes and the fracture mechanisms of ductile structural components under high velocity impact are investigated numerically and theoretically. Attention is focused on the formation and propagation of through-thickness cracks, which is difficult to experimentally track down using currently available instruments.

Studied are three typical and challenging types of impact problems: (i) rigid mass-to-beam impact, (ii) the Taylor test, and (iii) dynamic compression tests on an axisymmetric hat specimen. Using an existing finite element code (ABAQUS/Explicit) implemented with the newly developed Bao-Wierzbicki's (BW) fracture criterion, a number of distinct failure modes including fragmentation, shear plugging, tensile tearing in rigid mass-to-beam impact, confined fracture, petalling, and shear cracking in the Taylor test, are successfully recreated for the first time in the open literature. All of the present predictions are in qualitative agreement with experimental observations. This investigation convincingly demonstrates the applicability of the BW's fracture criterion to high velocity impact problems and at the same time provides an insight into deficiencies of existing fracture loci.

Besides void growth, the adiabatic shear banding is another basic failure mechanism often encountered in high velocity impact. This failure mechanism and subsequent fracture is studied through numerical simulation of a recently conducted compression test on a hat specimen. The periodical occurrence of hot spots in the propagating adiabatic shear bands is successfully captured. The relation between hot spots and crack formation is revealed. The numerical predictions correlate well with experimental results.

An explicit expression controlling through-thickness crack growth is proposed and verified by performing an extensive parametric study in a wide range of input variables. Using this expression, a two-stage analytical model is formulated for shear plugging of a beam/plate impacted by a flat-nosed projectile. Obtained theoretical solutions are compared with experimental results published in the literature showing very good agreement.

Three theoretical models for rigid mass-to-beam impact, the single, double, and multiple impact of beam-to-beam are derived from the momentum conservation principle. The obtained closed-form solutions, which are applicable to the axial stretching dominated case, are validated by finite element analysis.

Thesis Supervisor: Tomasz Wierzbicki
Title: Professor of Applied Mechanics

Acknowledgments

I would like to express my deep gratitude to Professor Tomasz Wierzbicki for his guidance, support, and encouragement during my four years at MIT, and for providing me with Research Assistantship all along. I wish to thank Professors Klaus-Jürgen Bathe, Nicholas M. Patrikalakis, and Franz-Josef Ulm for their participation in my thesis committee and for their insightful comments. Thanks are due to Professor Frank A. McClintock for taking time to teach me fracture mechanics, and for his valuable advice and patience during my first years at MIT.

I am thankful to my colleagues at the Impact and Crashworthiness Lab, Dr. Mulalo Doyoyo, Dr. Yingbin Bao, Dr. Dirk Mohr, Mr. Young-Woong Lee, Mr. Liang Xue, Ms. Li Zheng, Mr. Yuanli Bai, for creating a pleasant, stimulating, and productive working environment. I wish to thank my friends, specially, Dr. Weigang Chen, for his recommendation when applying to MIT, Dr. Zhiyong Yang and Mr. Yile Li for sharing with me their experience and continuing encouragement. My appreciation is also extended to Ms. Sheila McNary for her assistance in administrative matters, and to Ms. Jean Sucharewicz for helping solve at one time my visa problem.

I gratefully acknowledge my parents-in-law, my brother and my sister-in-law for their understanding and support.

I am sincerely indebted to my wife, Jiayun, for her love, encouragement, tolerance of my sitting in front of a computer in numerous sunshine days, and also for delicious food that she was making during those sunny and rainy days.

This dissertation is dedicated to my parents for their love and sacrifice.

Contents

List of Figures	13
List of Tables	23
Nomenclature	24
1 Introduction	31
1.1 Background and motivation	31
1.2 Problem statement	33
1.3 Research objectives	34
1.4 Outline of the thesis	35
2 Review of Fracture Approaches in High Velocity Impact	39
2.1 Stress intensity factors and J-integrals	39
2.2 Cohesive element methods	40
2.3 The Gurson model	43
2.4 Ductile fracture criteria	44
2.4.1 Stress triaxiality	44
2.4.2 Strain rates	45
2.4.3 Temperature	47
3 Qualitative Analysis of Failure Modes	51
3.1 Introduction	51
3.2 Failure modes in rigid mass-to-beam impact	55
3.2.1 Introduction	55
3.2.2 Finite element modeling	56

3.2.3	Tensile tearing	58
3.2.3.1	2024-T351 aluminum alloy	59
3.2.3.2	Weldox 460 E steel	62
3.2.3.3	Thin vs. thick beams	64
3.2.4	Through-thickness shear plugging	66
3.2.4.1	Flat-nosed projectile	66
3.2.4.2	Round-nosed projectile	68
3.2.5	Transition from tensile tearing to shear plugging	71
3.2.6	Residual velocities	74
3.2.7	Discussions	77
3.3	Failure modes in the Taylor test	79
3.3.1	Introduction	79
3.3.2	Finite element modeling	80
3.3.3	Mushrooming deformation	82
3.3.4	Confined fracture	82
3.3.5	Petalling	85
3.3.6	Shear cracking	89
3.3.7	Discussions	93
3.4	Adiabatic shear banding under dynamic compression	94
3.4.1	Introduction	94
3.4.2	Experimental set-up	97
3.4.3	Finite element modeling	98
3.4.4	Evolution of adiabatic shear bands	102
3.4.5	Crack formation and growth	107
3.4.6	Temperature fields	114
3.4.7	Effect of fracture strains	117
3.4.8	Adaptive vs. fixed meshing	118
3.4.9	Concluding remarks	119
4	Properties of Through-Thickness Crack Growth	121
4.1	Introduction	121
4.2	Development of crack growth curve	122

4.3	Crack initiation sites	124
4.4	Crack initiation vs. propagation	126
4.5	Parametric study on crack growth	130
4.5.1	Finite element modeling	130
4.5.2	Impact velocity	131
4.5.3	Projectile mass	131
4.5.4	Beam thickness	133
4.5.5	Plane-strain beam	134
4.5.6	Circular plate	135
4.6	Crack propagation speed	137
4.7	Discussions	139
5	Numerical Aspects of Ductile Fracture Prediction	143
5.1	Material constitutive model	143
5.2	Fracture model	148
5.3	Mesh size effects in high velocity impact	150
5.3.1	Introduction	150
5.3.2	Why sensitivity to mesh size	150
5.3.3	Adiabatic shear banding	152
5.3.4	Crack formation and propagation	155
5.3.5	How to remedy mesh size sensitivity	160
6	Effect of Ductile Fracture Criteria on Impact Failure	163
6.1	Introduction	163
6.2	Ductile fracture criteria	164
6.2.1	Bao-Wierzbicki's fracture locus	164
6.2.2	Johnson-Cook's fracture locus	166
6.2.3	Constant fracture strain	169
6.3	Comparison of predicted failure patterns	171
6.3.1	Rigid mass-to-beam impact	171
6.3.1.1	Flat-nosed projectile	171
6.3.1.2	Round-nosed projectile	175
6.3.2	The Taylor test	177

6.3.3	Compression tests on the axisymmetric hat specimen	183
6.4	Partial conclusions	185
7	Derivation of Analytical Benchmark Solutions	187
7.1	Background	187
7.2	Rigid mass-to-beam impact	190
7.2.1	Introduction	190
7.2.2	Flat-nosed projectile	191
7.2.2.1	Problem formulation	191
7.2.2.2	Velocity and deformation	193
7.2.2.3	Strain and critical impact velocity	195
7.2.2.4	Energy dissipation	196
7.2.2.5	Range of applicability	197
7.2.3	Round-nosed projectile	200
7.2.4	Comparison with finite element solutions	205
7.2.5	Discussions	209
7.3	Single impact of beam-to-beam	210
7.3.1	Introduction	210
7.3.2	Problem formulation	211
7.3.3	Solutions for velocity and deformation	217
7.3.4	Tensile strains and critical velocity to fracture	222
7.3.5	Location and time of fracture	224
7.3.5.1	The struck beam at $\alpha > \beta$	224
7.3.5.2	The struck beam at $\alpha < \beta$	224
7.3.5.3	The striking beam at $\alpha > \beta$	226
7.3.5.4	The striking beam at $\alpha < \beta$	227
7.3.6	Fracture scenarios	227
7.3.6.1	Case 1	227
7.3.6.2	Case 2	228
7.3.6.3	Case 3	228
7.3.6.4	Case 4	228
7.3.6.5	Case 5	229

7.3.7	Deflection after fracture	230
7.3.8	Comparison with finite element solutions	232
7.3.9	Discussion	234
7.4	Multiple impact of beam-to-beam	235
7.4.1	Introduction	235
7.4.2	Double impact	236
7.4.2.1	Problem formulation	237
7.4.2.2	Assumptions	240
7.4.2.3	Velocity history	242
7.4.2.4	Deflection and plastic strain	244
7.4.2.5	Kinetic energy and plastic energy	247
7.4.2.6	Critical impact velocities	248
7.4.2.7	Double impact by two identical rigid masses	249
7.4.2.8	Double impact by two intact striking beams	253
7.4.3	Multiple impact	256
7.4.3.1	Problem formulation	256
7.4.3.2	Velocity history	259
7.4.3.3	Deflection	261
7.4.3.4	Tensile strain and critical impact velocity	261
7.4.3.5	Multiple rigid mass impact	267
7.4.4	Partial conclusions	271
7.5	Dynamic shear plugging	272
7.5.1	Introduction	272
7.5.2	Critical indentation depth	274
7.5.3	Perforation analysis for a circular plate	276
7.5.3.1	Stage I: indentation	277
7.5.3.2	Stage II: crack propagation	279
7.5.3.3	Crack propagation speed	282
7.5.3.4	Shear zone width	284
7.5.4	Perforation analysis for a beam	287
7.5.5	Coupled shear-tension analysis	288
7.5.5.1	Circular plate	289

7.5.5.2	Beam	293
7.5.6	Validation of the analytical solution	293
7.5.6.1	Experiments on 2024 aluminum alloy plates	293
7.5.6.2	Experiments on Weldox 460 E steel plates	296
7.5.7	Transition from tensile tearing to shear plugging	301
7.5.8	Comparison with previous analytical solutions	302
7.5.9	Concluding remarks	303
8	Conclusions and Recommendations	305
8.1	Summary of results	305
8.2	Suggestions for future studies	308
A	Choice of Parameters in Finite Element Modeling	311
	Bibliography	314

List of Figures

1-1	A “clean” cut driven by the wings of a Boeing 767 into the facade of the North Tower.	32
2-1	Schematic representation of the fracture process zone, the J- and K-dominant zones ahead of the crack tip.	41
2-2	Schematic representation of a separation decohesive law.	42
2-3	The ratio of the fracture strain vs. the strain rate.	47
2-4	The ratio of the fracture strain vs. the temperature rise.	48
3-1	Schematic representation of eight possible failure modes in perforation problems.	52
3-2	Spallation of plate-to-plate impact.	54
3-3	Fragmentation of a ring under explosive loading.	54
3-4	Schematic representation of a long beam struck by a rigid, round-nosed mass.	56
3-5	Finite element model of a beam impacted by a rigid, round-nosed projectile.	57
3-6	Failure process of the 2024-T351 aluminum alloy beam impacted by the round-nosed mass at $V_0 = 220$ m/s.	60
3-7	History of the effective plastic strain and the stress triaxiality of the starter point of the crack located at the proximal surface of the 2024-T351 aluminum beam at $V_0 = 220$ m/s.	61
3-8	History of the effective plastic strain and the stress triaxiality of the end point of the crack located at the distal surface of the 2024-T351 aluminum beam at $V_0 = 220$ m/s.	61
3-9	Crack formation in the Weldox 460 E steel beam struck by the round-nosed mass moving at $V_0 = 375$ m/s.	62

3-10	History of the effective plastic strain and the stress triaxiality of the starter point of the crack located at the distal surface of the Weldox 460 E steel beam at $V_0 = 375$ m/s.	63
3-11	Diffuse necking preceding fracture for the Weldox 460 E steel beam impacted by the rigid mass moving at $V_0 = 250$ m/s.	63
3-12	Failure process of the round-nosed mass impact on the aluminum alloy beam of $h = 2$ mm and $\mu = 0.1$ at $V_0 = 270$ m/s.	65
3-13	Tensile tearing of a 2024-0 aluminum circular plate of $h = 1.27$ mm struck by a round-nosed projectile of $d = 12.7$ mm at $V_0 = 89.6$ m/s.	65
3-14	Perforation process of flat-nosed mass impact on the aluminum alloy beam at $V_0 = 240$ m/s.	67
3-15	Failure pattern of the 2024-T351 aluminum alloy beam impacted by the round-nosed mass at $V_0 = 300$ m/s.	69
3-16	History of the effective plastic strain and the stress triaxiality of the starter point of the crack located in the middle of the thickness for the aluminum beam at $V_0 = 300$ m/s.	69
3-17	Failure process of the 2024-T351 aluminum alloy beam impacted by the round-nosed mass at $V_0 = 400$ m/s.	70
3-18	Fragmentation of a 2024-T4 aluminum circular plate of $h = 6.35$ mm struck by a hard-steel sphere of $d = 6.35$ mm at $V_0 = 863.52$ m/s.	70
3-19	Failure process of the Weldox 460 E steel beam impacted by the round-nosed mass at $V_0 = 450$ m/s.	72
3-20	History of the effective plastic strain and the stress triaxiality of the starter point of the crack located at the proximal surface of the Weldox 460 E steel beam at $V_0 = 450$ m/s.	73
3-21	Crack trajectories mapped back on the undeformed shape represented by dark elements for the Weldox 460 E steel beam at various impact velocities.	73
3-22	Plastic energy dissipated vs. initial impact velocity for the aluminum and steel beams.	75
3-23	Residual velocity vs. initial impact velocity for the aluminum and steel beams.	76
3-24	Comparison of the residual velocity between the round-nosed and flat-nosed projectiles for the 2024-T351 aluminum alloy beam.	77

3-25 Schematic representation of a cylindrical projectile impacting against a rigid wall in the Taylor test.	80
3-26 Finite element model of the projectile-target system in the Taylor test. . . .	81
3-27 Mushrooming deformation process of the Weldox 460 E steel projectile at $V_0 = 400$ m/s.	83
3-28 Confined fracture.	84
3-29 History of the normalized stress components at a point in the symmetry axis of the projectile.	84
3-30 History of the axial displacement of the central point of the front surface. . .	86
3-31 History of the effective plastic strain and the stress triaxiality at a point at the symmetric axis of the projectile.	86
3-32 Petalling process of the Weldox 460 E steel projectile at $V_0 = 600$ m/s. . . .	87
3-33 Petalling of a 4340 steel cylinder at $V_0 = 529$ m/s.	88
3-34 History of the effective plastic strain and the stress triaxiality of a point at the outer edge of the front surface for the Weldox 460 E steel projectile at $V_0 = 600$ m/s.	89
3-35 Spiral shear cracks on the lateral surface of the 2024-T351 aluminum alloy projectile at $V_0 = 240$ m/s.	91
3-36 History of the effective plastic strain and the stress triaxiality at a point on the edge of the front surface of the 2024-T351 aluminum alloy projectile at $V_0 = 240$ m/s.	91
3-37 Shear cracks on the lateral surface of two swaged tungsten alloy cylinders in the symmetric Taylor test.	92
3-38 Shear cracking of a 4340 steel cylinder at $V_0 = 315$ m/s.	92
3-39 Schematic representation of impact tests on the hat specimen using direct compressive Hopkinson pressure bar system.	99
3-40 Geometrical shape and size of the modified axisymmetric hat specimen. . . .	99
3-41 Finite element model around the gauge section of the axisymmetric hat specimen.	100
3-42 Scanning electronic micrograph showing the generated adiabatic shear band at $V_0 = 27.6$ m/s.	101

3-43	Effective plastic strain field around the interior corner in the initial phase ($t = 12 \mu\text{s}$) at $V_0 = 27.6 \text{ m/s}$	102
3-44	Formation and propagation of the adiabatic shear bands along the gauge section at $V_0 = 27.6 \text{ m/s}$	103
3-45	Time history of the effective plastic strain and the effective stress of a typical point located in the middle of the adiabatic shear band at $V_0 = 27.6 \text{ m/s}$. .	104
3-46	Stress collapse at four material points within the adiabatic shear band initi- ating at the interior corner at $V_0 = 27.6 \text{ m/s}$	106
3-47	Time history of the stress triaxiality of four material points within the adia- batic shear band initiating at the interior corner at $V_0 = 27.6 \text{ m/s}$	106
3-48	Adiabatic shear band length vs. impact velocity.	108
3-49	Adiabatic shear band length vs. time at $V_0 = 27.6 \text{ m/s}$	108
3-50	Process of crack propagation from the interior corner at $V_0 = 27.6 \text{ m/s}$ and $\bar{\epsilon}_f = 0.2$ with the cut-off value for the negative stress triaxiality.	109
3-51	The profiles of the stress triaxiality along the shear band at $t = 24 \mu\text{s}$ right before the crack formation.	111
3-52	Crack length vs. impact velocity at $\bar{\epsilon}_f = 0.2$ with the cut-off value.	111
3-53	Shear bands and cracks generated along the gauge section at $V_0 = 29.0 \text{ m/s}$.	112
3-54	Time history of effective plastic strain of four material points within the adiabatic shear band initiating at the exterior corner at $V_0 = 27.6 \text{ m/s}$	112
3-55	The crack and shear band generated around the interior corner at $V_0 =$ 27.6 m/s	113
3-56	Temperature distribution along two lines across the adiabatic shear bands at $V_0 = 27.6 \text{ m/s}$	114
3-57	Transient temperature fields around the interior corner at $V_0 = 27.6 \text{ m/s}$. .	115
3-58	Periodical occurrence of hot spots within the adiabatic shear band at $V_0 =$ 27.6 m/s	116
3-59	The predicted length of the crack initiating at the interior corner as a function of the magnitude of the fracture strain.	118
3-60	Temperature contours using fixed meshing at $V_0 = 27.6 \text{ m/s}$	119
4-1	Schematic representation of through-thickness shear cracks.	123

4-2	Crack formation and growth of the plane-stress beam of $h = 10$ mm impacted by the projectile of $\mu = 0.1$ and $2r/d = 0.50$ at $V_0 = 240$ m/s ($d = 20$ mm).	125
4-3	Crack formation of the 2024-T351 aluminum alloy beam of $h = 10$ mm impacted by the round-nosed mass of $\mu = 0.1$ at $V_0 = 300$ m/s.	127
4-4	Damage accumulation of three points along the crack of the plane-stress beam of $h = 10$ mm impacted by the flat-nosed projectile of $\mu = 0.1$ at $V_0 = 240$ m/s.	129
4-5	Time history of the stress triaxiality and the effective plastic strain of the point (Point C) located at the distal surface of the plane-stress beam of $h = 10$ mm impacted by the flat-nosed projectile of $\mu = 0.1$ at $V_0 = 240$ m/s.	129
4-6	Finite element meshes of the impacted zone of a beam struck by a flat-nosed mass.	130
4-7	Crack propagation at various impact velocities for the plane-stress beam of $h = 10$ mm and $\mu = 0.1$	132
4-8	Crack propagation at various mass ratios for the plane-stress beam of $h = 10$ mm at $V_0 = 240$ m/s.	132
4-9	Crack propagation in the plane-stress beam of various thicknesses at $V_0 = 240$ m/s and $\mu = 0.1$	133
4-10	Crack propagation in the plane-strain beam of $h = 10$ mm at $V_0 = 240$ m/s.	134
4-11	Velocity history of the projectile for the circular plate, and plane-stress and plane-strain beams of $h = 10$ mm at $V_0 = 240$ m/s and $\mu = 0.1$	135
4-12	Failure pattern of the circular plate of $h = 10$ mm struck by the cylindrical projectile with $V_0 = 240$ m/s and $\mu = 0.1$	136
4-13	Crack propagation in the circular plate of $h = 10$ mm at various impact velocities and mass ratios.	136
4-14	Time history of crack extension at various impact velocities for the plane-stress beam of $h = 10$ mm and $\mu = 0.1$	138
4-15	Average crack tip speeds vs. mass ratios for the plane-stress beam of $h = 10$ mm at $V_0 = 240$ m/s.	138
4-16	Instantaneous crack tip speeds vs. time for the plane-stress beam of $h = 10$ mm and $\mu = 0.1$	139
4-17	Crack propagation fitted by piecewise linear functions.	141

5-1	von Mises stress vs. effective plastic strain under various strain rates and temperature for Weldox 460 E steel.	145
5-2	Equivalent stress versus plastic strain under various strain rates and temperature for 2024-T351 aluminum alloy.	147
5-3	Schematic representation of strain softening and strain hardening.	151
5-4	Comparison of the generated cracks and adiabatic shear bands at $t = 48 \mu\text{s}$ and $V_0 = 27.6 \text{ m/s}$ between two mesh models.	154
5-5	Comparison of temperature rise along the gauge section at $t = 32 \mu\text{s}$	155
5-6	Schematic representation of a circular Weldox 460 E steel plate impacted by a flat-nosed cylindrical, hard projectile in the Børvik et al.'s experiments.	156
5-7	Three axisymmetric mesh models for the Weldox 460 E steel circular plate impacted by the rigid cylindrical projectile.	157
5-8	Comparison of residual velocities among experimental results and numerical solutions based on three mesh models.	158
5-9	Calculated residual velocity vs. element number through the thickness of the steel plate.	158
5-10	Comparison of crack growth in the steel circular plate at $V_0 = 277.5 \text{ m/s}$ among three mesh models.	159
5-11	Time history of the von Mises stress and the effective plastic strain of a typical element at the crack at $V_0 = 277.5 \text{ m/s}$ based on the medium mesh model.	159
6-1	Specimens used to calibrate the BW's fracture criterion. Courtesy Y. Bao.	164
6-2	The Bao-Wierzbicki's ductile fracture locus for 2024-T351 aluminum alloy.	166
6-3	Fracture loci for Weldox 460 E steel.	168
6-4	A new type of specimen for the determination of fracture properties of a ductile material in the range of the negative stress triaxiality.	169
6-5	Constant fracture criteria with and without the cut-off value for the stress triaxiality.	170
6-6	Three fracture loci for 2024-T351 aluminum alloy.	171
6-7	Comparison of the stress triaxiality of a point at the impact interface among three fracture loci.	173

6-8	Comparison of the effective plastic strain of a point at the impact interface among three fracture loci.	173
6-9	Comparison of the failure patterns of a plane-strain aluminum alloy beam impacted by a flat-nosed projectile at $V_0 = 240$ m/s among three fracture criteria.	174
6-10	Failure pattern of a 2024-T351 aluminum alloy circular plate impacted by a steel projectile at $V_0 = 245$ m/s.	175
6-11	Comparison of the failure patterns of a plane-strain aluminum alloy beam impacted by a round-nosed projectile at $V_0 = 300$ m/s among three fracture criteria.	176
6-12	Comparison of failure patterns of the Weldox 460 E steel projectile at $V_0 = 600$ m/s among various fracture options.	179
6-13	Comparison of the size of the failed region in the undeformed form for the Weldox 460 E steel projectile at $V_0 = 600$ m/s.	180
6-14	Comparison of the velocity history of the rear surface of the Weldox 460 E steel projectile at $V_0 = 600$ m/s among four cases.	181
6-15	Comparison of the velocity history of the rear surface of the 2024-T351 aluminum alloy projectile at $V_0 = 240$ m/s between Johnson-Cook's and Bao-Wierzbicki's fracture loci.	181
6-16	Comparison of the final fracture patterns for the 2024-T351 aluminum alloy projectile at $V_0 = 240$ m/s.	182
6-17	Comparison of shortening history of the 2024-T351 aluminum alloy projectile at $V_0 = 240$ m/s based on the JC's and BW's fracture loci, respectively.	182
6-18	Predicted fracture pattern of the specimen using the constant fracture strain without the cut-off value at $V_0 = 27.6$ m/s.	184
6-19	Comparison of the time history of the effective stress between the fracture strain with and without the cut-off value.	185
7-1	A close-up view of the damaged exterior columns of the south facade of the South Tower of the World Trade Center.	188
7-2	Structural component arrangement inside an airplane wing.	189
7-3	Schematic representation of a beam impacted by a rigid, blunt-nosed projectile.	191

7-4	Schematic representation of transient velocity profiles.	194
7-5	Schematic representation of stress distribution along the thickness and the neutral axis.	198
7-6	Wrapping of the beam-string around the round nose of the projectile in the supersonic phase.	201
7-7	Transient velocity of the projectile vs. contact angle in the supersonic phase.	203
7-8	Distribution of plastic tensile strain at various mass ratios.	205
7-9	Comparison of transient transverse velocity profiles of the beam impacted by the flat-nosed projectile with $\mu = 0.05$ and $V_0 = 229$ m/s.	207
7-10	Displacement of the flat-nosed rigid mass vs. time at various combination of the impact velocity and the mass ratio.	207
7-11	Comparison of transient transverse deflection profiles of the beam impacted by the flat-nosed projectile with $\mu = 0.05$ and $V_0 = 229$ m/s.	208
7-12	Comparison of the transient deformation profiles of the 2024-T351 aluminum alloy beam impacted by the round-nosed projectile with $\mu = 0.1$ and $V_0 =$ 200 m/s.	208
7-13	Mechanical and geometrical parameters of the striking and struck beams. . .	211
7-14	Schematic representation of plastic deformation patterns of both beams. . .	213
7-15	Transient velocity profiles for both beams at a certain time after impact. . .	213
7-16	Free body diagram for the impacted zone.	214
7-17	Time history of the transverse velocity in the deformed region at various relative values of α and β	218
7-18	Transient deflection profiles of the struck beam for various values of α and β .	220
7-19	Transient deflection profiles of the striking beam for various values of α and β .	221
7-20	Plastic tensile strain variation along the beams for various values of α and β .	223
7-21	Tensile strains versus distance for the struck beam with $\alpha > \beta$ under various impact velocities.	224
7-22	Fracture location for the struck beam with $\alpha < \beta$	225
7-23	Fracture location as a function of the impact velocity for the striking beam at $\alpha < \beta$	226
7-24	Five fracture scenarios.	229

7-25	Plots of deflection profiles of the struck beam after fracture of the striking beam.	231
7-26	Comparison of tensile strain in the striking beam for the case of the struck beam with and without fracture ($\alpha > \beta$).	232
7-27	Comparison of transient deflection profiles of the striking beam at $V_0 = 240$ m/s.	233
7-28	Comparison of transient deflection profiles of the struck beam at $V_0 = 240$ m/s.	233
7-29	Schematic representation of double impact of beam-to-beam.	236
7-30	Transient velocity field in three beams after the second impact.	239
7-31	Velocity field of the struck beam after decomposition.	242
7-32	Velocity variation with time for $V_{1,1}$ and $V_{1,2}$ in the double impact case. . .	244
7-33	Deflection profiles of the struck beam after the second impact and comparison with of the single impact event.	245
7-34	Strain variation along the struck beam for different values of η	246
7-35	Critical velocity variation with time interval in the double impact case. . . .	248
7-36	Schematic of deformation and fracture of the beams in the double impact case.	250
7-37	Maximum tensile strains versus mass ratios for different values of η in the case of double rigid mass impact.	251
7-38	Critical mass ratio α determining the extreme value of the maximum tensile strain.	252
7-39	Critical velocity variation with time interval for different values of α and β .	254
7-40	Comparison of the critical velocity to fracture the struck beam among three cases.	255
7-41	Schematic of multiple impact of beam-to-beam.	256
7-42	Schematic of the velocity field in the multiple impact case.	257
7-43	Decomposition of the velocity field in the multiple impact case	258
7-44	Temporal variation of the velocities of the struck beam in the multiple impact case.	260
7-45	Comparison of the displacement at $x_1 = 0$ among three cases.	261
7-46	Tensile strains versus mass ratios for different time intervals for Case 1. . .	265
7-47	Tensile strain versus time intervals for different mass ratios for Case 1. . . .	265
7-48	Tensile strain versus impact number.	266

7-49	Comparison of tensile strains versus mass ratio between Case 1 and Case 2.	269
7-50	Comparison of tensile strains versus time interval between Case 1 and Case 2.	269
7-51	Tensile strains versus mass ratios for different values of η for Case 2.	270
7-52	Schematic representation of two stages: indentation and crack growth.	276
7-53	Schematic representation of a free, stationary plastic body struck by a rigid projectile.	277
7-54	Time history of the instantaneous crack propagation speed of a 2024-T351 aluminum alloy circular plate.	283
7-55	Average crack propagation speed vs. target thickness for a 2024-T351 aluminum alloy circular plate.	284
7-56	Plastic shear strain contour showing plastically deformed zone around a crack.	285
7-57	Schematic representation of a shear element in the shear zone.	286
7-58	Schematic of a transient velocity profile in a target.	290
7-59	Schematic of the initial length and the bending response.	291
7-60	Comparison of the velocity history of the projectile impacting against a circular plate made of 2024-T351 aluminum alloy.	294
7-61	Residual velocity vs. impact velocity.	295
7-62	Time history of pressure and equivalent stress of three material points.	296
7-63	Axial shock wave speed vs. impact velocity for plates with various thicknesses.	297
7-64	Crack length vs. indentation depth for three cases in Børvik et al.'s tests.	298
7-65	Residual velocity vs. impact velocity for the Weldox steel target.	300
7-66	Dissipated energy vs. initial impact velocity for a specific case with $h = 10$ mm.	301
7-67	Comparison of the ballistic limit among various analytical solutions and experimental results.	302

List of Tables

2.1	Material constants for the JC's fracture model defined in Eq. (6.2).	46
5.1	Material constants for Weldox 460 E steel	145
5.2	Material constants for 2024-T351 aluminum alloy	147
5.3	Material constants for 91W-61Ni-3Co tungsten alloy	148
7.1	Comparison of the residual velocity between the experimental and numerical results.	298

Nomenclature

A, B, C, n, q five material constants in the JC's constitutive model

a crack length

$2b$ width of the beam

c transverse plastic stress wave speed

c_L longitudinal stress wave speed

c_p shock wave speed

c_R Rayleigh stress wave speed

c_v specific heat

D damage indicator

D_1, \dots, D_5 five material constants in the JC's fracture model

D_{av} average damage indicator

D_c critical damage

d breadth/diameter of the projectile

E kinetic energy

E_0 initial kinetic energy of the projectile

ΔE loss of the kinetic energy during the stress wave propagation

ΔE_0 loss of the kinetic energy in the impacted zone

e	width of the shear zone
\bar{e}	average width of the shear zone
H	Heaviside function
h	thickness
I	momentum
I_p	transverse momentum in the projectile-plug system
I_t	transverse momentum in the target
i	subscript, $i = 1$ denotes the struck beam and $i = 2$ represents the striking beams
j	subscript denoting the impact number
K, λ	material constants used in Eq. (4.1)
k	dimensionless factor defined in Eq. (7.206)
k_1	shear force per unit length
l	length of the beam/diameter of the circular plate
M_0	weight of the projectile
$M_{b,0}$	pure bending moment
M_b	bending moment
\bar{M}_b	bending moment per unit length
m	mass per unit length
N	axial tensile force
N_0	pure axial tensile force
n	total number of the striking beams
P	interaction force in the impacted zone between two beams

R	ratio of the fracture strain
r	radius
T	temperature
T^*	homologous temperature
T_0	room temperature
T_m	melting temperature
ΔT	temperature rise
t	time
t_1	time duration of the first phase in shear plugging
t_2	time duration of the second phase in shear plugging
t_f	time duration of the shear plugging process
u	indentation depth
u_{cr}	critical indentation depth
u_i	indentation depth at crack formation
u_L	longitudinal displacement
V	transverse velocity
V_0	initial impact velocity
V_0^*	common velocity of the impacted zone and the projectile immediately after impact
$V_{0,u}$	upper bound of the impact velocity for Eq. (4.1)
V_{bl}	ballistic limit
V_{cr}	critical impact velocity to fracture
V_c	critical volume

V_r	residual velocity
ΔV	velocity increment
v	crack propagation speed
v_{\max}	maximum crack propagation speed
\bar{v}	average crack propagation speed
W	energy dissipated
w	transverse deflection
w_0	displacement of the projectile
w_p	deflection of the plug
w_t	deflection of the target
$\Delta w'$	plastic deformation slope increment
x	axial coordinate
α	mass parameter defined in Eq. (7.77)
β	velocity parameter defined in Eq. (7.77)
χ	the fraction of plastic work converted to heat
η	dimensionless parameter defined in Eq. (7.126)
γ	normalized plastic slope defined in Eq. (7.180)
γ_f	shear fracture strain
κ	bending curvature
μ	mass ratio of the impacted zone of the target to the projectile
ν	Poisson's ratio
ϕ	wrapping angle
ϕ_f	critical wrapping angle to fracture

ψ	dimensionless parameter defined in Eq. (7.254)
ρ	density
σ_0	plastic flow stress
σ_h	hydrostatic stress (mean stress)
σ_y	initial yielding stress
$\sigma_\theta, \sigma_r, \sigma_z$	stress components in the cylindrical coordinate system
$\bar{\sigma}$	von Mises stress
τ	time parameter defined in Eq. (7.77)
τ_0	plastic shear flow stress
θ	dimensionless parameter defined in Eq. (7.127)
ε	tensile strain
ε_{\max}	maximum tensile strain
$\bar{\varepsilon}$	effective strain
$\bar{\varepsilon}_f$	fracture strain
$\bar{\varepsilon}_{pl}$	effective plastic strain
$\dot{\bar{\varepsilon}}_0$	reference strain rate
$\dot{\bar{\varepsilon}}_{pl}$	plastic strain rate
ζ	initial length defined in Eq. (7.243)
ξ	location of the stress wave front
ζ	location of neutral axis
$] $	jump of a given quantity
$'$	differentiation with respect to x
\cdot	differentiation with respect to t

Chapter 1

Introduction

1.1 Background and motivation

In the September 11th attack, two airplanes traveling at 264 m/s (590 mph) and 210 m/s (470 mph) crashed, respectively, into the South and North Towers of the World Trade Center [1]. The damage sustained during the impact processes eventually led to the collapse of the Twin Towers. Video clips and graphs clearly show that the exterior columns were cut through by the airplane wings within the first milliseconds of the events, see Fig. 1-1. The disaster of the space shuttle *Columbia* was also closely related to high velocity impact fracture. A breach in the thermal protection system on the left wing of the Orbiter was generated as a piece of insulating foam dropped and struck the wing at a relative velocity of 244 m/s (545 mph) [2]. This tiny crack finally resulted in the breakup of the space shuttle during re-entry.

A question is naturally raised: how to improve the survivability of these critical structures in high velocity impact. Since structural failure is caused primarily by fracture, a fundamental understanding of mechanisms and mechanics of dynamic ductile fracture is one of the most important steps to solve the problem.

As Rosakis and Ravichandran [3] pointed out in a review article, dynamic ductile fracture remains unexplored. Experimentally, it is difficult to track down crack formation and growth, and to capture stress and temperature fields in the vicinity of the tip of a propagating crack using currently available instruments. Most of experimental studies in the

literature concentrated on the examination of post-test specimens. Numerical investigations into dynamic ductile fracture often confront lack of an adequate fracture criterion.



Fig. 1-1: A “clean” cut driven by the wings of a Boeing 767 into the facade of the North Tower [1].

In high velocity impact, fracture often occurs at an impacted zone where compression is dominant. As deflection increases, compression may give way to shear and tension. For such a problem, a fracture criterion formulated and calibrated from tensile tests alone would not be able to predict a realistic fracture mode. A specimen under compression would fail by a different mechanism from that under tension. Recently, a ductile fracture criterion that covers a wide loading range was developed by Bao and Wierzbicki [4, 5] from a series of compressive, shearing, tensile tests and parallel numerical simulations. The Bao-Wierzbicki’s (BW’s) fracture locus seems promising in predicting crack formation and growth in a target under impact loading. The present thesis is also motivated by a need to establish the applicability of this criterion to high velocity impact problems.

1.2 Problem statement

The impact velocities of interest in this thesis fall in the subordnance range. It is commonly accepted by, e.g. Backman and Goldsmith [6], Zukas [7], Goldsmith [8], that the upper limit of the subordnance velocity range is about 500 m/s. At an ordnance velocity, localized pressure may exceed the strength of materials by an order of magnitude and thus a metal would behave more like a fluid. Because of high kinetic energy imparted to a local region, fragmentation is a common failure mode for an armor plate. At a low impact velocity of the same order of the traveling velocity of ground vehicles (about 60 mph = 26.8 m/s), global plastic deformation of a target would be a dominant response rather than fracture. At a velocity in-between these two limiting values, both global deformation of a target and local response of an impacted zone have to be taken into account simultaneously. Fracture is a common phenomenon, and a number of distinct failure modes can be identified from post-test specimens.

The fracture process is a problem of multiple length scales spanning from inter-atomic separation through micro-scale void growth and coalescence to macro-cracking through the thickness and width of structural elements. Various numerical procedures for fracture analysis have been developed at different length scales, e.g. atomistic simulations ($O(10^{-10}$ m)) [9], discrete dislocation plasticity at mesoscale ($O(10^{-7}$ m)) [10], etc. In the present thesis, the problem is attacked in the context of conventional continuum mechanics at a macro scale ($O(10^{-3}$ m)), and fracture of a body is described in terms of stresses, strains, and their histories. Attention is focused on through-thickness crack propagation at a structural component level. This approach is feasible for engineering applications. At the same time, targets of consideration are assumed to be made of ductile metals and do not have any preexisting notches or cracks. This ensures that large plastic deformation would develop in a wide region before fracture and targets would fail by ductile fracture rather than brittle fracture.

1.3 Research objectives

The major objectives of the present thesis are to:

- Numerically recreate a number of macroscopic failure modes including tensile tearing and shear plugging in rigid mass-to-beam impact, confined fracture, petalling, and shear cracking in the Taylor test, and to provide an insight into corresponding fracture mechanisms.
- Study evolution of adiabatic shear bands and subsequent fracture in an axisymmetric hat specimen under dynamic compression, to capture a series of hot spots inside a propagating adiabatic shear band observed in experiments, and to reveal the relation between hot spots and crack formation.
- Demonstrate the applicability of the newly developed Bao-Wierzbicki's ductile fracture criterion to high velocity impact events, and to point out deficiencies of existing fracture models in the literature.
- Propose an analytical expression controlling through-thickness crack growth for a beam/plate impacted by a flat-nosed projectile, and to verify this expression in a wide range of all input variables, and to determine crack propagation speeds in ductile shear plugging.
- Investigate factors causing mesh size sensitivity, to study mesh size effects on growth of cracks and development of adiabatic shear bands, and to determine the reasonable element size.
- Develop, respectively, three theoretical models for rigid mass-to-beam impact, the single impact of beam-to-beam, the multiple impact of a stationary beam by an arbitrary number of striking beams, and to obtain closed-form solutions.
- Build a two-stage theoretical model for shear plugging of a beam/plate under mass impact, and to verify derived analytical solutions.

1.4 Outline of the thesis

The present thesis consists of eight chapters and a bibliography of cited references. The arrangement of the thesis is subject-oriented, i.e. each chapter studies a specific issue associated with high velocity impact. Detailed literature reviews are made on almost each subject.

Chapter 2 critically reviews the applicability of four types of existing fracture approaches in the literature to high velocity impact problems. These approaches include: (i) stress intensity factors and J-integrals, (ii) cohesive element methods, (iii) the Gurson model, and (iv) ductile fracture criteria. This chapter concludes that the last type of fracture procedure is the most suitable to predict crack formation and propagation in a specimen under high intensity stress wave loading.

The newly developed Bao-Wierzbicki's fracture model is one type of ductile fracture criteria. Chapter 3 attempts to assess the effectiveness of the BW's criterion in predicting formation and growth of cracks in high velocity impact cases. Considered are three challenging problems: (i) rigid mass-to-beam impact, (ii) the Taylor test, and (iii) dynamic compression tests on an axisymmetric hat specimen.

Chapter 3.2 investigates the failure response of a beam under rigid mass impact. If the energy imparted by a projectile is sufficiently high, a target would fracture. Depending on various combinations of all the input variables such as impact velocities, specimen and target geometry, etc. many macroscopic failure modes would develop for a single target including fragmentation, shear plugging, tensile tearing, etc. This section offers an insight into corresponding failure mechanisms.

Chapter 3.3 recreates numerically the failure modes and the failure processes of an impacting solid cylinder in the Taylor test. In contrast to rigid mass-to-beam/plate impact, the cylindrical projectile is deformable and susceptible to fracture, and the stationary target is rigid in the Taylor test. The projectile response is dominated by compression during the impact process and thus the Taylor test can be used as a benchmark problem for the examination of a fracture locus in the range of the negative stress triaxiality. Three distinct macroscopic fracture modes are identified from numerical results: confined fracture inside

the cylinder, petalling of the front surface, and shear cracking on the lateral surface.

In contrast to void growth as a basic failure mechanism for a specimen under tension, adiabatic shear banding usually occurs under dynamic compression. Adiabatic shear bands often serve as precursors of ductile fracture, and provide initiation sites and propagation paths for cracks. Chapter 3.4 presents an investigation into adiabatic shear banding and subsequent fracture for an axisymmetric hat specimen under direct compressive Hopkinson bar loading. As opposed to previous research published in the literature, fracture phenomenon is clearly separated from adiabatic shear banding, and crack formation is thought of as a final, catastrophic failure mode in this study.

Chapter 4 focuses on formation and propagation of through-thickness cracks in shear plugging of a beam/plate impacted by a rigid mass moving at a high velocity. First, a crack growth curve relating crack length to indentation depth is proposed. An extensive parametrical study is performed to verify this relationship in a wide range of impact velocities, projectile weight, target thickness, etc. Crack propagation speeds are calculated. Effects of a propagating crack on damage accumulation are investigated.

Chapter 5 discusses three important aspects of numerical prediction of ductile fracture. The first part (Chapter 5.1) introduces the Johnson-Cook material constitutive model. Corresponding material coefficients as well as calibration procedures for three metals: Weldox 460 E steel, 2024-T351 aluminum alloy, 91W-61Ni-3Co tungsten alloy are summarized. The second part reports the implementation of a ductile fracture model in ABAQUS/Explicit. The last part (Chapter 5.3) is devoted to a study of mesh size effects. First, two factors giving rise to mesh size sensitivity: high strain gradients and strain softening, are recognized. The research is conducted, respectively, for two typical problems: perforation of a circular plate by a rigid cylindrical projectile and adiabatic shear banding of a hat specimen under dynamic compression. Finally, Chapter 5.3 discusses four types of methods to remedy mesh size effects.

The first part of Chapter 6 introduces three types of ductile fracture loci: the Bao-Wierzbicki's, the Johnson-Cook's, and the constant critical effective plastic strain. The formulation and the calibration procedure of these criteria are critically reviewed. This survey reveals that there are large differences in the formulation in the range of the negative

stress triaxiality. Effects of the type of ductile fracture loci on the numerical prediction of failure patterns and failure processes are studied through three types of problems that are the same as studied in Chapter 3. The results are presented in Chapter 6.3.

As complementary to the numerical investigations in the preceding chapters, Chapter 7 develops four benchmark analytical solutions. In Chapter 7.2, the momentum conservation approach proposed by Wierzbicki and Hoo Fatt [11, 12] for a string/membrane under rigid, flat-nosed mass impact is revisited. The range of applicability of this approach is determined. The approach is applied to the case of a round-nosed projectile in this section. Obtained closed-form solutions are verified by numerical simulations.

Motivated by the September 11th attack, the momentum conservation approach is extended to the single impact problem of beam-to-beam, in which the striking and struck beams represent the wing of the airplane and one of the exterior columns of the Twin Towers, respectively. Both beams are deformable and fracturable. The closed-form solution is developed in Chapter 7.3 for such a problem. Five fracture scenarios are described and the corresponding conditions are specified. Finite element solutions are pursued to corroborate the theoretical analysis.

The momentum conservation approach is further extended to the multiple impact event of beam-to-beam in Chapter 7.4, in which a stationary beam is impacted sequentially by arbitrary number of beams. This theoretical model is also motivated by the September 11th attack. The striking beams represent structural components of the airplane wing. For simplicity, attention is focused on the impact response of the struck beam. Theoretical solutions for deflection and plastic tensile strain are obtained.

The momentum conservation approach is applicable to a target undergoing large deformation, in which axial stretching is dominated and thus tensile tearing is a favorable failure mode. At a high impact velocity, a target may fail by shear plugging instead of tensile tearing. In Chapter 7.5, the crack growth curve proposed in Chapter 4 is used to develop a theoretical shear plugging model for a beam/plate impacted by a flat-nosed projectile. Closed-form solutions are obtained for residual velocities, ballistic limits, shear zone width, etc. Comparison with experimental results published in the open literature is made showing very good agreements.

Chapter 8 concludes the present thesis, summarizes major results, and suggests future research topics.

Chapter 2

Review of Fracture Approaches in High Velocity Impact

2.1 Stress intensity factors and J-integrals

Several types of fracture approaches have been proposed in the literature to predict crack formation and growth under static and dynamic loading. This chapter attempts to critically review the applicability of these fracture approaches to high velocity impact problems.

Stress intensity factors and J-integrals were developed for specimens with a preexisting notch. This approach found wide applications in predicting response of structural components with a flaw. It is well known from continuum mechanics that the stress and strain fields are singular in the vicinity of a loaded notch tip. Stress intensity factors and J-integrals can be thought of as a measure of the intensity of the singularity field, and correlates the near tip deformation with far-field loading. The critical stress intensity factors and J-integrals, depending on material properties, loading conditions, etc. are able to predict the onset of crack growth. However, these fracture criteria are not suitable for an initially uncracked body. In the present thesis, all the targets considered are assumed to be virgin without any preexisting notches or cracks.

The critical question is whether the critical stress intensity factor or J-integral would be able to serve as a criterion for the prediction of the crack growth once a crack is generated in an initially uncracked body? To answer this question, we need to revisit the development

of the stress intensity factor and J-integral. Recall, that the stress intensity factors are derived from the theory of elasticity and the J-integral was defined based on the small-strain deformation theory of plasticity. For a real, elastic-plastic material, there always exists a *fracture process zone* ahead of a stationary or advancing crack. In this zone, materials are subjected to finite plastic strain and separate microscopically due to void nucleation, growth, and coalescence if a specimen fails by ductile fracture. This deformation and failure mechanisms are beyond the capability of either the theory of elasticity or the small-strain, deformation theory of plasticity. Hence, the utility of the stress intensity factor or the J-integral as fracture criteria would depend on the extent of the so-called K-dominance or J-dominance. In other words, the fracture process zone has to be contained well within the region over which the stress and strain singularity fields provide a good approximation to the real elastic-plastic solution, see Fig. 2-1. This condition is often violated for through-thickness crack formation and growth in an initially uncracked beam/plate of a ductile material. Without any preexisting notches, large plastic deformation would develop in a wide region before the formation of a crack. For a thin or intermediately thick specimen, the fracture process zone, comparable to the plastically deformed region in size, would possess a large part of the target thickness. The K-dominance or J-dominance would not exist in such a case. Hence, neither the stress intensity factor nor the J-integral is an effective fracture criterion for the present problems. By contrast, for a pre-notched plate under in-plane impact, stresses and strains always concentrate in the vicinity of the notch tip, and a crack would be generated and advance in a region still dominated by the stress intensity factors or the J-integral. The critical value of either K or J is applicable as a fracture criterion, as demonstrated by Pandolfi et al. [13] for a three-point bend test specimen with a pre-notch under impact loading.

2.2 Cohesive element methods

As a promising numerical approach to simulate dynamic fracture processes, the cohesive element method that attempts to incorporate the physics of material separation into the numerical formulation has already received much attention, e.g. Needleman [14, 15], Xu

and Needleman [16], Camacho and Ortiz [17], etc. In contrast to conventional finite element procedures, randomly distributed cohesive interface elements are introduced between bulk elements in this method. In addition to the traditional constitutive modeling of the bulk elements, a decohesive law is implemented for the cohesive interface elements.

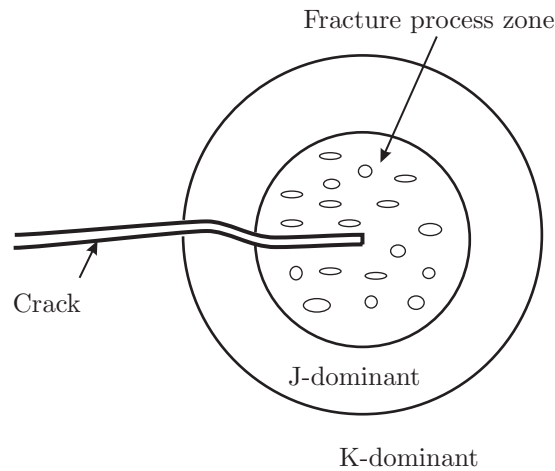
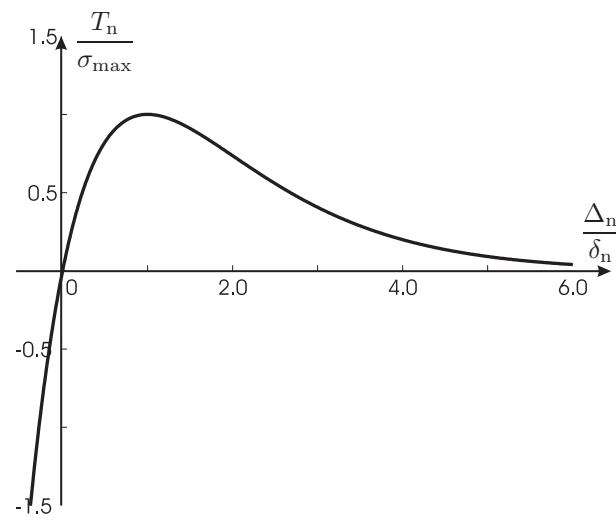


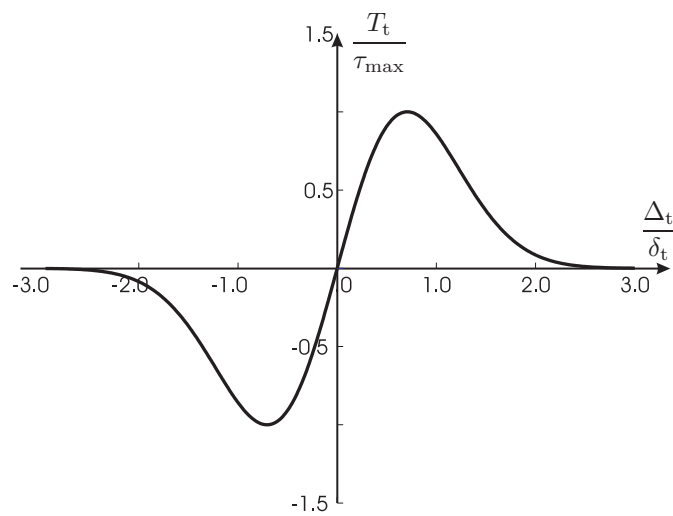
Fig. 2-1: Schematic representation of the fracture process zone, the J- and K-dominant zones ahead of the crack tip.

Many traction-displacement laws have been proposed in the literature, see a short review by Chandra and Shet [18]. A common feature among them is that the traction across the interface reaches a maximum with increasing interfacial separation, then decreases, and eventually vanishes allowing a complete decohesion. Figure 2-2 shows typical normal and shear traction-displacement laws. The area below the curve represents the fracture energy. The cohesive element method was used by Pandolfi et al. [19] to predict dynamic ductile ring expansion, necking, and subsequent fragmentation. The numerical simulations are shown to correlate well with experimental results. However, the critical energy as a criterion for ductile fracture remains controversial. The effective plastic strain and the stress triaxiality are not taken into account in the traction-displacement curve that is essentially stress-dependent. Both factors are believed to be two of the most important parameters controlling ductile fracture. The author believes that this type of the cohesive element method would be more suitable for cleavage fracture of brittle materials rather than for ductile fracture.

Recently, Tvergaard [20, 21] introduced a modified Gurson model to account for the effect of void nucleation inside the cohesive elements for crack growth of a pre-notched plate under small scale yielding conditions. The applicability of this procedure to other types of ductile fracture problems remains to be seen.



(a) Normal traction



(b) Shear traction

Fig. 2-2: Schematic representation of a separation decohesive law.

2.3 The Gurson model

It has long been recognized that the predominant mechanism of ductile fracture is void nucleation, growth, and coalescence. It is also true in dynamic cases. Since McClintock's [22] and Rice and Tracey's [23] pioneer work on the growth of an isolated cylindrical and spherical void embedded in an infinite perfectly-plastic body, two types of approaches for ductile fracture mechanics have been developed in the literature. The first class incorporates damage accumulation into the continuum constitutive model and failing elements eventually lose their load carrying capability. In such a way, the damage softening due to the growth of micro-voids is accounted for in material modeling.

A typical example in this class is the Gurson model. In his well-known Ph.D. thesis, Gurson [24] proposed a general form of the yield function and an associated plastic flow rule for porous metals. This model was modified and improved subsequently by Tvergaard [25], Tvergaard and Needleman [26]. Hence, it is also referred to the Gurson-Tvergaard-Needleman (GTN) model in the literature. The Gurson model has been widely employed to predict various failure modes in dynamic fracture events. For example, Worwick and Pick [27], Addessio et al. [28] simulated, respectively, void growth in the front region of a cylinder in the Taylor test, i.e. confined fracture, which will be addressed in detail in Chapter 3.3. Spallation was captured numerically with the Gurson material constitutive equation in a plate-to-plate impact by Zhou and Clifton [29].

Besides the stress-strain curves for the fully dense matrix material, seven material coefficients in the Gurson model need to be calibrated for a single material. Due to the strong coupling between the material constitutive equation and the damage accumulation, it is not easy to determine these unknown parameters. Extensive applications of the Gurson model in industrial practices would depend on the availability of the material coefficients and the reliability of the calibration procedure.

2.4 Ductile fracture criteria

The second class of ductile fracture approaches uncouples the damage accumulation with the material constitutive equation. The damage accumulation is calculated based on an experimentally/numerically developed fracture locus, and is separated from the evolution of the stress-strain relation. The simulation of crack formation and growth is fulfilled by suddenly setting the stiffness of failing elements to zero or releasing connecting nodes.

Mainly driven by industrial applications, a number of simple ductile fracture criteria have been proposed in the literature, e.g. McClintock [22], Rice and Tracey [23], Hancock and Mackenzie [30], Cockcroft and Latham [31], Bao and Wierzbicki [4], Bao et al. [32], etc. Their effectiveness in the prediction of crack formation for various problems has been assessed by many researchers, e.g. Wifi et al. [33], Komori [34], Bao and Wierzbicki [35], etc. Compared with the Gurson model, these fracture criteria can be relatively easily calibrated and implemented in finite element codes, and thus have been widely used in industrial practices. This type of fracture criteria will be implemented in ABAQUS/Explicit and used throughout the present thesis. We will address the detailed calibration procedure and their features in Chapter 6.

A generic form of ductile fracture criteria can be defined by an integral with respect to the effective plastic strain $\bar{\epsilon}_{pl}$

$$\int_0^{\bar{\epsilon}_{pl}} f(\text{stress states, strain rates, temperature, ...}) d\bar{\epsilon}_{pl} \geq D_c(\text{material}), \quad (2.1)$$

where D_c is the critical damage at the point of fracture, which clearly is an intrinsic property of a material, and f is generally a function of the components or invariants of the stress tensor, strain rates, and temperature, etc. Under quasi-static loading and isothermal conditions, effects of the latter two variables on the damage accumulation can be neglected.

2.4.1 Stress triaxiality

As shown theoretically by McClintock [22] and Rice and Tracey [23] for the growth of microvoids, and experimentally by Bridgman [36] for tensile tests on round bars, hydrostatic pressure (mean stress) has a strong influence on the fracture mode and the fracture strain,

although hydrostatic pressure does not change plastic flow. The stress triaxiality, defined as the ratio of the hydrostatic pressure σ_h to the von Mises stress $\bar{\sigma}$, is commonly introduced in the literature to represent the stress state mentioned in Eq. (2.1). Note, that the hydrostatic pressure is the first invariant of the stress tensor and the von Mises stress is the square root of the second invariant. Both invariants are independent of a coordinate system, and thus suitable for large plastic deformation.

By superposing a constant hydrostatic pressure on a tensile round bar, Bridgman [36] found that the dominant failure mechanism changes from void growth to shear slip as the magnitude of pressure increases. A similar trend was also found by Bao and Wierzbicki [4]. The ability of a specimen to resist fracture, measured by the effective plastic strain at fracture, is a strong function of the stress triaxiality.

We will come back to this issue in Chapter 6 to demonstrate several ductile fracture loci and their calibration procedure.

2.4.2 Strain rates

High velocity impact problems involve large plastic deformation, high strain rates, and elevated temperature. Due to high strain rates, heat generated by a large portion of plastic energy would not have sufficient time to escape to surrounding materials, which leads to temperature rise. Both strain rates and temperature clearly have an effect on fracture characteristics of a specimen.

The effect of strain rates can be simply quantified by a ratio of the experimentally obtained fracture strain under dynamic loading conditions to that under quasi-static loading conditions. Johnson and Cook [37] proposed that this ratio is a logarithmic function of the strain rates

$$R_{\text{strain rate}} = 1 + D_4 \ln \left(\frac{\dot{\epsilon}_{\text{pl}}}{\dot{\epsilon}_0} \right) \quad (2.2)$$

where $\dot{\epsilon}_{\text{pl}}$ and $\dot{\epsilon}_0$ are the actual plastic and reference strain rates, respectively, and D_4 is the material constant. Johnson and Holmquist [38] provided the values of D_4 for more than ten commonly used metals, see Table 2.1 (as quoted by Nicholas and Rajendran [39]). They concluded that generally the strain to fracture slightly increases with the strain rate.

However, some limitations in the determination of the material constant D_4 should be mentioned. As indicated in Ref. [37], D_4 is obtained simply by comparing the fracture strain of a tensile specimen at $\dot{\varepsilon} = 500 \text{ s}^{-1}$ with that at $\dot{\varepsilon}_0 = 1 \text{ s}^{-1}$, i.e. only two test points were used for one material. The strain rate (500 s^{-1}) considered is much lower than the value commonly encountered in high velocity impact events, which is of the order of 10^4 s^{-1} .

Table 2.1: Material constants for the JC's fracture model defined in Eq. (6.2).

Materials	D_1	D_2	D_3	D_4	D_5
OFHC Copper	0.54	4.89	-0.30	0.014	1.12
Cartridge Brass	0.0	2.65	-0.62	0.028	0.0
Nickel 200	0.0	4.04	-1.84	0.0	0.0
Armco Iron	-2.2	5.43	-0.47	0.016	0.63
Carpenter Electric Iron	0.0	3.69	-1.40	0.016	0.63
1006 Steel	0.0	2.07	-1.22	0.016	0.63
2024-T351 Aluminum	0.13	0.13	-1.5	0.011	0.0
7039 Aluminum	0.14	0.14	-1.5	0.018	0.0
4340 Steel	-0.8	2.1	-0.5	0.002	0.61
S-7 Tool Steel	0.0	0.56	-1.5	0.0	0.0
Tungsten	0.0	0.33	-1.5	0.042	0.0
Depleted Uranium	0.0	0.10	-1.5	0.042	0.0
Weldox 460 E Steel [40]	0.0705	1.732	-0.54	-0.015	0.0
AA5083-H116 Aluminum [41]	0.0261	0.263	-0.349	0.147	16.8

More elaborate tensile tests on the strain rate sensitivity of the fracture strain were performed, respectively, by Børvik et al. [40] for Weldox 460 E steel and by Clausen et al. [41] for AA5083-H116 aluminum alloy. The strain rates range from 10^{-4} s^{-1} to 10^3 s^{-1} . The material constant D_4 obtained through curve-fitting are also listed in Table 2.1. It is interesting to note that in contrast to other metals, the ductility of Weldox 460 E steel decreases with the increasing strain rate. The fracture strain of AA5083-H116 aluminum alloy is much more sensitive to that of other materials. These facts show that the strain rate

sensitivity is quite complicated and much work need to be carried out to fully understand these phenomena.

Figure 2-3 shows the variation of the ratio as a function of the strain rate, as quanted by Eq. (2.2). It appears that for 2024-T351 aluminum alloy and Weldox 460 E steel, the difference is less than 20% at the strain rate up to 10^4 s^{-1} . Hence, compared with the stress triaxiality, the effect of the strain rate on the fracture strain can be neglected.

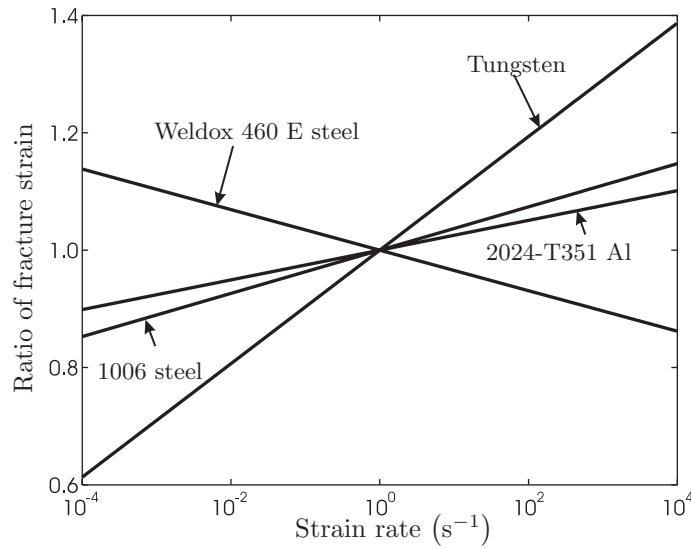


Fig. 2-3: The ratio of the fracture strain vs. the strain rate.

2.4.3 Temperature

Similarly to the strain rate, the effect of the temperature rise can be quantified by a ratio of the fracture strain at an elevated temperature to that at room temperature. The specimens were heated to a certain temperature and then stretched to fracture under quasi-static loading conditions. In such a way, the effect of the strain rate on the fracture strain can be isolated from that of the temperature rise. Johnson and Cook [37] suggested a linear relationship between the ratio of the fracture strain and the temperature rise

$$R_{\text{temperature}} = 1 + D_5 T^* \quad (2.3)$$

where D_5 are the material constant and its values for different materials are given in Table 2.1, and T^* is the homologous temperature, defined by

$$T^* = \frac{T - T_0}{T_m - T_0}, \quad (2.4)$$

where T is the current temperature, T_0 is the room temperature, and T_m is the melting temperature. The values of D_5 for more than ten metals were given by Johnson and Holmquist [38] as quoted by Nicholas and Rajendran [39], and are also listed in Table 2.1. It is understood that Eq. (2.3) does not apply to fracture at very low temperature.

Figure 2-4 shows the ratio of the fracture strain as a function of temperature for Weldox 460 E steel. This graph is re-plotted using the experimental data provided by Børvik et al. [40]. It is seen that the fracture strain does not change much for the temperature rise lower than 300 K but suddenly increases above this value.

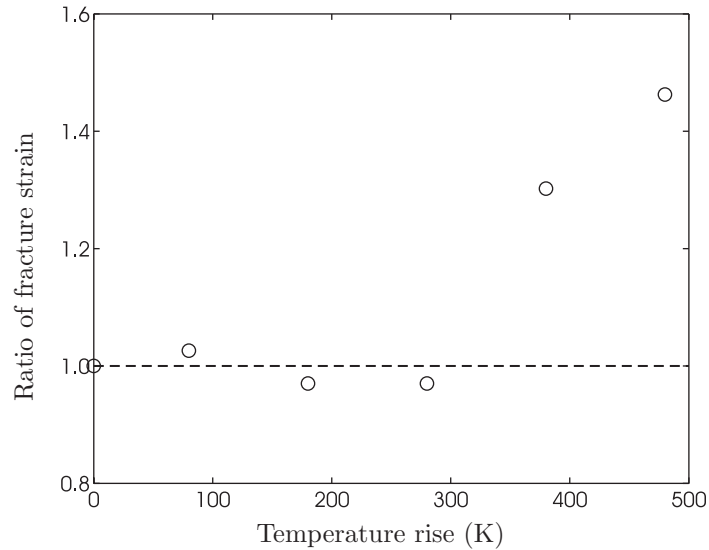


Fig. 2-4: The ratio of the fracture strain vs. the temperature rise. The circles represent the experimental results by Børvik et al. [40].

By assuming adiabatic conditions, a local temperature rise ΔT during an impact process can be quickly estimated from energy balance

$$\Delta T = \chi \frac{\sigma_0 \bar{\epsilon}_f}{\rho c_v} \quad (2.5)$$

where ρ is the material density; c_v is the specific heat; σ_0 is the plastic flow stress; $\bar{\epsilon}_f$ is the fracture strain; and χ is the fraction of plastic work converted to heat. It is generally accepted that $\chi \cong 0.9$ [42]. At $\bar{\epsilon}_f = 1.0$, the temperature rise calculated from Eq. (2.5) is $\Delta T \approx 210$ K for Weldox 460 E steel and 2024-T351 aluminum alloy. This temperature rise is lower than 300 K in Fig. 2-4. Hence, it can be concluded that temperature rise due to adiabatic conditions would not have much influence on fracture characteristics of a specimen made of Weldox 460 E steel.

Chapter 3

Qualitative Analysis of Failure

Modes

3.1 Introduction

High velocity impact problems have long been studied from various aspects. A comprehensive survey on the mechanics and physics of projectile impact was performed by Backman and Goldsmith [6] up to 1977, by Anderson and Bodner [43] up to 1988, and by Corbett et al. [44] up to 1994. Goldsmith [8] summarized investigations into non-standard collisions, penetration, perforation of targets, e.g. oblique impact. There are also several excellent books in this area, e.g. Johnson [45], Zukas et al. [46] and Zukas [47], etc. From these references, the reader can trace backwards to a number of earlier contributions.

Many macroscopic failure modes have been identified from high velocity impact experiments in the literature. For example, Woodward [48] classified more than ten possible failure modes for a target struck by a rigid projectile, see Fig. 3-1. An occurrence of a specific failure mode would depend on material properties and geometry of an impacting system.

These experimental observations impose a challenging problem: can one use a single fracture criterion to capture all the possible macroscopic failure modes in high velocity impact events? Should the basic failure mechanism of all these macroscopic fracture modes be void nucleation, growth, and coalescence, then the answer to this question should be

simple. Recently, a new ductile fracture locus that covers a whole range of the stress triaxiality was developed by Bao and Wierzbicki [4, 5]. This fracture criterion involves three distinct branches, each controlled by a different fracture mode.

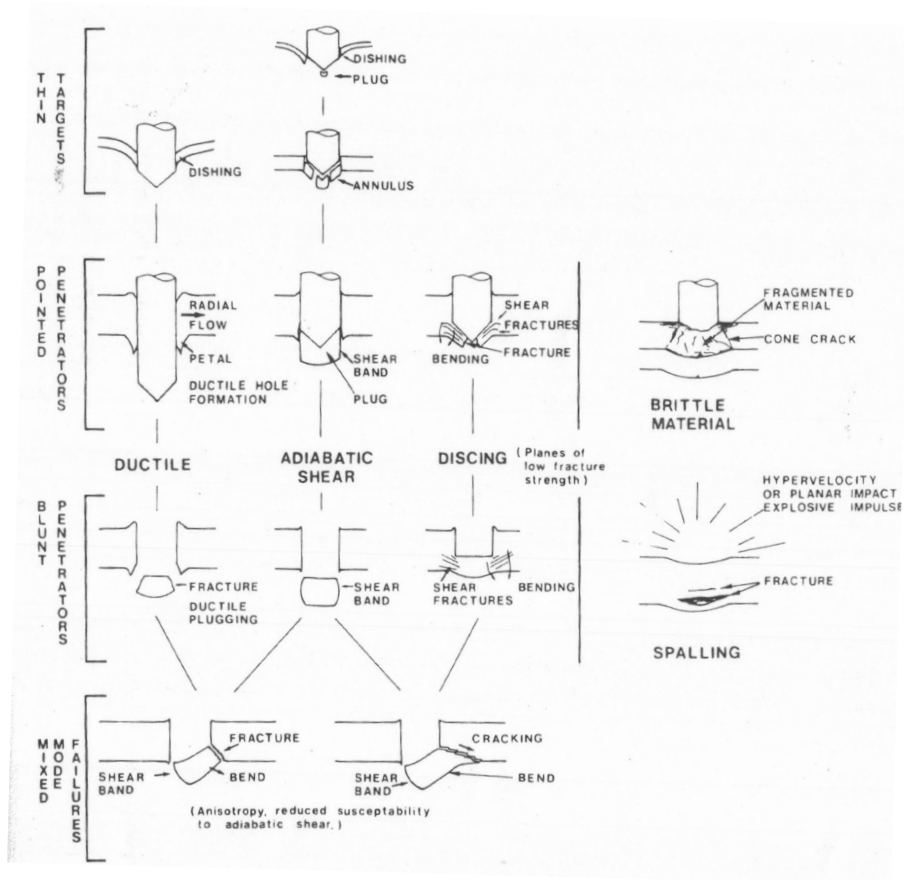


Fig. 3-1: Schematic representation of more than ten possible fracture modes in perforation problems [48].

The objective of the present chapter is to examine the applicability of the Bao-Wierzbicki's ductile fracture criterion to various high velocity impact problems, and to investigate the corresponding fracture mechanics and processes. This goal is achieved through studying three typical and challenging problems in impact engineering. The first problem considered is rigid mass-to-beam impact, in which a target beam is at rest and a rigid projectile moves at a high velocity. The struck beam may fail by either tensile tearing, shear plugging, or a

combined action, which compete with each other. A study on this problem will be presented in Chapter 3.2.

The second impact problem is the Taylor test. In contrast to rigid mass-to-beam impact, a striking cylinder is deformable and breakable while a struck body is assumed to be rigid in the Taylor test. At a sufficiently high impact velocity, a projectile may exhibit various failure modes: petalling, shear cracking, or confined fracture. Numerical recreation of these macroscopic fracture modes using a three-dimensional finite element model is the subject of Chapter 3.3.

Different from void growth under tension, adiabatic shear banding, one kind of thermo-plastic instability, usually occurs in a continuum body predominated by compression. A shear band often serves as a site for crack formation and a weak path for crack propagation. Chapter 3.4 will be devoted to reveal the mechanism of adiabatic shear banding and subsequent fracture for an axisymmetric hat specimen under dynamic compressive loading.

It should be mentioned that the newly developed BW's fracture locus also successfully captured two other failure modes: spallation and fragmentation, both of which will not be addressed in the present thesis. Figure 3-2 shows a spalling failure pattern of plate-to-plate impact, in which a thick circular plate is impacted by a flying thin plate made of the same material [49]. A crack is generated by the interaction of incident and reflected stress waves through the thickness of both plates. Similarly to tensile tearing and shear plugging in rigid mass-to-beam/plate impact, the basic fracture mechanism behind the spallation is also void nucleation, growth, and coalescence. However, different from shear plugging and tensile tearing, the failure process of spalling is controlled by high stress triaxialities and low plastic strain amplitudes. Figure 3-3 shows fragmentation of an elastic-plastic ring under implosive loading.

The objective of the subsequent sections is to demonstrate that using a single fracture criterion one would be able to predict with a great realism a variety of failure patterns in high velocity impact problems.

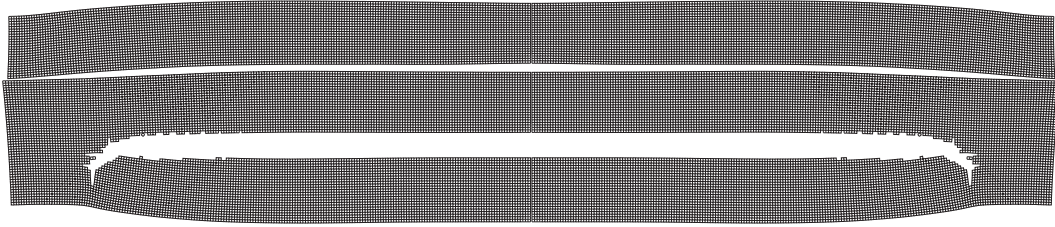


Fig. 3-2: Spallation of plate-to-plate impact. Both circular plates are made of 2024-T351 aluminum alloy. The initial impact velocity is $V_0 = 350$ m/s.



Fig. 3-3: Fragmentation of a ring under explosive loading.

3.2 Failure modes in rigid mass-to-beam impact

3.2.1 Introduction

This section studies the failure response of a beam under rigid mass impact. Immediately upon impact, a compressive stress wave is generated and propagates through the target thickness. The impacted zone of the target beneath the projectile is dominated by compression and shear in the initial phase. As transverse disturbances (transverse plastic stress waves) travel away from the impacted zone, the target acquires the transverse momentum and is deflected. As the deformation of the target increases, compression and shear will give way to bending and subsequently axial stretching. Depending on various combinations of all the input variables such as the impact velocity and weight of the projectile, a single target may exhibit various macroscopic fracture modes. For example, a target would be either sheared off in the initial phase or torn apart in the later phase.

The problem of rigid mass impact on a beam/plate has long been investigated, mostly experimentally, to understand the failure mechanism. Goldsmith and Finnegan [50] discussed effects of material properties and presented two pictures of post-mortem specimens clearly showing distinct failure modes for steel and aluminum plates. Corran et al. [51] performed a series of tests by changing the aspect ratio of the projectile nose diameter to the target thickness. They found that the target plate fails by tensile tearing at a small ratio while by shear plugging at a large ratio. Levy and Goldsmith [52] summarized a number of experimental results for thin plates. Failure modes such as petalling, shear plugging, tensile tearing were identified. Low velocity impact experiments of a very heavy projectile on a beam/plate ($V_0 < 10$ m/s) were conducted by Jones & Jones [53] and Shen et al. [54], respectively, in which necking preceding tensile tearing was identified at impacted points and boundaries. Børvik et al. [55, 56] systematically carried out perforation tests on a circular plate struck by a cylindrical projectile of a flat, round, and conical nose in parallel with a series of numerical simulations.

Compared with the abundance of experimental studies, papers on numerical simulations appear to be scarce. This situation may result from a lack of an adequate ductile fracture criterion. The newly developed Bao-Wierzbicki's fracture locus could hopefully fill partially

this gap. In this section, the failure process of a wide beam impacted by a rigid, round-/flat-nosed projectile is simulated using ABAQUS/Explicit [57]. Two materials: 2024-T351 aluminum alloy and Weldox 460 E steel, are considered, respectively. The impact velocity of the projectile ranges from 180 m/s to 600 m/s so that various failure modes can be generated. Attention is focused on the identification of the failure mode and the investigation of the failure mechanism.

3.2.2 Finite element modeling

Consider a long beam of solid, rectangular cross-section impacted by a rigid, round-nosed (flat-nosed) projectile, see Fig. 3-4. The beam is of the length $l = 1000$ mm, the width $2b = 100$ mm, and the thickness $h = 10$ mm. The rigid projectile is of the diameter (breadth) $d = 20$ mm, and the mass ratio of the impacted zone of the target to the projectile $\mu = 0.1$. The mass ratio is defined in Eqs. (4.2) and (4.3), respectively, for the beam and circular plate cases. The initial impact velocity V_0 is varied from 180 m/s to 400 m/s for the 2024-T351 aluminum beam and from 240 m/s to 600 m/s for the Weldox 460 E steel beam.

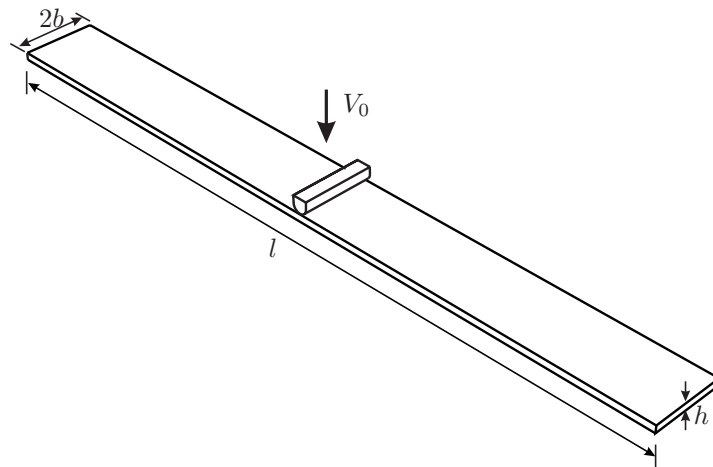


Fig. 3-4: Schematic representation of a long beam struck by a rigid, round-nosed mass.

Since a main interest of the present study is on crack formation and propagation through the target thickness, a two-dimensional finite element model was built to reduce computational costs. 4-node plane strain elements (CPE4R) in the ABAQUS/Explicit element library was adopted, considering that the width of the beam is much larger than the thickness. The projectile was represented by a rigid surface. The “hard” contact constraint, which allows the projectile to rebound from the target, was applied at the impact interface. At the same time, interaction between the rigid mass and the beam was assumed to be frictionless.

Very fine square meshes with the size $0.2 \text{ mm} \times 0.2 \text{ mm}$ were generated in the impacted zone and relatively coarse meshes for far fields, see Fig. 3-5. There are fifty elements through the beam thickness. The technique of element removal was used to model crack formation and growth. Therefore, the element size in the critical area has to be very small to keep the loss of mass and energy minimum. A detailed study on mesh size sensitivity addressed in Chapter 5.3 indicates that the present element size is able to give a correct solution.

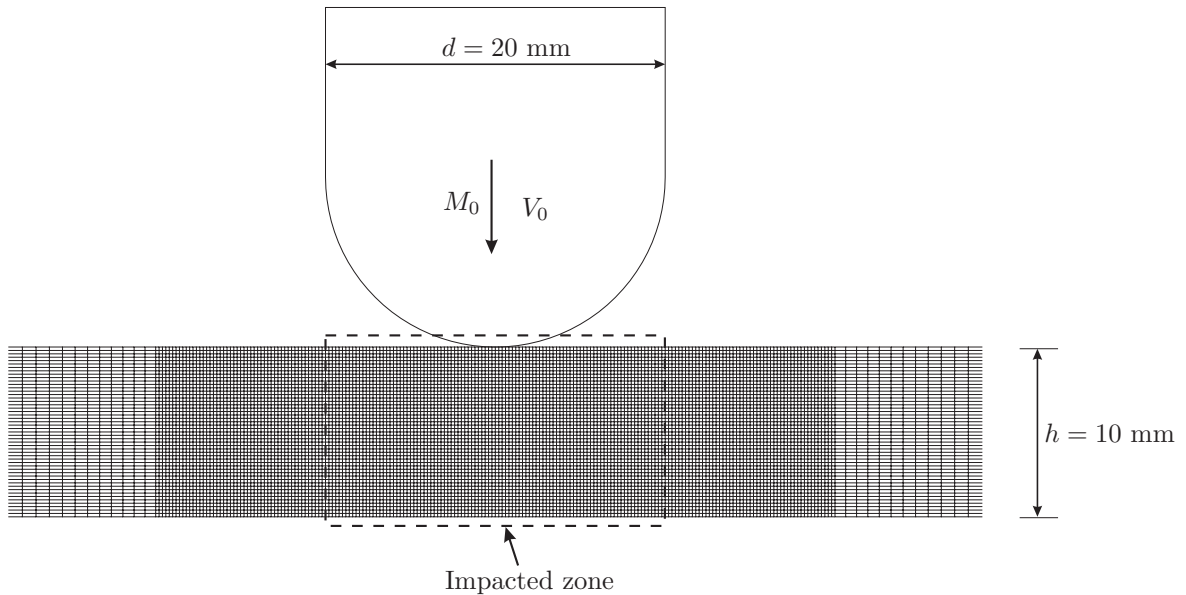


Fig. 3-5: Finite element model of a beam impacted by a rigid, round-nosed projectile.

The fixed boundary condition was prescribed at both ends of the beam. The beam is sufficiently long so that it would break before transverse plastic stress waves arrive at the ends at an impact velocity even well in excess of the ballistic limit of the beam. However, the boundary conditions will play a role at a relatively low impact velocity, and the whole beam undergoes plastic deformation before fracture.

Considered in the present research were two materials: 2024-T351 aluminum alloy and Weldox 406 E steel, representing a less and a more ductile metal, respectively. The Johnson-Cook's (JC's) material constitutive model was defined in the calculation. The detailed discussion on the JC's model and the determination of the material coefficients for both materials will be addressed in Chapter 5.1. The Bao-Wierzbicki's fracture locus was implemented for 2024-T351 aluminum alloy. The Weldox 460 E steel fracture locus calibrated by Børvik et al. [40] was modified to include the cut-off value for the negative stress triaxiality. Both fracture loci will be critically reviewed in Chapter 6.

3.2.3 Tensile tearing

Compression and shear are dominant in the impacted zone immediately after impact. If the target does not fail in this phase, it will enter into the phase in which bending and subsequently axial stretching are dominant as the transverse deflection increases. Tensile stresses due to either/both of bending and axial stretching would lead to crack formation and growth in the struck beam. This is similar to the Mode I fracture mode in the classical elastic fracture mechanics (EFM). However, the problem considered here is more complicated since ductile fracture is controlled by not only stress states but also plastic deformation. Both depends on mechanical properties and geometrical size of the impact system. In the following, the fracture pattern and fracture mechanism of tensile tearing in rigid mass-to-beam will be investigated.

3.2.3.1 2024-T351 aluminum alloy

Figure 3-6 shows the formation and propagation of a crack for the aluminum beam at $V_0 = 220$ m/s. The crack initiates at the proximal surface of the beam and then propagates slantly through the thickness. The two end points of the crack, located at the proximal and distal surfaces of the beam, respectively, are selected to reveal the failure mechanism. It can be seen from Figs. 3-7 and 3-8 that local bending response is dominant in the impacted zone in the initial phase. The point at the proximal surface is predominantly under compression ($\sigma_h/\bar{\sigma} \approx -0.8$) while the point at the distal surface under tension ($\sigma_h/\bar{\sigma} \approx 1/\sqrt{3}$). The local bending direction is changed at $t \approx 0.2$ ms. The stress state of the upper part of the impacted zone becomes positive indicating predominant tension. Damage rapidly accumulates in this phase until the crack is formed. As the crack grows downwards, the ligament becomes shorter. The end point at the distal surface is still dominated by compression due to local bending. Finally, the remainder of the ligament is completely sheared off. Correspondingly, both the stress triaxiality and the effective plastic strain suffer a jump at fracture, see Fig. 3-8. A conclusion can be drawn that the crack formation is mainly due to tension and the crack growth is driven by tension/shear. Fracture may also depend on the history effect as the sign of the triaxiality changes from compression to tension [58]. The history effect is not pursued further in this study.

It is not easy to identify a specific failure mode from a final fracture pattern of a specimen under complex multi-axial loading. To some extent, it would rely on an observer's experience and knowledge. By tracking down the time history of the stress triaxiality and the effective plastic strain, the failure mode can be discerned in a simple way as demonstrated here.

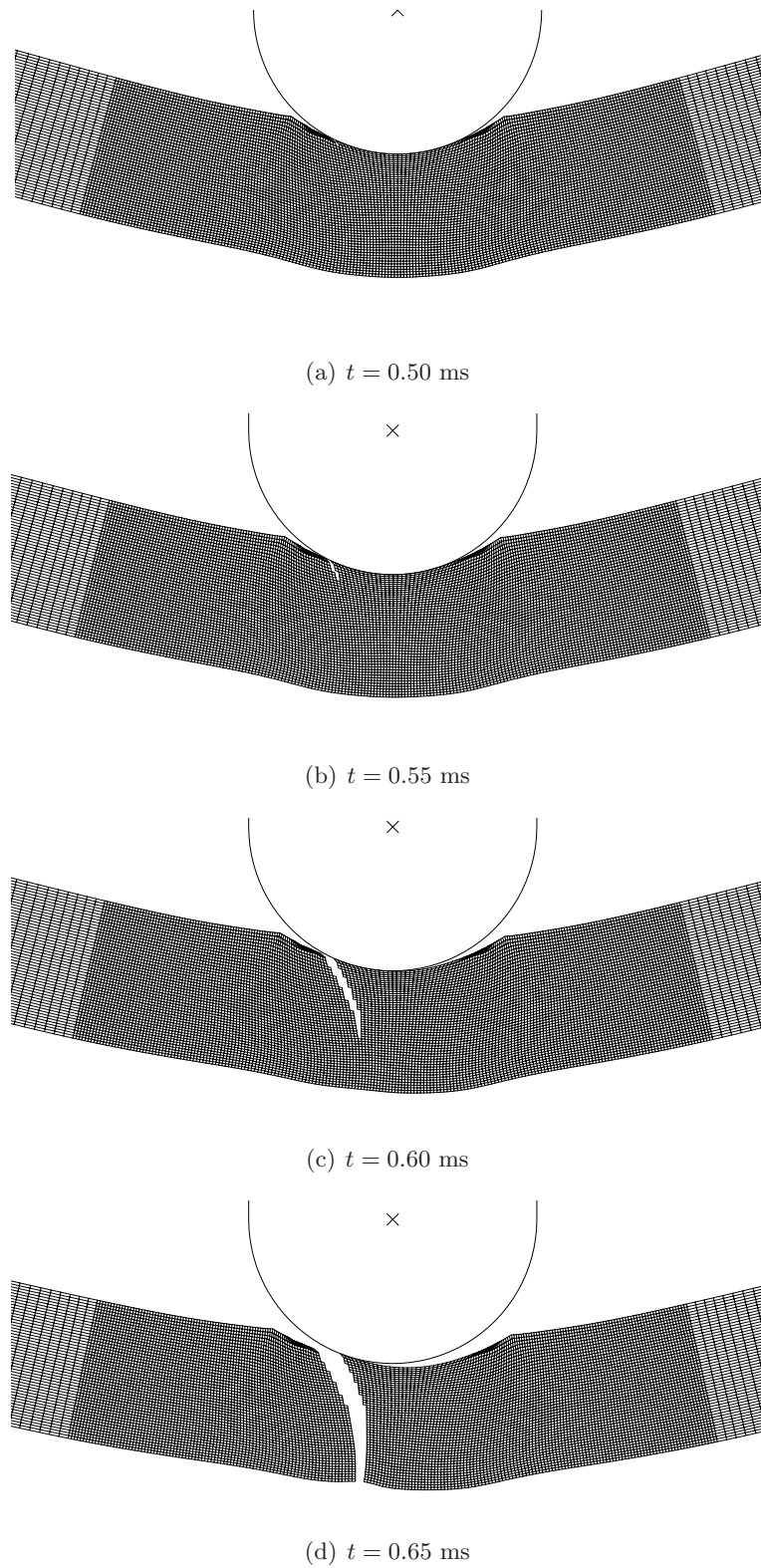


Fig. 3-6: Failure process of the 2024-T351 aluminum alloy beam impacted by the round-nosed mass at $V_0 = 220$ m/s.

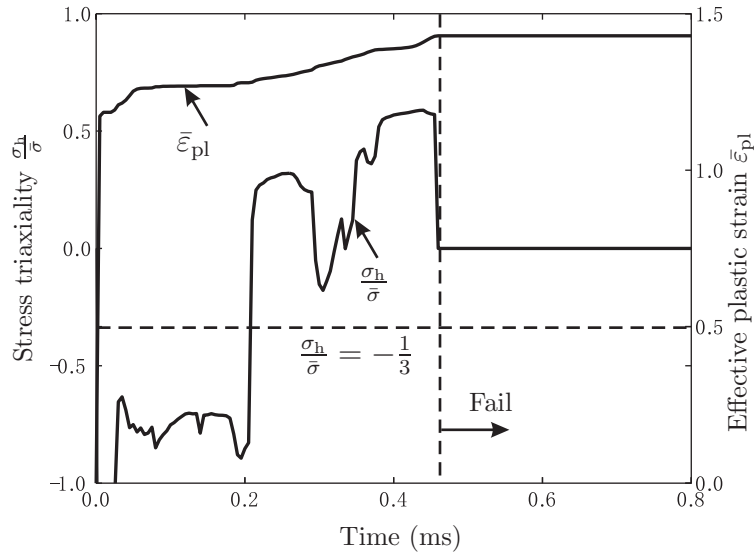


Fig. 3-7: History of the effective plastic strain and the stress triaxiality of the starter point of the crack located at the proximal surface of the 2024-T351 aluminum beam at $V_0 = 220$ m/s.

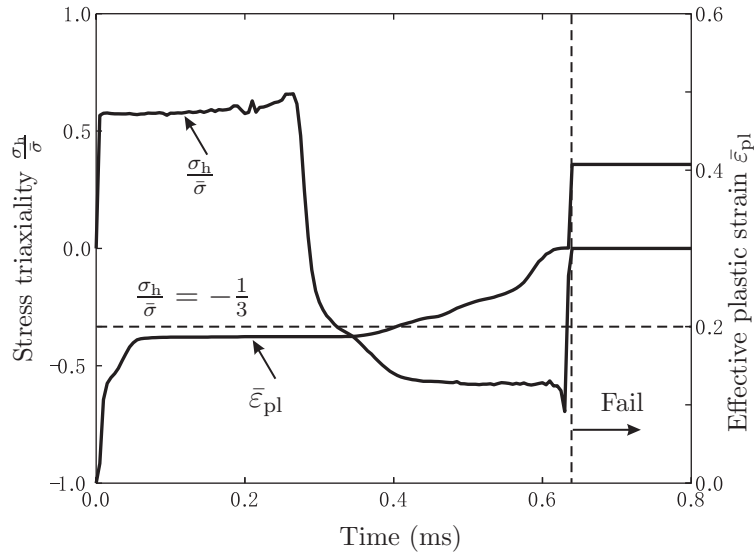


Fig. 3-8: History of the effective plastic strain and the stress triaxiality of the end point of the crack located at the distal surface of the 2024-T351 aluminum beam at $V_0 = 220$ m/s.

3.2.3.2 Weldox 460 E steel

As shown in Fig. 3-6, thinning or necking preceding fracture is not evident in the impacted zone, though the aluminum alloy beam fails by tensile tearing. Due to its lower ductility, the aluminum beam breaks before entering into the axial stretching dominated phase. But this is not the case for the more ductile Weldox 460 E steel beam. As shown in Fig. 3-9, the impacted zone of the steel beam becomes quite thin due to local axial stretching at $V_0 = 375$ m/s. This through-thickness thinning is also called localized necking. A crack initiates first on the distal surface of the necking area and propagates upwards. Then two cracks occur on the proximal surface and grow downwards (one of them is arrested). Finally, these cracks link together to form a through-thickness gap. Clearly, the crack formation on the distal surface is purely due to tension. The crack starter point on the distal surface is selected to track down its time history of the stress triaxiality and the effective plastic strain, see Fig. 3-10. It appears that the stress triaxiality is almost kept constant during the impact process and is very close to 0.58. $\sigma_h/\bar{\sigma} = 1/\sqrt{3}$ is the exact value for a plane-strain block under uniaxial tension. At the same time, the crack propagation is driven mostly by the axial tensile force since the generated crack is located almost at the central axis of the beam, see Fig. 3-21(d).

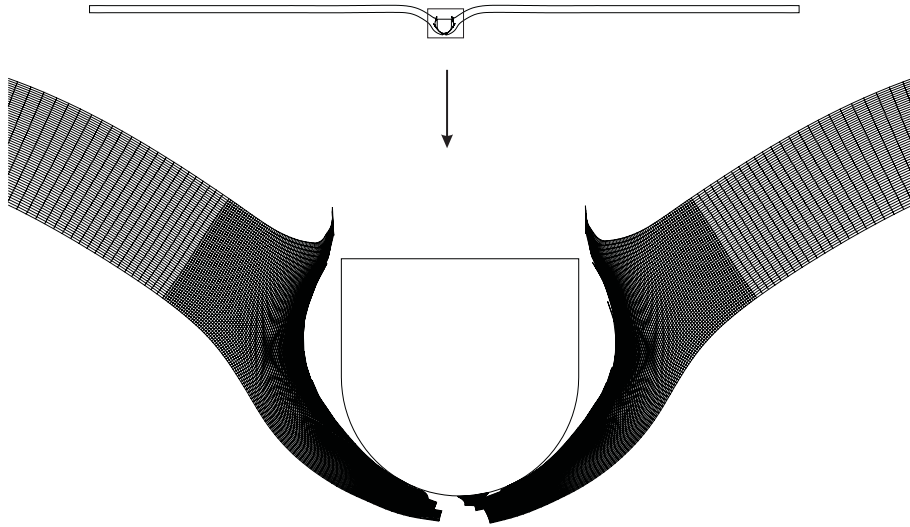


Fig. 3-9: Crack formation in the Weldox 460 E steel beam struck by the round-nosed mass moving at $V_0 = 375$ m/s.

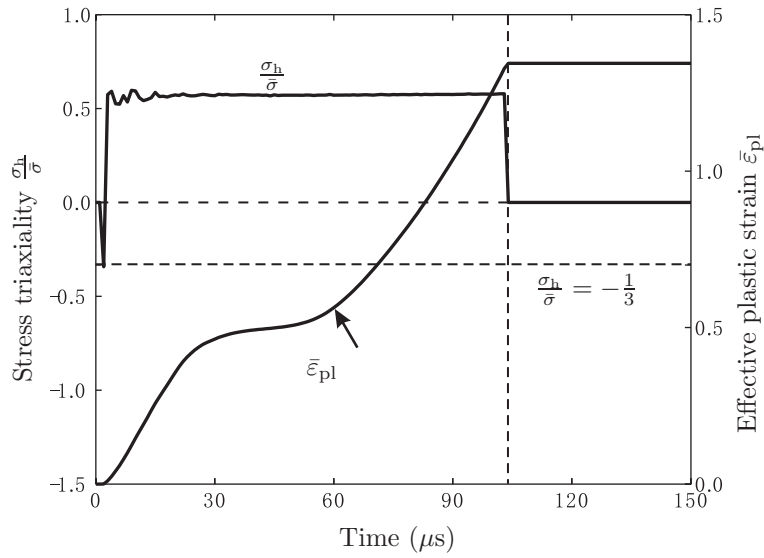


Fig. 3-10: History of the effective plastic strain and the stress triaxiality of the starter point of the crack located at the distal surface of the Weldox 460 E steel beam at $V_0 = 375$ m/s.

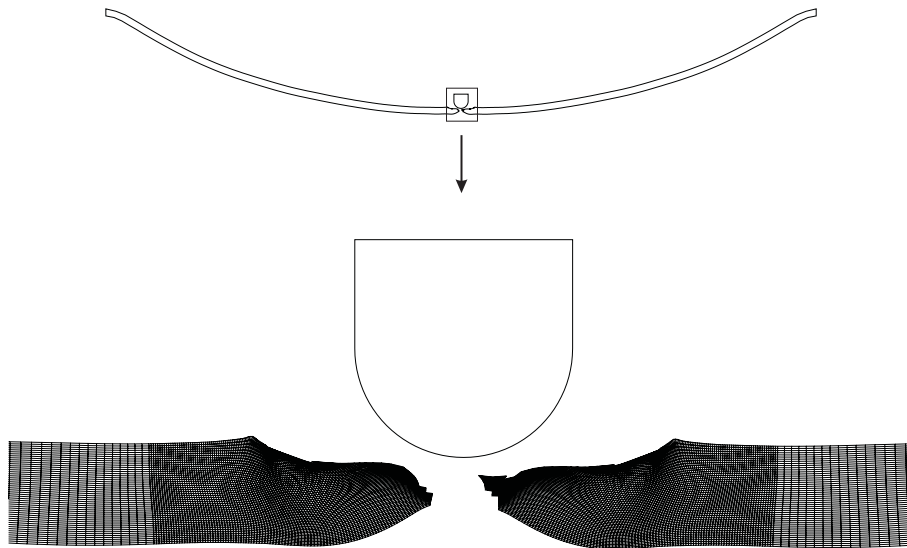


Fig. 3-11: Diffuse necking preceding fracture for the Weldox 460 E steel beam impacted by the rigid mass moving at $V_0 = 250$ m/s.

At an impact velocity near the ballistic limit, one can say that diffuse necking precedes crack formation, see Fig. 3-11. Also, the global deformation of the beam reaches the clamped ends at necking. The maximum transverse deflection is several times larger than the target thickness. Since both ends of the beam are fixed, large axial tensile force would develop. Axial stretching is mainly responsible for necking and subsequent tensile tearing of the impacted zone.

3.2.3.3 Thin vs. thick beams

Besides the material ductility, the aspect ratio of the target thickness to the diameter of the projectile also has an effect on the formation of a specific failure mode. Figure 3-12 shows the failure process of a 2024-T351 aluminum alloy beam of $h = 2$ mm ($h/d = 0.1$) at $V_0 = 270$ m/s, in which the weight of the projectile was adjusted to keep the mass ratio $\mu = 0.1$ same as the previous cases (Note, that the thickness of the previous considered beam was $h = 10$ mm). It is seen that two cracks initiate at the distal surface due to tension, and grow upwards until a plug is formed. This type of tensile tearing process was observed in a wide range of the impact velocity from the ballistic limit $V_{bl} = 205$ m/s to $V_0 = 400$ m/s for this beam. By contrast, shear plugging is the favorable failure mode for the aluminum beam of $h/d = 0.5$ under the same impact conditions. This numerical finding that thin beams tend to fail by tensile tearing is consistent with experimental observations by Levy and Goldsmith [52], see Fig. 3-13.

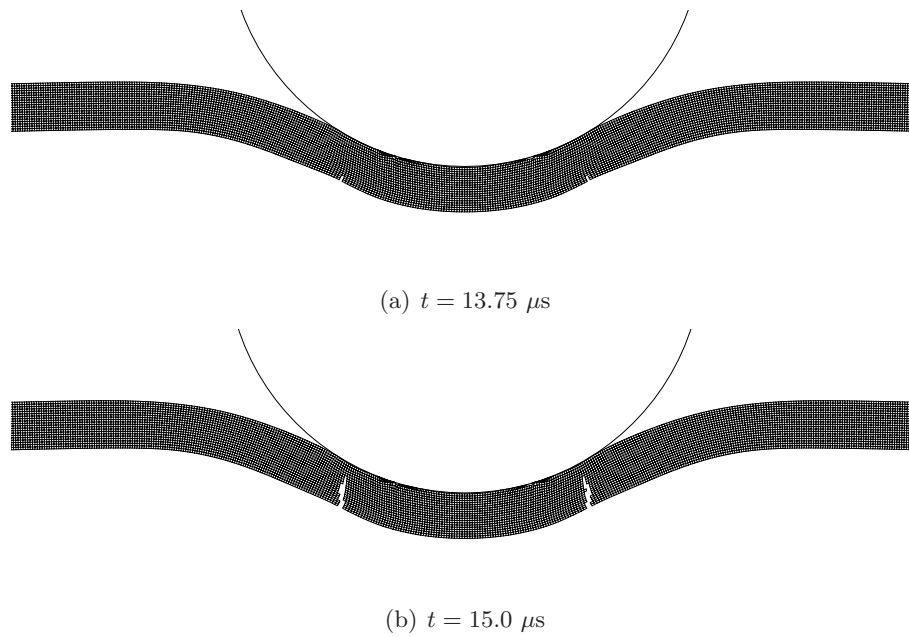


Fig. 3-12: Failure process of the round-nosed mass impact on the aluminum alloy beam of $h = 2 \text{ mm}$ and $\mu = 0.1$ at $V_0 = 270 \text{ m/s}$.

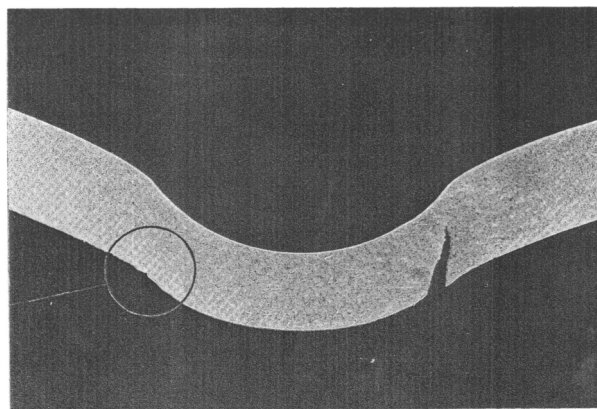


Fig. 3-13: Tensile tearing of a 2024-0 aluminum circular plate of $h = 1.27 \text{ mm}$ struck by a round-nosed projectile of $d = 12.7 \text{ mm}$ at $V_0 = 89.6 \text{ m/s}$ [52].

3.2.4 Through-thickness shear plugging

Competing with tensile tearing, shear plugging is another possible failure mode in rigid mass-to-beam impact. At a high velocity, a beam would tend to be cut through in the impacted zone due to localized compression and shear before undergoing large global plastic deformation. Similarly to the Mode II in the classical elastic fracture mechanics, the formation and propagation of the crack in shear plugging is propelled mainly by the shear force. The failure mode and failure mechanism of shear plugging will be studied next for the flat-nosed and round-nosed projectiles, respectively.

3.2.4.1 Flat-nosed projectile

Figure 3-14 shows the shear plugging process of the aluminum alloy beam impacted by the flat-nosed rigid mass moving at $V_0 = 240$ m/s. The thickness of the beam is $h = 10$ mm and the aspect ratio of the beam thickness to the projectile diameter is $h/d = 0.5$. It appears that the region of the beam below the projectile is deeply indented and undergoes large plastic deformation, but no elements fail in this zone throughout the impact process since compression is dominant. As the impacted zone deepens into the projectile, the stress concentration occurs around the sharp corners and the elements in this region are severely distorted due to shear. Two cracks are induced on the proximal surface of the beam, and rapidly propagate through the beam thickness ahead of the projectile. Finally, a plug is formed and ejected from the beam. It is seen that the global deformation of the beam is much smaller than the target thickness. This failure process is characterized by indentation of the impacted zone and through-thickness crack propagation. The existence of the two-phase deformation mode will help to develop a theoretical model of shear plugging, which will be presented in Chapter 7.5.

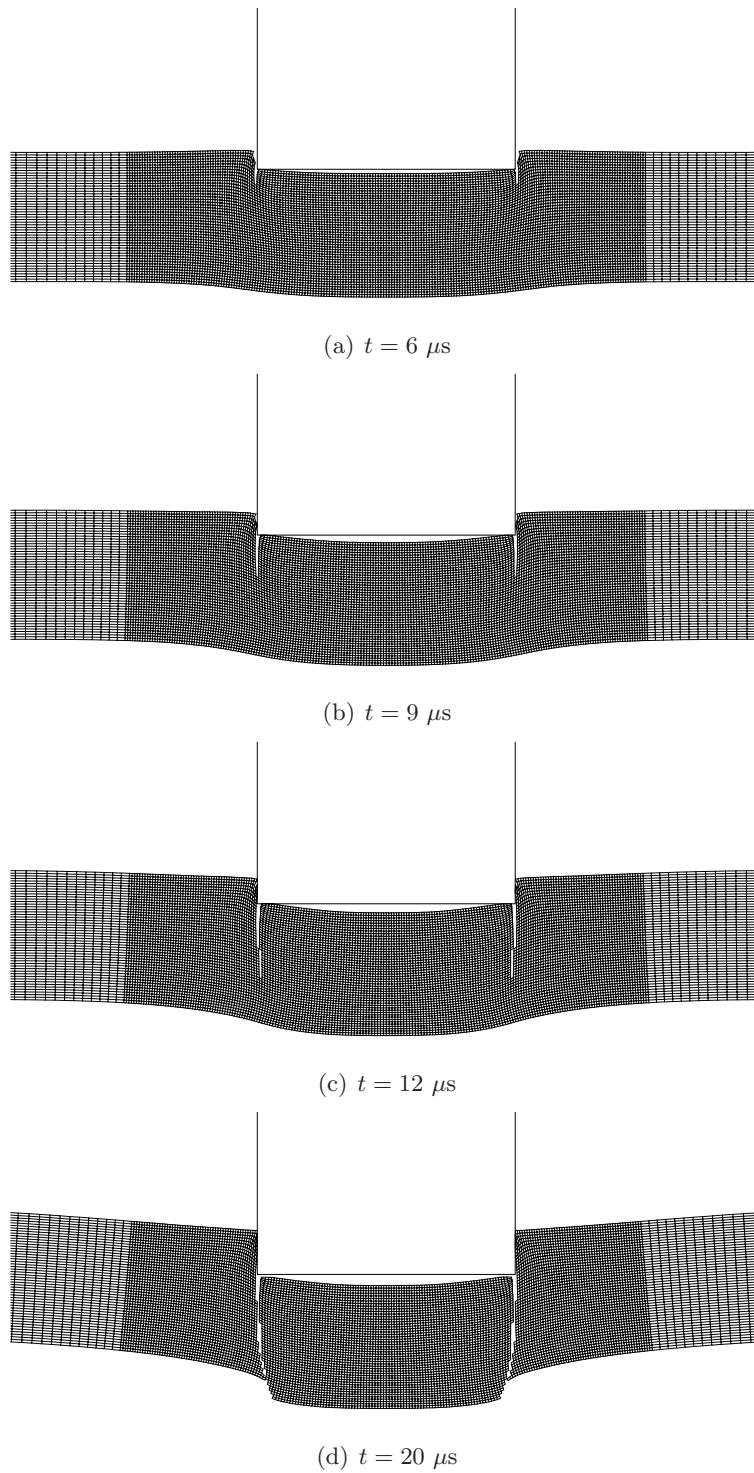


Fig. 3-14: Perforation process of flat-nosed mass impact on the aluminum alloy beam at $V_0 = 240$ m/s.

3.2.4.2 Round-nosed projectile

In the case of a round-nosed projectile the failure process is different. Cracks initiate in the middle of the beam and propagate upwards and downwards at the same time. As shown in Fig. 3-15, two through-thickness cracks are generated and subsequently a plug is formed and ejected at $V_0 = 300$ m/s. The failure pattern corresponds to the so-called discing in the case of a circular plate, which is commonly seen in the literature. The fracture mode can be discerned by observing the history of the stress triaxiality during the impact process, see Fig. 3-16. As the compressive stress wave, generated immediately upon impact, passes through the impacted zone, the crack starter point is predominantly under compression, represented by the stress triaxiality lower than $-1/3$. After $t = 9 \mu\text{s}$, the stress triaxiality falls mainly in the range from $-1/3$ to 0, in which fracture is controlled mainly by shear decohesion [4]. A large part of damage accumulates in this phase. We believe that bending response does not much contribute to crack initiation since the crack starter point is located in the middle of the beam thickness.

At a much high impact velocity, the beam would fail by fragmentation. But the basic failure mechanism behind it is still shear cracking. Figure 3-17 shows the failure process of the aluminum alloy beam at $V_0 = 400$ m/s. It appears that four sequential cracks initiate in the middle of the beam, and grow through the thickness. The energy imparted by the rigid mass exceeds the carrying capability of the impacted zone of the beam at such a high velocity that it has to break into three pieces to dissipate the available kinetic energy. This failure pattern is similar to the experimental results presented by Goldsmith and Finnegan [50], see Fig. 3-18, in which a 2024-T4 aluminum plate of $h = 6.35$ mm struck by a hard-steel sphere of $d = 6.35$ mm at $V_0 = 863.52$ m/s broke into three pieces. A gradual transition from shear plugging to fragmentation with the increasing impact speed has been successfully predicted by the present fracture model.

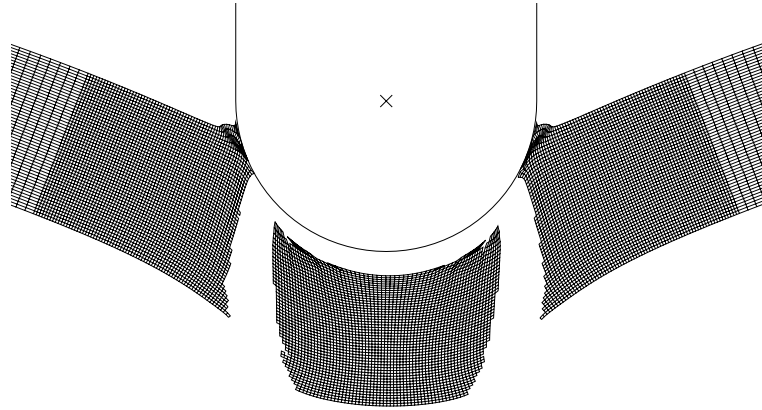


Fig. 3-15: Failure pattern of the 2024-T351 aluminum alloy beam impacted by the round-nosed mass at $V_0 = 300$ m/s.

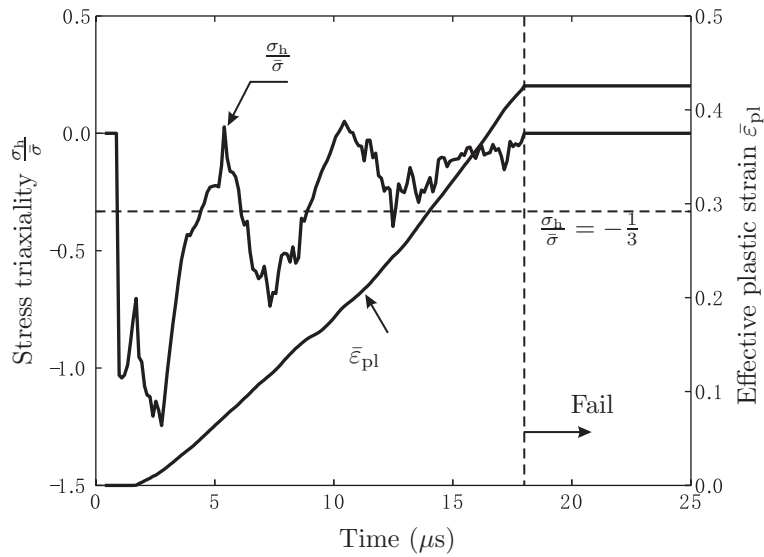


Fig. 3-16: History of the effective plastic strain and the stress triaxiality of the starter point of the crack located in the middle of the thickness for the aluminum beam at $V_0 = 300$ m/s.

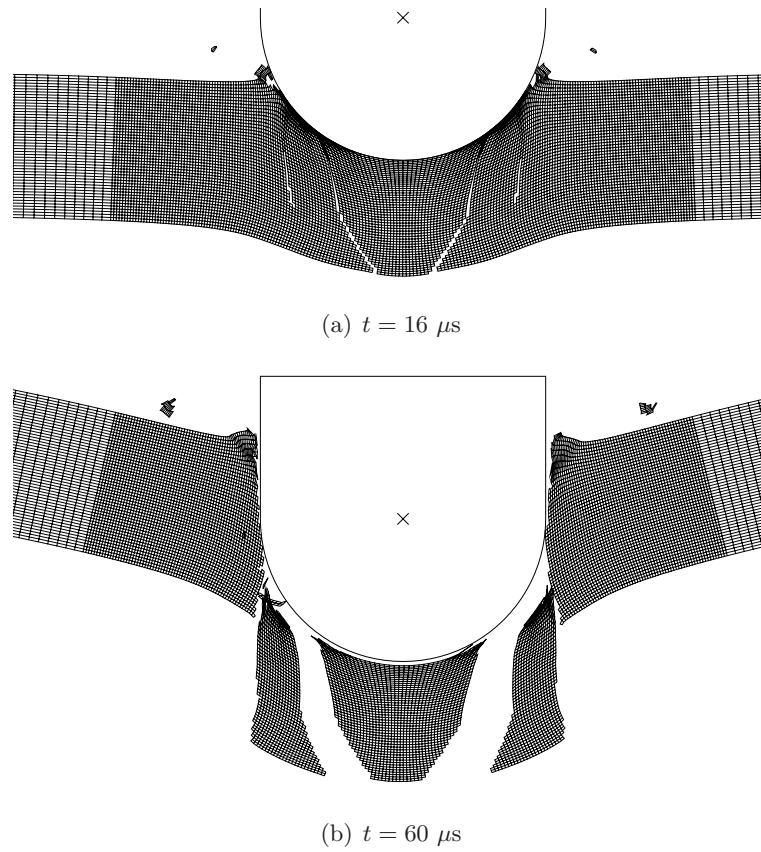


Fig. 3-17: Failure process of the 2024-T351 aluminum alloy beam impacted by the round-nosed mass at $V_0 = 400$ m/s.

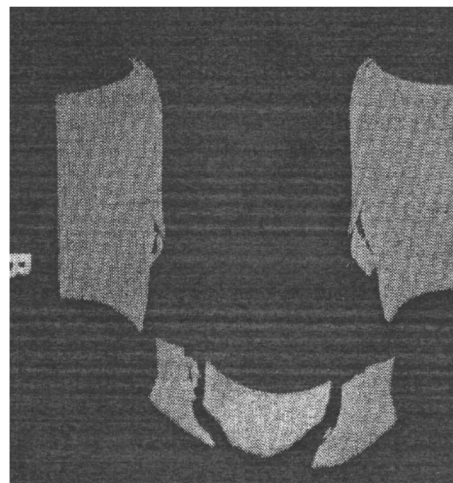


Fig. 3-18: Fragmentation of a 2024-T4 aluminum plate of $h = 6.35$ mm struck by a hard-steel sphere of $d = 6.35$ mm at $V_0 = 863.52$ m/s [50].

3.2.5 Transition from tensile tearing to shear plugging

In general, a target fails by tensile tearing at an impact velocity near the ballistic limit and by shear plugging at a velocity well above the ballistic limit. At the intermediate impact velocity, both axial stretching and shear are important to crack formation and growth, i.e. a target may fail by a mixed mode of tensile tearing and shear plugging. Figure 3-19 shows the failure process of the Weldox 460 E steel beam at $V_0 = 450$ m/s. The impacted zone of the beam is deeply indented and becomes thinner due to local stretching. Eventually, two cracks initiate on the proximal surface, and grow downwards until a plug is formed and ejected. A crack starter point on the proximal surface is selected to track down the time history of the stress triaxiality and the effective plastic strain, see Fig. 3-20. It can be seen that stress wave loading is dominant, and the stress triaxiality oscillates severely in the initial phase. The time elapsed between the subsequent peaks is $5 \mu\text{s}$, which is equal to the time of the shear wave to pass two thicknesses of the beam. As time increases, the stress triaxiality slowly increases and settles down around 0.5 until the accumulated damage reaches the critical value. Hence, the failure of the beam at this velocity may be attributed to the combined action of tension and shear.

As indicated by the name, a plug is always generated in shear plugging. Figure 3-21 shows the crack trajectories projected on the undeformed shape of the Weldox steel beam at $V_0 \geq 375$ m/s. The area between the cracks represents the size of the plug. The mass of the plug is always smaller than that of the impacted zone in the case of the round-nosed projectile while the plug is almost equal in weight to the impacted zone for the shear plugging case with a flat-nosed projectile. The decrease in the volume of the plug with the impact velocity is consistent with experimental results [52]. At $V_0 \leq 375$ m/s, the Weldox steel beam fails by tensile tearing and only one through-thickness crack is generated, i.e. there is no plug generated.

Besides the impact velocity, the transition of the failure mode also depends on the weight and nose shape of a projectile, as demonstrated by Teng and Wierzbicki [59]. For conciseness, these results are not addressed in the present thesis.

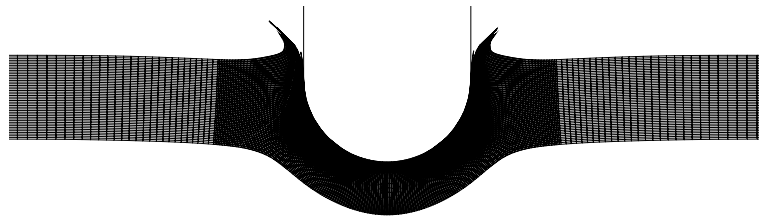
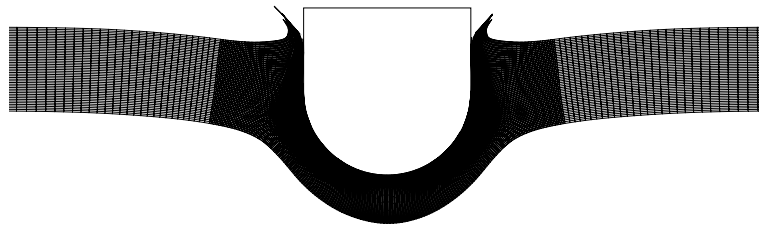
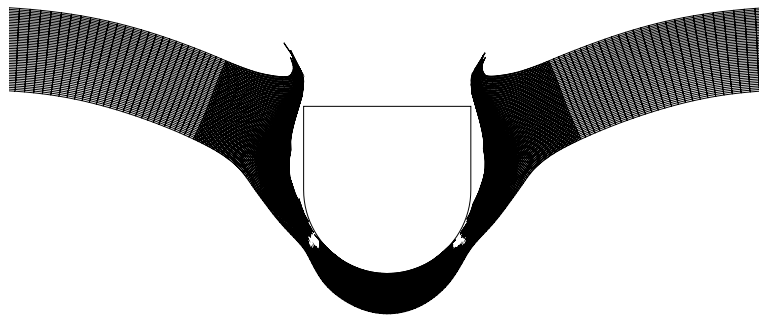
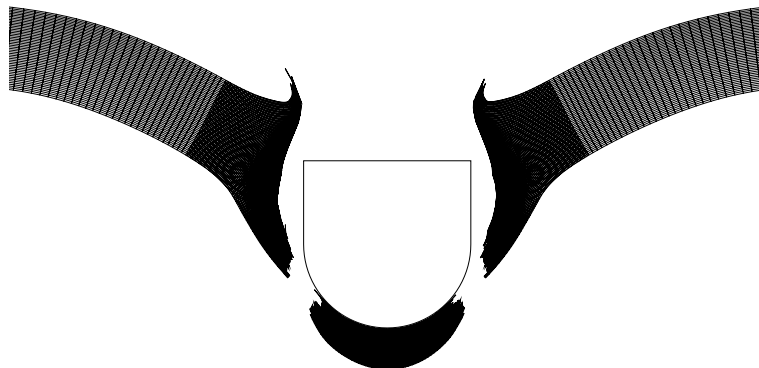
(a) $t = 30 \mu s$ (b) $t = 42 \mu s$ (c) $t = 78 \mu s$ (d) $t = 96 \mu s$

Fig. 3-19: Failure process of the Weldox 460 E steel beam impacted by the round-nosed mass at $V_0 = 450$ m/s.

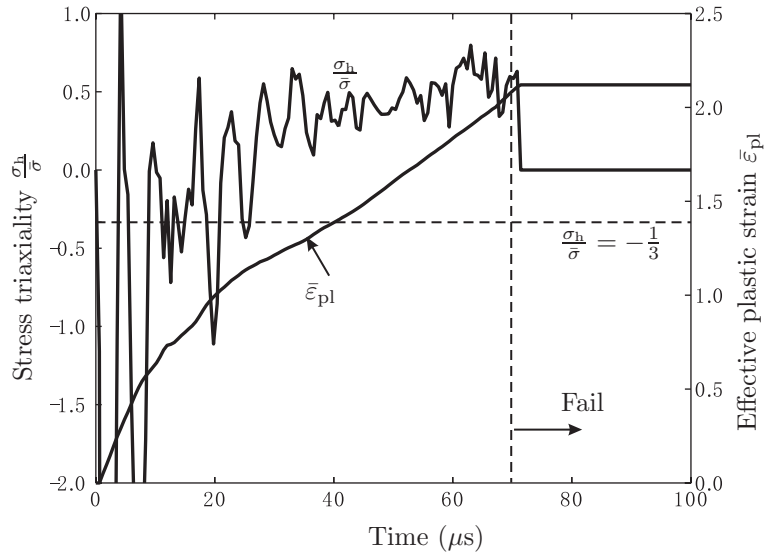


Fig. 3-20: History of the effective plastic strain and the stress triaxiality of the starter point of the crack located at the proximal surface of the Weldox 460 E steel beam at $V_0 = 450$ m/s.

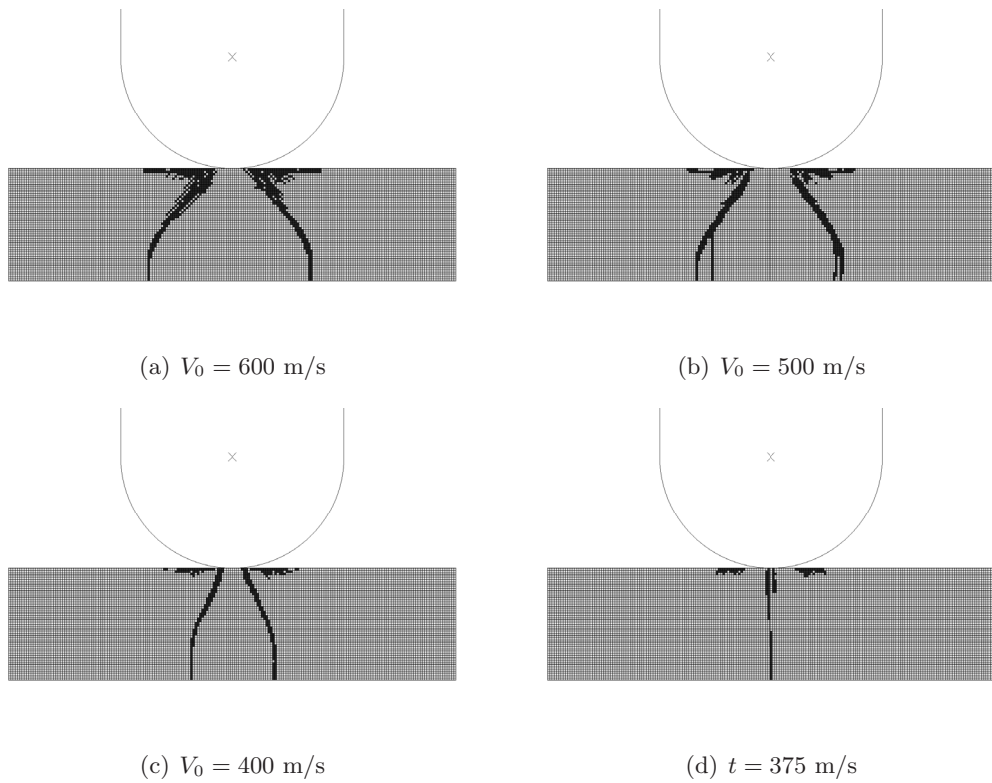


Fig. 3-21: Crack trajectories mapped back on the undeformed shape represented by dark elements for the Weldox 460 E steel beam at various impact velocities.

The transition of the failure modes can be clearly seen by tracking down the energy dissipation as a function of the impact velocity, see Fig. 3-22. At the impact velocity below the ballistic limit, almost all the kinetic energy of the projectile is completely absorbed by the target. The dissipated plastic energy increases with the impact velocity, reaches a maximum value at the ballistic limit, and suffers a jump if the impact velocity slightly increases. Such a drop in energy dissipation just above the ballistic limit is consistent with experimental results by Corran et al. [51] and Børvik et al. [56].

As shown in Fig. 3-22(a), for the aluminum beam, tensile tearing occurs in a very narrow range of the impact velocity from $V_{bl} = 215$ m/s to 240 m/s and shear plugging becomes the favorable failure mode at $V_0 > 240$ m/s. For the steel beam (Fig. 3-22(b)), diffuse necking preceding fracture is evident at $240 \leq V_0 \leq 300$ m/s. The steel beam fails by tensile tearing mostly due to thinning and local bending at $300 \leq V_0 \leq 375$ m/s. The combined action of tension and shear gives rise to two through-thickness cracks leading to the failure of the steel beam at $V_0 \geq 375$ m/s. Above this velocity, shear plugging is dominant.

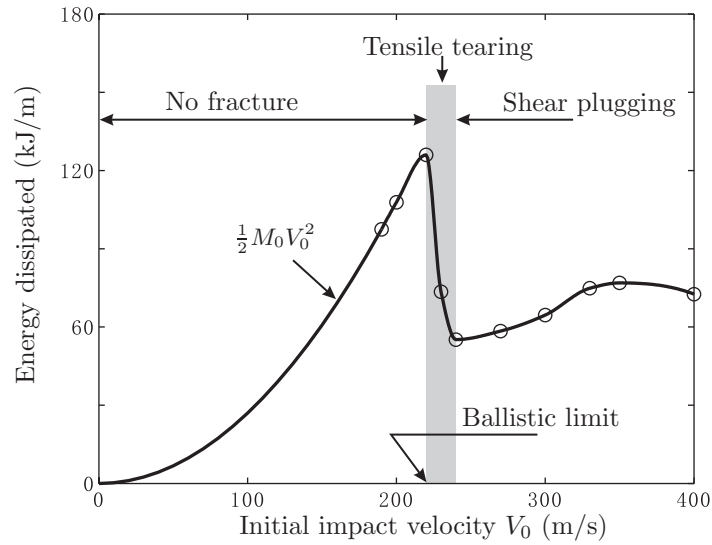
Both the aluminum alloy and Weldox steel beams fail by tensile tearing at an impact velocity just above the ballistic limit. In such a case, the target undergoes large transverse deflection and thus the plastic energy is dissipated in a large region. By contrast, in shear plugging, energy dissipation localizes near and in the impacted zone. The absorbed energy in tensile tearing is much higher than that in shear plugging.

3.2.6 Residual velocities

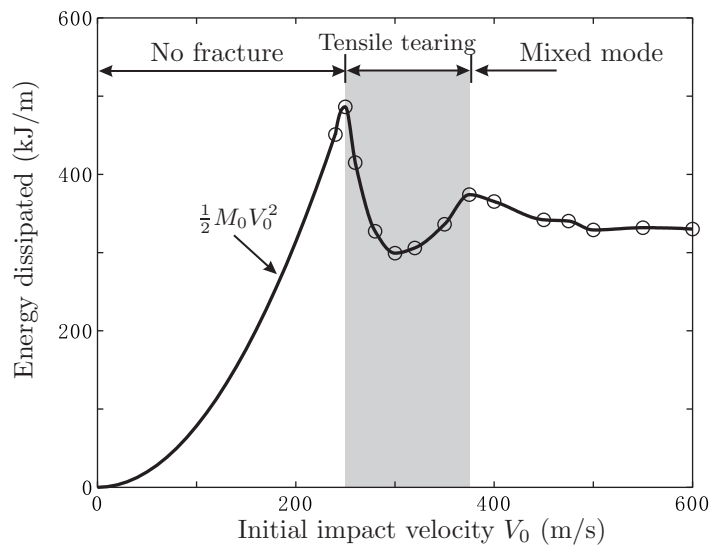
The residual velocity of the projectile is defined as the velocity at which the projectile completely passes through the target. Plots of the initial impact velocity V_0 vs. the numerically calculated residual velocity V_r are given in Fig. 3-23 for the round-nosed projectile, which is fitted well by

$$\left(\frac{V_r}{V_{bl}}\right)^{4.0} = 0.656 \left[\left(\frac{V_0}{V_{bl}}\right)^{4.0} - 1 \right], \quad (3.1)$$

where $V_{bl} = 215$ m/s and $V_{bl} = 245$ m/s are the ballistic limits, respectively, for the 2024-T351 aluminum alloy and Weldox 460 E steel beams. Note, that Eq. (3.1) is applicable to both beams.

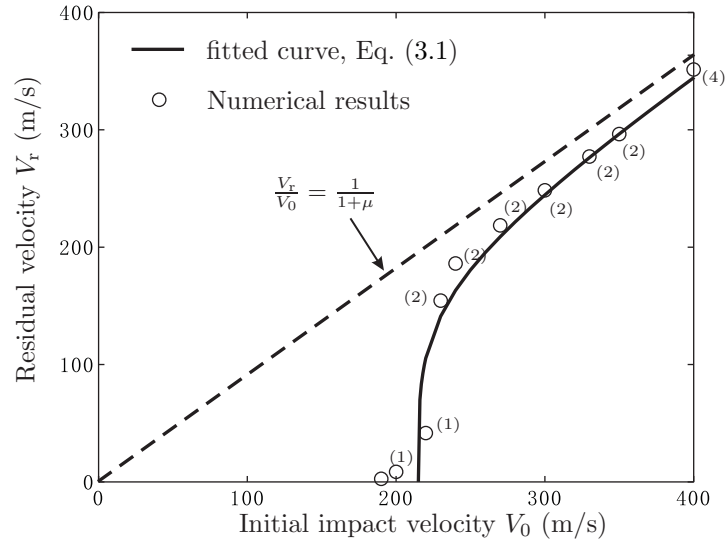


(a) 2024-T351 aluminum alloy beam

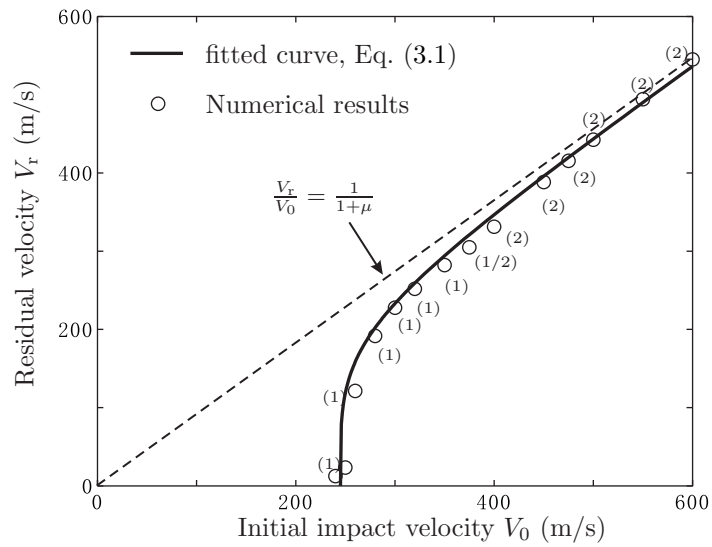


(b) Weldox 460 E steel beam

Fig. 3-22: Plastic energy dissipated vs. initial impact velocity for the aluminum and steel beams.



(a) 2024-T351 aluminum alloy beam



(b) Weldox 460 E steel beam

Fig. 3-23: Residual velocity vs. initial impact velocity for the aluminum and steel beams. The number inside the parenthesis represents the number of generated cracks.

Comparison of the residual velocity between the flat-nosed and the round-nosed projectile is very interesting and is shown in Fig. 3-24. The residual velocity for the flat-nosed mass is higher than that for the round-nosed mass under the same impact conditions. Large differences occur only near the ballistic limit. The ballistic limit for the flat-nosed projectile is $V_{bl} = 206$ m/s lower than $V_{bl} = 215$ m/s for the round-nosed projectile. The sharp corners of the flat-nosed projectile induce the formation and propagation of the cracks and make the target easier to be perforated.

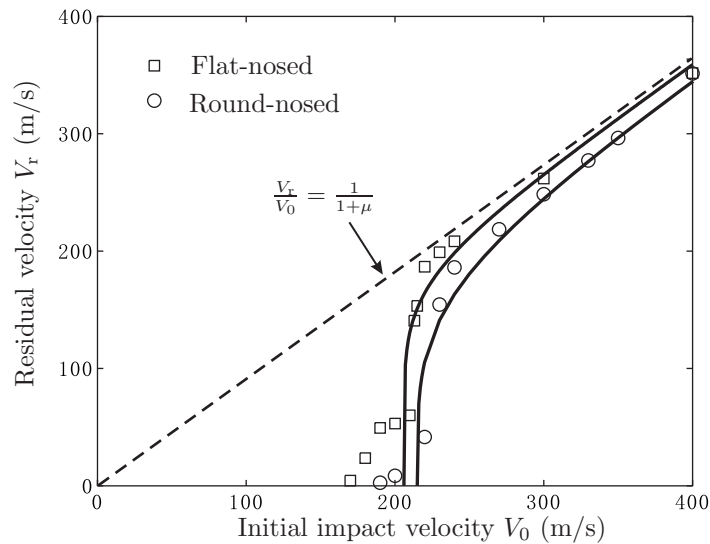


Fig. 3-24: Comparison of the residual velocity between the round-nosed and flat-nosed projectiles for the 2024-T351 aluminum alloy beam.

3.2.7 Discussions

The deformation and failure response of a long metal beam impacted by a rigid, round-/flat-nosed projectile was investigated numerically using the newly developed BW's ductile fracture locus. Several distinct failure modes have been identified including fragmentation, shear plugging, and tensile tearing. The failure mechanisms were investigated by tracking down the time history of the effective plastic strain and the stress triaxiality. Attention is focused on the transition of the failure modes from the tension dominated to shear dominated mechanism with the increasing impact velocities. The effects of the material ductility are highlighted by introducing two metals: 2024-T351 aluminum alloy and Weldox

460 E steel. It is revealed that tensile tearing is a favorable failure mode for both materials at a velocity near the ballistic limit. The steel beam tends to break by tensile tearing while the aluminum beam fails by shear plugging at an impact velocity well above the ballistic limit. The numerical findings are consistent with experimental observations presented in the literature. The present research provides an insight into the mechanics and mechanisms of ductile fracture of beams under rigid mass impact. At the same time, it is clearly demonstrated that the BW's fracture criterion is capable of capturing crack formation and distinct failure modes.

Considered here is the plane-strain beam, which corresponds to a wide beam. The author also investigated the plane-stress case and observed a similar transition of the failure modes as a function of the impact velocity. The relevant results were presented in Ref. [60]. In this study, the mass ratio was kept constant while the impact velocities were varied. If the impact velocity is kept constant, the failure mode of a beam would change from shear plugging to tensile tearing as the mass ratio increases. Such an investigation was also conducted by Teng and Wierzbicki [59].

3.3 Failure modes in the Taylor test

3.3.1 Introduction

The Taylor test in which a deformable flat-nosed cylinder is fired against a fixed, rigid wall was originally proposed to determine dynamic yield stresses of materials [61]. As large plastic deformation, high strain rates, and elevated temperature are involved, the Taylor test is also widely used as a benchmark problem to verify material constitutive models by comparing numerical prediction with experimental response, e.g. Johnson and Holmquist [62], and Rohr et al. [63]. A careful literature review reveals that over 400 papers relating to the Taylor test have been published over the past 50 years [64]. Most of the papers focus on dynamic yield stresses and material constitutive models, but only few authors investigated fracture phenomena and fracture mechanisms in the Taylor test. Cracks or fragments will be generated in the Taylor test if a cylinder is fired at a sufficiently high velocity. Couque [65] observed several spiral cracks formed on the lateral surface of a cylinder in the symmetric Taylor tests on swaged tungsten alloy. Woodward et al. [66] presented several pictures illustrating tensile splitting as well as fragmentation in steel specimens. Grady and Kipp [67] found from sectioned post-test specimens that a number of voids nucleate, grow, and coalesce in the front region of the projectile near the impact interface. The Gurson material model [24] was used by Worswick and Pick [27], and Addessio et al. [28] to simulate the process of void growth.

Compared with a great number of experimental studies and numerical simulations of the process of mushrooming deformation, numerical prediction of fracture in the Taylor test appears to be lacking in the literature. In fact, numerical prediction of crack growth in a three-dimensional body under multi-axial dynamic loading is still a challenging problem. Because several distinct fracture modes may occur separately or simultaneously in a single cylinder in the Taylor test, the applicability of a specific ductile fracture criterion can be examined by performing tests and parallel numerical simulations. In particular, the Taylor test can be used to investigate effects of negative hydrostatic stress on fracture mechanisms and failure modes, since the whole cylinder is predominantly under compression during the impact process.

This section attempts to formulate the classical Taylor problem with fracture. The deformation and failure process of a cylinder in the Taylor test is simulated using ABAQUS/Explicit implemented with the BW's ductile fracture criterion. The objective of this research is to capture all the possible macroscopic fracture modes observed in experiments and to investigate corresponding failure mechanisms. Similarly to the preceding case of rigid mass-to-beam impact, the initial impact velocity of the cylinder is varied from 240 m/s to 600 m/s, and both 2024-T351 aluminum alloy and Weldox 460 E steel are considered. In such a way, effects of the impact velocity and the material ductility on the occurrence of a specific failure mode will be revealed.

3.3.2 Finite element modeling

Consider normal impact of a flat-nosed cylindrical projectile onto a rigid wall, see Fig. 3-25. The cylindrical projectile is of the diameter $d = 6$ mm and the length $l = 30$ mm. The friction coefficient between the front surface of the projectile and the rigid wall is assumed to be 0.1.

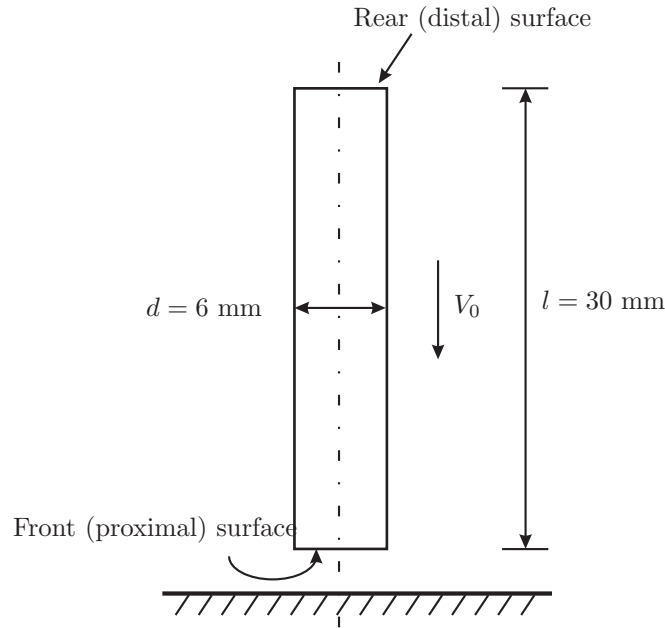


Fig. 3-25: Schematic representation of a cylindrical projectile impacting against a rigid wall in the Taylor test.

As observed from the retrieved specimens [66], either tensile splitting or spiral cracking develops on the lateral surface of the projectile. Hence, a three-dimensional solid finite element model was built rather than an axisymmetric model, see Fig. 3-26. 8-node, linear brick elements with reduced integration (C3D8R) were used. Very fine meshes were generated in the front part where fracture was expected to occur, while relatively coarse meshes were used in the rear part of the cylinder. Totally there are 120,000 elements in the finite element model. The struck wall was modeled as a rigid circular surface. The kinematic contact constraint was prescribed at the impact interface, which allows the projectile to elastically rebound from the rigid wall at the end of the impact process. It is assumed that failed elements are still capable of resisting pressure, but neither tension nor shear. Since compression is dominant in the cylinder during the impact process, generated cracks may close.

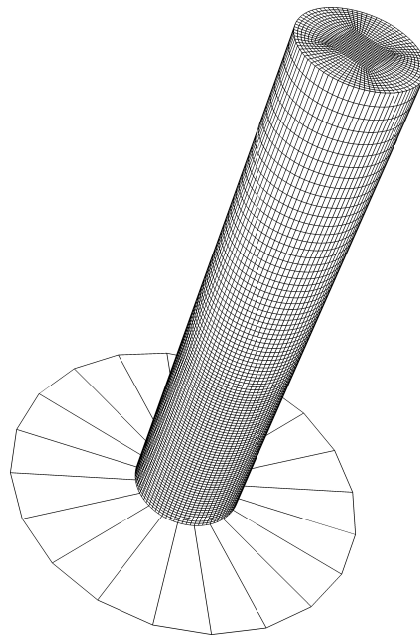


Fig. 3-26: Finite element model of the projectile-target system in the Taylor test.

3.3.3 Mushrooming deformation

Immediately upon impact, elastic waves followed by plastic waves are generated at the impact interface. The plastically deformed region gradually expands as the plastic stress wave travels away from the front surface. At the same time, the elastic stress wave propagates back and forth between the rear surface and the elastic-plastic interface. The cylinder gradually slows down, and finally rebounds from the rigid wall as the stored elastic energy is released. The front part of the cylinder bulges out due to compression while the rear part keeps almost undeformed. This deformation process of the cylinder illustrated in Fig. 3-27 shows a familiar mushroom-like deformation mode in the Taylor test. There is an extensive literature on this subject where comparison is made between the experimentally measured and numerically predicted mushrooming profiles, specimen shortening, and time history of the velocity of the rear surface. Our plasticity model is consistent with previous findings but does not bring any new features. What is entirely new is the prediction of fracture that will be dealt with in the remaining of the section.

3.3.4 Confined fracture

At a relatively low impact velocity, a number of voids or even cracks may be generated inside specimens although no cracks are observed on the exterior surface. This type of failure relating to void nucleation, growth, and coalescence has been demonstrated experimentally by, e.g. Worswick and Pick [27], and Addessio et al. [28], and also numerically using the Gurson material model. In the present study this failure mode is successfully recreated using the conventional plasticity model combined with a suitable ductile fracture criterion. As shown in Fig. 3-28, several elements fail in the region near the front surface and the symmetry axis. Since the failed elements are confined by the rigid wall and the surrounding intact materials, this type of failure in the Taylor test is term “confined fracture” here.

A typical point located at the symmetry axis is selected to illustrate the loading history of the failed region, see Fig. 3-29. Immediately upon impact, compressive stress waves are generated in both axial and radial directions. At about $t = 0.76 \mu s$ a radial unloading stress wave of extremely high amplitude arrives at the symmetry axis. As the radial stress waves travel back and forth from the symmetry axis to the free lateral surface, all the three stress

components of the stress tensor (σ_r , σ_θ , σ_z) oscillate with time. The average period is about $1.87 \mu\text{s}$.

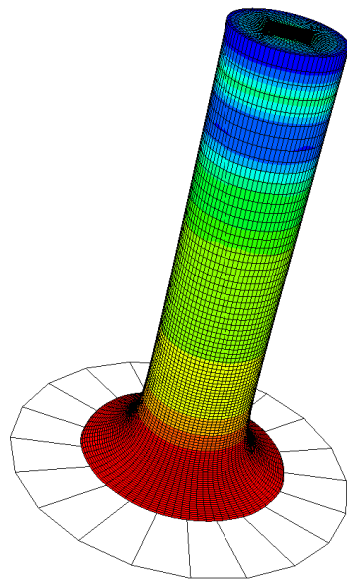
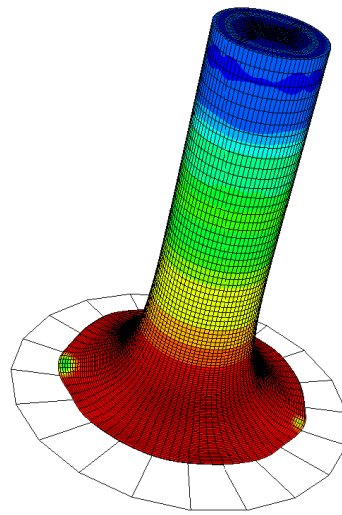
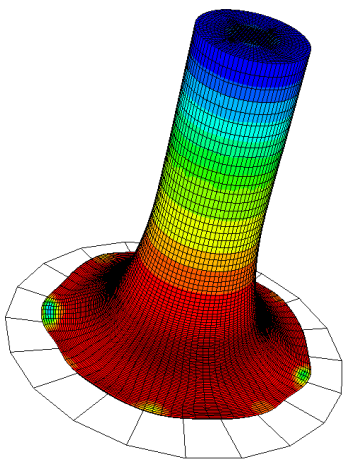
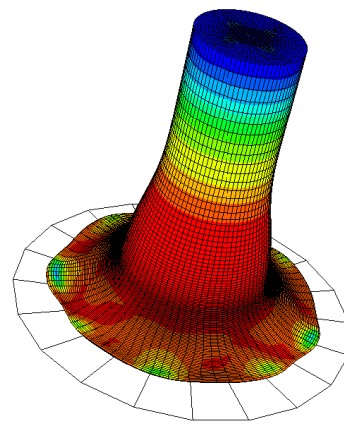
(a) $t = 10 \mu\text{s}$ (b) $t = 20 \mu\text{s}$ (c) $t = 30 \mu\text{s}$ (d) $t = 40 \mu\text{s}$

Fig. 3-27: Mushrooming deformation process of the Weldox 460 E steel projectile at $V_0 = 400 \text{ m/s}$.

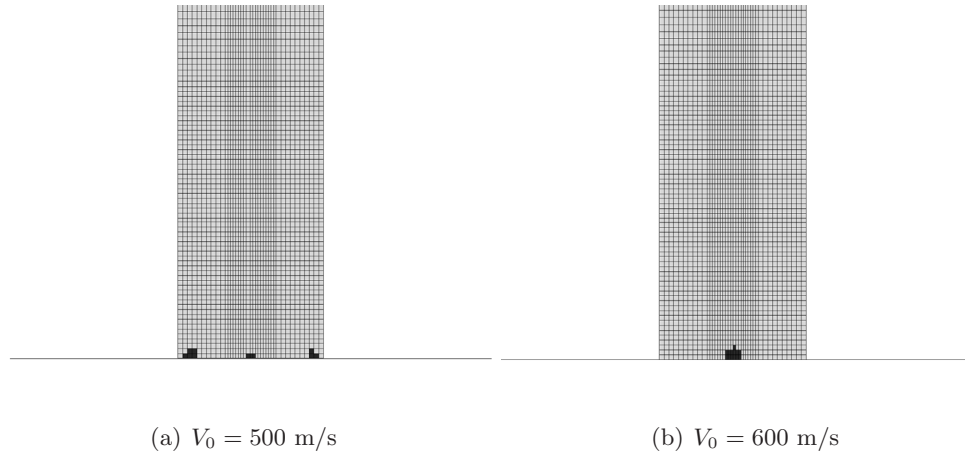


Fig. 3-28: Confined fracture: failed regions represented by dark elements in an axial section of the Weldox 460 E steel projectile. Failed elements in this figure were brought back to the initial, undeformed configuration.

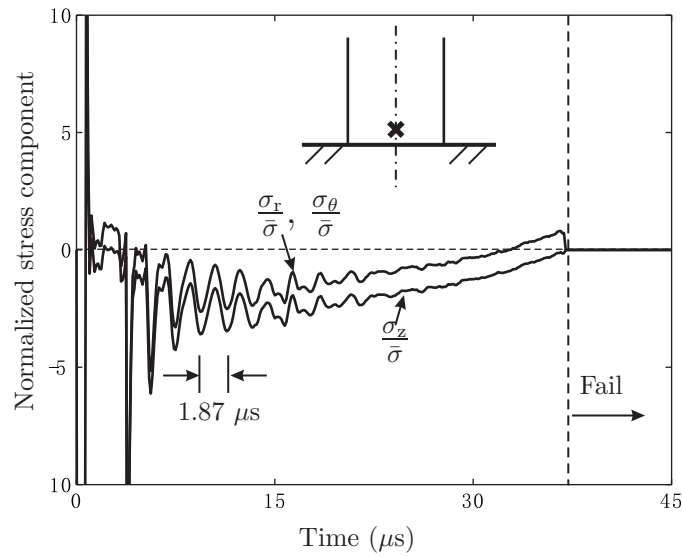


Fig. 3-29: History of the normalized stress components at a point in the symmetry axis of the projectile. The point is 0.6 mm away from the front surface.

Figure 3-30 shows the history of the axial displacement of the central point of the front surface. Contrary to intuition, the central part of the front surface does not always stay at a close contact with the rigid wall. Immediately after impact a small gap between the front surface and the rigid wall is temporarily formed, which closes after about $t = 4 \mu\text{s}$ until the whole projectile elastically rebounds from the rigid wall. This finding is consistent with the numerical results by Worswick and Pick [27] and Addressio et al. [28] using the Gurson material model.

The first several stress waves are mainly responsible for void nucleation and coalescence inside the specimen, see Fig. 3-31. As the gap closes, the compression becomes dominant in the central part of the cylinder and correspondingly, the stress triaxiality is lower than $-1/3$. Hence, the void growth takes place mainly in the initial phase of the impact process and is suppressed later on.

The size of the failed region inside the specimen increases with the impact velocity, see Fig. 3-28. In the case with a relatively low impact velocity, nucleated and coalesced voids or cracks may be still observed from sectioned post-test specimens. However, at a much higher velocity, the voids and cracks generated in the initial phase of the impact process could disappear or are difficult to discern due to subsequent crush by the surrounding materials.

3.3.5 Petalling

As the initial impact velocity increases further to $V_0 = 600 \text{ m/s}$, another fracture mode: petalling, is predicted in the Weldox 460 E steel cylinder. The process of deformation and fracture of the projectile at $V_0 = 600 \text{ m/s}$ is shown in Fig. 3-32. In contrast to the previous cases with low impact velocities, a number of small cracks are generated on the front surface under radial stress wave loading. However, only four major cracks survive and propagate radially toward the symmetry axis. The growth of the cracks is mostly driven by tensile hoop stresses. As the velocity of the rear part of the cylinder decreases, these cracks are finally arrested.

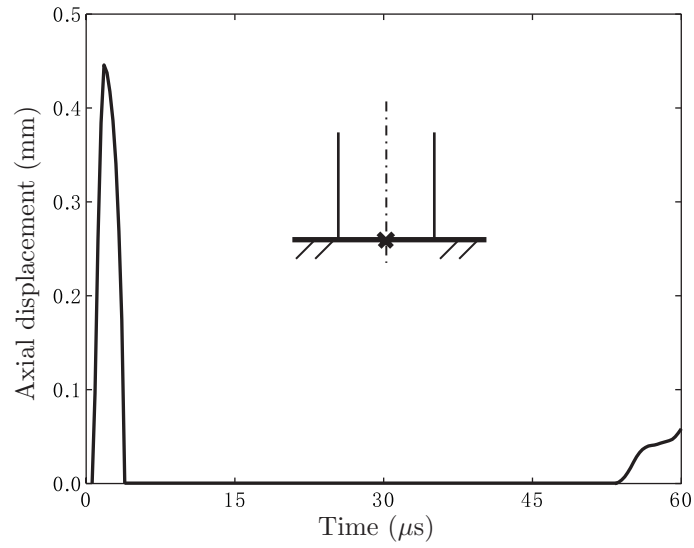


Fig. 3-30: History of the axial displacement of the central point of the front surface.

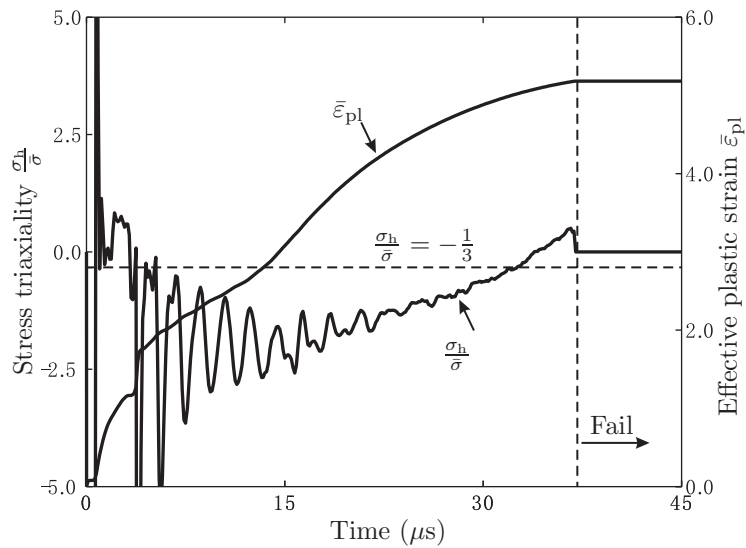


Fig. 3-31: History of the effective plastic strain and the stress triaxiality at a point at the symmetric axis of the projectile. The point is 0.6 mm away from the front surface.

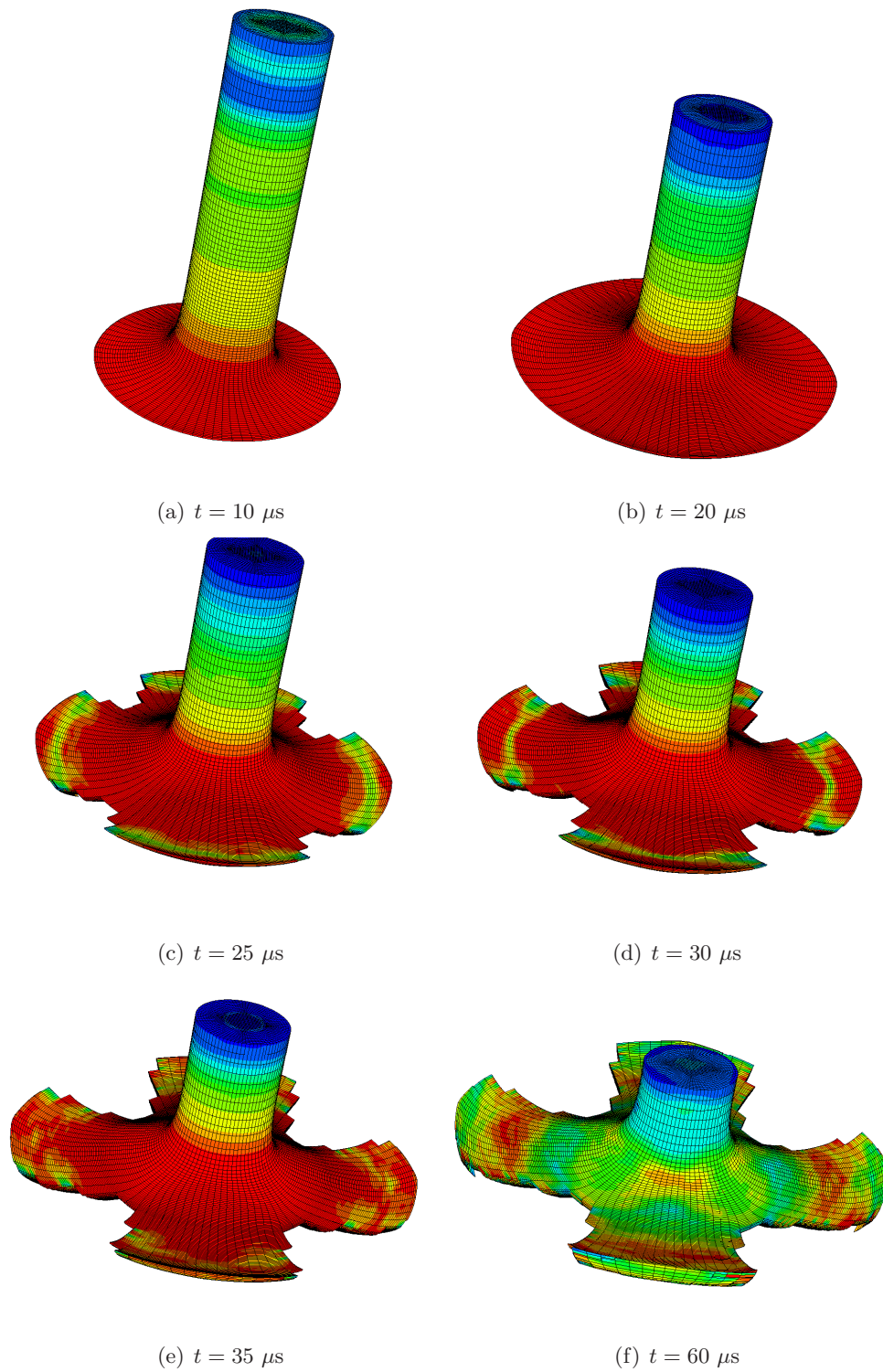


Fig. 3-32: Petalling process of the Weldox 460 E steel projectile at $V_0 = 600 \text{ m/s}$.

Our numerical prediction is qualitatively consistent with experimental results published in the open literature. Figure 3-33 shows petalling of a 4340 steel projectile cylinder fired at $V_0 = 529$ m/s [68]. About eight petals were generated in the front part of the cylinder. By contrast, the present numerical simulation predicts four petals for the Weldox 460 E steel cylinder. The number of the petals probably depends on the impact velocity, the ductility of the material, and the geometrical size of the projectile, which needs to be further investigated.

The failed elements are removed to show crack initiation and growth in Fig. 3-32. In reality, the crack formation is due to separation of materials microscopically and macroscopically. Therefore, the crack openings illustrated in Fig. 3-32 may be a little larger than real ones.

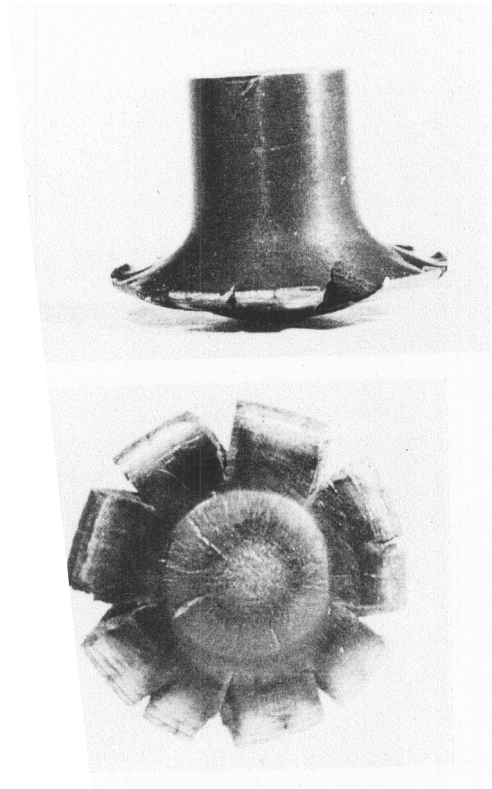


Fig. 3-33: Petalling of a 4340 steel cylinder at $V_0 = 529$ m/s. The steel was tempered at 1000 F [68].

To provide an insight into the failure mechanism of petalling, a point located at the periphery of the front surface is chosen to demonstrate the history of the stress triaxiality and the effective plastic strain. As show in Fig. 3-34, the stress triaxiality at this point is always positive except in the very beginning. Its value is very close to $1/3$ during the whole impact process, which indicates the predominantly uniaxial stress state at this point. In actuality, the periphery of the front surface moves upward in the mushrooming deformation process and is disconnected from the rigid wall immediately after impact. Hence, the tensile hoop stress is the only acting stress component at the periphery of the front surface.

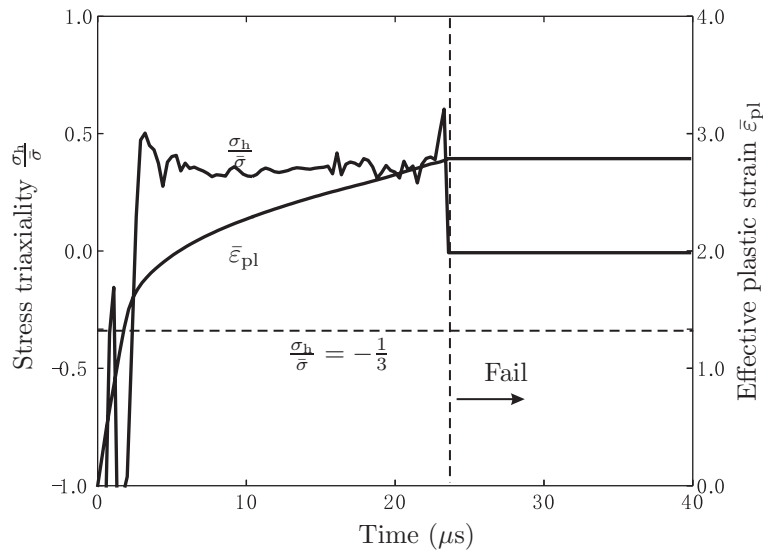


Fig. 3-34: History of the effective plastic strain and the stress triaxiality of a point at the outer edge of the front surface for the Weldox 460 E steel projectile at $V_0 = 600$ m/s.

3.3.6 Shear cracking

The third possible fracture mode in the Taylor test is identified as shear cracking. Consider the 2024-T351 aluminum alloy cylinder fired at $V_0 = 240$ m/s. The Bao-Wierzbicki's fracture locus was defined in the simulation.

As the front part of the projectile near the rigid wall bulges out, several cracks initiate at the periphery of the front surface, and grow spirally on the lateral surface of the projectile,

see Fig. 3-35. This failure pattern is similar to that in quasi-static upsetting tests where a shear crack is formed near the equator of a specimen due to barreling and resulting tensile hoop stress (The front surface of the projectile in the Taylor test is equivalent to the equator plane of the cylinder in the upsetting test.).

A typical point at the periphery of the front surface, where a crack initiates, is selected to illustrate the history of both the stress triaxiality and the effective plastic strain. As seen from Fig. 3-36, a large part of the stress triaxiality during the impact process falls in the range from -0.3 to 0.0 , which are typical values in upsetting tests [4]. Due to dominant compression, there is friction between the newly formed crack surfaces, which destroys micro-characteristics on the newly generated crack surfaces, and makes the crack surface more smoother in Mode II than in Mode I.

The present numerical prediction agrees qualitatively well with the experimental results published in the literature. Couque [65] conducted a symmetric Taylor test on swaged tungsten alloy of static elongation of 10%. Several spiral shear cracks of 45° were generated on the lateral surface of the projectile, see Fig 3-37. Papirno et al. [68] also observed shear cracking on the lateral surface of a 4340 steel projectile cylinder moving at $V_0 = 315$ m/s. The cylinder was tempered at 400 F before the test. By contrast, in the previous petalling case, the steel cylinder was tempered at 1000 F.

No shear cracking is observed for the projectile made of Weldox 460 E steel in a wide range of the impact velocity. Note, that Weldox 460 E steel is more ductile than 2024-T351 aluminum alloy and swaged tungsten alloy. Correspondingly, in upsetting tests a ductile short cylinder can be pressed to a large extent without any evidence of shear cracks on the lateral surface. Hence, shear cracking would more likely take place in a less ductile projectile while tensile petalling in a more ductile cylinder. At a higher impact velocity, shear cracks initiating on the lateral surface would grow toward the interior of the projectile, and eventually the front region of the projectile would break into several parts.

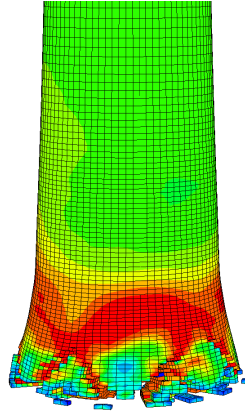


Fig. 3-35: Spiral shear cracks on the lateral surface of the 2024-T351 aluminum alloy projectile at $V_0 = 240$ m/s.

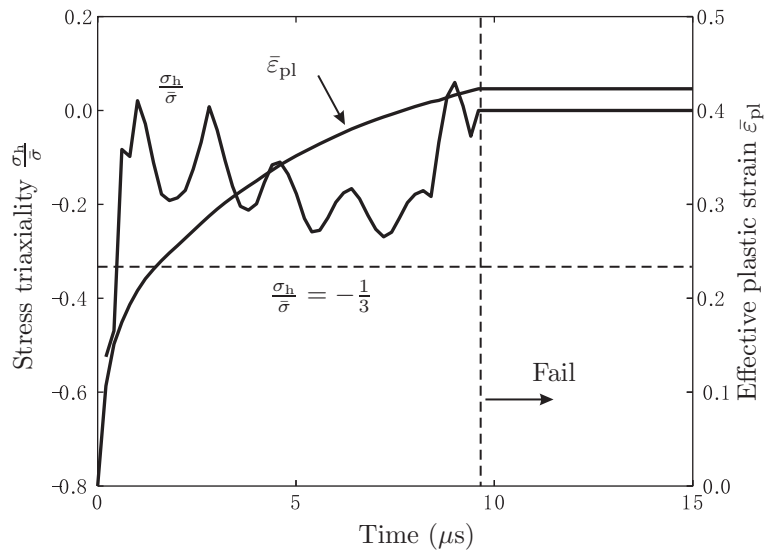


Fig. 3-36: History of the effective plastic strain and the stress triaxiality at a point on the edge of the front surface of the 2024-T351 aluminum alloy projectile at $V_0 = 240$ m/s.

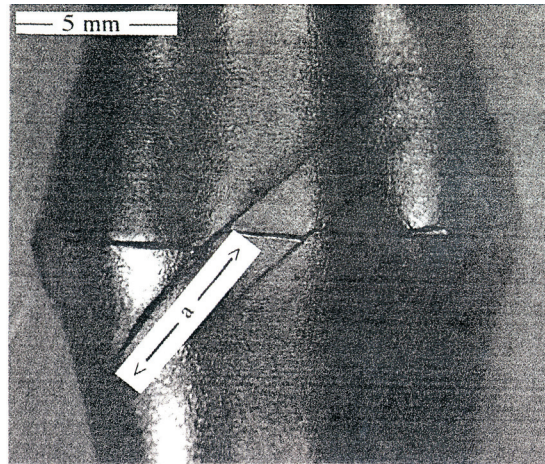


Fig. 3-37: Shear cracking on the lateral surface of two swaged tungsten alloy cylinders in the symmetric Taylor test [65].

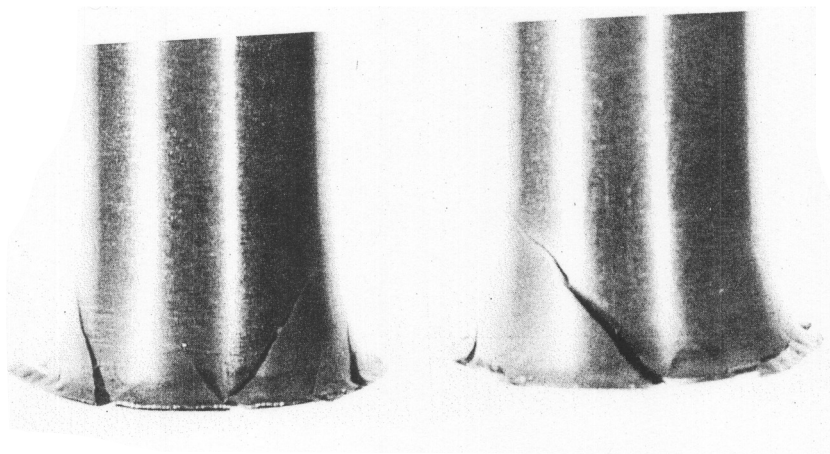


Fig. 3-38: Shear cracking of a 4340 steel cylinder at $V_0 = 315$ m/s. The steel was tempered at 400 F [68].

3.3.7 Discussions

In this section, the mechanisms of fracture in the Taylor test were investigated numerically on basis of the newly developed Bao-Wierzbicki's ductile fracture locus. Three possible fracture modes were successfully recreated: confined fracture inside the cylinder, petalling of the front surface, and shear cracking on the lateral surface, all of which are consistent with experimental observations presented in the open literature. Petalling would more likely take place in a more ductile projectile fired at a higher velocity while shear cracking in a less ductile material. Confined fracture is a common failure mode for both materials, which occurs in a wide range of the impact velocity. Tests are being planned at the Ernest Mach Institute in Germany to validate the present numerical findings experimentally.

Besides the three failure modes studied in the present section, adiabatic shear banding followed by shear cracking may also occur in the Taylor test, depending on material properties and impact velocities. The minimum edge length of the present finite element model is about $200 \mu\text{m}$, which is much larger than the typical width of adiabatic shear bands (about $1 - 100 \mu\text{m}$). It is difficult to use such large elements to capture evolution of an adiabatic shear band. The transition from adiabatic shear banding to fracture will be studied in the next section using a much finer mesh model.

3.4 Adiabatic shear banding under dynamic compression

3.4.1 Introduction

Under high strain rates, a large part of plastic work for metallic materials is converted to heat leading to temperature rise. If thermal softening exceeds strain and strain rate hardening, homogeneous plastic deformation will give way to localized, band-like adiabatic shear deformation. These bands are narrow zones of intense plastic strain embedded in a homogeneously deforming region. Adiabatic shear banding often act as precursors of ductile fracture and provide initiation sites and propagation pathes for cracks. The transition from adiabatic shear banding to fracture remains elusive although both are closely related. In most of cases, adiabatic shear banding is not clearly separated from subsequent fracture. Adiabatic shear banding has been simply thought of in the literature as a kind of failure mode in much the same way as sheet metal necking is identified as a failure. Little research goes further to investigate the formation and propagation of cracks within fully developed adiabatic shear bands. In actuality, adiabatic shear bands still adhere to matrix materials and a deformed body keeps its integrity if no cracks are generated. The materials within adiabatic shear bands would recover some strength after impact and are capable of resisting successive loadings. Thus, only cracking is a final, catastrophic failure mode.

The immediate objective of this section is to study numerically the formation and propagation of cracks within adiabatic shear bands. Due to its importance in impact engineering and high speed machining, adiabatic shear banding has been extensively studied in the past three decades. A number of theoretical models were developed in the literature. Most of papers published before 1992 were reviewed by Bai and Dodd [42]. Wright [69] summarized some theoretical solutions in a recent monograph. The theoretical analyses are very helpful to understand the formation, evolution, and structure of adiabatic shear bands. However, these simple models could not provide insights into the transition from adiabatic shear banding to fracture.

Many experiments on adiabatic shear banding were performed. However, most of them were limited to metallurgical examinations on post-test specimens. To track the evolution of adiabatic shear bands, Marchand & Duffy [70] and Zhou et al. [71] used, respectively, a

linear array of 12 and 16 infrared temperature detectors to measure temperature distribution across a propagating adiabatic shear band. Using a square array of 64 infrared temperature detectors in a single edge-notched plate under projectile impact, Guduru et al. [72, 73] found for the first time that the temperature field is composed of an array of transient, periodical “hot spots” along fully developed adiabatic shear bands. This contradicts the well accepted assumption in theoretical models that the temperature field has a laminar structure within adiabatic shear bands. Since temperature rise is due to the conversion of plastic work into heat, the turbulent temperature field can be an indication for the formation and propagation of cracks within adiabatic shear bands. Hence, this experimental finding poses two interesting questions: *can one use conventional finite element procedures to recreate the turbulent temperature field within adiabatic shear bands? and is there any relationship between the periodicity in the temperature field and the formation of cracks?*

Numerical methods provide detailed information on stress states, which help better understand a complex process of wave propagation and the formation and propagation of shear bands and cracks. However, only a few numerical studies were published on this subject in contrast to numerous experimental and theoretical investigations. The major challenges of numerical simulations are to model the growth of adiabatic shear bands, the propagation of subsequent cracks within adiabatic shear bands, and the transition from brittle fracture to shear bands or vice versa. The first two issues will be explored in this section.

In the companion paper, Zhou et al. [74] performed numerical simulations on the formation and propagation of an adiabatic shear band in a single edge-notched steel plate under projectile impact. The propagation of the shear band was assumed to be controlled by a critical plastic strain. The material within shear bands after the stress collapse was modeled as a Newtonian fluid, which can resist pressure and shear stresses. However, their simulations did not capture the nonuniform temperature field within the shear band. A thermoviscoplastic constitutive model coupled with damage evolution was developed by Lodygowski and Perzyna [75], in which adiabatic shear banding and fracture is automatically resolved. Mason and Worswick [76] studied numerically and experimentally the formation and propagation of adiabatic shear bands and following cracks in punch tests. The max-

imum shear stress (MSS), which corresponds to the stress level when thermal softening prevails over strain and strain rate hardening, was used as a criterion for formation of the adiabatic shear band and at the same time as a fracture criterion. Because of its simplicity, the maximum shear stress criterion was often employed in theoretical analysis, e.g. Li and Jones [77]. The problem formulated by Zhou et al. [71] was also investigated by Li et al. [78, 79] using the meshfree Galerkin method. Compared with conventional finite element procedures, the meshfree scheme is able to eliminate the mesh alignment sensitivity, and thus curved shear bands or cracks can be easily modeled. Most impressively, Li et al. [78, 79] successfully captured the hot spots within the adiabatic shear band. Nevertheless, they did not go further to investigate the formation of cracks, since the impact velocity considered was quite low.

It should be mentioned that the transition from adiabatic shear banding to the subsequent fracture within shear bands considered in the present research is different from the phenomenon investigated by Kalthoff and Winkler [80], and Zhou et al. [71]. Kalthoff and Winkler [80] conducted a series of impact tests on a steel specimen with two parallel edge cracks. They found that the specimens with a sharp notch tip usually fail by brittle fracture due to tensile stresses at a low impact velocity, and the failure mode was changed to adiabatic shear banding as the impact velocity increases to a certain level. Based on finite element analysis, Needleman and Tvergaard [81] proposed that the maximum tensile stress would be reduced due to thermal softening associated with high strain rates so that the brittle fracture would be suppressed at a high impact velocity. A reverse transition from adiabatic shear banding to brittle fracture was observed by Zhou et al. [71] in a single edge notched plate under projectile impact, in which a brittle crack initiated at the tip of an arrested adiabatic shear band. The transition either from brittle fracture to shear banding or vice versa depends on loading configurations and impact velocities. However, the intrinsic mechanism of this transition is still not clear but it is outside the scope of the present research.

Recently, impact tests on a modified axisymmetric hat specimen made of 25% swaged 91W-6Fe-3Co tungsten alloy were performed by Couque [82, 83] using a direct compressive Hopkinson pressure bar system (DCHP). The adiabatic shear band was generated in the

gauge section of the specimen and then was followed by fracture. In the present section, this problem is investigated numerically using the finite element code ABAQUS/Explicit. The BW's fracture criterion was implemented in the calculation to predict the formation and propagation of the crack. Attention is focused on the transition of the failure modes from the adiabatic shear banding to fracture. Complementary to the experiments, the present numerical simulation provides an insight into the mechanism of the formation and propagation of the shear band and the subsequent crack.

3.4.2 Experimental set-up

The direct compressive Hopkinson pressure bar system (DSHP), which was first developed by Dharan and Hauser [84] to determine a compressive stress-strain relationship under high strain rates, was used to generate adiabatic shear bands in a modified axisymmetric hat specimen. Figure 3-39 illustrates the experimental setup. The specimen was placed against a Hopkinson pressure bar of the length 448 mm and the diameter 20 mm. A striker bar of the length 90 mm and the diameter 20 mm was launched by a gas gun. The impact velocity ranges from 20 to 50 m/s to ensure elastic loading on the pressure and striker bars.

The axisymmetric hat-like specimen originally proposed by Meyer and Manwaring [85] was modified by Couque [82, 83], see Fig. 3-40. Its gauge section is tilted at an angle of 32.6° with regard to the loading axis. At such an angle, the pressure would be evenly distributed along the gauge section before an adiabatic shear band occurs [82]. By contrast, the pressure concentrates at the corners of the original hat specimen with the gauge section parallel to the central axis. The exterior and interior corners have the radii of $r = 120 \mu\text{m}$ and $150 \mu\text{m}$, respectively. Due to geometrical discontinuities, both corners act as the initiation sites of adiabatic shear bands as well as cracks in the same way as the notch tip of a pre-notched plate.

A number of loading configurations and specimens were suggested in the literature to induce adiabatic shear bands, e.g. projectile impact on a single edge notched plate [71], punch tests on circular plates placed against dies [76], torsional tests on short thin-walled tubes [70], etc. All these tests have a common feature that shear loading is dominant. Differently, the present hat specimen is predominantly under compression during the impact

process. Predominant pressure will suppress void nucleation and growth in the specimen, and thus the formation of adiabatic shear bands could be more easily observed, especially for less ductile materials.

All the pressure bar, the striker, and the specimen were made of tungsten alloys. Because of their high density and strength, tungsten alloys are often used as kinetic energy penetrators, in which adiabatic shear banding is a common failure mode due to predominant compression. A better understanding of adiabatic shear banding will help to improve the performance of tungsten alloy penetrators.

3.4.3 Finite element modeling

The whole impact system exhibits multiple levels of deformation in various components and regions. Both the striker bar and the pressure bar undergo elastic deformation. The gauge section of the specimen, in which an adiabatic shear band is expected to occur, is subjected to localized plastic straining while the other part of the hat specimen experiences little plastic deformation. In order to reduce computational cost, we used elements of different size to solve this multiple level response. First, a two-dimensional finite element model was built using four-node axisymmetric elements with reduced integration (CAX4R) since all the components are symmetric in respect to the central axis. Uniform, square meshes with the edge length 1 mm were used to discretize the striker bar and the pressure bar. Very fine meshes with the element size about $10 \mu\text{m} \times 10 \mu\text{m}$ were generated in the region around the gauge section of the specimen, see Fig. 3-41. With such small elements, the exterior and interior round corners of the specimen can be modeled with a reasonable accuracy. High stress and strain gradients associated with stress concentration in the vicinity of the round corners can be captured. This is important since the adiabatic shear bands initiate at the round corners. Relatively large elements were generated in the other part of the specimen. The whole FE model has a total of 89,380 elements.

Mesh generation is not a trivial problem for numerical simulation of adiabatic shear bands. The size of elements in the region where an adiabatic shear band may occur, should be much smaller than its width. Otherwise, the prediction of adiabatic shear bands would be delayed or even impossible. As can be measured from Fig. 3-42, the width of the present

adiabatic shear band along the gauge section is about $40 \mu\text{m}$, which is four times as large as the edge length of the present elements. With such meshes, the formation and evolution of adiabatic shear bands can be automatically resolved.

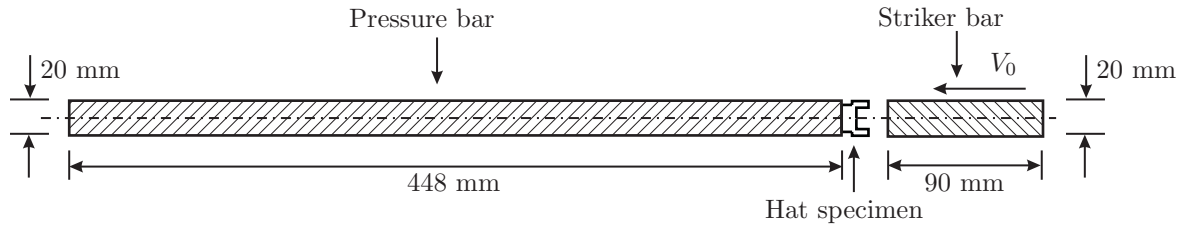


Fig. 3-39: Schematic representation of impact tests on the hat specimen using direct compressive Hopkinson pressure bar system.

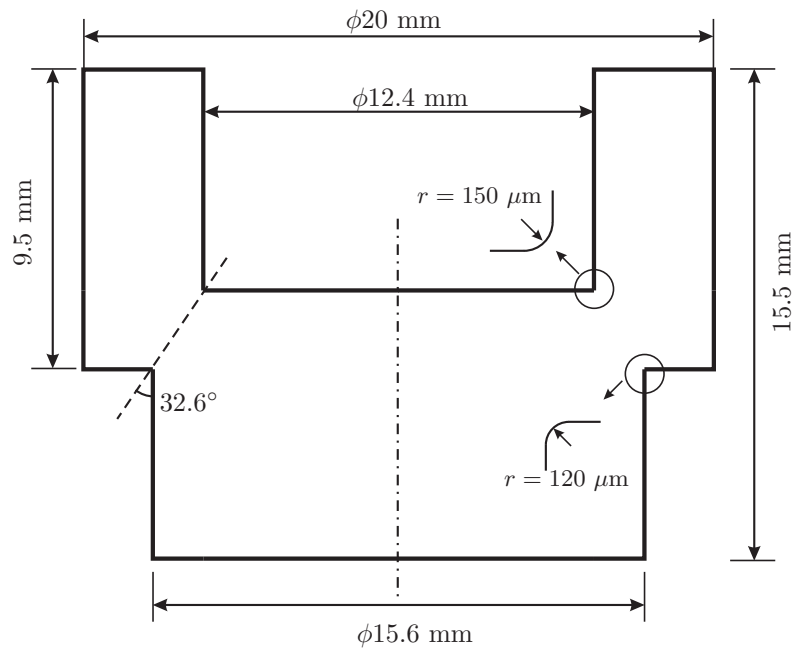


Fig. 3-40: Geometrical shape and size of the modified axisymmetric hat specimen.

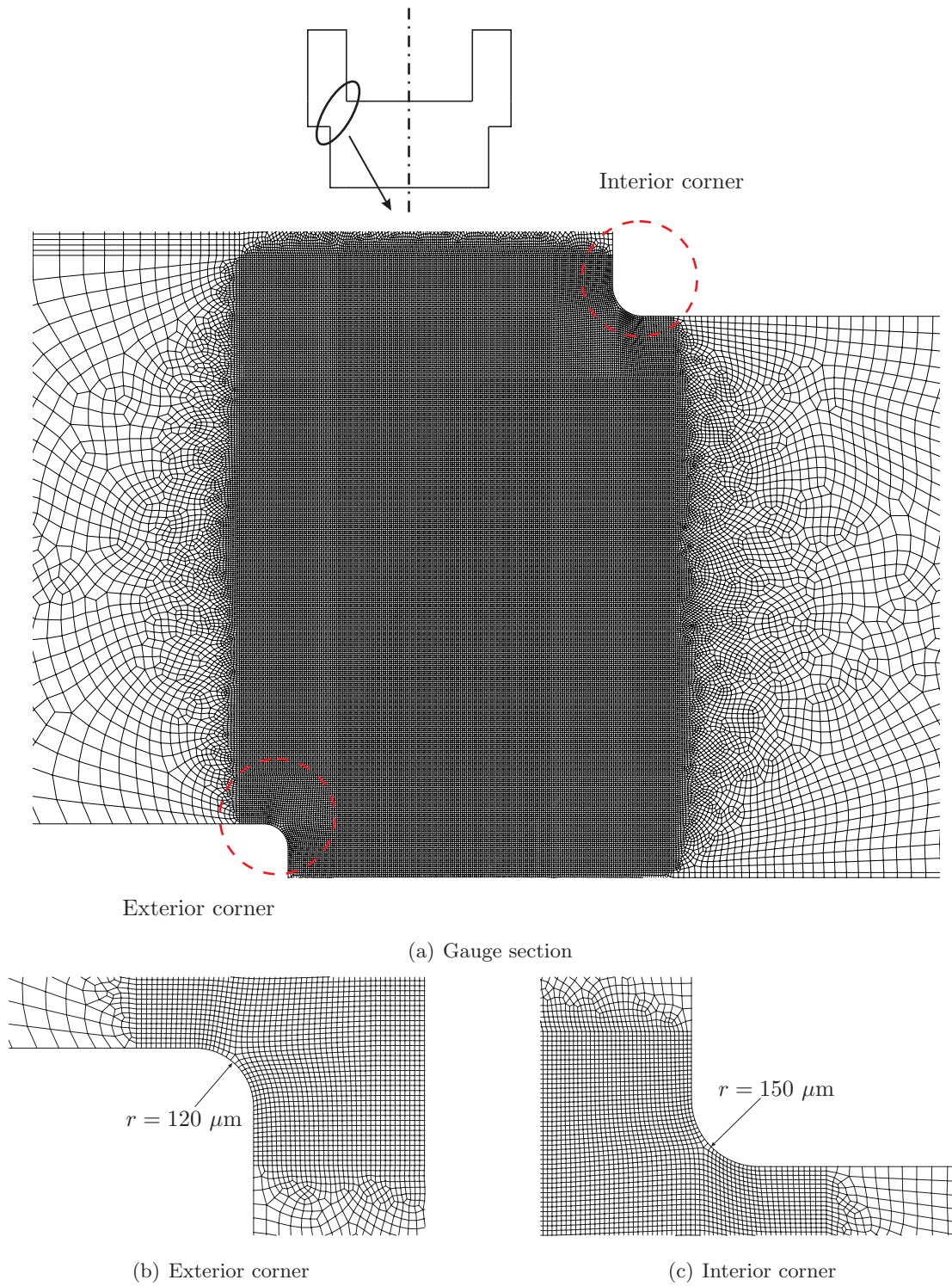


Fig. 3-41: Finite element model around the gauge section of the axisymmetric hat specimen.

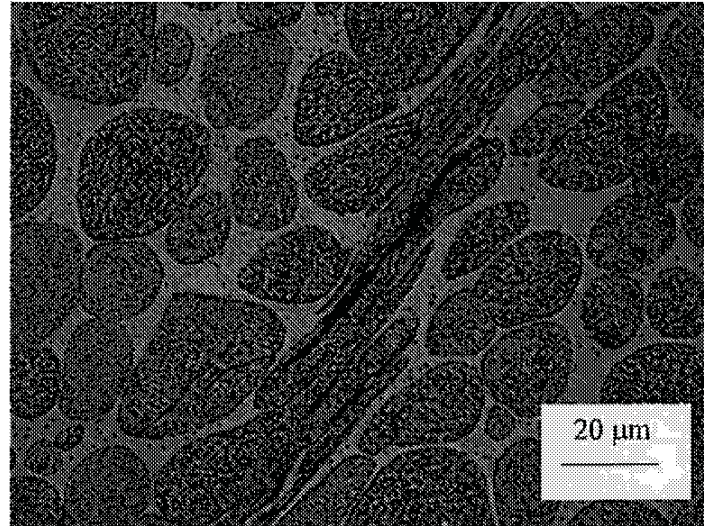


Fig. 3-42: Scanning electronic micrograph showing the generated adiabatic shear band at $V_0 = 27.6$ m/s.

The materials within the fully developed adiabatic shear band are severely degraded and are subjected to large plastic deformation. If fixed Lagrangian meshes are used, the elements inside the band would be highly distorted so that the solution may lose accuracy at the end of the impact process. To overcome the shortcoming of fixed meshing, the technique of Arbitrary Lagrangian-Eulerian (ALE) adaptive meshing implemented in ABAQUS was introduced to remesh the critical region around the gauge section at every incremental step. The ALE adaptive meshing is able to maintain high-quality meshes in the critical region and to provide accurate solutions. It should be mentioned that the ALE adaptive meshing does not increase or decrease the number of elements during the calculation, i.e. it does not refine meshes around the newly generated crack tip.

Since both the striker bar and the pressure bar undergo elastic deformation, it is correct to consider an elastic material model for both bars. The Johnson-Cook's (JC's) material model implemented in ABAQUS/Explicit was used to represent the stress-strain relation for the hat specimen under high strain rates and temperature. The material coefficients for 91W-6Ni-3Co tungsten alloy are listed in Table 5.3.

It is assumed in the present numerical simulation that the simple JC's material model is still applicable to the fully developed shear band, which is usually characterized by low

load carrying capability and high strain rates as well as high temperature near the melting point. Its effectiveness will be examined later on.

Since no fracture locus for 91W-61Ni-3Co tungsten alloy is available currently, a simple constant fracture strain with the cut-off value for the negative stress triaxiality at $-1/3$ was implemented in the present calculation, see Fig. 6-5(b). Effect of the magnitude of the fracture strain on the fracture response will be investigated.

3.4.4 Evolution of adiabatic shear bands

Immediately after impact, high stresses develop at both corners of the specimen due to the geometrical discontinuity. This stress concentration eventually evolves into two stress bands from each corner. The longer band grows along the gauge section, and the shorter, ear-like one occurs on the side of impact at about 45° to the symmetric axis, see Fig. 3-43. The growth of the shorter band is suppressed after the occurrence of shear localization. This kind of stress distribution is similar to what was seen in the impact experiments on the single edge notched plate by Guduru et al. [73] and in the numerical solutions by Needleman and Tvergaard [81].

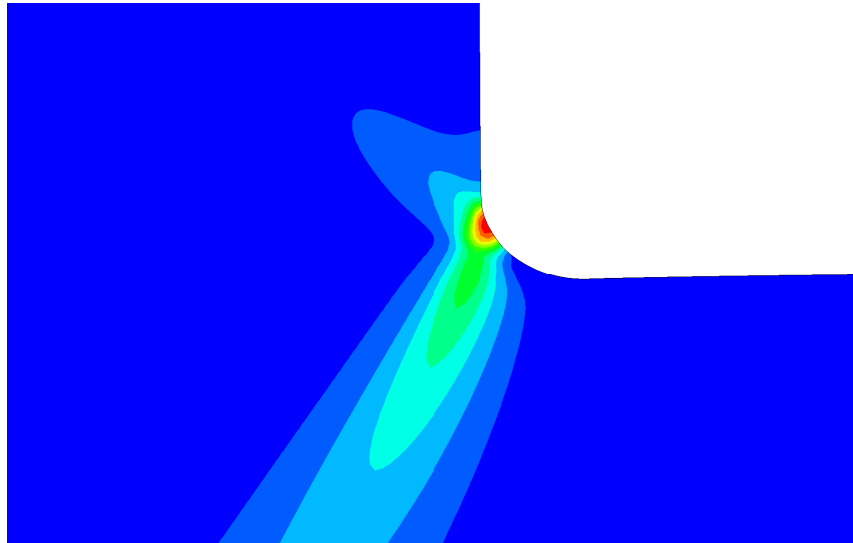


Fig. 3-43: Effective plastic strain field around the interior corner in the initial phase ($t = 12 \mu\text{s}$) at $V_0 = 27.6 \text{ m/s}$.

During the impact process, a large part of plastic work is converted to heat leading to temperature rise and degradation of the material strength. As thermal softening exceeds strain and strain rate hardening, which first occurs at the corners, the homogeneous plastic deformation described above becomes unstable and eventually collapses into a localized, band-like mode. The narrow shear bands initiate at the exterior and interior corners, respectively, grow towards each other, and are finally arrested in the middle of the gauge section, see Fig. 3-44. The bands are characterized by high plastic strains and high temperature.

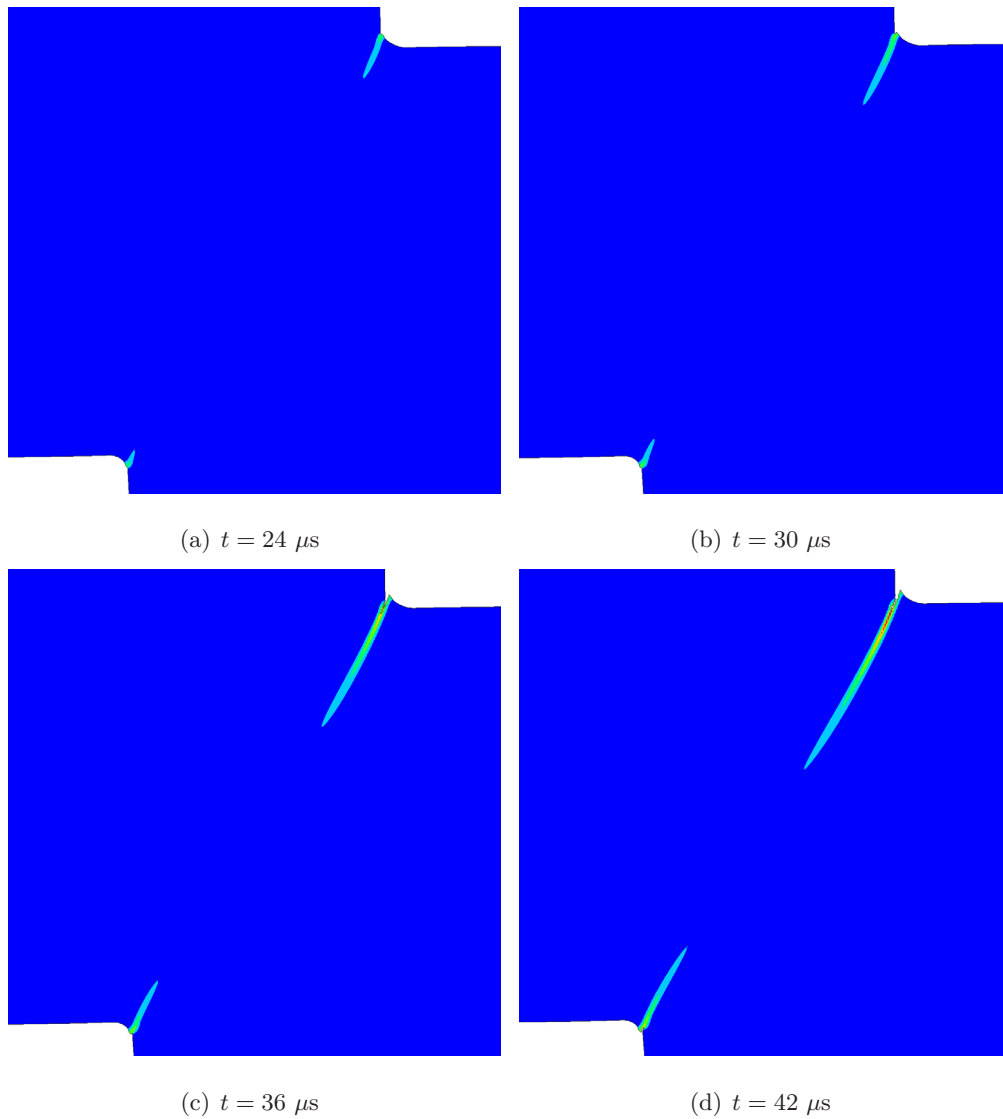


Fig. 3-44: Formation and propagation of the adiabatic shear bands along the gauge section at $V_0 = 27.6$ m/s. The colors represent the magnitude of the effective plastic strain.

A typical material element was selected to demonstrate the development of stress states of the adiabatic shear band, see Fig. 3-45. In the initial stage, the material element undergoes homogeneous deformation. As soon as the stress reaches the maximum value, the material element loses stability and the deformation becomes inhomogeneous. In this stage, the stress almost stays at a plateau value while the plastic strain gradually increases. In Stage IV, the stress rapidly decreases and at the same time the effective plastic strain sharply increases, i.e. the so-called stress collapse occurs [86]. The stress collapse is a very important concept, which provides a driving force for the propagation of the shear band in a similar way as the singularity at the notch tip propels crack growth. This stage is also accompanied by high strain rates. The average value in the present case is $\dot{\epsilon} \approx 3.5 \times 10^5 \text{ s}^{-1}$. After the stress collapse, three situations may develop depending on the location of the material element and the impact velocity, see Fig. 3-46. The material element may break at the end of Stage III (stress collapse, like Element A), or continue plastic deformation until fracture (like Element B), or undergo elastic unloading recovery (like Element C and D).

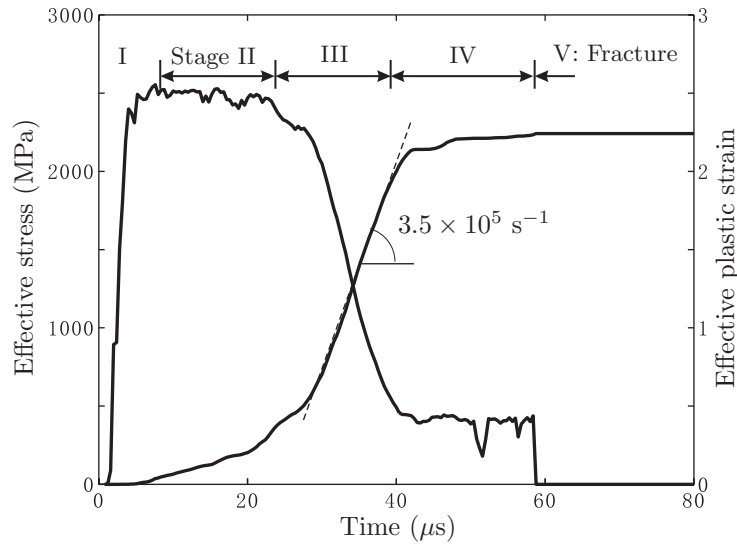


Fig. 3-45: Time history of the effective plastic strain and the effective stress of a typical point located in the middle of the adiabatic shear band at $V_0 = 27.6 \text{ m/s}$.

The stress collapse is one type of strain softening in which stresses decrease as a function of strains. The strain softening is usually caused by temperature rise, damage, or the combined action of these two factors. Damage softening is associated with growth of voids and/or micro-cracks. There is no clear definition in the literature what actually gives rise to the stress collapse in the adiabatic shear band. Here, four material points along the adiabatic shear band were selected to track down the development of the stress states during the process, which may provide an insight into the mechanism of the stress collapse, see Figs. 3-46 and 3-47. It appears that the stress triaxialities of these points are always lower than $-1/3$ except at several instances for Element A and B. Note, that $\sigma_m/\bar{\sigma} = -1/3$ corresponds to the uniaxial compressive state. Timothy and Hutchings [87] pointed out that voids, if exist before the impact, would not grow in size under predominant compression. Therefore, the stress collapse in the present case is purely due to thermal softening rather than damage softening. The combined action of thermal and damage softening may be responsible for the stress collapse in the edge-notched plate under projectile impact, e.g. Kalthoff and Winkler [80], and Zhou et al. [71]. In their cases, shear loading is dominant, though compression also presents around the notch tip, and thus void growth may participate in the stress collapse as evidenced by the scanning electron micrographs of the shear band surfaces of the post-test specimens (Figs. 4a and 4c of Ref. [71]).

It should be mentioned that the propagation of the adiabatic shear band was successfully captured using the single material constitutive model in this paper. The present formulation is much simpler than others proposed in the literature. For example, a multi-physics material model was used by Zhou et al. [74], and Li et al. [78, 79] in which the material was modeled as an elastic, thermo-viscoplastic material and a viscous fluid, respectively, before and after the stress collapse. A similar treatment that the fully-developed adiabatic shear band was represented by an ideal compressible fluid was proposed by Batra and Nechitailo [88]. They thought that it would be difficult to simulate the automatical advance of a shear band if it is represented by a single constitutive model. Since two material models were subsequently used by Zhou et al. [74] and Li et al. [78, 79] in the calculation, a criterion to predict the stress collapse that was given by a rate-dependent critical strain was implemented.

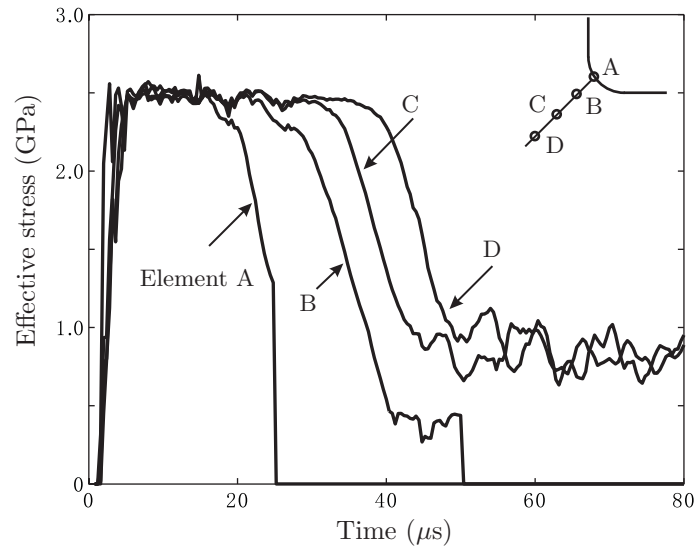


Fig. 3-46: Stress collapse at four material points within the adiabatic shear band initiating at the interior corner at $V_0 = 27.6$ m/s.

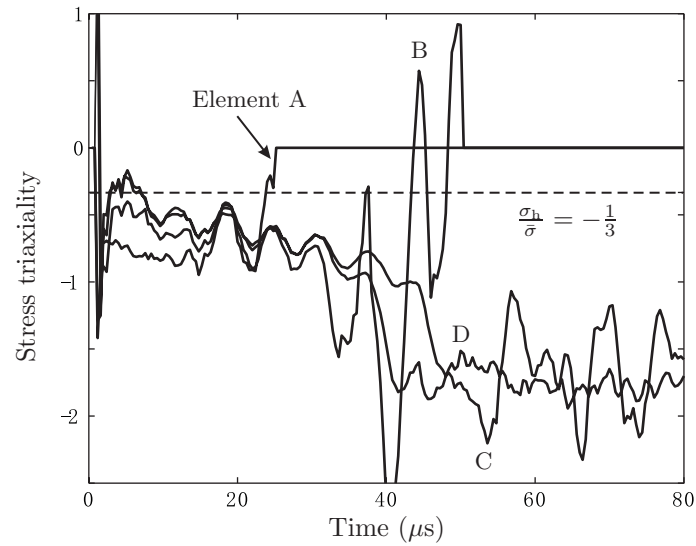


Fig. 3-47: Time history of the stress triaxiality of four material points within the adiabatic shear band initiating at the interior corner at $V_0 = 27.6$ m/s.

To numerically determine the transient and final length of the adiabatic shear band, a suitable criterion has to be introduced. Several criteria were suggested in the literature, e.g. maximum shear stresses, critical plastic strains [74], critical temperature rise [79], etc. These critical values can be calibrated from tests in combination with numerical solutions. Two impact tests were carried out by Couque [82, 83]. The length of the generated adiabatic shear band is 32% and 71% of the gauge section, respectively, at $V_0 = 26.8$ m/s and 27.6 m/s. The case with $V_0 = 27.6$ m/s is used to calibrate the critical temperature rise, which is given by $\Delta T_{cr} = 250$ K. However, it should be pointed out that the present critical temperature rise corresponds to the edge length of 10 μm since the numerical solution may be sensitive to the mesh size. At the same time, another test can be used to verify this critical temperature rise. It appears that very good agreements exist between the numerical prediction and the experimental results at $V_0 = 26.8$ m/s, see Fig. 3-48. The numerical results also indicate that the adiabatic shear band extends through the whole gauge section at about $V_0 > 28.0$ m/s. Figure 3-49 shows the growth of the adiabatic shear band initiating from the interior corner.

Note, that the present shear band has an angle with the mesh edges. However, the shear band does not grow either horizontally or vertically. Hence, for the present problem the propagation of the adiabatic shear band is mainly controlled by the loading condition and is not sensitive to the mesh alignment.

3.4.5 Crack formation and growth

The adiabatic shear banding is immediately followed by cracking. Two cracks initiate at the exterior and interior corners, respectively, and propagate along the adiabatic shear band, see Fig. 3-50. The adiabatic shear band of intense plastic deformation and high temperature provides a weak path for crack propagation. The cracks are finally arrested within the adiabatic shear band at $V_0 < 29.0$ m/s.

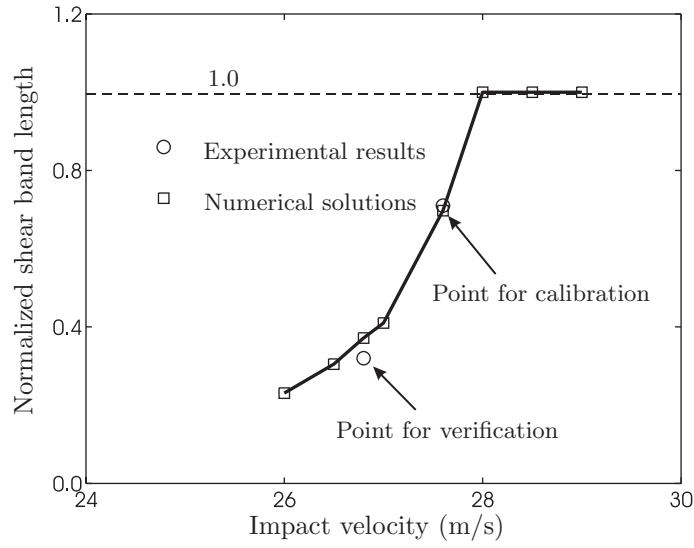


Fig. 3-48: Adiabatic shear band length vs. impact velocity.

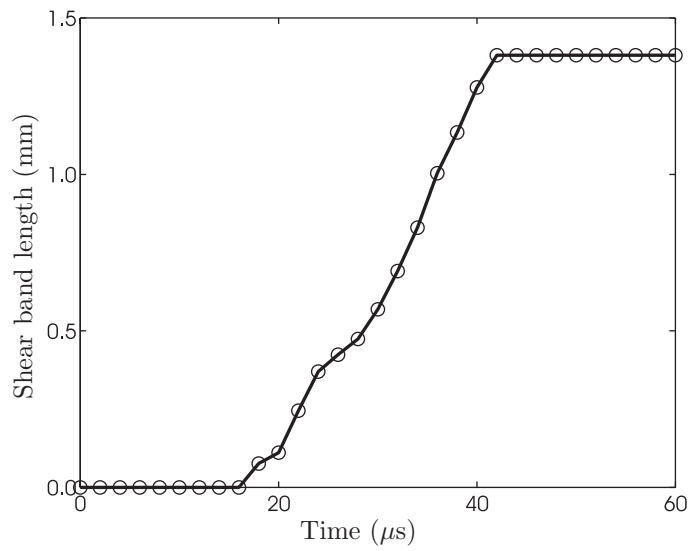


Fig. 3-49: Adiabatic shear band length vs. time at $V_0 = 27.6$ m/s.

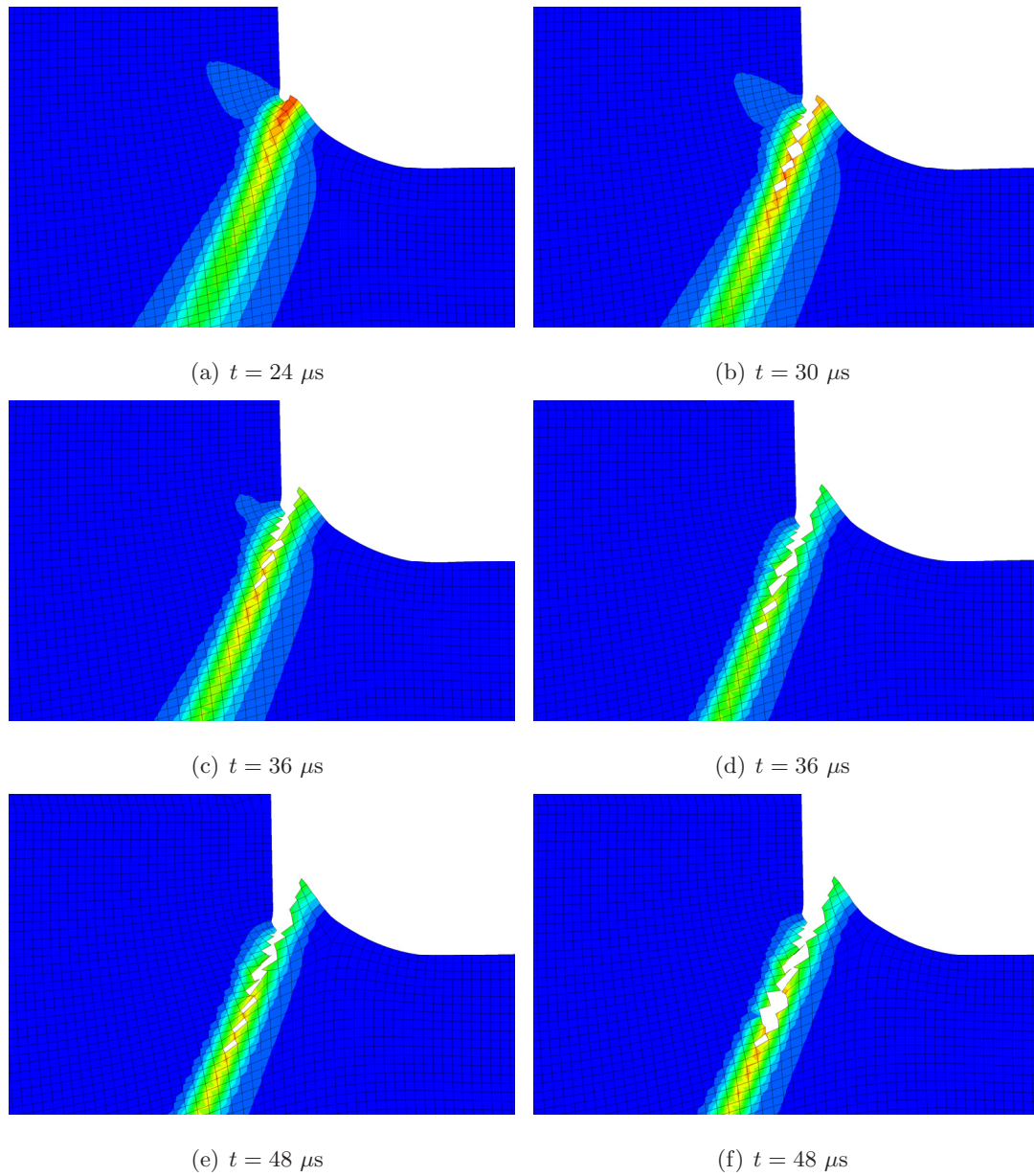


Fig. 3-50: Process of crack propagation from the interior corner at $V_0 = 27.6$ m/s and $\bar{\epsilon}_f = 0.2$ with the cut-off value for the negative stress triaxiality.

As shown in Fig. 3-46, Element A and B, whose stresses suddenly drop to zero, have been broken. It is interesting to investigate the corresponding fracture mechanism since Element A and B seem to be always dominated by compression. A close look at Fig. 3-47 reveals that the stress triaxialities of both elements are higher than $-1/3$ at the end of the loading stage or at the start of the unloading stage. During the stress collapse, unloading stress waves were generated within the adiabatic shear band. The damage would quickly accumulate in this stage, since the material strength is severely degraded during and/or after the stress collapse. A similar mechanism was proposed by Timothy and Hutingson [87] based on careful metallurgical examinations on a post-test titanium alloy plate impacted by a hard steel sphere. Several adiabatic shear bands developed in the impacted zone beneath the projectile. Voids were also found inside the adiabatic shear bands at a high impact velocity. They proposed that the formation of the voids was due to shear recovery of the indentation at the later stage of the impact process.

The stress triaxiality is not uniform along the shear band, as stated by Fig. 3-51, but increases from large negative value at the center to positive at the edge. The statement made in Ref. [82] that fracture was observed at high negative hydrostatic stress of $\sigma_m = -1.5$ GPa does not seem to be correct. Such a state may prevail in the central portion of the gauge section but not near the edges.

Clearly, the length of the generated cracks is a function of the impact velocity of the striker bar, see Fig. 3-52. It appears that at a relatively low velocity the crack initiating from the exterior corner is a little shorter than that from the interior corner, however, it becomes much longer at a high velocity. Figure 3-53 shows that at $V_0 = 29.0$ m/s the predicted cracks were arrested in the gauge section before meeting each other. If the velocity is sufficiently high, the specimen would break into two parts.

As can be seen from Fig. 3-54, the magnitude of the effective plastic strain within the adiabatic shear band reaches about 2.4, which is much higher than the fracture strain in uniaxial tension. Since the stress state is predominantly compressive, the nucleation, growth, and coalescence of voids would be suppressed. Correspondingly, the increases in the effective plastic strain will not contribute to the damage accumulation in the calculation. A material element may keep intact although its effective plastic strain is very large. In

such a sense, large compressive stresses make the material more ductile [5].

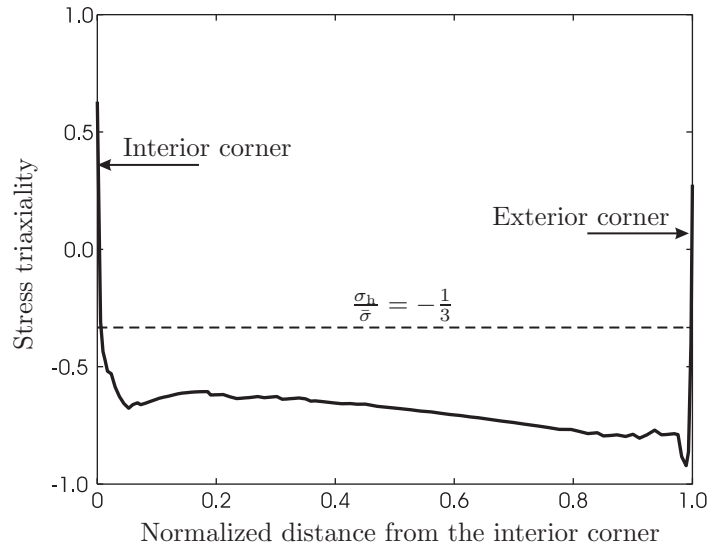


Fig. 3-51: The profiles of the stress triaxiality along the shear band at $t = 24 \mu s$ right before the crack formation.

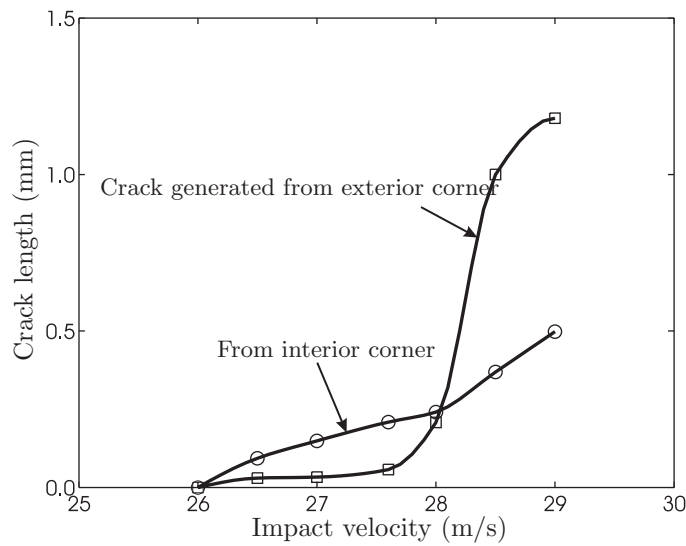


Fig. 3-52: Crack length vs. impact velocity at $\bar{\epsilon}_F = 0.2$ with the cut-off value.

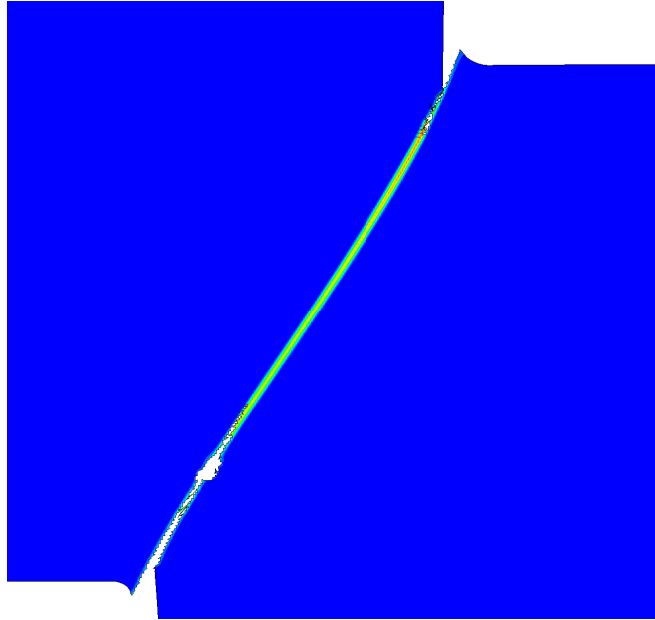


Fig. 3-53: Shear bands and cracks generated along the gauge section at $V_0 = 29.0$ m/s.

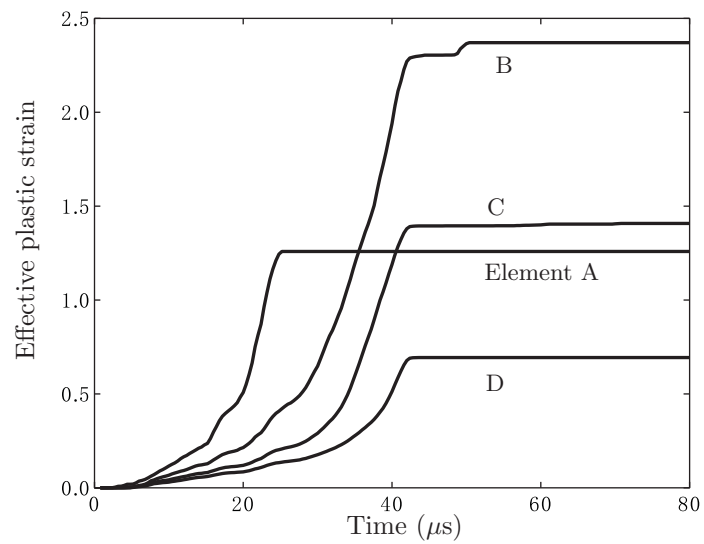
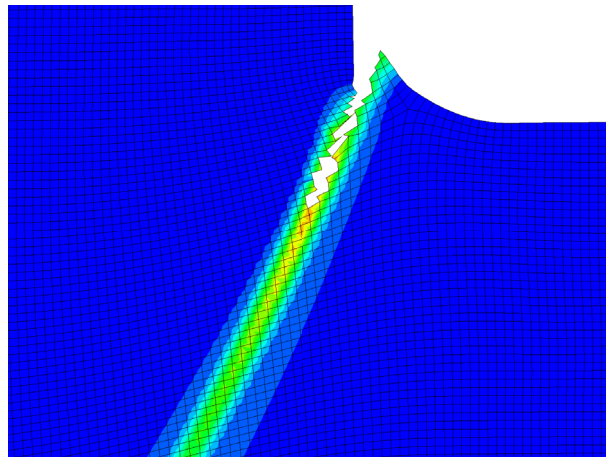
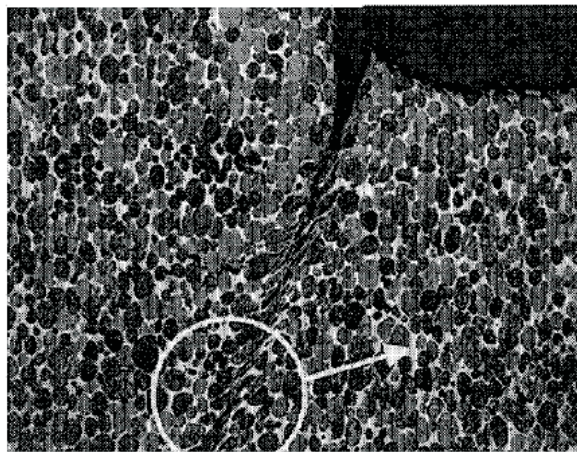


Fig. 3-54: Time history of effective plastic strain of four material points within the adiabatic shear band initiating at the exterior corner at $V_0 = 27.6$ m/s.

Figure 3-55 shows the comparison of the final fracture pattern between the numerical simulation and the test results by Couque [82]. At the same time, it can be seen from Fig. 3-52 that the numerically predicted crack length is very close to the experimentally measured values. Very good agreements between the test and simulation prove the correctness of the present numerical solutions.



(a) Numerical prediction



(b) Experimental results

Fig. 3-55: The crack and shear band generated around the interior corner at $V_0 = 27.6$ m/s.

3.4.6 Temperature fields

Figure 3-57 shows spatial and temporal evolution of temperature field along the gauge section of the specimen. It appears that the temperature is highly nonuniform within the adiabatic shear band. The high gradient of the temperature field across the adiabatic shear band can be clearly observed from two typical temperature profiles shown in Fig. 3-56. This cusp-shaped distribution across the shear band, i.e. the so-called canonical structure of the fully-developed adiabatic shear band [89], is consistent with experimental observations by, e.g. Marchand and Duffy [70], Zhou et al. [71]. The maximum temperature rise is about 1100 K at the impact velocity of $V_0 = 27.6$ m/s.

The most interesting finding of the present numerical solution is that temperature distribution is slightly turbulent, and a number of small regions of intense temperature develops periodically along the length of the adiabatic shear band, see Fig. 3-58. The average spacing between these “hot spots” is $23 \mu\text{m}$. Stresses and strains have similar patterns. In a way, these hot spots resemble vortices shed from a circular cylinder downstream into a wake. This result contradicts the assumption made in the theoretical models, e.g. Wright and Ravichandran [89], in which the plastic flow within the adiabatic shear band was laminar.

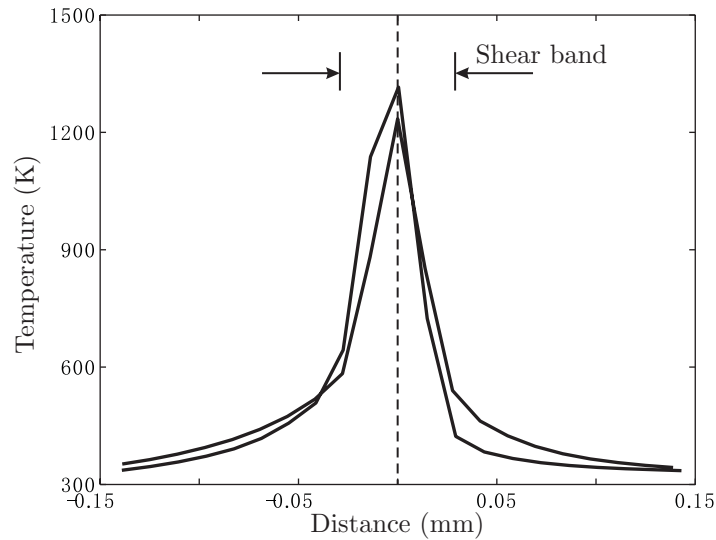


Fig. 3-56: Temperature distribution along two lines across the adiabatic shear bands at $V_0 = 27.6$ m/s.

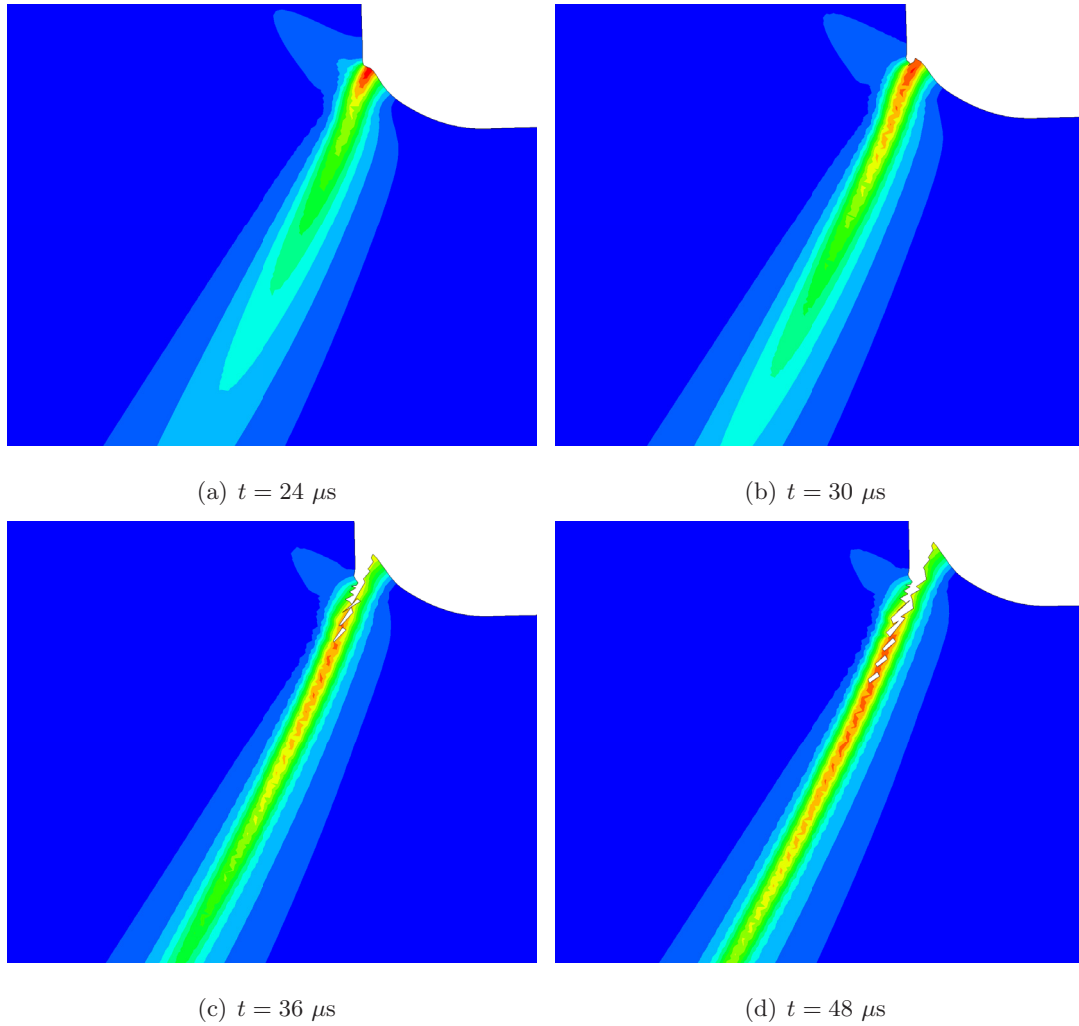


Fig. 3-57: Transient temperature fields around the interior corner at $V_0 = 27.6$ m/s.

The present numerical results are consistent with the experimental findings by Guduru et al. [72, 73]. They used a square array of 64 infrared temperature detectors and for the first time, recorded the evolution of two-dimensional temperature field of adiabatic shear bands in a single edge-notched steel plate under projectile impact. The loading configuration and specimen are entirely different from the present ones. The occurrence of the turbulent temperature field in both specimens may indicate that the turbulent temperature structure is an intrinsic feature of adiabatic shear bands.

Since temperature within adiabatic shear bands may rise to near the metal melting point, the materials would lose most of the load carrying capability and become very easy to

deform. At the same time, the surrounding materials experience little plastic strain. In such a sense, the behavior of the materials within the adiabatic shear band are very similar to that of a thin layer of viscous fluid confined between two rigid plates, i.e. the plane Couette flow in fluids [72]. Under a certain condition, the plane Couette flow would become unstable. For example, by assuming the fluid viscosity as a function of temperature, Yueh and Weng [90] proved that small perturbations would lead to the instability of the plane Couette flow if the Reynolds number exceeds a critical value. Based on two-dimensional perturbation analyses, Molinari and Leroy [91] derived the instability conditions and recreated spatially repeated temperature patterns using a thermo-viscoplastic constitutive model. In analogy to the plane Couette flow, Guduru et al. [72, 73] conjectured that the highly nonuniform temperature distribution would imply a new kind of thermo-mechanical instability developing within the adiabatic shear band.

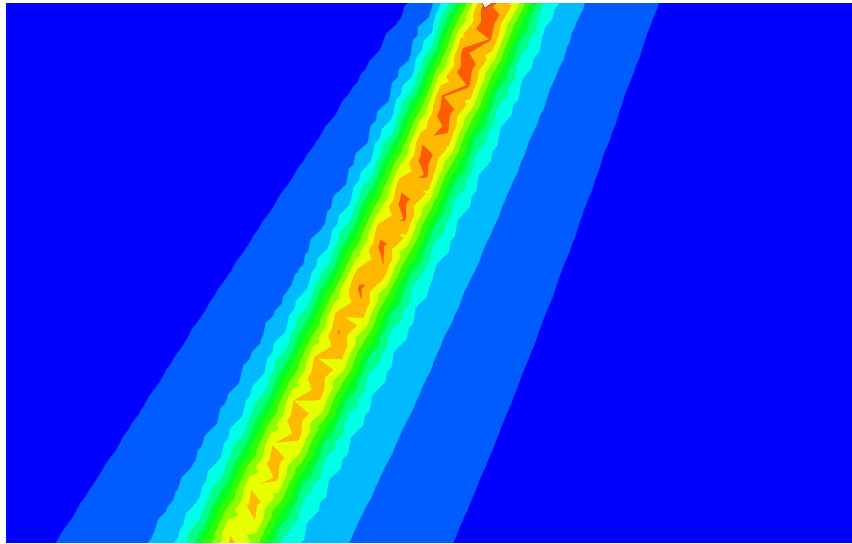


Fig. 3-58: Periodical occurrence of hot spots within the adiabatic shear band at $V_0 = 27.6$ m/s.

It should be emphasized that the spatially repeated hot spots within the adiabatic shear band were recreated in the present study using the conventional finite element procedure and the simple material constitutive model. This is completely different from Li et al.'s approach, in which the evolution of the temperature field in Guduru et al.'s experiment was captured using the mesh-free scheme and the multi-physics material models [78, 79]. It

seems that a key factor in capturing the hot spots is to use sufficiently small meshes rather than modify numerical methods or introduce complex material constitutive models.

A question was raised by Guduru et al. [72, 73] and Li et al. [78, 79] whether there is any implication of the hot spots on ductile fracture. No answer was given to this question. Since the spatial resolution of the infrared temperature detector used by Guduru et al. is about $110\ \mu\text{m}$, which may be much larger than the width of a shear crack, and thus it would be difficult to track down the crack growth. The present research, in which the adiabatic shear band and shear fracture were treated separately, provides an insight into this question. The physical role of the hot spots in ductile fracture becomes clear when we make a close look at the process of crack growth. As shown in Fig. 3-50 these hot spots offer a series of initiation sites of ductile fracture since higher temperature means larger plastic strains. The crack within the shear band was formed mainly by linkage rather than the propagation of a major crack. This mechanism is driven by mechanics rather than materials. By contrast, the nucleation and growth of voids independently at different sites as often seen in scanning electronic micrographs of fracture surfaces is usually due to material defects of micro-structures.

3.4.7 Effect of fracture strains

The fracture properties of a specific material depend on stress states, strain rates, temperature, material microstructures, and material processing, etc. Since no fracture locus is available currently for the 25% swaged 91W-6Ni-3Co tungsten alloy, it is necessary to investigate effects of the magnitude of the fracture strain on the predicted fracture response.

Figure 3-59 shows the numerically predicted crack length as a function of the magnitude of the fracture strain. Since the absolute magnitude of the crack length is lower than 1 mm while the fracture strain varies in a wide range from 0.1 to 0.5, it can be concluded that the fracture response is relatively not much sensitive to the magnitude of the fracture strain. At the same time, since cracking is far lag behind the occurrence of the shear band, the crack formation would not have much influence on the development of the adiabatic shear band.

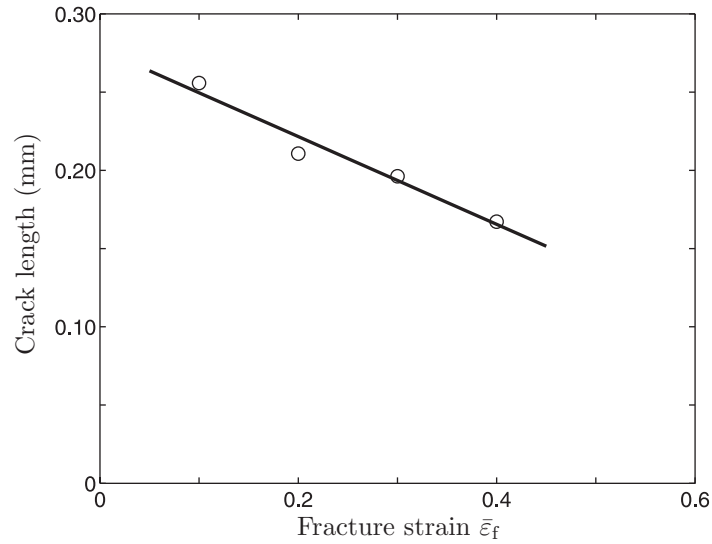


Fig. 3-59: The predicted length of the crack initiating at the interior corner as a function of the magnitude of the fracture strain.

3.4.8 Adaptive vs. fixed meshing

The materials within the adiabatic shear band is subjected to large plastic deformation. Originally regular meshes would be severely distorted if fixed meshing were used. As shown in Fig. 3-60 where a fixed Lagrangian mesh is used, the originally square elements undergo large rotation and stretching. Such low-quality meshes would be unable to provide sufficiently accurate results for the prediction of the following fracture. Arbitrary Lagrangian-Eulerian (ALE) adaptive meshing gives more accurate and robust solutions if numerical errors introduced in re-mapping solution variables from an old mesh to a new one are very small.

In some cases, adaptive meshing can speed up computation by improving the quality of severely deformed meshes. However, for the present problem the computational time increases from 12 hours (fixed meshing) to 26 hours (adaptive meshing) due to a number of remapping operations. Another disadvantage of adaptive meshing is the difficulty of tracking down the time history of the stress state of a specific material element, because the adapted mesh is not fixed to the same material point throughout the calculation. In the previous figures regarding the time history of the components of the stress and strain

tensors, fixed meshing was used in the calculation instead of adaptive meshing.

The hot spots can also be identified from Fig. 3-60. This confirms that the nonuniform structure of the adiabatic shear band does not result from adaptive meshing and spatial remapping of solution variables but an intrinsic feature of the adiabatic shear banding.

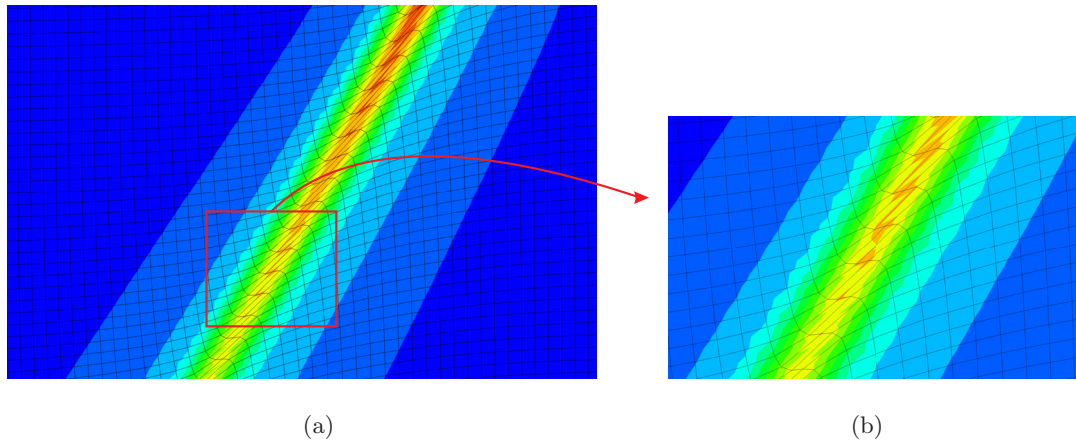


Fig. 3-60: Temperature contours using fixed meshing at $V_0 = 27.6$ m/s.

3.4.9 Concluding remarks

In this section, a recently performed impact experiment on an axisymmetric hat specimen was simulated using ABAQUS/Explicit. The formation and propagation of the adiabatic shear bands and the subsequent cracks were successfully captured and the corresponding mechanisms were investigated. In contrast to the existing analysis published in the literature, the fracture was clearly distinguished from the adiabatic shear band in this research. The adiabatic shear band was automatically resolved while the prediction of cracking was achieved by implementing the newly developed BW's fracture locus. It was found that the hot spots that periodically occur in the propagating shear band act as the initiation sites of the crack. Thus, the formation of the crack within the shear band resembles a linkage of small cracks rather than the growth of a single major crack. Comparison with the experimental results was made showing very good agreements, which verifies the accuracy of the present numerical simulations.

In the present tungsten alloy hat specimen, adiabatic shear banding is followed by shear

cracking. Another failure scenario also exists that shear crack precedes adiabatic shear banding, depending on impact configurations and material properties of targets. For a 2024-T351 aluminum alloy beam impacted by a rigid, flat-nosed mass moving at $V_0 = 240$ m/s, Teng and Wierzbicki [60] found that the plastic instability strain, which is in the range of $0.7 \sim 0.9$ [92], is much higher than the fracture strain. Hence, the beam would fail by shear cracking before adiabatic shear bands occur.

The typical width of adiabatic shear bands ranges from 10 to 100 μm depending on loading levels and grain size [42]. Several solid elements are needed to capture the formation and growth of adiabatic shear bands in the lateral direction. It should be noted that at such a fine scale, material microstructures would become equally important as mechanics for the formation of adiabatic shear bands. In the present study, the problem is still treated in the context of continuum mechanics. It is not clear how to take into account material microstructures in the numerical prediction of adiabatic shear bands.

Up to date, almost all research on adiabatic shear banding was done in laboratories at a component level. How to apply our understanding obtained from specially designed specimens to practical problems remains unclear. The width of adiabatic shear bands is typically 1 – 100 μm while the lower limit of the element edge length affordable in the calculation of real penetration problems is about 1 mm [93]. Using such elements, the prediction of adiabatic shear bands would be delayed or impossible. In tests, adiabatic shear bands are usually induced by specially designed geometrical discontinuities such as pre-notches, sharp corners, etc. By contrast, actual targets usually have smooth surfaces and thus adiabatic shear banding is caused mainly by microstructural inhomogeneities, which are quite random in real materials. It is more difficult to introduce material imperfections in numerical modelling than geometrical discontinuities.

Chapter 4

Properties of Through-Thickness Crack Growth

4.1 Introduction

Crack formation and growth has been extensively studied in the literature, mostly for elastic brittle materials and small plastic deformation problems. As Rosakis and Ravichanran [3] pointed out in a review article, the dynamic ductile fracture remains unexplored. This chapter studies the perforation problem of a metal beam/plate under high velocity mass impact. Numerous voids are often observed from scan electronic micrographs of post-test specimens ahead of an arrested crack tip and in the wake region of a generated crack, e.g. Børvik et al. [94]. At the same time, the fracture surface exhibits a number of dimples, e.g. Mason and Worswick [76], Dey [95] (Fig. 95). These experimental observations indicate that a metal target under high velocity impact tends to fail by ductile fracture. Hence, the perforation response belongs to dynamic ductile fracture. Comprehensive reviews on perforation mechanisms and analytical solutions can be found in the journal articles by Anderson and Bodner [43], Corbett et al. [44], and Goldsmith [8]. A main interest of the research presented in the literature was on the determination of ballistic limits of targets.

As compared to extensive literature on the ballistic limit, only few papers deal with through-thickness crack propagation, even though crack propagation is always involved in the perforation problem. Most of perforation experiments were performed on opaque plate

specimens such that crack growth through the target thickness is difficult to track down using currently available techniques. By contrast, finite element procedures are capable of overcoming this difficulty and giving abundant details about crack initiation, crack tip speeds, and crack trajectories, provided that these algorithms are equipped with a suitable material constitutive model and fracture model. Finite element methods have reached a state of maturity. Many commercial codes such as ABAQUS, LS-DYNA3D, etc. are capable of fulfilling these tasks. Some numerical studies were published in the open literature, e.g. Ambur et al. [96], Guo et al. [97], and Børvik et al. [56, 55]. Similarly to experimental investigations, attention was focused mainly on the numerical determination of ballistic limits while the formation and growth of cracks were not addressed in these papers.

In Chapter 3, we have successfully demonstrated the applicability of the BW's fracture criterion to high velocity impact problems. In this chapter, we will use this fracture locus to specifically investigate crack formation and propagation in shear plugging. We first propose an analytical expression controlling the growth of through-thickness cracks, and then perform an extensive parametric study to numerically verify this crack growth curve. In addition, effects of a propagating crack on damage accumulation are discussed and crack propagation speeds are calculated.

4.2 Development of crack growth curve

A beam/plate favorably fails by shear plugging if a projectile is heavy, of flat-nose shape, and moves at a high impact velocity. Two cracks usually initiate on the proximal surface and grow through the target thickness until to the distal surface. As shown in Chapter 3.2.4, during the shear plugging failure process, plastic deformations occur at three distinct scales: localized shear deformation through the target thickness, large compression of the impacted zone of the target directly beneath the projectile, and global plastic bending/axial stretching deformation. The last one is usually negligible at a high impact velocity compared with the first two plastic deformation. This kind of failure pattern can be described by means of two variables: the crack length a and the indentation depth u , as shown in Fig. 4-1. Preliminary

numerical results suggest the following relationship between these quantities [60]:

$$\frac{a}{h} = K \left[(1 + \mu) \frac{c}{V_0} \frac{u}{h} \right]^\lambda \quad (4.1)$$

where c is the transverse plastic wave speed defined in Eq. (7.4), K and λ are two material constants, and the mass ratio μ of the impacted zone of the target to the projectile is defined by

$$\mu = \frac{2\rho hbd}{M_0} \quad (4.2)$$

for a beam, and

$$\mu = \frac{\rho\pi h d^2/4}{M_0} \quad (4.3)$$

for a circular plate.

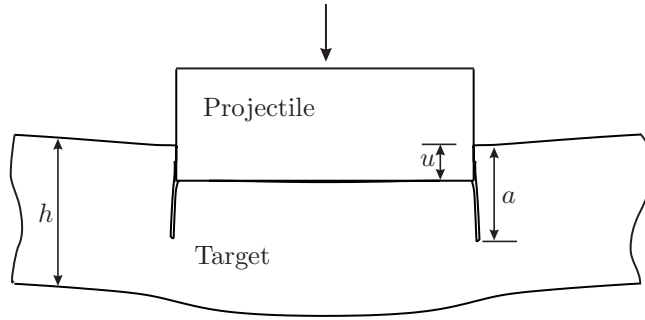


Fig. 4-1: Schematic representation of through-thickness shear cracks.

Differentiating Eq. (4.1) with respect to time gives the crack tip speed v :

$$\frac{v}{V} = \lambda K \left[(1 + \mu) \frac{c}{V_0} \right]^\lambda \left(\frac{u}{h} \right)^{\lambda-1}, \quad (4.4)$$

where $v = da/dt$; and $V = du/dt$ is the indentation rate. If the global deformation of the target can be neglected, V is just the velocity of the projectile. A derivation of the expressions for both instantaneous and average crack tip speeds^λ will be presented in Chapter 7.5.

It is impossible that the critical indentation depth would exceed the target thickness, which imposes a restriction on the range of applicability of Eq. (4.1). Setting $u = h$ and

$a = h$ in Eq. (7.206) gives the upper bound of the impact velocity, $V_{0,u}$,

$$\frac{V_{0,u}}{c} = K^{1/\lambda}(1 + \mu). \quad (4.5)$$

To date, no experimental results are available to corroborate the relationship between the crack length and the indentation depth. But a similar relationship was proposed earlier in the literature. McClintock and Slocum [98] found analytically that a crack along a shear band grows in an exponential way with shear displacement for a fully plastic plate under quasi-static Mode II loading.

It should be mentioned that Eq. (4.1) was originally obtained by curve-fitting crack growth for a specific case in which the initial impact velocity was varied and other parameters were kept constant [60]. The development of Eq. (4.1) in a purely analytical way remains open. The immediate objective of this chapter is to show that Eq. (4.1) derived for a specific set of input parameters is also valid in a wide range of impact velocities, plate thicknesses, and mass ratios. This is accomplished through an extensive parametric study in which only one parameter was varied at a time.

4.3 Crack initiation sites

In a pre-notched specimen, a crack always initiates at a small fracture process zone (FPZ) around the notch tip. This fracture process zone advances with the newly generated crack tip. Macroscopically, it looks like that a major crack propagates away from the notch tip. By contrast, all the targets considered in the present thesis do not have any damage before impact loading. The site of crack initiation will depend on a specific combination of all the input variables. This makes the problem interesting and at the same time difficult to track down the formation and growth of a crack in experiments.

In Chapter 3.2, we have already demonstrated several numerical examples with different sites of the crack initiation. In the case of the flat-nosed projectile moving at a high impact velocity, the cracks are always induced by the sharp corners on the proximal surface of the target due to the stress concentration, see e.g. Fig. 3-14. The sharp corners also drive the cracks to propagate through the target thickness until the cracks reach the distal surface of

the beam.

In the case with a round-nosed projectile, the impacted zone of a target gradually wraps with the rigid projectile. There are no stress concentration points on the proximal surface. The initiation site of a crack may be located on the distal surface of a target, e.g. see Fig. 3-12, in which a plane-strain beam of $h = 2$ mm is impacted by the projectile of the diameter $d = 20$ mm.

It is also possible that cracks initiate in the middle of a target. Figure 4-2 shows the crack formation of a plane-stress aluminum alloy beam impacted by a round-cornered projectile moving at $V_0 = 240$ m/s. It appears that two cracks first occur in the middle of a plane-stress beam and propagate upwards and downwards simultaneously until a plug is formed. The failure of the beam is due to a combined action of shear and tension [59].

In this chapter, the first case is of most interest and will be extensively studied. The crack growth curve given in Eq. (4.1) is not applicable to the latter two cases.

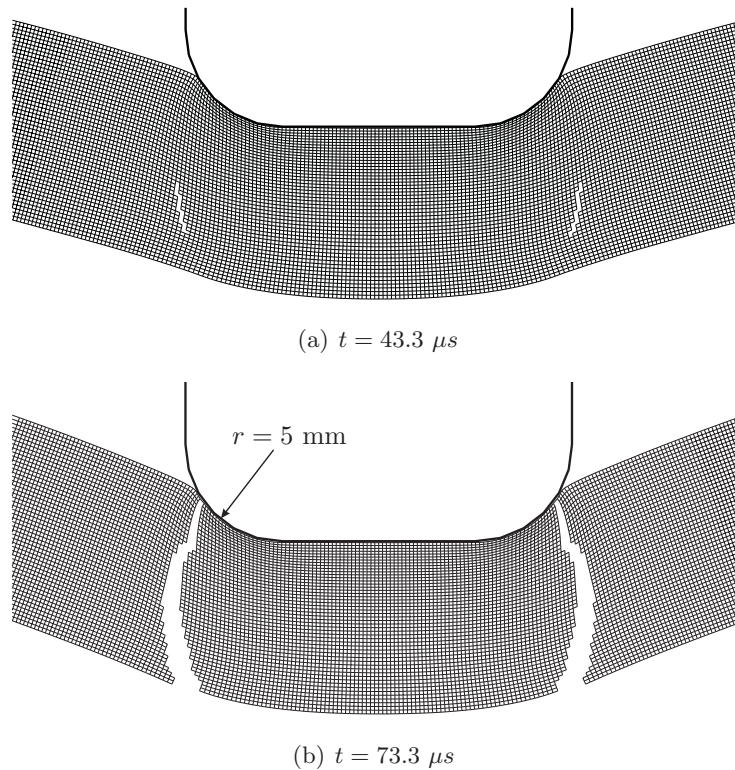


Fig. 4-2: Crack formation and growth of the plane-stress beam of $h = 10$ mm impacted by the projectile of $\mu = 0.1$ and $2r/d = 0.50$ at $V_0 = 240$ m/s ($d = 20$ mm).

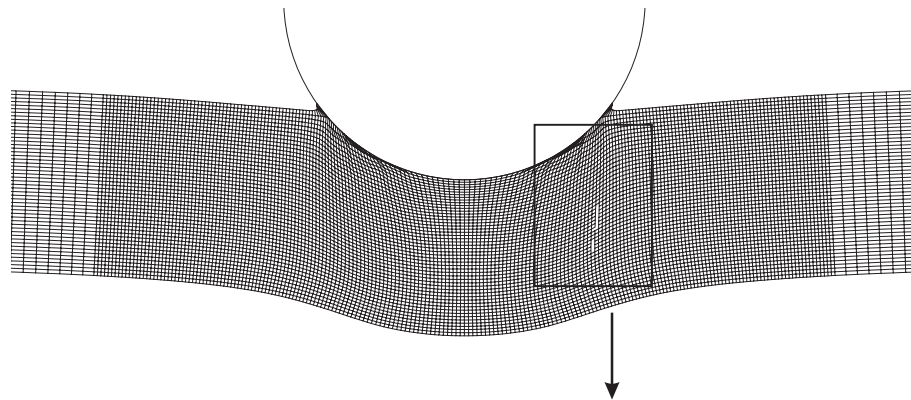
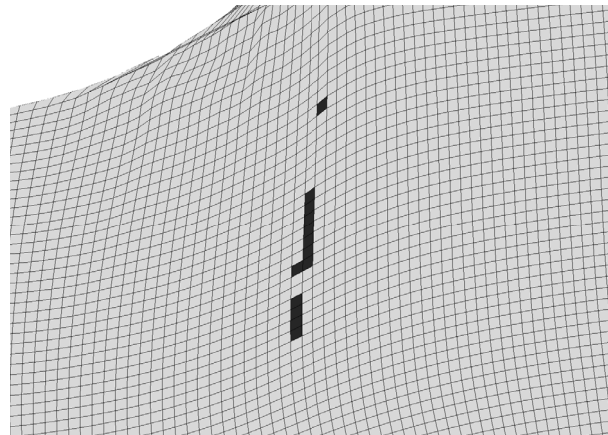
4.4 Crack initiation vs. propagation

Most of ductile fracture criteria including the BW's fracture locus were initially developed for crack formation. Crack propagation is essentially thought of as a sequence of fracture re-initiation for each failed element in applications. A question is naturally raised whether such an approach is correct since crack formation and propagation have different mechanisms [99]. An attempt is made in this section to explore the issue.

As a crack grows inside a originally continuum body, new boundaries are generated. The crack propagation process can be thought of as a series of new initial-boundary value problems. Different from the crack formation in an uncracked body, a propagating crack gives rise to the stress concentration at its tip, and at the same time, unloading stress waves emanate from the newly generated free boundaries. Both factors will contribute to variation of the stress and strain states of a region ahead of the crack tip. In such a sense, the crack formation has a different mechanism from the crack growth.

For a pre-notched specimen under loading, plastic deformation concentrates at the fracture process zone in the vicinity of the tip of a crack. By contrast, for an uncracked body under high intensity stress wave loading, a large part of the target thickness in a critical region already undergoes large plastic deformation before crack formation. A propagating crack would not add much damage on an element leading to its complete failure. Hence, the approximate treatment of crack propagation as a sequence of fracture re-initiation would give reasonable results such as residual velocities, failure patterns, and even crack tip speeds.

This is more true for a target under round-nosed mass impact, in which the geometry of a struck beam/plate keeps continuous and thus there is no stress concentration. Figure 4-3 shows the crack formation of a plane-strain beam under round-nosed mass impact. On close scrutiny, it can be observed that multiple fractures start at various points through the beam thickness almost at the same time. The through-thickness plug is formed mainly by linkage rather than propagation of a single crack. Note, that the time increment between Figs. 4-3(a) and 4-3(c) is only $1 \mu\text{s}$.

(a) $t = 18 \mu s$ 

(b) Dark represents the failed elements

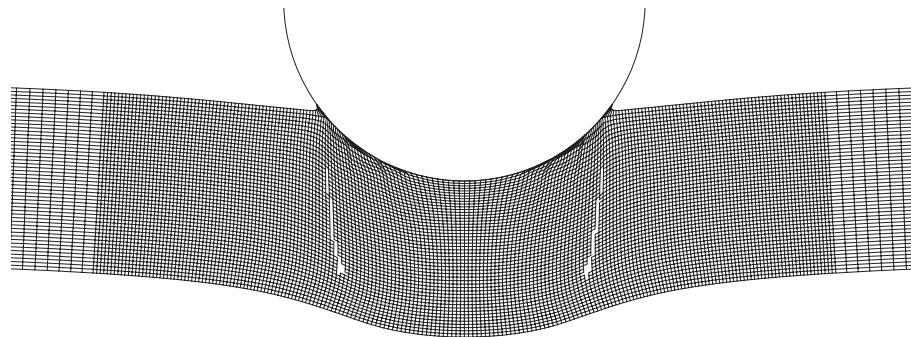
(c) $t = 19 \mu s$

Fig. 4-3: Crack formation of the 2024-T351 aluminum alloy beam of $h = 10$ mm impacted by the round-nosed mass of $\mu = 0.1$ at $V_0 = 300$ m/s.

In the flat-nosed case, two major cracks would be induced by the sharp corners of the projectile and grow all the way down to the distal surface. The propagating cracks would have a certain effect on the damage accumulation ahead of the crack. One simple way to investigate this effect is to make a comparison between two cases: one with a fracture locus implemented and the other without fracture. In the former case, failed elements are removed to model the crack formation and propagation while in the latter case, the target undergoes large plastic deformation but keeps intact. Figure 4-4 shows the damage evolution of three typical elements in the case of a plane-strain aluminum alloy beam impacted by a flat-nosed projectile. These three elements are located, respectively, on the proximal and distal surfaces, and in the middle of the beam. In the case with fracture, an element fails as soon as the damage indicator defined in Eq. (5.3) reaches unity. Certainly, both cases agree well in Element A located on the proximal surface before the damage indicator reaches the critical value. The damage accumulation of Element B is quite close to each other in both cases. This indicates that a propagating crack would not add much damage on the central part of the beam leading to its complete failure. In contrast to the Element A and B, there is large difference in the damage evolution of Element C at the end of the failure process. As the generated crack propagates down, the ligament of the beam is shortened. The growth of the crack and shortening of the ligament would contribute to the difference between both cases. However, it is difficult to discern their respective roles.

As can be observed from the definition of the damage index, Eq. (5.3), both the effective plastic strain and the stress triaxiality are equally important to the damage accumulation. Figure 4-5 shows the time history of the stress triaxiality and the effective plastic strain of Element C. It is seen that the growth of the crack and the shortening of the ligament do not have much influence on the stress triaxiality. However, this is not the case for the effective plastic strain, which rapidly increases at the end of the failure process in the case with fracture.

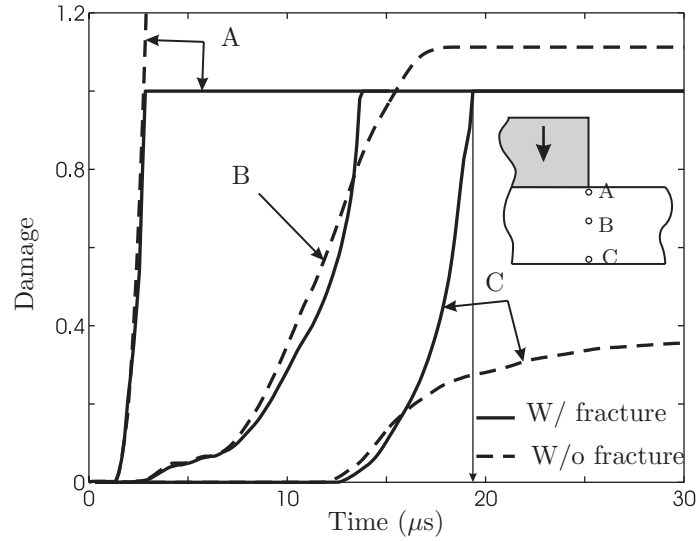


Fig. 4-4: Damage accumulation of three points along the crack of the plane-stress beam of $h = 10$ mm impacted by the flat-nosed projectile of $\mu = 0.1$ at $V_0 = 240$ m/s.

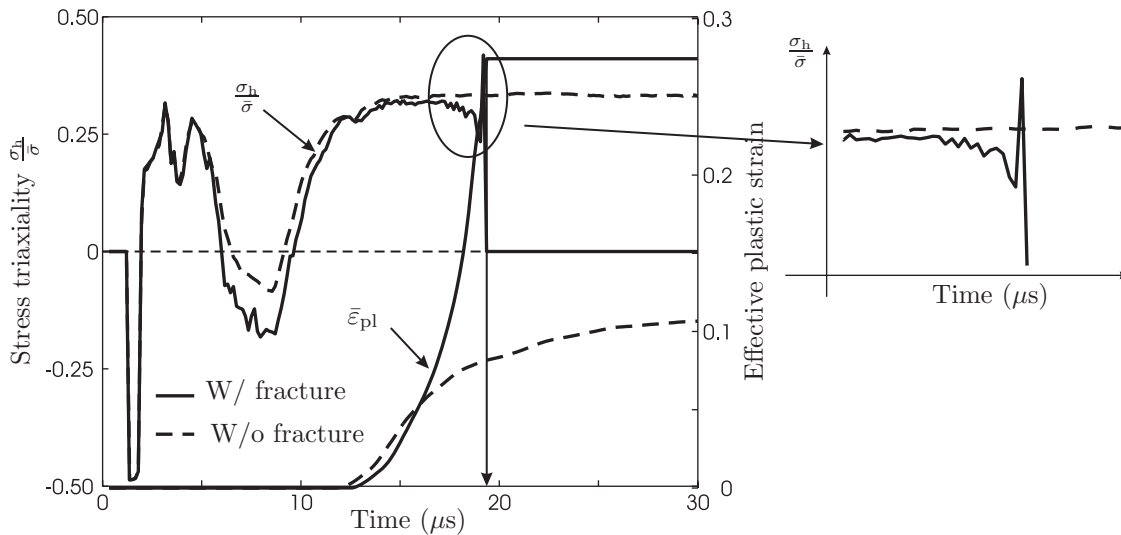


Fig. 4-5: Time history of the stress triaxiality and the effective plastic strain of the point (Point C) located at the distal surface of the plane-stress beam of $h = 10$ mm impacted by the flat-nosed projectile of $\mu = 0.1$ at $V_0 = 240$ m/s.

4.5 Parametric study on crack growth

4.5.1 Finite element modeling

Two types of projectile-target systems are considered in the present section: a long, solid beam of rectangular cross-section impacted by a rigid cubic projectile, and a large circular plate impacted by a flat-nosed, rigid, cylindrical projectile. In finite element modeling, both the beam length $l = 1.0$ m (the diameter of the circular plate) and the breadth $d = 20$ mm (the diameter) of the projectile were kept constant, while other geometrical and mechanical parameters such as the mass of the projectile M_0 , the thickness of the target h , the impact velocity V_0 , etc. were varied to investigate their effects on the perforation process.

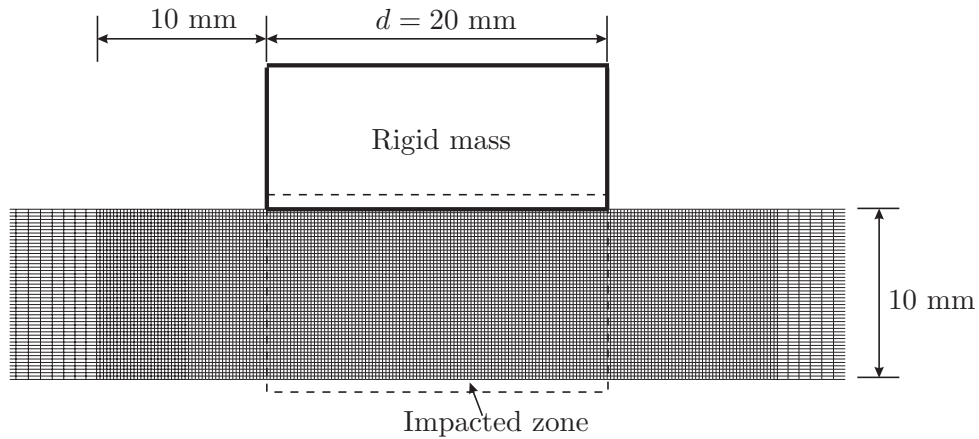


Fig. 4-6: Finite element meshes of the impacted zone of a beam struck by a flat-nosed mass.

Since attention is focused on crack propagation through the thickness, 2-D finite element models were built instead of 3-D solid element models. A narrow beam can expand laterally with little constraints when it is indented by a projectile. Thus, plane stress elements were suitable for this type of beams, while plane strain elements have to be used for a wide beam. For a circular plate under high velocity impact by a flat-nosed projectile, shear plugging is a favorable failure mode rather than petalling, and thus a 2-D model can also be built using axisymmetric elements. The deformation and possible failure of the projectile was not taken into account in the present formulation. The projectile is represented by a rigid surface in the finite element model.

One of the finite element mesh models is illustrated in Fig. 4-6 where the minimum

element size is $0.2 \text{ mm} \times 0.2 \text{ mm}$. The targets are assumed to be made of 2024-T351 aluminum alloy. The JC's material model and the BW's fracture locus were defined in the calculation.

4.5.2 Impact velocity

As demonstrated in Chapter 3, there are three possible failure modes for a beam/plate struck by a rigid projectile: tensile tearing, shear plugging, and adiabatic shear banding followed by fracture in the ascending order of the impact velocity. This chapter is concerned with shear plugging.

Clearly, the initial impact velocity is one of the most important parameters controlling the formation and growth of cracks. Figure 4-7 shows four crack propagation curves as a function of the normalized indentation depth. The target beam considered is of the thickness $h = 10 \text{ mm}$ and the rigid, flat-nosed projectile is of the mass ratio $\mu = 0.1$. The impact velocity was varied from 160 m/s to 300 m/s , while other parameters were kept constant.

As shown by Teng and Wierzbicki [60], this beam fails by tensile tearing at $V_0 < 180 \text{ m/s}$ while by shear plugging at $V_0 \geq 180 \text{ m/s}$. In tensile tearing, cracks rapidly propagate downwards until to the distal surface with little indentation. This corresponds to the vertical increase in the crack length at the end of the failure process for the case with $V_0 = 160 \text{ m/s}$, as shown in Fig. 4-7. In other three cases, the present target fails by shear plugging, and plots of crack length vs. indentation depth can be fitted well by Eq. (4.1) with $K = 10$ and $\lambda = 4$.

4.5.3 Projectile mass

Another parameter controlling the perforation process is the weight of the projectile. Its effect on the transition of the failure modes from tensile tearing to shear plugging was presented in Ref. [59]. It was found that the present beam of $h = 10 \text{ mm}$ fails by shear plugging at $V_0 = 240 \text{ m/s}$ if the mass ratio falls in the range of $\mu < 0.35$. Note, that the small mass ratio corresponds to the heavy projectile. In this range, Eq. (4.1) gives a rather good fit for the curves of instantaneous crack length vs. indentation depth using Eq. (4.1), see Fig. 4-8.

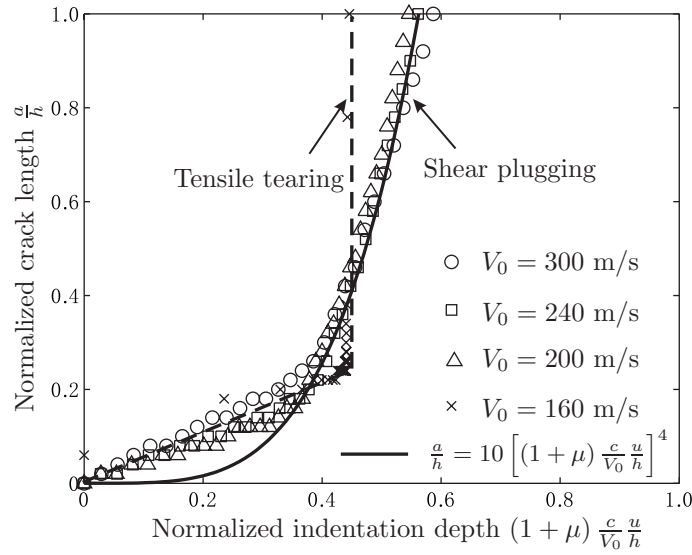


Fig. 4-7: Crack propagation at various impact velocities for the plane-stress beam of $h = 10$ mm and $\mu = 0.1$. The points represent the numerical results and the curve denotes Eq. (4.1). The dash line represents a fitting curve for the tensile tearing case at $V_0 = 160$ m/s.

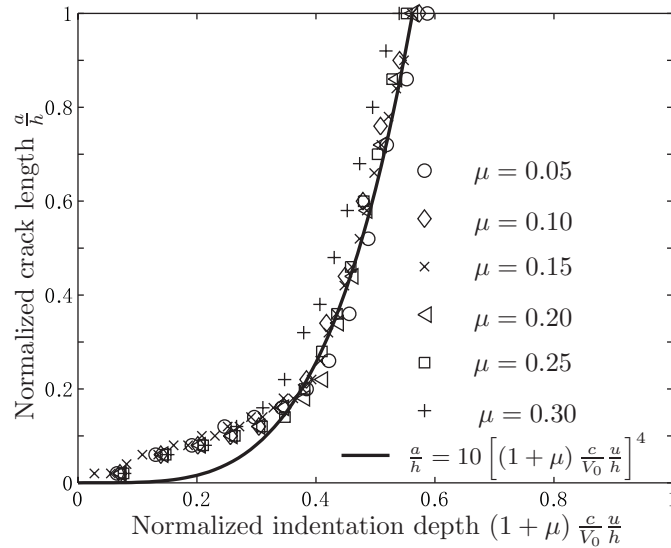


Fig. 4-8: Crack propagation at various mass ratios for the plane-stress beam of $h = 10$ mm at $V_0 = 240$ m/s.

4.5.4 Beam thickness

A target is thought of to be thin/thick if its thickness is much smaller/larger than the projectile breadth. An occurrence of a specific failure mode also depends on the aspect ratio of the beam thickness to the projectile breadth. But either a thin or intermediately thick target would fail by shear plugging if the impact velocity of the projectile is sufficiently high.

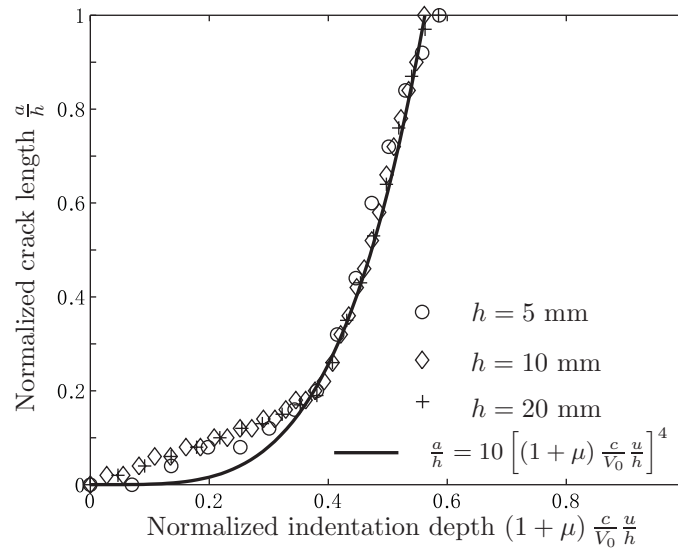


Fig. 4-9: Crack propagation in the plane-stress beam of various thicknesses at $V_0 = 240$ m/s and $\mu = 0.1$.

Effects of the plate thickness on the ballistic limit were extensively studied experimentally and numerically by Børvik et al. [100], and by Corran et al. [51]. They found that there is a kink in the curve of ballistic limits vs. thickness corresponding to the transition of the failure mode from tensile tearing to shear plugging. By contrast, effects of the target thickness on crack propagation are investigated here at an impact velocity well above the ballistic limits. Three cases with different aspect ratios $h/d = 0.25, 0.50$, and 1.0 were considered, respectively. The ratio of $h/d = 0.25$ corresponds to the case of a thin beam, while $h/d = 1.0$ to the case of a intermediately thick beam. In finite element modeling, the breadth of the projectile $d = 20$ mm, the mass ratio $\mu = 0.1$, and the impact velocity $V_0 = 240$ m/s were kept constant as well as the element size near and in the impacted zone.

As shown in Fig. 4-9, the relation between the crack length and the indentation depth can be fitted well by Eq. (4.1) with the same set of constants $K = 10$ and $\lambda = 4$. It indicates that as long as the target fails by shear plugging, the aspect ratio does not have much influence on crack propagation. Note, that this dimensionless group h/d does not enter into Eq. (4.1).

4.5.5 Plane-strain beam

In the preceding subsections, the target beam was discretized using plane-stress elements. As a counterpart to the plane-stress beam, a plane-strain beam is considered here, which represents a wide beam with large constraint in the lateral direction. The plane-stress and plane-strain models can be thought of as two limiting cases of a real beam with a finite breadth.

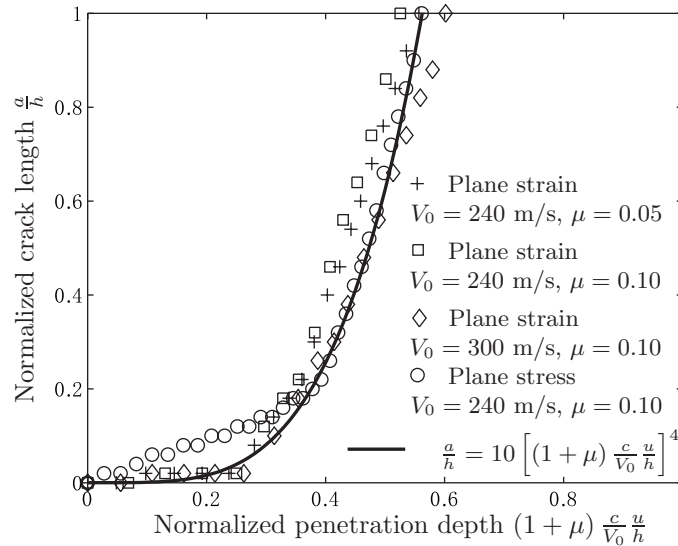


Fig. 4-10: Crack propagation in the plane-strain beam of $h = 10$ mm at $V_0 = 240$ m/s.

Since localized shear deformation is dominant, through-thickness crack propagation is not much influenced by the lateral constraint, as shown in Fig. 4-10. However, there is large difference in the velocity history of the projectile between the plane-stress and plane-strain cases, specially in the indentation phase, see Fig. 4-11. For the plane-stress case, the beam can expand in the lateral direction without any constraints when indented. But it is not the

case for the plane-strain beam. The projectile is much resisted by the plane-strain beam in the indentation phase, and thus its velocity decreases more rapidly. However, the residual velocities of the projectile are almost the same in both cases. This indicates that a large part of the kinetic energy is dissipated in the form of shear cracking rather than indentation.

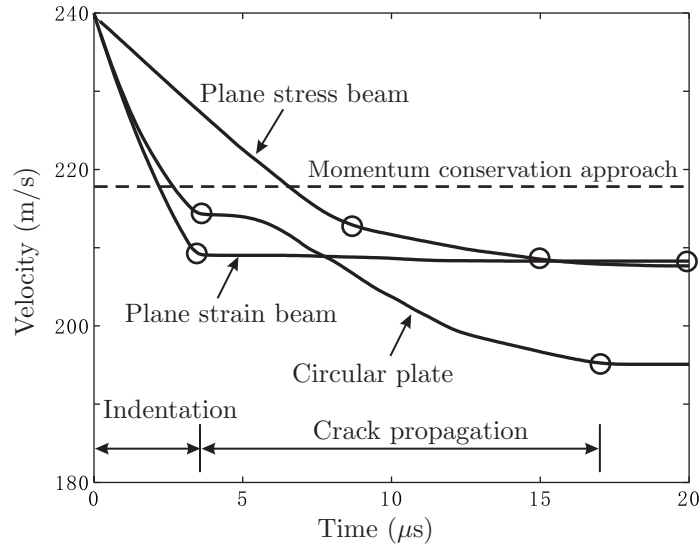


Fig. 4-11: Velocity history of the projectile for the circular plate, and plane-stress and plane-strain beams of $h = 10$ mm at $V_0 = 240$ m/s and $\mu = 0.1$.

4.5.6 Circular plate

Under high velocity impact, a circular plate would also fail by shear plugging, similar to the beam case. Figure 4-12 shows the shear failure pattern of a circular plate of $h = 10$ mm struck by a rigid, flat-nosed cylindrical projectile of $d = 2h = 20$ mm moving at $V_0 = 240$ m/s. This plastic deformation and failure pattern was captured using a two-dimensional axisymmetric finite element model. Since very localized shear deformation is dominant in shear plugging and such a deformation mode does not introduce additional axial or circumferential strains, crack propagation in the circular plate is similar to that in the beam in the second phase. The crack growth is almost the same as that in the beam except in the initial phase, see Fig. 4-13.

The velocity history of the projectile is shown in Fig. 4-11. It can be seen that the

residual velocity of the projectile in the circular plate case is lower than for the beam cases, because shear resistance is much larger in a circular plate than in a beam. A theoretical validation of this numerical finding will be presented in Chapter 7.5.

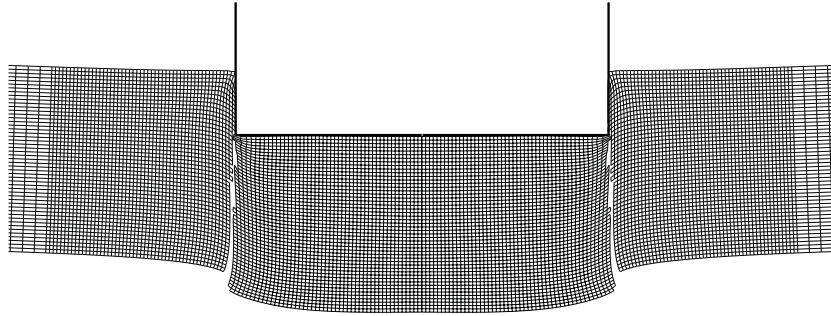


Fig. 4-12: Failure pattern of the circular plate of $h = 10$ mm struck by the cylindrical projectile with $V_0 = 240$ m/s and $\mu = 0.1$.

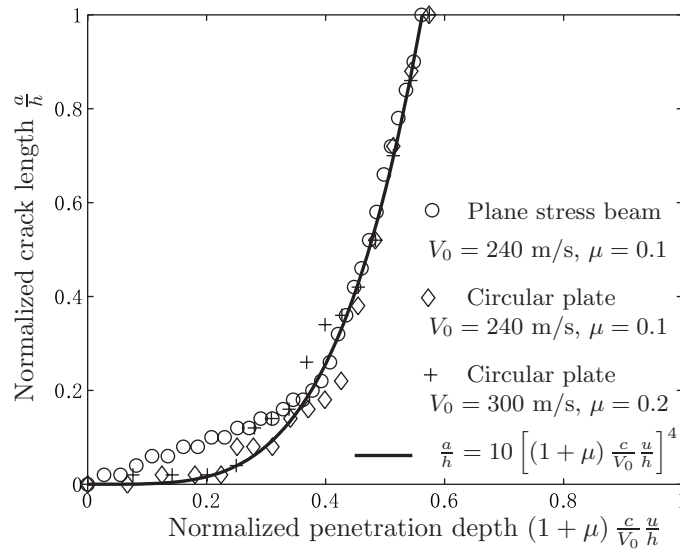


Fig. 4-13: Crack propagation in the circular plate of $h = 10$ mm at various impact velocities and mass ratios.

4.6 Crack propagation speed

The crack propagation speed is an important property of crack growth since crack propagation is closely related to energy dissipation through material separation. This topic has received much attention for elastic brittle materials, but not for elastic-plastic ductile metals [101].

The crack propagation speed is not a basic output variable in most of finite element codes, but it can be estimated from the crack growth curve by differentiating crack extension with respect to time. Figure 4-14 shows plots of crack extension vs. time for the plane-stress beam at various impact velocities. It appears that crack propagation in shear plugging consists of two phases. In the first phase, uniform indentation is dominant and cracks slowly grow, while in the second phase, localized shear deformation is dominant and crack propagation is much faster. This feature will be employed to develop a theoretical shear plugging model presented in Chapter 7.5. The time history of the crack length for the present cases is fitted well by a piecewise linear function. This indicates that constant average values can be used to approximate crack propagation speeds in the respective phases. The average crack propagation speed of the second phase is given by $v = 1056, 1007,$ and 707 m/s, respectively, for the impact velocity $V_0 = 300, 240,$ and 200 m/s. Clearly, the average crack propagation speed also depends on other parameters such as the target thickness, the projectile weight, etc. For instance, Figure 4-15 shows the relation between the average crack propagation speed of the second phase and the mass ratio.

The instantaneous crack propagation speed can be calculated using least square linear fitting for successive three points in plots of crack extension vs. time. This method was first suggested by Needleman [15]. It is seen from Fig. 4-16 that in general, the crack propagation speed increases with time, though there are some oscillations during the impact process. The crack propagation speed is sensitive to the initial impact velocity. Thus, in contrast to the elastic and plastic waves speeds, it is not a property of a material.

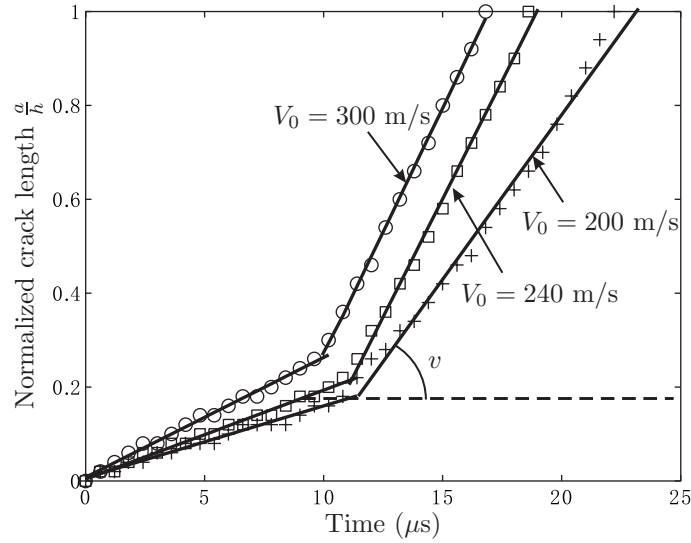


Fig. 4-14: Time history of crack extension at various impact velocities for the plane-stress beam of $h = 10 \text{ mm}$ and $\mu = 0.1$.

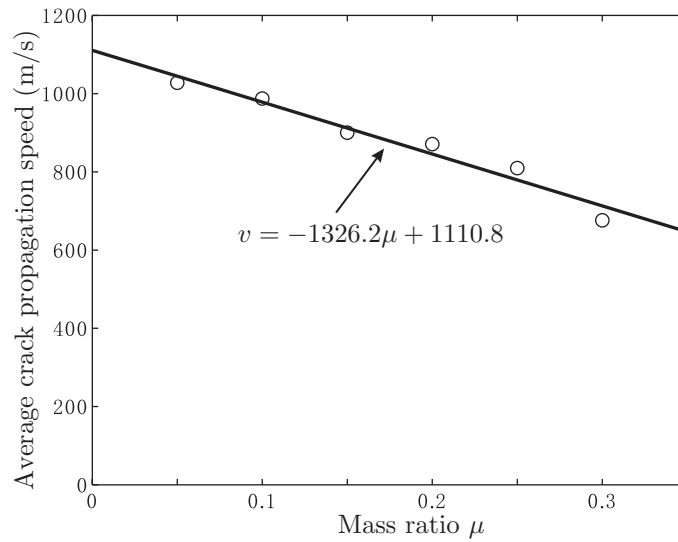


Fig. 4-15: Average crack tip speeds vs. mass ratios for the plane-stress beam of $h = 10 \text{ mm}$ at $V_0 = 240 \text{ m/s}$.

As can be seen from Figs. 4-15 and 4-16, the maximum crack tip speed is near 1500 m/s, and the average crack tip speed is of the order of 1000 m/s for 2024-T351 aluminum alloy. The average speed is 31% of the Rayleigh wave speed, and is twice as high as the transverse plastic wave speed c . The Rayleigh wave speed is given, for 2024-T351 aluminum alloy, by

$$c_R \approx 0.93 \sqrt{\frac{E}{2\rho(1+\nu)}} = 3000 \text{ m/s}. \quad (4.6)$$

The Rayleigh wave speed is usually thought of as the limiting speed of elastic shear crack propagation. This was determined from the energy view of point in the context of linear elastic continuum mechanics [102]. Due to plastic constraints at the propagating crack tip, it is believed that the limiting speed in a plastically deformed region would be much lower than the Rayleigh wave speed.

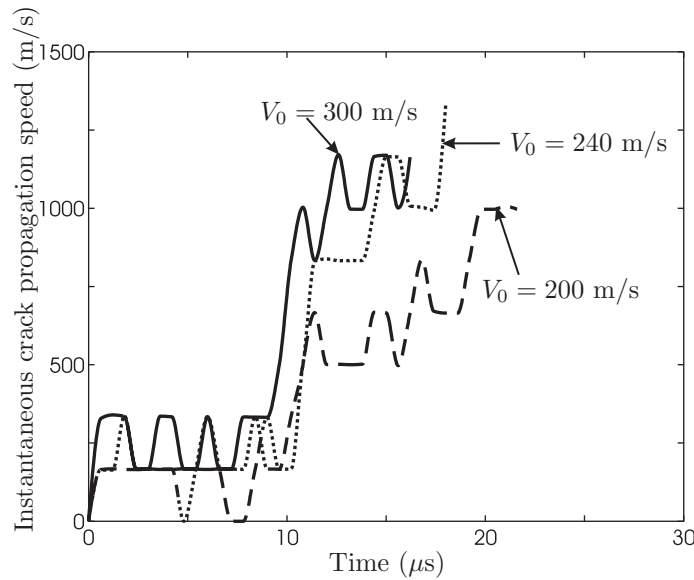


Fig. 4-16: Instantaneous crack tip speeds vs. time for the plane-stress beam of $h = 10 \text{ mm}$ and $\mu = 0.1$.

4.7 Discussions

As shown in the preceding sections, Eq. (4.1) relating the crack extension to the indentation depth is quite general and applicable to the beam case as well as the circular plate case,

provided that the targets fail by shear plugging. For 2024-T351 aluminum alloy, Eq. (4.1) with $K = 10$ and $\lambda = 4$ is suitable in a wide range of aspect ratios ($h/d \leq 1.0$), mass ratios ($\mu < 0.4$), and impact velocities (180 – 300 m/s). A limited study on Weldox 460 E steel has also been performed and it is found that $K = 0.5$ and $\lambda = 4$ fits well with numerical results. Note, that Weldox 460 E steel is more ductile than 2024-T351 aluminum alloy. The detailed results will be presented in Chapter 7.5.

It is believed that other expressions such as a polynomial function with several terms would give better curve-fitting for the relation of the crack length and the indentation depth. To be capable of deriving a closed-form solution for the shear-plugging problem, the power function as shown in Eq. (4.1) is used here. As an alternative, the crack propagation can also be well approximated by a piecewise linear function, see Fig. 4-17. Specifically for the plane strain beam case and the circular plate case, the piecewise linear function is given by

$$\frac{a}{h} = \begin{cases} 0 & 0 \leq u \leq u_i \\ 4.5 \left[(1 + \mu) \frac{c}{V_0} \frac{u}{h} \right] - 1.4 & u_i \leq u \leq u_{cr} \end{cases}, \quad (4.7)$$

where u_i is the indentation depth at which the cracks initiate, which is given by, for 2024-T351 aluminum alloy,

$$\frac{u_i}{h} = \frac{0.31 V_0}{1 + \mu c}. \quad (4.8)$$

The physical meaning of the piecewise linear fitting is that the whole perforation process can be ideally separated into two phases. In the first phase, only indentation is involved without crack growth. When the indentation depth reaches a certain level, the cracks initiate and propagate forwards at a constant velocity in the second phase.

Mesh size effects on the crack growth will be presented in Chapter 5.3. It is found that the crack propagation is not much sensitive to the mesh size since the problem is well-posed. This gives us much confidence on the applicability of Eq. (4.1).

No relevant experiments are available in the open literature to directly verify Eq. (4.1). The validity and applicability of the expression will be demonstrated by comparing the theoretical predictions based on the present expression with experimental results given in the open literature. Such a study is the subject of Chapter 7.5.

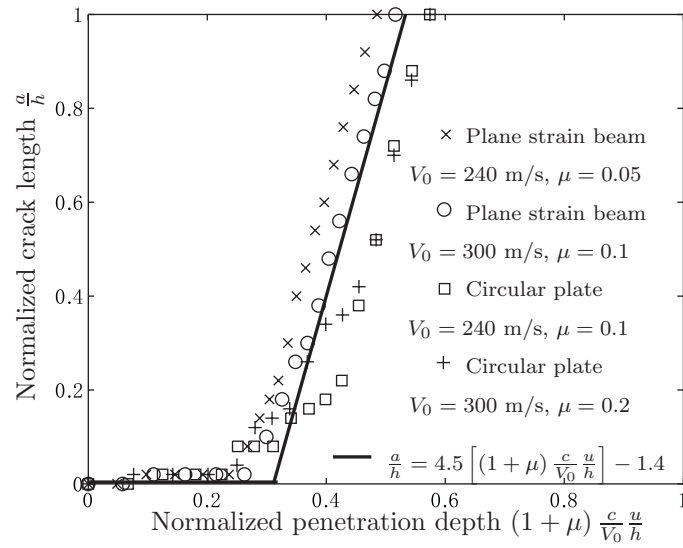


Fig. 4-17: Crack propagation fitted by piecewise linear functions.

Chapter 5

Numerical Aspects of Ductile Fracture Prediction

5.1 Material constitutive model

A high velocity impact event is characterized by large plastic strain, high strain rates, and temperature rise due to adiabatic heating. Interaction of these variables makes it difficult to develop a reasonable material constitutive model and to calibrate material coefficients. Nevertheless, a number of material models applicable to high velocity impact problems have been proposed [103]. Among them, the Johnson-Cook's (JC's) constitutive equation was widely used in the literature [104], because of its simple formulation and easy implementation in finite element codes. The yield function of the JC's model was defined by

$$\bar{\sigma} = [A + B\bar{\varepsilon}_{\text{pl}}^n] \left[1 + C \ln \left(\frac{\dot{\bar{\varepsilon}}_{\text{pl}}}{\dot{\bar{\varepsilon}}_0} \right) \right] \left[1 - \left(\frac{T - T_0}{T_m - T_0} \right)^q \right], \quad (5.1)$$

where A , B , n , C , and q are five material constants, which need to be calibrated from experiments. This model accounts for isotropic strain hardening, strain rate hardening, and temperature softening in the uncoupled form. The first term of the right hand side in Eq. (5.1) represents the quasi-static stress-strain relation at room temperature. The second term signifies effects of strain-rate hardening. The temperature dependence of the stress is taken into account through the third term. It should be pointed out that in the

computation, the material behaves elastically up to the point of initial yield and then follows Eq. (5.1).

All the impact processes are assumed be adiabatic in the present thesis, i.e. effects of heat conduction are not taken into account. That is true if heat generated by plastic work in a localized region does not have sufficient time to escape to surrounding materials. The temperature increase ΔT owing to plastic work can be written as

$$\Delta T = \int \frac{\chi}{\rho c_v} \sigma^{ij} d\varepsilon_{\text{pl}}^{ij}, \quad i, j = 1, 2, 3. \quad (5.2)$$

where σ^{ij} and $\varepsilon_{\text{pl}}^{ij}$ are the stress and plastic strain components.

Material properties have a strong influence on the plastic deformation and the failure process of a target under high intensity impact loading. Considered in the present thesis are three metals: Weldox 460 E steel, 2024-T351 aluminum alloy, and 91W-61Ni-3Co tungsten alloy in the order of decreasing ductility.

Weldox 460 E steel is characterized by high strength and high ductility at the same time. Both factors are equally important for an efficient energy absorption. Børvik and his coworkers [40, 105, 106] have extensively studied the mechanical properties of this material. The corresponding coefficients of the JC's material model were calibrated by minimizing the differences between the experimental results of tensile tests and the numerical prediction at a number of discrete points under various combinations of plastic strain, strain rates and temperature [40]. It should be pointed out that Børvik et al. [107] obtained two sets of the material constants of the JC's model for Weldox 460 E steel: one set corresponds to the case where damage softening was taken into account in the material constitutive model, the other applies to the case where the material model is uncoupled with the fracture model. In the present thesis, the latter set is used. The material coefficients of Weldox 460 E steel are listed in Table 5.1. Figure 5-1 shows the stress-strain relation under various combinations of strain rates and temperatures.

Table 5.1: Material constants for Weldox 460 E steel

E (GPa)	ν	ρ (kg/m ³)	$\dot{\epsilon}_0$ (s ⁻¹)	C
200	0.33	7850	5.00×10^{-4}	0.0123
c_v (J/kgK)	χ	T_m (K)	T_0 (K)	q
452	0.9	1800	293	0.94
A (MPa)	B (MPa)	n	σ_0 (MPa)	c (m/s)
490	383	0.45	808.6	321.0
D_1	D_2	D_3	D_4	D_5
0.0705	1.732	-0.54	0.015	0.0

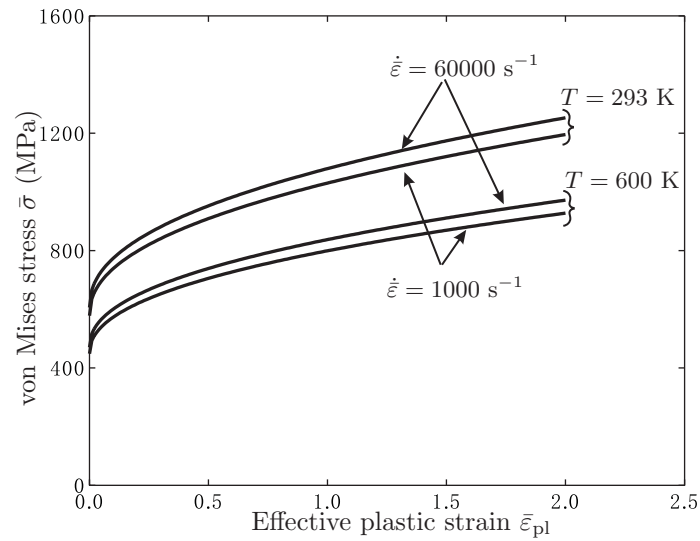


Fig. 5-1: von Mises stress vs. effective plastic strain under various strain rates and temperature for Weldox 460 E steel.

2024-T351 aluminum alloy is broadly used in aircraft industry, and was extensively investigated in the literature. Here, the quasi-static true stress-strain curve obtained by Bao and Wierzbicki [35] from uniaxial tensile tests on a round bar was implemented in the calculation. The determination of the stress-strain curve up to fracture is not a trivial problem even under quasi-static uniaxial loading. The stress and strain distribution becomes nonuniform in the necking area, and plastic flow is closely related to fracture. The trial-and-error method was used by Bao and Wierzbicki to force the numerical prediction of the load-displacement curve to be close as possible to the experimental results. Two other material constants in the JC model relating to effects of the strain rate and temperature were taken from the literature. The strain rate constant $C = 0.015$ was given by Johnson et al. [108], Lindholm and Johnson [109] for 2024-T351 aluminum alloy based on six torsion tests with the strain rate ranging from 0.088 s^{-1} to 123 s^{-1} . Note, that the strain rates up to $10^4 - 10^5 \text{ s}^{-1}$ are often encountered in high velocity impact. Lesure [110] obtained $C = 0.0083$ from split Hopkinson pressure bar (SHPB) tests with the strain rate up to 10^4 s^{-1} for 2024-T3 aluminum alloy (The difference between 2024-T3 and 2024-T351 aluminum alloy is that the T3 temper applies to flat sheets with less than 6.3 mm thickness, whereas the T351 temper with larger than 6.3 mm thickness [110]). Considering the range of the strain rates encountered in an actual case, $C = 0.0083$ obtained by Lesuer was used in the present material model. All the material constants used in the present constitutive equation are summarized in Table 5.2. As shown in Fig. 5-2, the 2024-T351 aluminum alloy stress-strain relation is much sensitive to temperature, but not to the strain rate.

The third metal used in the present thesis is 91W-61Ni-3Co tungsten alloy. Because of their high density and strength, tungsten alloys are often used in kinetic energy penetrators. Penetrators are subjected to predominant compression during the impact process and thus adiabatic shear banding is a common failure mode. The transition mechanism from adiabatic shear banding to subsequent fracture for a tungsten alloy specimen has been presented in Chapter 3.4. Table 5.3 lists all the relevant coefficients of 91W-61Ni-3Co tungsten alloy in the JC's material model [82].

Table 5.2: Material constants for 2024-T351 aluminum alloy

E (GPa)	ν	ρ (kg/m ³)	$\dot{\epsilon}_0$ (s ⁻¹)	C
74.66	0.3	2700	3.33×10^{-4}	0.0083
c_v (J/kgK)	χ	T_m (K)	T_0 (K)	q
875	0.9	775	293	1.0
A (MPa)	B (MPa)	n	σ_0 (MPa)	c (m/s)
352	440	0.42	565.5	457.6
D_1	D_2	D_3	D_4	D_5
0.13	0.13	-1.5	0.011	0.0

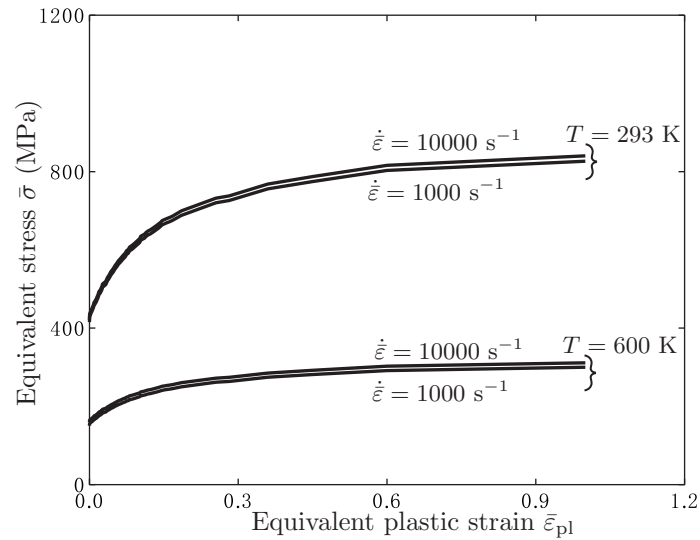


Fig. 5-2: Equivalent stress versus plastic strain under various strain rates and temperature for 2024-T351 aluminum alloy.

Table 5.3: Material constants for 91W-61Ni-3Co tungsten alloy

E (GPa)	ν	ρ (kg/m ³)	$\dot{\epsilon}_0$	C
370	0.3	17650	1	0.03
c_v (J/kgK)	χ	T_m (K)	T_0 (K)	q
150	0.9	1485	300	0.835
A (MPa)	B (MPa)	n	σ_y (MPa)	
1948	1875	0.95	1500	

5.2 Fracture model

To predict crack formation and growth, a fracture criterion has to be implemented in finite element codes. A scalar indicator is introduced in ABAQUS/Explicit to track down damage accumulation of each finite element. This damage indicator is defined as an integral with respect to the effective plastic strain:

$$D = \int_0^{\bar{\epsilon}_{pl}} \frac{d\bar{\epsilon}_{pl}}{\bar{\epsilon}_f \left(\frac{\sigma_h}{\sigma}, \dot{\epsilon}_{pl}, T \right)}. \quad (5.3)$$

where $\bar{\epsilon}_f$ is the fracture strain obtained from experiments as a function of the stress triaxiality, strain rates, and temperature. Compared Eq. (5.3) with the general definition of damage accumulation, Eq. (2.1), we have

$$f(\text{stress states, strain rates, temperature, ...}) = \frac{D_c}{\bar{\epsilon}_f \left(\frac{\sigma_h}{\sigma}, \dot{\epsilon}_{pl}, T \right)} \quad (5.4)$$

Eq. (5.3) indicates that each increment in the effective plastic strain in one calculation step will contribute to the damage accumulation in a nonproportional way, depending on the current values of the stress triaxiality, strain rate, and temperature. When the cumulative damage D exceeds unity at an integration point of an element, all the deviatoric stress components are suddenly set to zero. The whole element is considered to fail if the accumulated damage at all the integration points exceeds the critical value.

ABAQUS/Explicit provides two options to treat failed elements. Either the failed ele-

ments completely lose their load carrying capability, or the failed elements are still capable of resisting pressure but neither tension nor shear. If the former option is used, the failed elements will no longer participate in the calculation. The time step required for the computational stability will not be determined from these severely distorted elements. Hence, the calculation using the former option is much faster than the latter one. Unless specifically stated, the former option is activated in all the calculations in the present thesis. However, under complex loading conditions, a previously formed crack may close due to subsequent compressive loading, e.g. in the Taylor test. In such a case, the latter option is more reasonable.

In the present formulation, the damage model is assumed to be uncoupled from the material constitutive model. The onset of fracture is checked outside the calculation loop of stresses and strains. This formulation is much simpler than the Gurson's micromechanically based material model [24] and the phenomenologically based damage material model such as that proposed by Børvik et al. [40], in both of which the failed element gradually loses its load carrying capability. At the same time, the calibration of material coefficients in the present uncoupled formulation is much easier.

As reviewed in Chapter 2.4, both elevated temperature and strain rates do not have much influence on the fracture strain for 2024-T351 aluminum alloy and Weldox 460 E steel. Therefore, for simplicity, the fracture strain is assumed to be a function only of the stress triaxiality in the present thesis. The detailed fracture strain functions for 2024-T351 aluminum alloy and Weldox 460 E steel will be given in Chapter 6.

5.3 Mesh size effects in high velocity impact

5.3.1 Introduction

Mesh size sensitivity has been perplexing researchers for a long time. The accuracy and reliability of finite element solutions is often doubted for their possible mesh size dependence. Since a large part of the present thesis is devoted to the numerical investigations of the failure response, it is necessary to address this problem.

Mesh size effects have been extensively studied in the literature, e.g. Needleman and Tvergaard [111, 112], Zukas and Scheffler [113]. However, results obtained usually lack generality, i.e. they cannot be transferred from one type of problem or loading configuration to others. The present research focuses on adiabatic shear banding and high velocity perforation, in both of which large plastic deformation localizes in narrow zones and thus numerical modeling may be sensitive to the mesh size.

5.3.2 Why sensitivity to mesh size

In general, there are two factors leading to mesh size sensitivity: (i): high stress and strain gradients, and (ii): strain softening. A high stress and strain gradient is generated in the vicinity of the tip of a stationary or propagating crack, and in the zone of localized deformation such as deep necking and shear banding. If elements are not sufficiently small, large spatial gradients cannot be resolved and thus numerical results will exhibit mesh size sensitivity. This type of mesh size sensitivity can be diminished by refining meshes in critical regions.

Another factor giving rise to mesh size dependency is the strain softening. The strain softening characterized by a negative slope in the stress-strain curve (Fig. 5-3) is a common phenomenon for concrete and geomaterials, in which a number of microcracks are generated under loading leading to the decrease in the load carrying capability. To treat this type of material with densely distributed cracks as a continuum, the strain softening has to be taken into account in material constitutive modeling [114]. It should be pointed out that the strain softening is a macroscopic phenomenon and microscopically the heterogeneous microstructures always harden in a certain way.

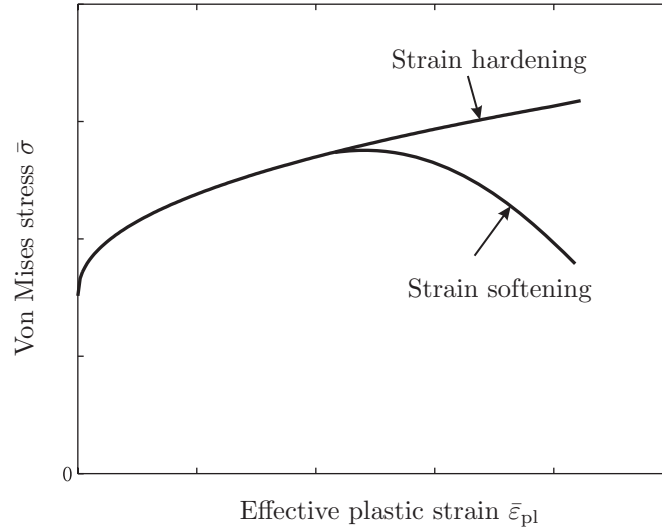


Fig. 5-3: Schematic representation of strain softening and strain hardening.

Similarly to brittle materials, ductile metals may also experience strain softening under high intensity loading owing to void nucleation, growth and coalescence in a critical region. Besides the damage softening, thermal effects also contribute to the strain softening in high velocity impact. Under high strain rates, temperature may arise by several hundred degrees or even up to a material melting point due to the conversion of plastic work into heat. When damage and thermal softening exceeds strain and strain rate hardening, a stress will decrease with an increasing strain. It should be mentioned that the strain softening usually occurs in a small zone and the whole specimen may still behave in a stable, hardening way.

As soon as the strain softening occurs, plastic deformation tends to localize in a region as narrow as possible with minimum energy dissipation. The mathematical background of the mesh size sensitivity resulting from the strain softening has been elucidated by, e.g. Read and Hegemier [115], Lasry and Belytschko [116] through an example of a longitudinal plastic stress wave traveling along a strain-softening bar. For a rate-independent material the longitudinal stress wave equation in an one-dimensional case is given by

$$\frac{\partial \sigma}{\partial \epsilon} \frac{\partial^2 u_L}{\partial x^2} = \rho \frac{\partial^2 u_L}{\partial t^2}, \quad (5.5)$$

where u_L is the longitudinal displacement. For a strain-hardening solid this governing differential equation is always hyperbolic and the stress wave speed is given by

$$c_L = \sqrt{\frac{1}{\rho} \frac{\partial \sigma}{\partial \varepsilon}}. \quad (5.6)$$

However, in the case of a strain-softening bar the governing equation becomes elliptic and the above expression loses its physical meaning since $\partial \sigma / \partial \varepsilon < 0$, i.e. the boundary and initial value problem becomes ill-posed. When finite element or finite difference procedures are applied to solve this type of equation, the strain softening inevitably gives rise to numerical instability. This problem can be easily remedied by introducing rate-dependence in material constitutive modeling. As Read and Hegemier [115] showed for two simple viscoplasticity models, the boundary and initial value problem will regain well-posedness. Needleman [111] pointed out that the rate-dependence implicitly introduces a length scale in governing equations that is a fraction of the elastic stress wave length. If this characteristic length scale is dominant over the edge length of elements, numerical solutions may be less sensitive to mesh size.

5.3.3 Adiabatic shear banding

The mesh sensitivity caused by the strain softening has been long recognized and clearly demonstrated by, e.g. Břazant [114] for brittle materials, in which the strain softening results from the formation of numerous microcracks. By contrast, mesh size effects on the numerical simulation of adiabatic shear banding are little investigated, although it is often doubted by researchers, e.g. Li et al. [78, 79] and Batra and Nechitailo [88]. As mentioned before, the problem with the strain softening would remain well-posed if a material viscoplasticity model is implemented in calculation. The objective of this numerical study is to see whether the internal length scale associated with the viscoplasticity model would be able to remove the mesh size sensitivity.

The example problem considered here is the same as addressed in Chapter 3.4, in which the minimum edge length of the finite elements was about 10 μm , one quarter of the width

of the adiabatic shear bands. In this section, a finer mesh model was built with the edge length equal to $5\ \mu\text{m}$. As shown in Fig. 5-4, the predicted adiabatic shear bands initiating, respectively, at the exterior and interior corners link together. By contrast, the adiabatic shear bands simulated using the $10\ \mu\text{m}$ mesh model were arrested in the central region of the gauge section, which is more consistent with the experimental observations. At the same time, the predicted cracks are much longer than the experimental results. Figure 5-5 shows the temperature rise along the gauge section at $t = 32\ \mu\text{s}$. It appears that the finer the mesh model, the higher temperature rise is. The difference in the temperature rise between both models becomes larger at the end of the impact process. A conclusion can be drawn that the present numerical modeling of the adiabatic shear banding is sensitive to mesh size even though the material viscoplasticity model has been implemented.

The mesh size sensitivity of the numerical results indicates that the present problem is still dominated by the element size rather than the viscous length scale. Li et al. [79] and Perzyna [117] pointed out that the length scale implicitly introduced in the viscoplasticity model should be of the order of $1\ \mu\text{m}$. Thus, the current edge length $5\ \mu\text{m}$ of the finer mesh model is still too large to give a convergent solution. However, if the edge length of an element is smaller than $1\ \mu\text{m}$, numerical simulations would become unaffordable.



(a) Edge length 10 μm



(b) Edge length 5 μm

Fig. 5-4: Comparison of the generated cracks and adiabatic shear bands at $t = 48 \mu\text{s}$ and $V_0 = 27.6 \text{ m/s}$ between two mesh models.

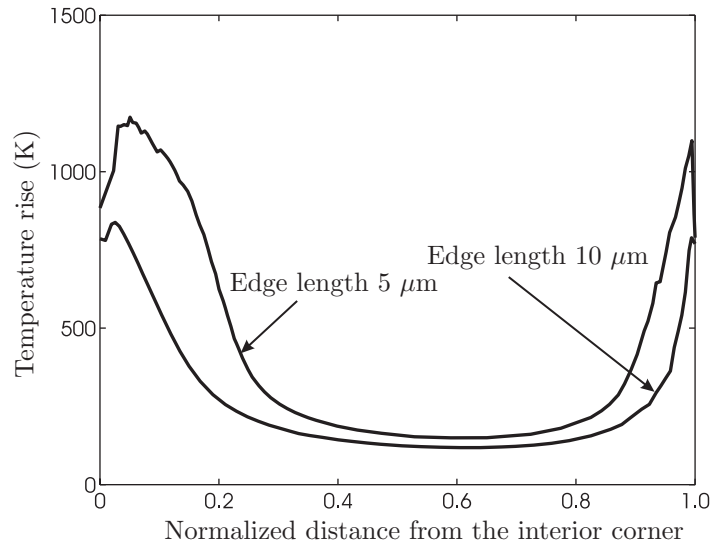


Fig. 5-5: Comparison of temperature rise along the gauge section at $t = 32 \mu s$.

5.3.4 Crack formation and propagation

In the process of adiabatic shear banding, a velocity field becomes discontinuous across a shear band. In a fracture process, new free boundaries are generated as a crack propagates inside a continuum. The deformation and stress fields become discontinuous across a crack. The advancement of a crack is achieved by setting the deviatoric stresses of failed elements to zero and thus they can deform arbitrarily. This technique of modeling the formation and growth of cracks has been implemented in commercial finite element codes, which is termed “Element Deletion” in ABAQUS/Explicit [57]. This technique is inevitably associated with the element size. Fracture, which physically means a separation of materials, tends to localize in a narrow zone consisting of an array of elements irrespective of their size in finite element modeling. Hence, it is necessary to investigate the extent of mesh size effects on the prediction of crack formation and propagation.

As an example problem considered is a Weldox 460 E steel circular plate perforated by a hard cylindrical projectile, see Fig. 5-6. Børvik et al. [100] provided the ample experimental results, which allow us to verify the accuracy of the present numerical procedure. Four axisymmetric finite element models with different element size were built. Three such models are shown in Fig. 5-7. The minimum edge length of square elements in these models

were 0.4 mm, 0.2 mm, 0.1 mm, and 0.05 mm, respectively, for the coarse, medium, fine, and very fine mesh models.

Plots of the initial impact velocity vs. the residual velocity are shown in Fig. 5-8. It appears that at an impact velocity well above the ballistic limit, in which the plate fails mainly by shear plugging, the predicted residual velocity is not much sensitive to the element size. However, the prediction of the ballistic limit itself clearly depends on mesh size. Tensile tearing is a favorable failure mode at an impact velocity near the ballistic limit. This conclusion is consistent with Børvik et al.'s numerical finding presented in Ref. [55].

Figure 5-9 shows the predicted residual velocity as a function of the element number through the plate thickness. It seems that the residual velocity converges to an asymptote as the element size decreases. The convergence of the residual velocity indicates other global solution variables such as energy dissipation and target deflection can also be correctly predicted if the mesh size is sufficiently small.

In contrast to energy and velocities, strains and crack growth can be regarded as local parameters. It can be seen from Fig. 5-10 that the growth of the crack is only slightly dependent on the mesh size in the later stage and the initiation of crack growth clearly depends on the mesh size, which is similar to what Needleman [15] obtained using the cohesive interface formulation for a plane-strain block with a central pre-crack under dynamic loading.

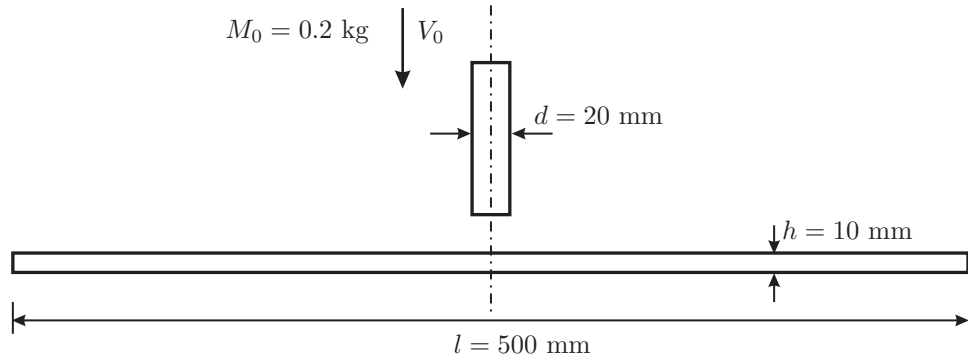
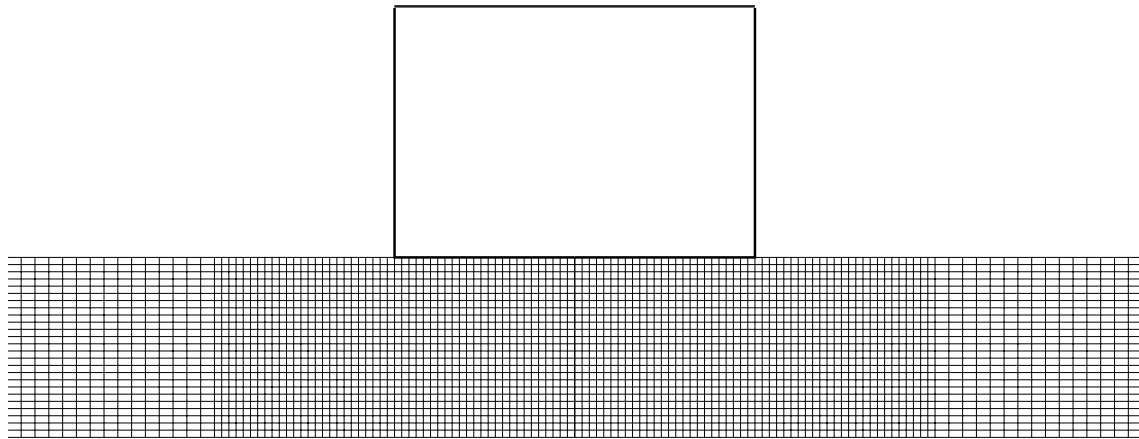
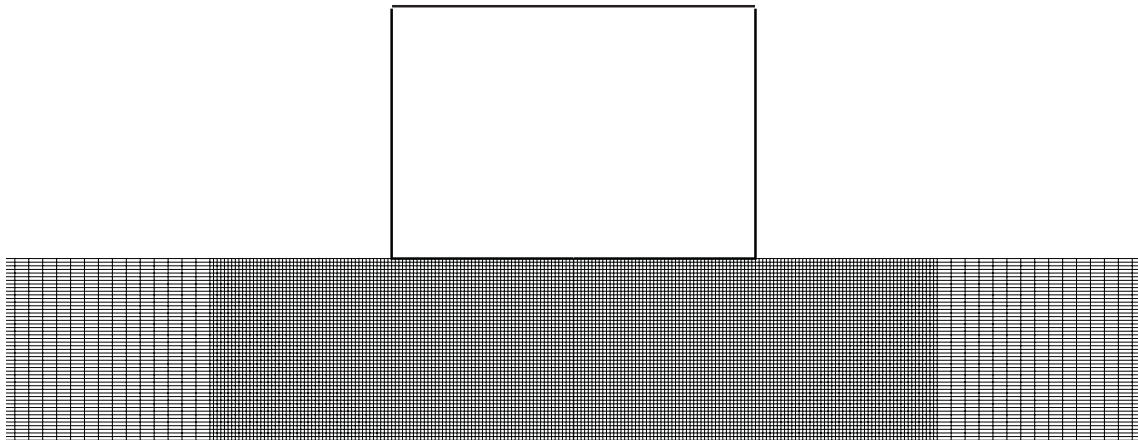


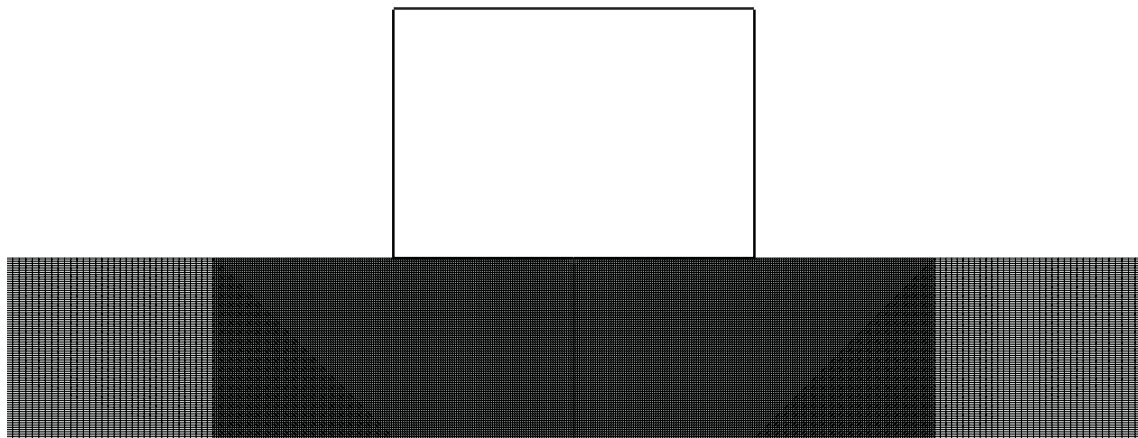
Fig. 5-6: Schematic representation of a circular Weldox 460 E steel plate impacted by a flat-nosed cylindrical, hard projectile in the Børvik et al.'s experiments [100].



(a) Coarse mesh model: 25 elements through the thickness



(b) Medium mesh model: 50 elements through the thickness



(c) Fine mesh model: 100 elements through the thickness

Fig. 5-7: Three axisymmetric mesh models for the Weldox 460 E steel circular plate impacted by the rigid cylindrical projectile.

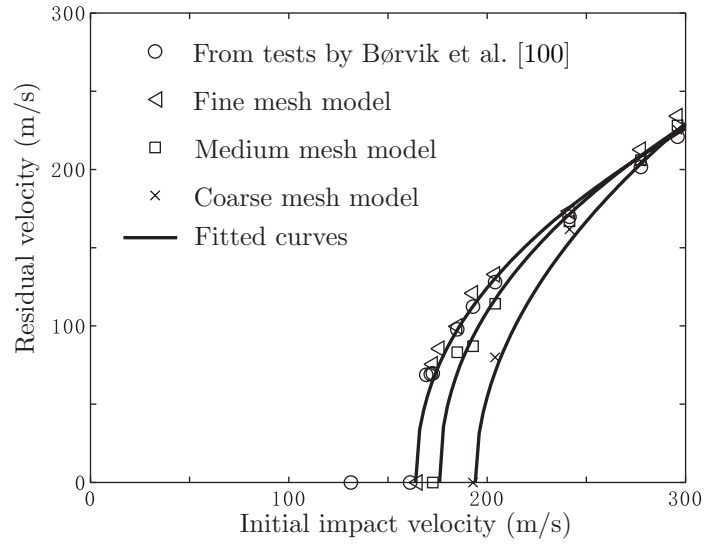


Fig. 5-8: Comparison of residual velocities among experimental results and numerical solutions based on three mesh models.

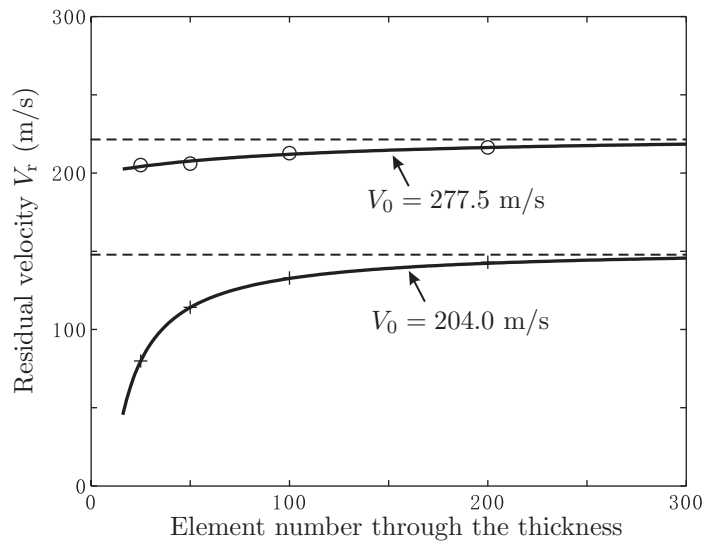


Fig. 5-9: Calculated residual velocity vs. element number through the thickness of the steel plate.

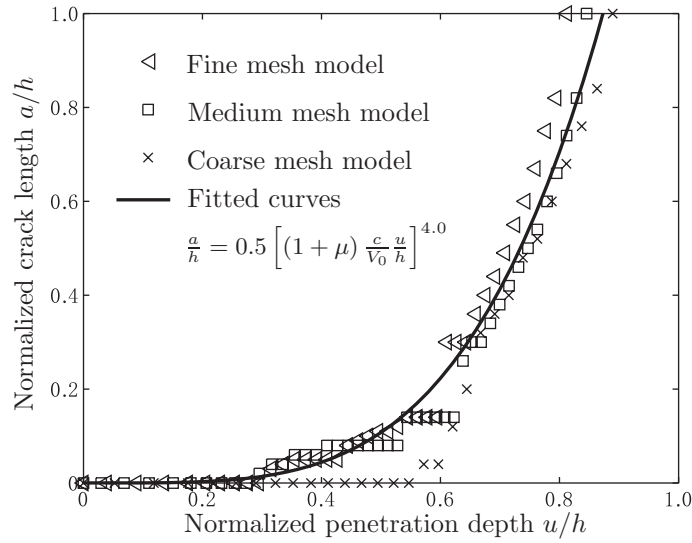


Fig. 5-10: Comparison of crack growth in the steel circular plate at $V_0 = 277.5$ m/s among three mesh models.

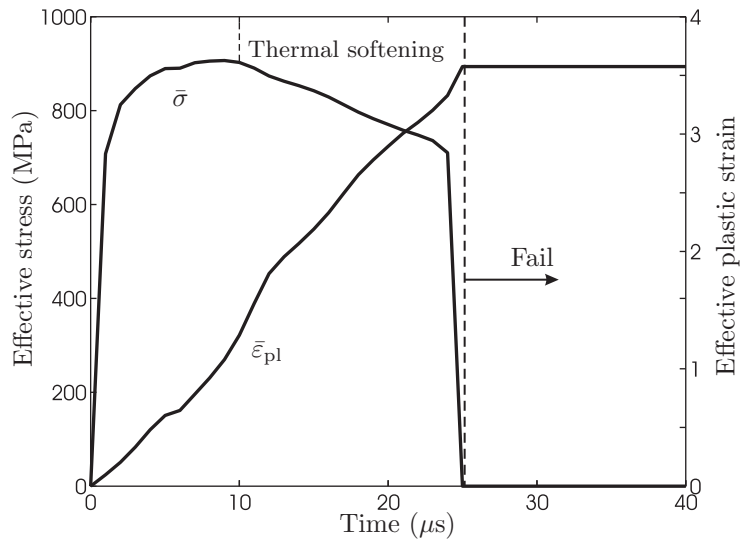


Fig. 5-11: Time history of the von Mises stress and the effective plastic strain of a typical element at the crack at $V_0 = 277.5$ m/s based on the medium mesh model.

In the present calculation, the damage model is uncoupled with the material model, i.e. the damage softening due to void growth is not taken into account in the material constitutive model. A finite element suddenly fails as soon as its damage reaches a critical value. It can be seen from Fig. 5-11 that the von Mises stress of a typical element first increases, reaches a maximum value, then decreases due to the thermal softening, and finally drops to zero. This sudden failure can be thought of as one kind of the damage softening, which may be responsible for mesh size sensitivity in the present numerical solutions.

5.3.5 How to remedy mesh size sensitivity

Many approaches have been proposed in the literature to overcome the mesh sensitivity of finite element solutions. In conventional finite element analysis, elements are just a mathematical representation of a continuum body and the size is usually determined by the requirement of spatial resolution of stress and strain fields, i.e. the element size does not have any physical implication. One of the simplest way to remedy mesh size sensitivity is to equip the element size with a physical meaning. This idea can be directly implemented without any modification of commonly used material constitutive models and fracture models. Redanz et al. [118] suggested that the mesh size could be approximately equal to the particle size. Alternatively, the mesh size can be associated with the size of a fracture process zone ahead of a propagating crack, where micro-cracks or micro-voids nucleate, grow, and eventually coalesce with the major crack.

The second type of approach is to introduce a critical volume, which consists of several elements around the critical node. The damage indicator D_{av} is averaged over this critical volume V_c while stresses and strains are still calculated at a single element level, i.e.

$$D_{av} = \frac{1}{V_c} \int D(x) dV \quad (5.7)$$

This formulation was proposed by Holmes et al. [119], and Giovanola and Kirkpatrick [120] and has been implemented in LS-DYNA3D. The critical volume is associated with the grain size or spacing of inclusions. Recently, Lee et al. [121] showed that in the necking and fracture process of a tensile flat specimen the volume averaging procedure makes the

critical damage parameter D_c independent of the mesh size. At the same time this procedure introduces a new parameter which is the critical volume V_c to fracture.

The third type of approach is the development of nonlocal constitutive models, in which a characteristic or internal length scale is implemented. In such a way, the prediction of fracture is not only controlled by stresses and strains but also related to material microstructures. Several formulations originated from this idea have been proposed, e.g. Tvergaard and Needleman [122]. The characteristic length was considered to represent the average grain size or the average void spacing. Kamel et al. [123] found that at least three elements are needed along the characteristic length to obtain a convergent solution.

However, these approaches are not applicable to the failure analysis of large structures such as ship grounding or car collision. Due to limitation of computational resources, shell elements have to be used instead of solid elements and shell elements have to be much larger than the microstructural characteristic length such as the fracture process zone. Different methods need to be explored to solve the problem of mesh size sensitivity. A preliminary study that the calibration and application of a fracture criterion is based on the same shell element size was performed by Simonsen and Törnqvist [124], and Lee et al. [121]. However, whether the obtained empirical fracture criterion associated with the specific element size is applicable to another type of specimen or loading configuration remains an open question.

Chapter 6

Effect of Ductile Fracture Criteria on Impact Failure

6.1 Introduction

A number of ductile fracture criteria have been proposed in the literature, e.g. McClintock [22], Rice and Tracey [23], Cockcroft and Latham [31], Johnson and Cook [37], Bao and Wierzbicki [4, 5], etc. The applicability of some of them was examined by, e.g. Wifi et al. [33] and Komori [34] for bulk forming processes, and Bao and Wierzbicki [35] for simple tensile and compression tests.

Because of simple calibration procedures and easy implementation, the Johnson-Cook's fracture locus (JC) and the critical effective plastic strain have been incorporated into popular commercial finite element codes such as LS-DYNA3D, ABAQUS, etc. Both have received much attention, in particular, in impact engineering. These fracture criteria were usually calibrated from tensile tests on smooth and notched axisymmetric specimens, e.g. Johnson and Cook [37], Børvik et al. [40], etc. In a real situation, a structural component may be subjected to tension, shear as well as compression before failure. As demonstrated in Chapter 3.2, the impacted zone, in which cracks are usually generated, undergoes large plastic compression in the initial phase, and then bending and axial stretching until fracture. It will certainly be appropriate to ask whether one would be able to use a fracture locus obtained from tensile tests alone to predict fracture in a case where compression may be

dominant.

The immediate objective of the present chapter is to study effects of the type of ductile fracture criteria on the failure response of high velocity impact events. The first part of this chapter introduces three fracture loci: the BW's fracture locus, the JC' fracture model [37], and the constant critical fracture strain, and reviews respective calibration procedures. In the second part, the latter two fracture loci will be used to predict the fracture process and the fracture pattern of the three impact problems: rigid mass-to-beam impact, the Taylor test, and dynamic compression tests on an axisymmetric hat specimen, all of which have already been investigated in Chapter 3 using the BW's fracture criterion. Comparison of numerical results among them will be made and some conclusions will be drawn.

6.2 Ductile fracture criteria

6.2.1 Bao-Wierzbicki's fracture locus

Recently, a complete fracture locus in the space of the effective plastic strain and the stress triaxiality was developed by Bao and Wierzbicki [4, 5] for 2024-T351 aluminum alloy. This fracture criterion was formulated and calibrated from a series of upsetting, shear, and tensile tests with parallel numerical calculations. Figure 6-1 shows all the specimens used in the development of the BW's fracture locus.



Fig. 6-1: Specimens used to calibrate the BW's fracture criterion. Courtesy Y. Bao.

This criterion covers the entire range of the stress triaxiality and consists of three branches corresponding to different fracture mechanisms, see Fig. 6-2. Tensile tests on smooth and notched round bars provided the fracture strains in the range of the stress triaxiality from 0.4 up. In this range, void nucleation, growth, and coalescence is the predominant failure mechanism. Compression tests on short cylinders with different ratios of height to diameter, i.e. upsetting tests, gave the fracture strains in the range of the stress triaxiality from $-1/3$ to 0.0. Note, that $\sigma_h/\bar{\sigma} = 0$ corresponds to a pure shear (torsional) condition. The failure mechanism for a specimen dominated by compression is not fully understood but was called “shear decohesion” by Wierzbicki and Bao [5]. This transition of fracture mechanism as a function of the stress triaxiality is not new. Fifty years ago, Bridgman [36] observed that the fracture patterns of tensile bars shifted from conventional cup-cone to shear slip on a single plane by increasing the magnitude of hydrostatic pressure superposed on specimens. The fracture strains in the intermediate range of the stress triaxiality from 0 to 0.4 were obtained from combined compression and shear tests on butterfly-like specimens. In this range, the specimens may fail by a mixed mechanism of shear slip and void growth.

One of the most important features of this new locus is the concept of the cut-off value for the negative stress triaxiality at $-1/3$. $\sigma_h/\bar{\sigma} = -1/3$ represents the stress state of a specimen under uniaxial compression. The mechanism behind the cut-off value is that preexisting microvoids would not expand, i.e. damage would not accumulate, if a material is predominantly under compression ($\sigma_h/\bar{\sigma} < -1/3$). By revisiting Bridgman’s experimental results [36] and performing theoretical analysis of upsetting tests, Wierzbicki and Bao [5] confirmed the correctness of the cut-off value.

It should be pointed out that the existence of the cut-off value does not mean that a specimen under predominant compression would never fail. As shown in Chapter 3.4, adiabatic shear banding would emerge under dynamic compressive loading. Adiabatic shear banding is a completely different failure mechanism from void growth.

Another observation can be made from Fig. 6-2 is that the fracture strain at pure shear is lower than that at pure tension. This feature is not an isolated phenomenon only for 2024-T351 aluminum alloy. Four of five metals collected by McClintock [125] possess the

same trend. Johnson and Cook [37] also obtained the same feature for 4340 steel as the one found by Bao and Wierzbicki [4], although the “inconvenient” torsional point was neglected in the calibration of the fracture locus. It is this property that gives rise to three distinct branches of the BW’s fracture locus.

Curve-fitting the points in Fig. 6-2 gives the following analytical expressions for the BW’s fracture locus

$$\bar{\epsilon}_f = \begin{cases} \infty & \frac{\sigma_h}{\bar{\sigma}} \leq -\frac{1}{3} \\ 0.1225 \left(\frac{\sigma_h}{\bar{\sigma}} + \frac{1}{3}\right)^{-0.46} & -\frac{1}{3} < \frac{\sigma_h}{\bar{\sigma}} \leq 0 \\ 1.9 \left(\frac{\sigma_h}{\bar{\sigma}}\right)^2 - 0.18 \frac{\sigma_h}{\bar{\sigma}} + 0.21 & 0 \leq \frac{\sigma_h}{\bar{\sigma}} \leq 0.4 \\ \exp\left(-1.944 \frac{\sigma_h}{\bar{\sigma}}\right) & 0.4 \leq \frac{\sigma_h}{\bar{\sigma}} \end{cases} \quad (6.1)$$

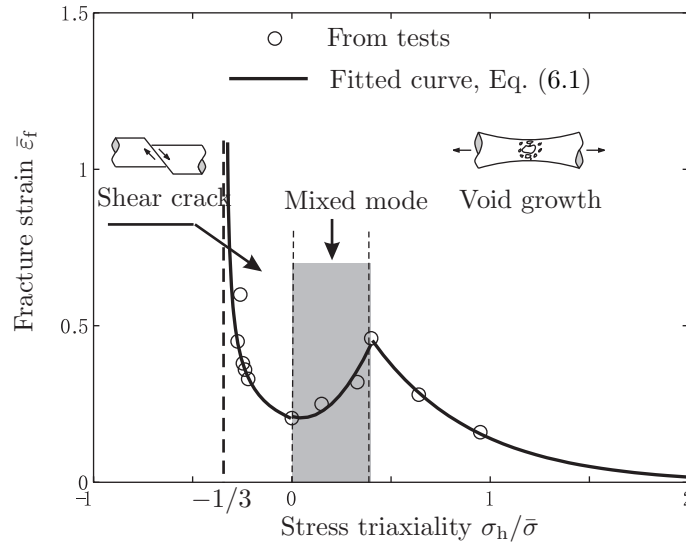


Fig. 6-2: The Bao-Wierzbicki’s ductile fracture locus for 2024-T351 aluminum alloy.

6.2.2 Johnson-Cook’s fracture locus

In companion with their material constitutive equation, Johnson and Cook [37] proposed a fracture criterion for dynamic loading problems. Similarly to the material constitutive model, the fracture strain was assumed to be a function of the stress triaxiality, strain rates,

and temperature in an uncoupled form, defined by

$$\bar{\epsilon}_f = \left[D_1 + D_2 \exp \left(D_3 \frac{\sigma_h}{\bar{\sigma}} \right) \right] \left[1 + D_4 \ln \left(\frac{\dot{\bar{\epsilon}}_{pl}}{\dot{\bar{\epsilon}}_0} \right) \right] \left[1 + D_5 \frac{T - T_0}{T_m - T_0} \right]. \quad (6.2)$$

where D_1, \dots, D_5 are five material constants. The first term in the brackets in the right hand side of Eq. (6.2) has the same form as proposed by Hancock and Mackenzie [30], and represents fracture characteristics of a specimen under quasi-static loading conditions at room temperature. Since an exponential function was employed in the first term, Johnson and Cook implied that the fracture locus could be represented by one continuous curve in the entire range and the fracture strain decreases with the increasing stress triaxiality. This assumption is opposite to Bao and Wierzbicki's experimental findings [4, 5]. The second and third terms signify effects of the strain rate and temperature on the fracture strain, respectively. As discussed in Chapter 2.4, both effects can be neglected for 2024-T351 aluminum alloy and Weldox 460 E steel. Five material constants are given in Tables 5.1 and 5.2 for Weldox 460 E steel and 2024-T351 aluminum alloy, respectively.

The calibration procedure of the JC's fracture model was not specifically addressed for 2024-T351 aluminum alloy in the open literature. But Johnson and Cook [37] indeed described the calibration procedure for OFHC copper, Armco iron, and 4340 steel. The relation between the fracture strain and the stress triaxiality was constructed based on quasi-static tests at room temperature. Tensile tests on smooth and notched axisymmetric specimens were performed and gave the fracture strain in the range of the stress triaxiality from 1/3 to 1.2. Johnson and Cook also conducted a torsional test on a thin-walled tubular specimen, which provided the fracture strain at $\sigma_h/\bar{\sigma} \approx 0$. They did not carried out any other experiments to determine the fracture strains in the range of $\sigma_h/\bar{\sigma} < 0.4$ including the negative stress triaxiality. Instead, an exponential function was enforced to fit the test data and extrapolated to cover the whole range of the stress triaxiality. The extension may be questionable since various failure mechanisms are evolved in different ranges of the stress triaxiality.

Following Johnson and Cook's formulation and calibration procedure, Børvik and his coworkers [40, 105, 106] performed a series of tensile tests on smooth and notched round

bars and parallel numerical simulations to determine the constants of the JC's fracture model for Weldox 460 E steel. Because neither shear nor compression tests were conducted, all the obtained experimental results covered the fracture strain in the range of the stress triaxiality only from $1/3$ up. Similarly, the extrapolation of the fracture locus to the range of the negative stress triaxiality was carried out by Børvik et al. [40] in practical applications, see Fig. 6-3. Since the cut-off value for the negative stress triaxiality at $\sigma_h/\bar{\sigma} = -1/3$ is applicable to all ductile metals, the JC's fracture locus calibrated by Børvik et al. is modified to incorporate this feature, see Fig. 6-3. The latter one was used in all the calculations presented in Chapter 3.

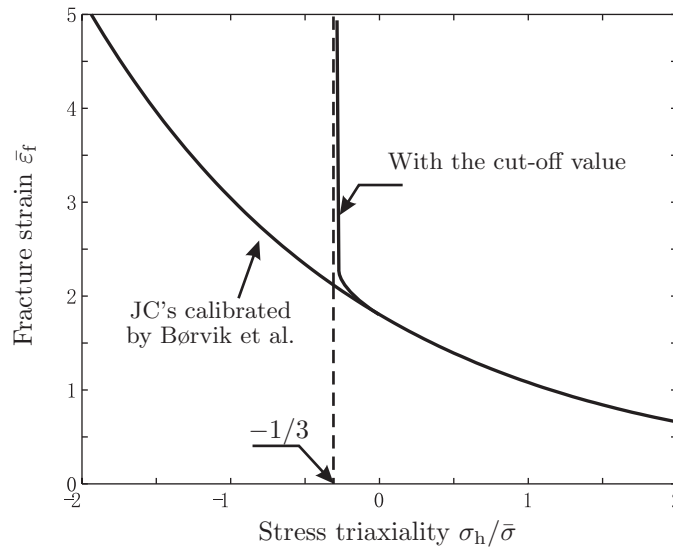


Fig. 6-3: Fracture loci for Weldox 460 E steel.

In actuality, it is more difficult to determine fracture properties of a specimen under a predominant compression rather than tension. Upsetting tests, which are often used to determine fracture strains in the range of the negative stress triaxiality, lose the applicability for a very ductile metal. A ductile cylinder in upsetting tests can be compressed to a large extent without any signs showing crack formation. Recently, a new type of specimen was specifically designed in the Impact and Crashworthiness Lab, MIT, to determine fracture characteristics of a ductile material in the range of the negative stress triaxiality, see Fig. 6-4.

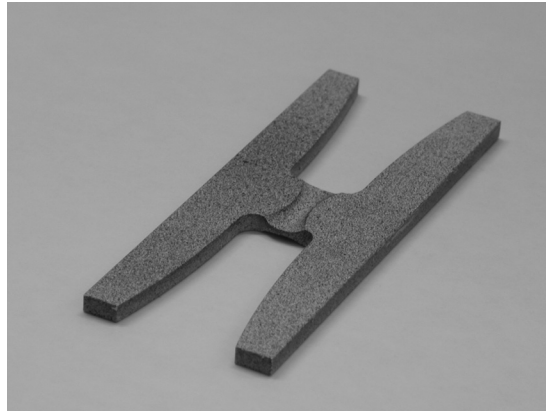


Fig. 6-4: A new type of specimen for the determination of fracture properties of a ductile material in the range of the negative stress triaxiality. Courtesy of Bao, Bai, and Wierzbicki.

6.2.3 Constant fracture strain

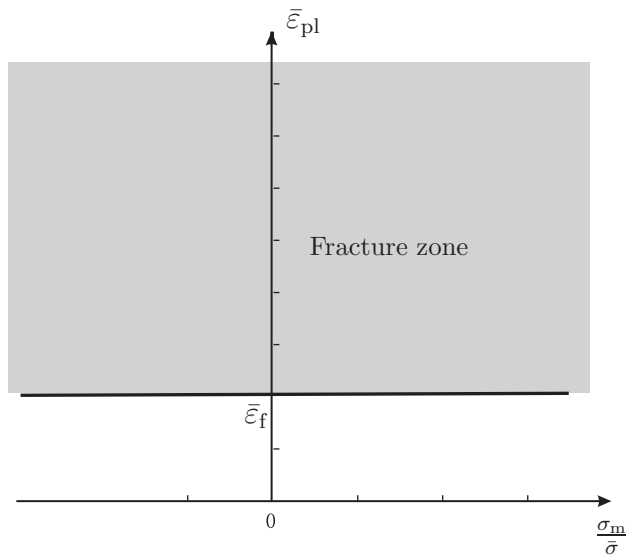
A critical effective plastic strain independent of the stress triaxiality has been widely used as a criterion in the prediction of ductile fracture (Fig. 6-5(a)), because it can be conveniently calibrated from tests and easily implemented in finite element codes, e.g. Anderson and Bonder [43], Guo et al. [97].

This simple fracture criterion, which is usually calibrated from tensile tests, is indeed able to capture crack formation and propagation in cases where tension is dominant and the stress triaxiality varies in a narrow range during the failure process [32]. However, this fracture locus may lose its applicability to compression-dominated problems or complicated loading cases.

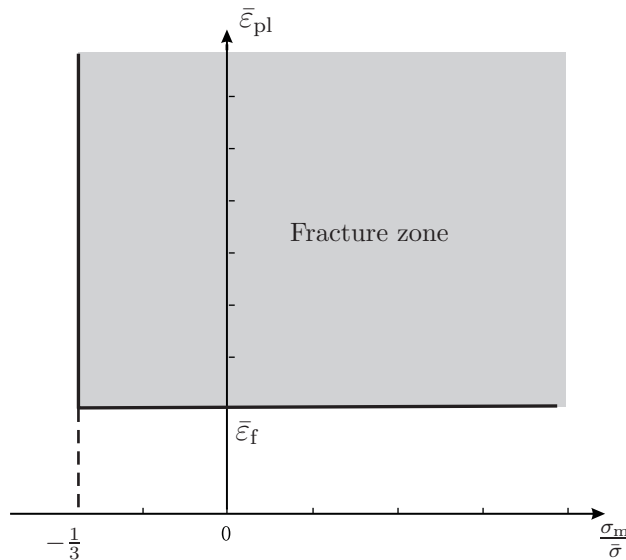
A complete determination of the fracture locus for a specific material is not an easy task. A preliminary study indicates that the cut-off value has a much larger effect on the predicted fracture response than the magnitude of the fracture strain [60]. By considering this fact, a modified constant fracture strain criterion with the cut-off value for the negative stress triaxiality at $-1/3$ has been proposed by Teng and Wierzbicki [60], see Fig. 6-5(b). This type of fracture locus has been used in Chapter 3.4 for predicting crack growth preceded by adiabatic shear banding.

Figure 6-6 shows comparison of the fracture loci for 2024-T351 aluminum alloy among the BW's model, the JC's model, and the constant fracture strain. The extrapolated range

of the JC's fracture locus is represented by a dash curve. It appears that there are large differences among these fracture loci in the range of the negative stress triaxiality. This discrepancy becomes critical for high velocity impact events, since cracks always initiate and grow in the region where shear and compression is dominant ($\sigma_h/\bar{\sigma} < 1/3$).



(a) Independent of the stress triaxiality



(b) With the cut-off value

Fig. 6-5: Constant fracture criteria with and without the cut-off value for the stress triaxiality.

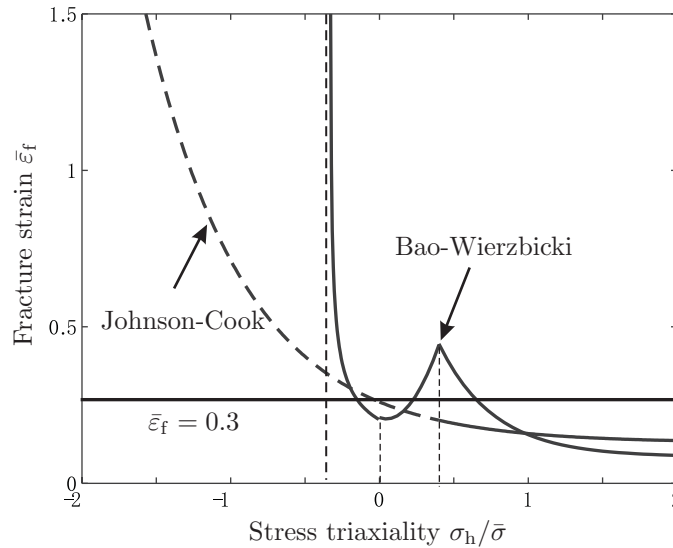


Fig. 6-6: Three fracture loci for 2024-T351 aluminum alloy.

6.3 Comparison of predicted failure patterns

6.3.1 Rigid mass-to-beam impact

6.3.1.1 Flat-nosed projectile

Consider first a plane-strain 2024-T351 aluminum beam of thickness $h = 10$ mm impacted by a flat-nosed projectile of $\mu = 0.1$ moving at $V_0 = 240$ m/s. The three fracture loci shown in Fig. 6-6 were implemented in the calculations, respectively.

A representative finite element at the impact interface is selected to study the stress state of the impacted zone during the failure process. It is seen from Fig. 6-7 that the stress triaxiality of this element is about -0.6 during the impact process, which is much lower than the cut-off value $-1/3$. At the same time, the effective plastic strain of this element rapidly increases and exceeds the fracture strain $\bar{\epsilon}_f = 0.3$, see Fig. 6-8. These data clearly indicate that the impacted zone undergoes large plastic compressive deformation. Since the constant critical strain fracture criterion assumes that the damage accumulation is independent of the stress state, the element fails as soon as the the effective plastic strain reaches the critical value ($\bar{\epsilon}_f = 0.3$). The failed element completely loses its load carrying capability. Correspondingly, the stress triaxiality drops to zero. Although large fracture strains are

associated with the negative stress triaxiality in the JC's model, damage accumulation still results in the failure of this element. As mentioned in the preceding section, the JC's fracture locus in the range of the negative stress triaxiality was obtained by extrapolation. By contrast, the BW's fracture model predicts that this element is still capable of resisting further plastic deformation.

Figure 6-9 shows comparison of the predicted failure patterns of the beam among three fracture criteria. It appears that in the case of the constant fracture strain, the elements of the impacted zone beneath the projectile immediately fail and are artificially removed layer by layer until the impact velocity of the projectile decreases to a certain level. Finally, the remaining ligaments are sheared off. By arbitrarily raising the magnitude of the fracture strain, the element removal of the impacted zone could be prevented. However, this increase in the fracture strain would at the same time make impossible to capture crack propagation through the target thickness, which occurs at a relatively low fracture strain. Hence, it is necessary to account for the stress triaxiality in the calculation of damage. It can also be seen from Fig. 6-9 that the JC's fracture criterion predicts that a number of elements around the sharp corners of the projectile are eroded. The removal of these elements below the projectile subsequently results in an unrealistic failure mode.

In contrast to the constant fracture strain and the JC's fracture locus, the BW's fracture model predicts a reasonable failure pattern. No elements in the impacted zone are eroded in the calculation, since the BW's fracture locus cover the whole range of the stress triaxiality. This failure mode qualitatively agrees well with experimental observations, e.g. Børvik et al. [56], Mescall [126]. Figure 6-10 shows a cross-section of the post-test aluminum alloy circular plate, which was struck by a steel cylindrical projectile moving at $V_0 = 245$ m/s [126]. Two through-thickness cracks are clearly visible and the generated plug has almost the same thickness as the surrounding part.

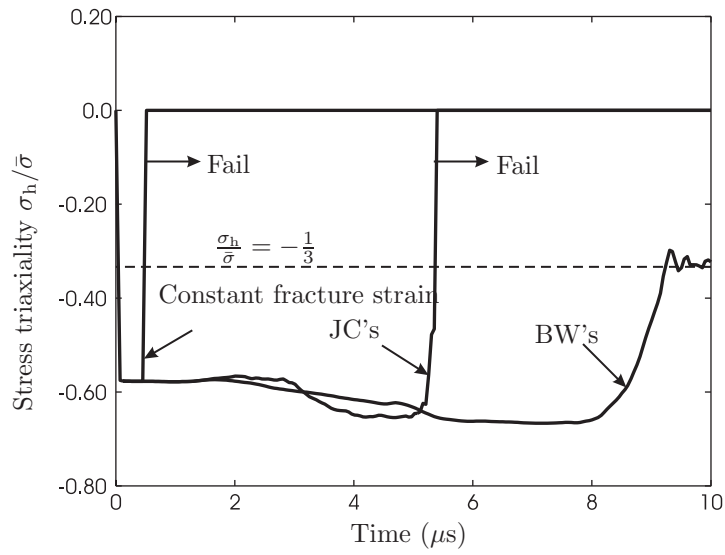


Fig. 6-7: Comparison of the stress triaxiality of a point at the impact interface among three fracture loci.

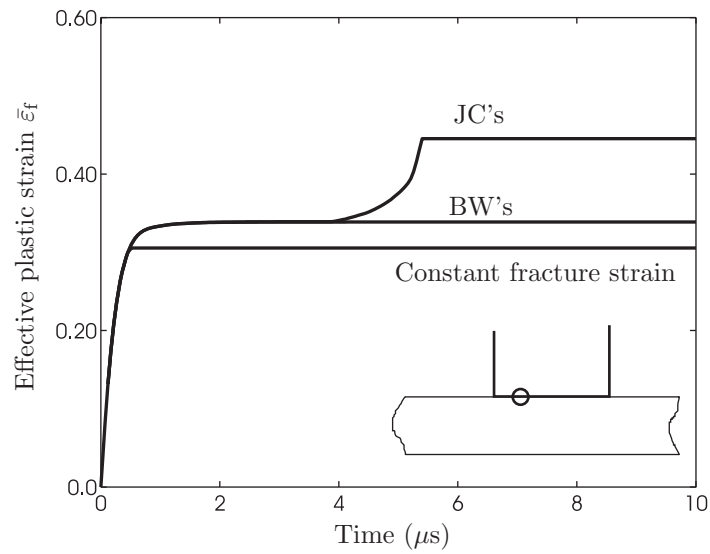


Fig. 6-8: Comparison of the effective plastic strain of a point at the impact interface among three fracture loci.


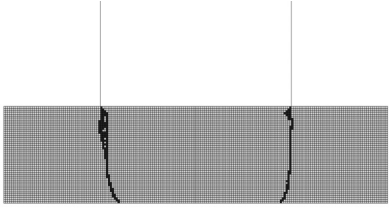

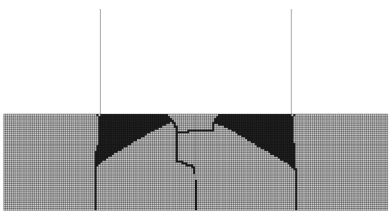

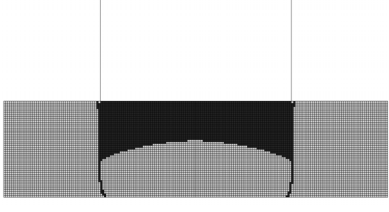
Fracture criteria	Fracture patterns	Failed elements
Bao-Wierzbicki's Eq. (6.1)		
Johnson-Cook's Eq. (6.2)		
Const. frac. strain $\bar{\epsilon}_f = 0.3$		

Fig. 6-9: Comparison of the failure patterns of a plane-strain aluminum alloy beam impacted by a flat-nosed projectile at $V_0 = 240$ m/s among three fracture criteria. The black areas represent failed elements.

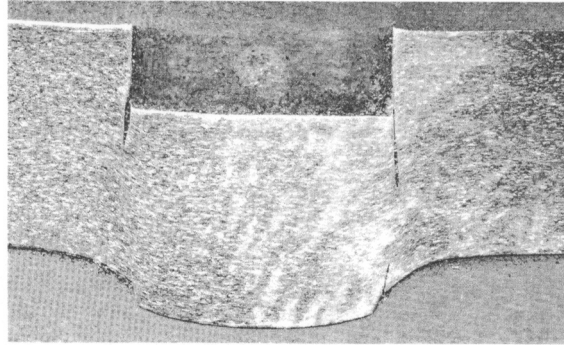


Fig. 6-10: Failure pattern of a circular 2024-T351 aluminum alloy plate impacted by a steel projectile at $V_0 = 245$ m/s [126].

6.3.1.2 Round-nosed projectile

The second problem considered is a plane-strain 2024-T351 aluminum beam of $h = 10$ mm impacted by a round-nosed projectile of $\mu = 0.1$ moving at $V_0 = 300$ m/s. Figure 6-11 shows three numerically predicted failure patterns and failure areas of the beam based on the three fracture loci, respectively. Similarly to the preceding flat-nosed case, the impacted zone of the target is dominantly by compression in the initial phase of the process. Since the constant fracture strain and the JC's fracture locus implicitly assume that a material under compression could fracture, a large part of the impacted zone is eroded leading to different final fracture modes. By contrast, the BW's fracture locus predicts two clean crack trajectories through the whole beam thickness. This predicted fracture pattern seems more realistic.

The element removal of a large part of the impacted zone was also observed by Børvik et al. [40] using the JC's fracture criterion for a Weldox 460 E steel circular plate impacted by a round-nosed and a conical-nosed projectile, respectively, (Fig. 14 in Ref. [107]). Their numerical results further reveal the deficiencies of the JC's fracture criterion for high velocity impact problems.

Because many elements are removed almost at the same time, it is difficult to track down crack propagation using the JC's fracture criterion and the constant critical strain. By contrast, the BW's fracture locus is capable of capturing the process of crack propagation, as shown in Chapter 4.

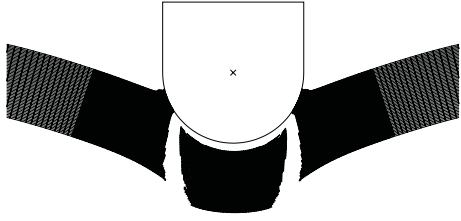
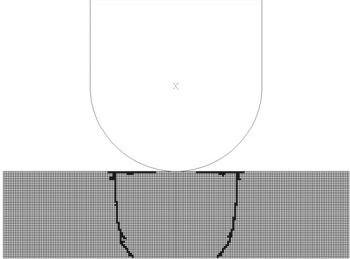
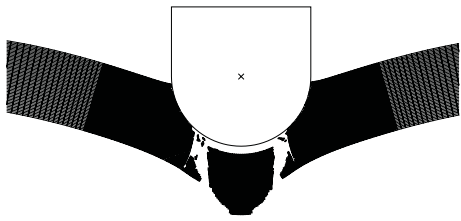
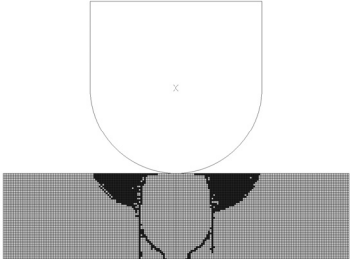
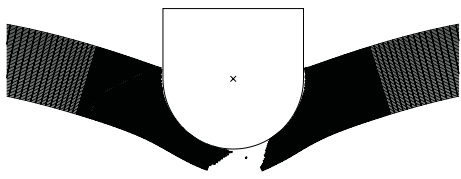
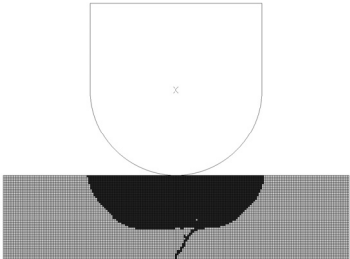
Fracture criteria	Fracture patterns	Failed elements
Bao-Wierzbicki's Eq. (6.1)		
Johnson-Cook's Eq. (6.2)		
Const. frac. strain $\bar{\epsilon}_f = 0.3$		

Fig. 6-11: Comparison of the failure patterns of a plane-strain aluminum alloy beam impacted by a round-nosed projectile at $V_0 = 300$ m/s among three fracture criteria. The black areas of the graphs in the right column represent failed elements.

6.3.2 The Taylor test

In rigid mass-to-beam/plate impact, only the impacted zone beneath the projectile is dominated by compression, and this compression would give way to bending and probably axial stretching in the later phase. By contrast, compression controls the entire cylinder in the Taylor test during the impact process. Hence, the Taylor test is a benchmark problem for examining a ductile fracture criterion, in particular, in the range of the negative stress triaxiality.

Chapter 3.3 has clearly demonstrated the effectiveness of the BW's fracture locus in the prediction of the failure response of a cylinder in the Taylor test. Here, the JC's criterion will be used to simulate the impact process of this cylinder under the same conditions. Additionally, two options of the treatment of failed elements will be explored: either the failed element completely lose the load carrying capability or are still able to resist pressure but neither shear nor tension.

Figure 6-12 shows the final fracture patterns of the Weldox 460 E steel projectile at $V_0 = 600$ m/s among four combinations of fracture options. All the failed elements have been removed to illustrate the generated cracks and fragments. It appears that the fracture locus without the cut-off value predicts more petal numbers and/or longer crack length than that with the cut-off value. In a way fracture models that disregard the effect of the cut-off value make materials artificially brittle. A number of fragments escape from the projectile in the case where the failed elements are assumed to completely lose the load carrying capability, see the graphs on the left hand side of Fig. 6-12. These fracture patterns probably are unrealistic, since the cylinder is made of a much ductile material.

The effect of the cut-off value on the predicted failure pattern of the cylinder becomes evident when comparing the failed region among these four cases, see Fig. 6-13. Note, that the central part of the cylinder is predominantly under compression. The size of the failed region is much smaller in the cases with the cut-off value than without the cut-off value. In reality, failed materials would be still attached to specimens. The size of the failed region may be determined by checking metallurgical microstructures of post-test specimens.

Besides different fracture patterns, the time history of the velocity of the rear surface of the cylinder can also be studied to distinguish among various types of fracture criteria.

Immediately upon impact, an axial elastic stress wave is generated followed by a plastic stress wave traveling at a much lower velocity. As the axial elastic stress wave propagates back and forth from the rear surface to the elastic-plastic boundary, the velocity of the rear surface decreases in a step-wise way. The movement of the rear surface can be measured using the so-called VISAR (Velocity Interferometer System for Any Reflector) technique. The measured time history of the velocity of the rear surface can be used to verify material constitutive models by comparing with numerical results, e.g. as proposed by Rohr et al. [63]. However, tracking the velocity history appears not to be very effective to examine a fracture criterion if a cylinder fails by petalling in the Taylor test. As shown in Fig. 6-14, there is not much difference in the calculated velocity history of the rear surface among four cases. However, this observation is not true for shear cracking. As we can see from Fig. 6-15, the JC's and BW's fracture loci give different velocity-time histories for 2024-T351 aluminum alloy where the projectile fails by shear cracking.

The effects of the type of ductile fracture criteria on the failure response of 2024-T351 aluminum alloy were also investigated. Figure 6-16 shows the final fracture patterns of the aluminum cylinder at $V_0 = 240$ m/s using the JC's and BW's fracture loci, respectively. In contrast to the BW's fracture locus, the JC's fracture model does not capture shear cracking on the lateral surface of the cylinder. Elements in the front part of the cylinder are artificially eroded layer by layer until the impact velocity is decreased to a certain level, which leads to a shorter final length of the cylinder, see Fig. 6-17. This seems unrealistic. Tests are being planned to verify the accuracy of the above numerical simulations.

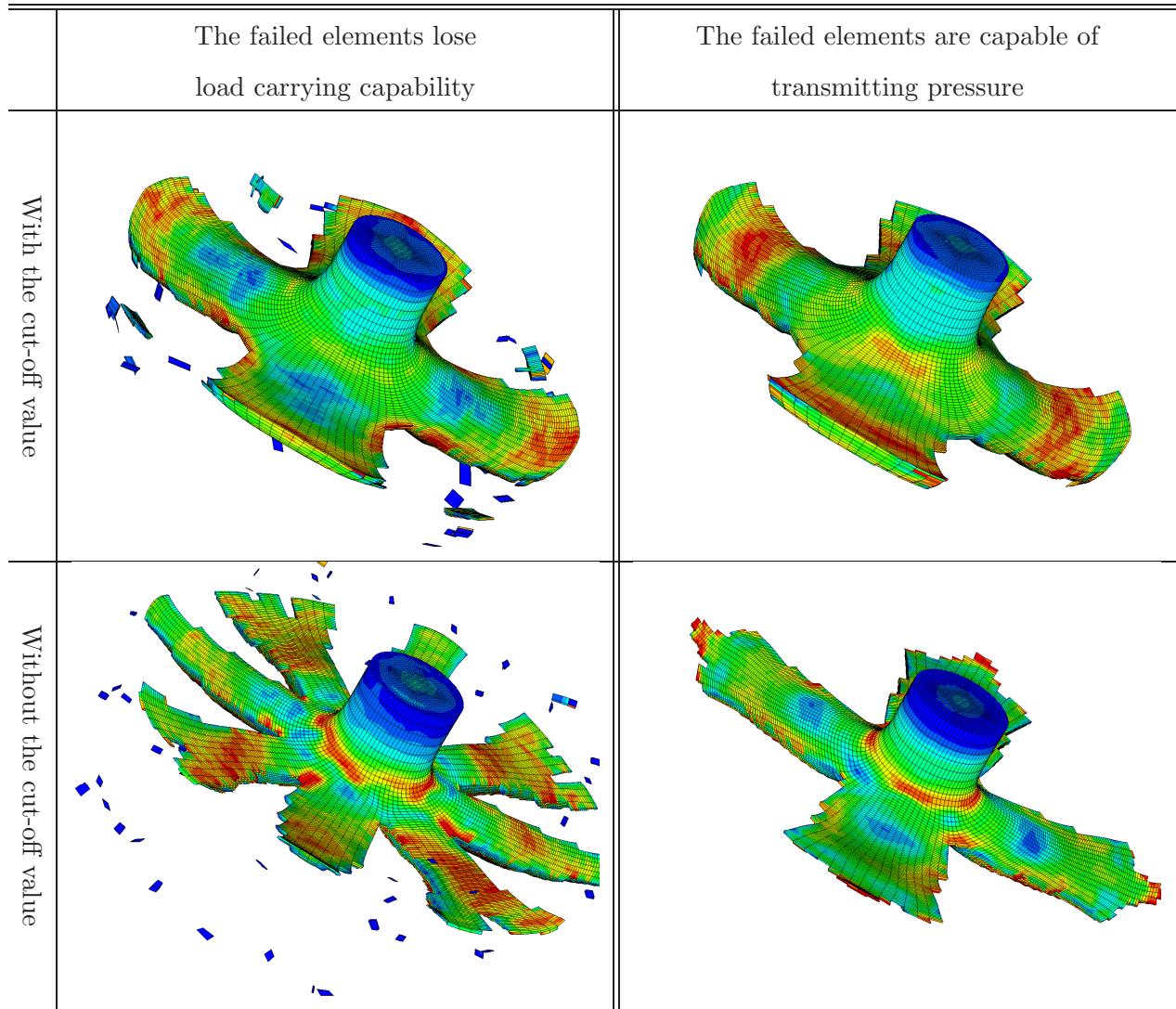


Fig. 6-12: Comparison of failure patterns of the Weldox 460 E steel projectile at $V_0 = 600$ m/s among various fracture options.

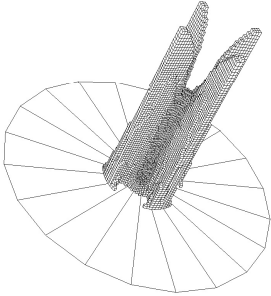
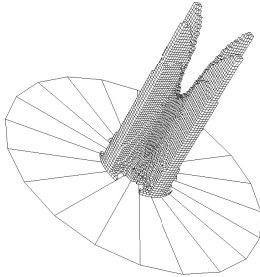
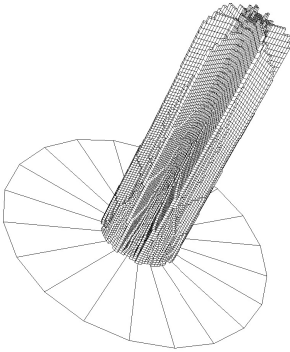
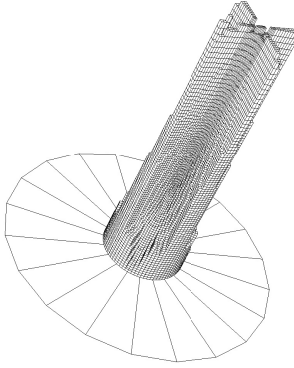
	The failed elements lose load carrying capability	The failed elements are capable of transmitting pressure
With the cut-off value		
Without the cut-off value		

Fig. 6-13: Comparison of the size of the failed region in the undeformed form for the Weldox 460 E steel projectile at $V_0 = 600$ m/s.

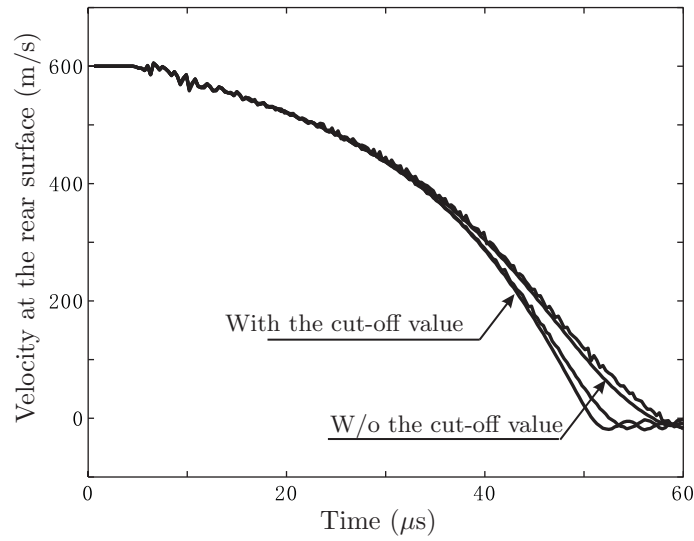


Fig. 6-14: Comparison of the velocity history of the rear surface of the Weldox 460 E steel projectile at $V_0 = 600$ m/s among four cases.

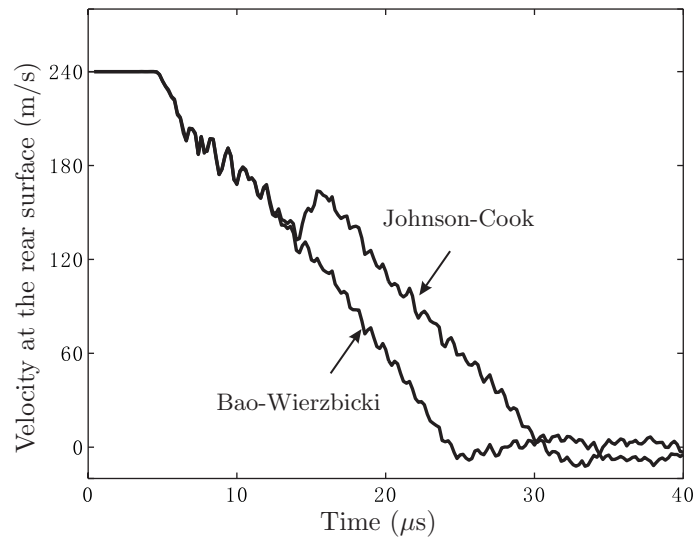


Fig. 6-15: Comparison of the velocity history of the rear surface of the 2024-T351 aluminum alloy projectile at $V_0 = 240$ m/s between Johnson-Cook's and Bao-Wierzbicki's fracture loci.

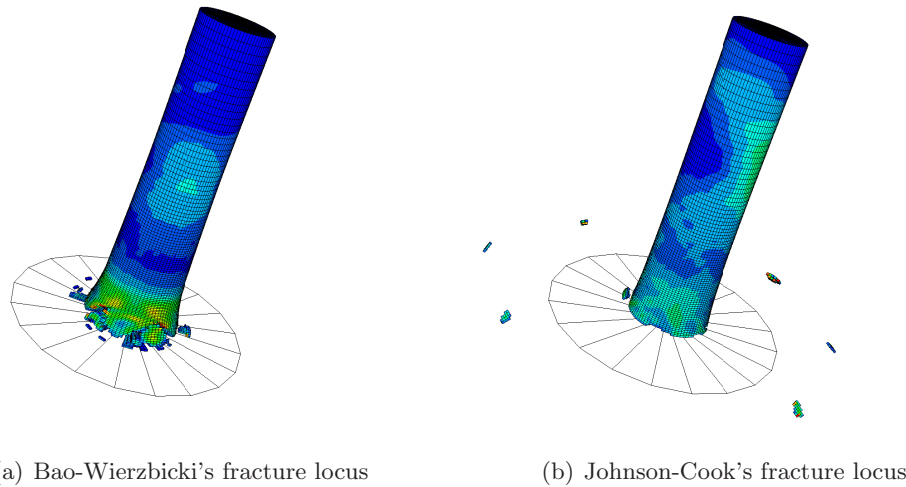


Fig. 6-16: Comparison of the final fracture patterns for the 2024-T351 aluminum alloy projectile at $V_0 = 240$ m/s. It is assumed in both cases that the failed elements are still capable of transmitting pressure. The failed elements have been removed to show generated cracks.

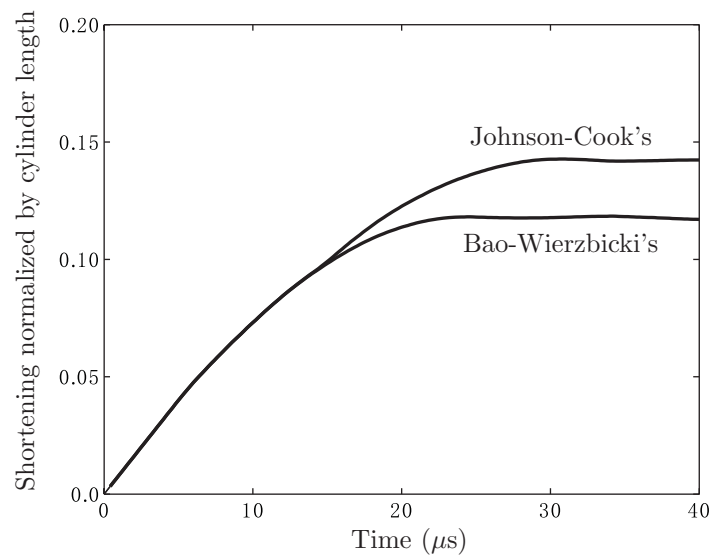


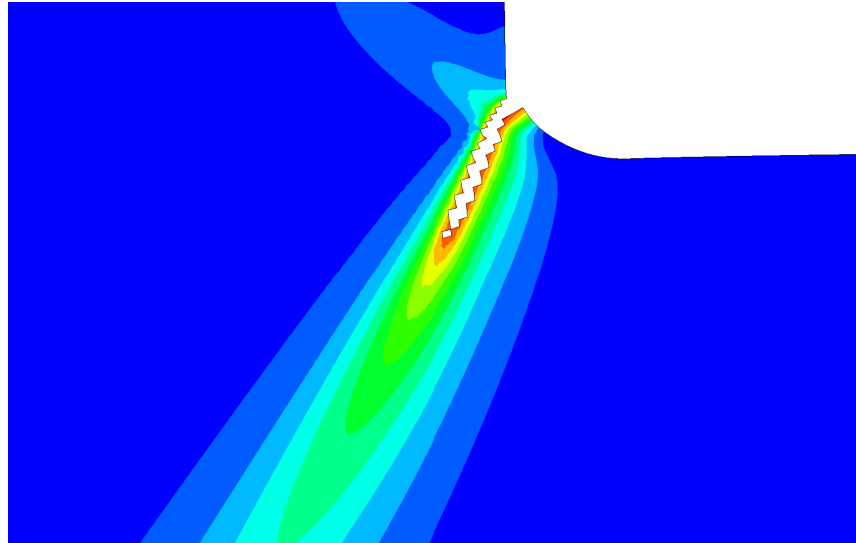
Fig. 6-17: Comparison of shortening history of the 2024-T351 aluminum alloy projectile at $V_0 = 240$ m/s based on the JC's and BW's fracture loci, respectively.

6.3.3 Compression tests on the axisymmetric hat specimen

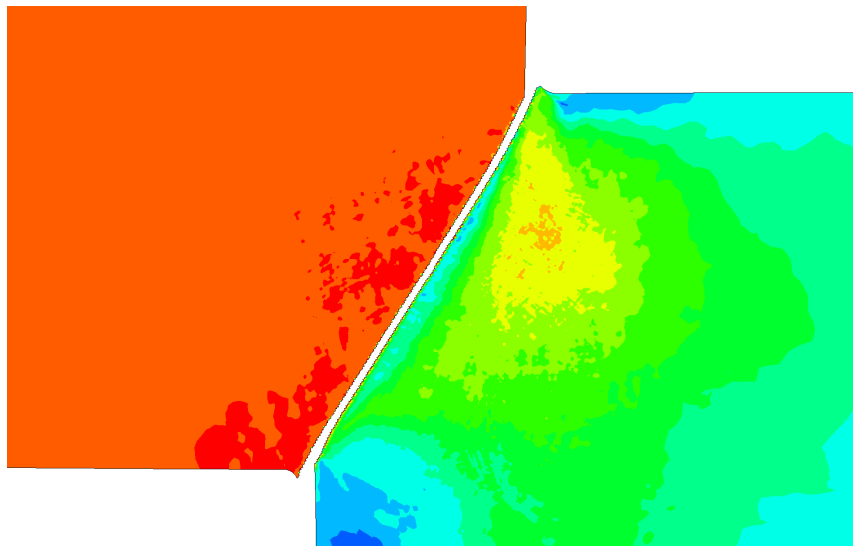
The dynamic compression test on the axisymmetric hat specimen has been investigated in Chapter 3.4. Adiabatic shear banding and subsequent fracture was successfully captured using a constant fracture strain with the cut-off value for the negative stress triaxiality. Here, a constant fracture strain of $\bar{\epsilon}_f = 0.4$ without the cut-off value was assigned in the calculation. As shown in Fig. 6-18, two cracks initiate at the exterior and interior corners, respectively, and propagate towards each other. As these two cracks link together, the whole specimen breaks into two parts before $t = 24 \mu\text{s}$. It can also be seen that no adiabatic shear banding is captured. The cracks are generated before the homogeneous plastic deformation narrows down into a localized shear band. This failure pattern is not consistent with the experimental observations that both cracks and shear bands were generated and arrested inside the gauge section at $V_0 = 27.6 \text{ m/s}$.

An element near the interior corner was selected to illustrate the difference in the time history of the von Mises stress between two cases, see Fig. 6-19. It appears that the chosen element fails before undergoing the stress collapse in the case without the cut-off value, which is not realistic. As Marchand and Duffy [70] observed from torsional tests on thin-walled tubes, the fracture within the shear band was usually preceded by the stress collapse, which can be considered to be an indicator for the formation of the adiabatic shear band.

Since voids do not nucleate and grow under predominant compression, the increase in effective plastic strains would not contribute to the accumulation of damage. However, for the constant fracture strain criterion without the cut-off value for the stress triaxiality, damage accumulation is in proportional to the increase in the effective plastic strain, which leads to the present unrealistic numerical results.



(a) Crack formation in the vicinity of the interior corner at $t = 21 \mu s$ (Enlarged)



(b) $t = 24 \mu s$

Fig. 6-18: Predicted fracture pattern of the specimen using the constant fracture strain without the cut-off value at $V_0 = 27.6$ m/s. All the failed elements have been removed to show the generated crack.

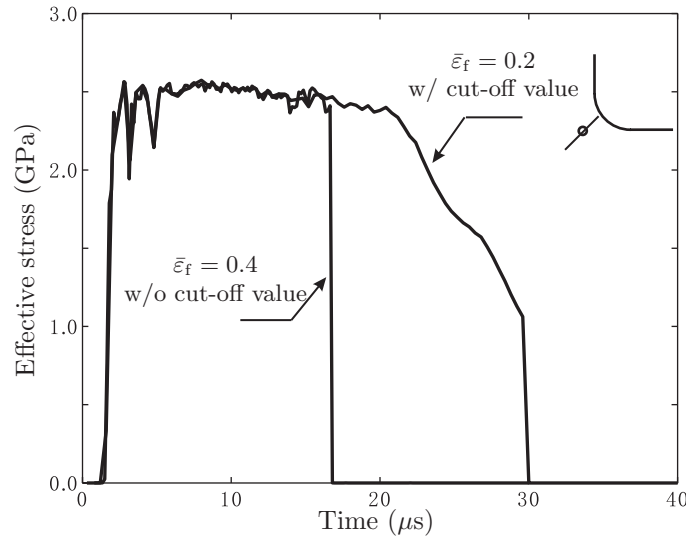


Fig. 6-19: Comparison of the time history of the effective stress between the fracture strain with and without the cut-off value.

6.4 Partial conclusions

In this chapter, the formulation and the calibration of the BW's and JC's fracture loci, and the constant fracture strain has been critically reviewed. Their applicability to three typical types of high velocity impact problems has been assessed: rigid mass-to-beam impact, the Taylor test, and dynamic compression tests on a hat specimen. Since the JC's fracture model and the critical fracture strain were calibrated from tensile tests alone, they do not represent real fracture characteristics of a material dominated by compression. This deficiency leads to the prediction of the unrealistic failure patterns and processes of the targets under high velocity impact. At the same time, this investigation further demonstrates the effectiveness of the BW's fracture locus in predicting high velocity impact fracture.

Chapter 7

Derivation of Analytical Benchmark Solutions

7.1 Background

In the September 11th attack, two Boeing 767 airplanes traveling at 264 m/s (590 mph) and 210 m/s (470 mph) crashed, respectively, into the South and North Towers of the World Trade Center [1]. The impact damage eventually led to the collapse of the Twin Towers. Soon after the event, the Federal Emergency Management Agency (FEMA) [1] performed a detailed survey of the damage to the outer facade of the Twin Towers. Several failure modes of the exterior columns can be identified from Fig. 7-1 [127]. Some exterior columns, probably impacted by the wing tip, were deeply indented and torn apart while others, struck by the wing root, the engine, and the fuselage, were clearly sheared off. At the same time, the bolt connection of several columns were also broken.

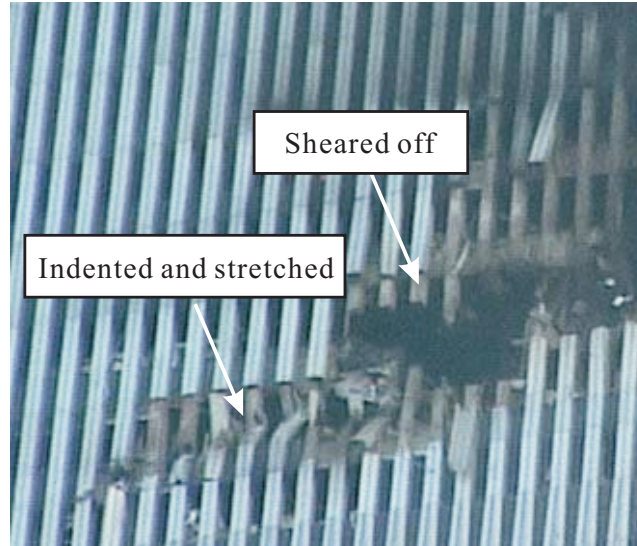


Fig. 7-1: A close-up view of the damaged exterior columns of the south facade of the South Tower of the World Trade Center [127]. ©C. Sorensen.

The immediate objective of this chapter is to develop mathematically trackable theoretical models to better understand the plastic deformation and fracture process of both the exterior columns and the airplane wings at the first milliseconds of the attack. At the same time, the theoretical analyses are rather general and can be applied to any beams of solid-section made of same or different materials.

Due to almost fully loaded fuel tank, the wings of the Boeing 767 were much heavier than the exterior columns of the Twin Towers. As a first approximation, the impacting segments of the wing can be modeled as rigid masses moving at a certain velocity while the exterior column as a plastically deforming beam. The theoretical model of rigid mass-to-beam impact will be presented in Chapter 7.2.

Since both the exterior columns and the airplane wings must have undergone considerable plastic deformation before rupture, it is more reasonable to simultaneously consider the exterior column and the portion of the wing as two plastically deforming and fracturing beams. The interactive failure of two impacting beams is the subject of Chapter 7.3.

As shown in Fig. 7-2, the structural arrangement of a modern airplane wing is quite complicated, consisting of open section beams, ribs, and a skin reinforced by stringers. The exterior columns must have been impacted sequentially by these components when the

airplanes cut through the wall of the Twin Towers. The theoretical analysis of multiple impact of beam-to-beam will be performed in Chapter 7.4.

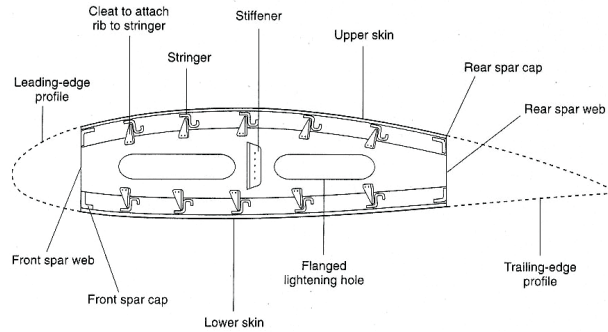


Fig. 7-2: Structural component arrangement inside an airplane wing.

In the development of the above three theoretical models arranged in the order of increasing complexness, the target is assumed to undergo large plastic deflection and thus it tends to fail by tensile tearing due to dominant axial stretching. As demonstrated in Chapter 3.2.4, shear plugging is another possible failure mode of a beam/plate under rigid mass impact, in which plastic deformation localizes in the impacted zone. The theoretical solution for shear plugging will be addressed in Chapter 7.5.

7.2 Rigid mass-to-beam impact

7.2.1 Introduction

The plastic deformation and failure response of a beam impacted by a rigid mass has been extensively studied in the past. About a decade ago, research was driven mostly by the problem of low velocity heavy body impact on thin-walled cylinders such as oil pipes and tubular members of offshore platforms [128, 129]. Interest in this kind of problem has been renewed since the September 11th attack. A theoretical model of rigid mass-to-box beam impact was developed by Wierzbicki and Teng [130] to estimate the critical impact velocity of the wing of the airplane to cut through the hollow exterior columns.

Many tests on a beam struck by a falling rigid body were performed by Jones and his coworkers [131, 132]. The impact velocity obtained using a drop tower were limited to 20 m/s, which are an order of magnitude lower than the cruising speed of the Boeing 767. Bending response is dominant at such a low impact velocity. Theoretical models with a moving plastic bending hinge were proposed by, e.g. Jones and his coworker [133, 134], Yu and Stronge [128], etc.

By analogy, Yu and Stronge [128], Wierzbicki and Hoo Fatt [11, 12] developed an analytical model of plastic beam/string-on-plastic foundation for a thin cylindrical shell under projectile impact. The solution of Yu and Stronge is applied to the case where bending is equally important as axial stretching. By contrast, Wierzbicki and Hoo Fatt studied the axial stretching dominated case, which usually occurs at a high impact velocity. The problems formulated by Wierzbicki and Hoo Fatt were also solved by Mihailescu et al. [135, 136] using a rigorous shock wave approach. The identical results were obtained.

The first objective of the present section is to review the theoretical model of rigid mass-to-beam impact proposed by Wierzbicki and Hoo Fatt [12]. The range of applicability of this theoretical solution, which was absent in Ref. [12], is determined here. At the same time, the theoretical analysis, which originally applied to the flat-nosed projectile, is extended to the case with a round-nosed projectile. Finite element calculations are performed and compared with the closed-form solutions. This study will provide a solid foundation for the formulation of the more complicated events of the single and multiple impact of beam-to-

beam, which will be presented in the following sections.

7.2.2 Flat-nosed projectile

7.2.2.1 Problem formulation

Consider a plastic beam/string struck by a flat-nosed rigid mass, Fig. 7-3. The beam/string is stationary and the rigid projectile moves at the velocity, V_0 . The cubic projectile is of the mass M_0 , and the breadth d . The beam/string is of a solid, rectangular cross-section with the breadth $2b$ and the thickness h . The impact velocity is assumed to be high enough so that the problem is controlled by local inertia and wave propagation. Therefore neither the length of the beam nor far-field boundary conditions are entering the problem.

The beam/string is assumed to be rigid-perfectly plastic, characterized by the plastic flow stress σ_0 . The plastic flow stress is an average stress over the strain path all the way to fracture for an elastic-plastic strain-hardening material, which can be expressed as

$$\sigma_0 = \frac{1}{\bar{\epsilon}_f} \int_0^{\bar{\epsilon}_f} \bar{\sigma}(\bar{\epsilon}_{pl}) d\bar{\epsilon}_{pl}, \quad (7.1)$$

In such a way, the total energy absorbed by plastic deformation in a real material would be the same as that in the present plastic material. At the same time, effects of strain hardening, strain rates, and temperature can be included indirectly in the calculation of the plastic flow stress in an average sense.

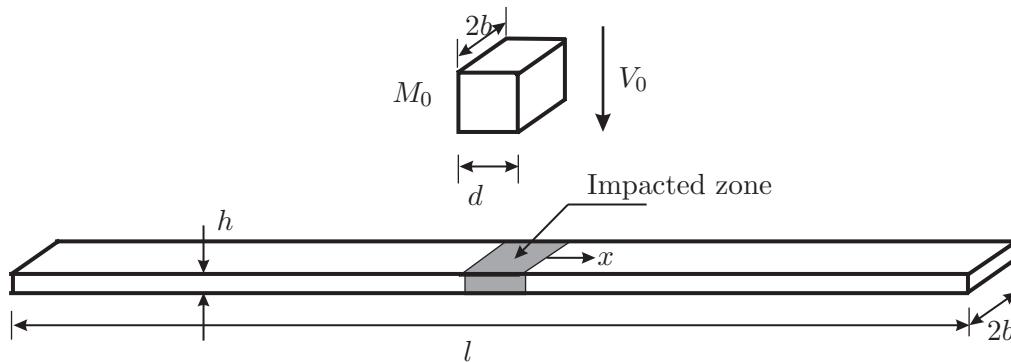


Fig. 7-3: Schematic representation of a beam impacted by a rigid, blunt-nosed projectile. The axial coordinate x is measured from the central axis of the beam.

Immediately upon impact, two transverse plastic stress waves are generated in the impacted zone and travel outward down the beam. The equation of motion of the string under moderately large deflection is

$$(N_0 w')' = m \ddot{w}, \quad (7.2)$$

where the term in the left hand side is the vertical component of the axial tensile force; the term in the right hand side represents the inertial force; $N_0 = 2\sigma_0 b h$ is the axial tensile force acting on the cross-section; $m = 2\rho b h$ is the mass per unit length; the symbols prime and dot denote differentiation with respect to the spatial coordinate x and time t , respectively. This equation is applicable to a beam under large deformation if bending contribution can be neglected. This issue will be discussed later on.

Substituting the expressions for N_0 and m into Eq. (7.2), we obtain the familiar wave equation

$$c^2 w'' = \ddot{w}, \quad (7.3)$$

where c is the speed of the transverse plastic stress wave, defined by

$$c = \sqrt{\frac{\sigma_0}{\rho}}. \quad (7.4)$$

It is assumed that the impacted zone immediately acquires the same transverse velocity as the projectile. This is true for a thin beam. From the principle of linear momentum conservation, the common velocity at $t = 0$ is given by

$$V_0^* = \frac{V_0}{1 + \mu}. \quad (7.5)$$

The problem is subject to the following initial conditions

$$w(x, t = 0) = 0; \quad (7.6)$$

and

$$V(x, t = 0) = V_0^* \left[1 - \text{H} \left(x - \frac{d}{2} \right) \right]. \quad (7.7)$$

where H is a Heaviside function. The rigid mass is decelerated by the vertical component

of the membrane force, which furnishes a boundary condition for the problem,

$$2N_0 w' = M_0 (1 + \mu) \ddot{w} \quad \text{at} \quad x = \frac{d}{2}. \quad (7.8)$$

Another boundary condition is the zero deformation ($w = 0$) at the moving wave front $\xi = ct$.

Both the velocity and deformation slope suffer jumps at the wave front while the transverse deformations are continuous. The kinematic and dynamic continuity conditions require, respectively,

$$\dot{w}] + \dot{\xi} w'] = 0, \quad \text{at} \quad x = \xi + \frac{d}{2}, \quad (7.9)$$

and

$$N_0 w'] + m\dot{\xi} \dot{w}] = 0, \quad \text{at} \quad x = \xi + \frac{d}{2} \quad (7.10)$$

where $\dot{\xi} = c$, and the symbol $]$ denotes a jump of a given quantity across the wave front, e.g. $\dot{w}] = \dot{w}|_{x+} - \dot{w}|_{x-}$. Since the deflection slope and the velocity ahead of the wave front are equal to zero, both continuity conditions can be simplified, respectively, as

$$V + cw'|_{x=\xi} = 0, \quad (7.11)$$

and

$$N_0 w'|_{x=\xi} + mcV = 0. \quad (7.12)$$

In actuality, the above two equations are identical to each other since $c^2 = N_0/m$.

7.2.2.2 Velocity and deformation

It is assumed that the material element at the stress wave front is instantaneously stretched and rotated, and the plastic deformation of this element keeps constant in the remaining part of the impact process. Thus, the wave front carries all the deformation information in a similar way as a propagating plastic hinge. In such a way, the already deformed region of the beam behind the wave front undergoes a rigid body translation with a uniform velocity. Figure 7-4 shows several transient velocity profiles in the deformed regions. By contrast,

the transverse velocity field is assumed to be of a triangular form in the bending solution, e.g. Jones [133] and Yu and Stronge [128], in which the rotation angle of the plastic bending hinge increases with time.

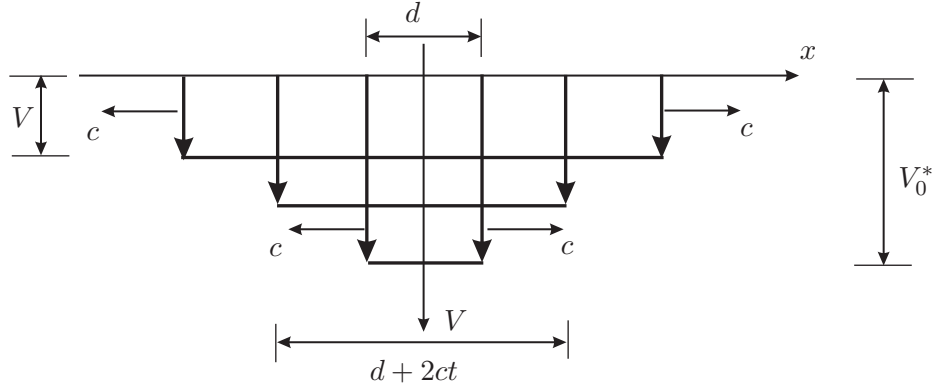


Fig. 7-4: Schematic representation of transient velocity profiles.

Based on the assumption that the transient velocity and acceleration field of the deformed region is constant in space, one can solve Eq. (7.2) by integrating with respect to x from $x = d/2$ to $x = \xi + d/2$

$$N_0 w' \Big|_{x=d/2}^{x=\xi+d/2} = m\ddot{w}\xi. \tag{7.13}$$

Substituting the boundary condition at $x = d/2$, Eq. (7.8), and the dynamic continuity condition, Eq. (7.12), into Eq. (7.13) yields

$$2mc\dot{w} + (M_0 + md + 2m\xi)\ddot{w} = 0. \tag{7.14}$$

This ordinary differential equation can also be derived in a straightforward way by invoking the principle of linear momentum conservation

$$\frac{d}{dt} [(M_0 + md + 2m\xi)\dot{w}] = 0. \tag{7.15}$$

The term inside the brackets denotes the total transverse momentum of the system. Solving

the above equation for \dot{w} gives the transient velocity

$$\frac{V}{V_0} = \frac{1}{1 + \mu + 2\mu ct/d}. \quad (7.16)$$

A point of the beam located at a distance x from the impacted area begins to deflect only after $t = (x - d/2)/c$ when the transverse stress wave arrives. Thus, the transverse deflection of the beam, w , is

$$w = \int_{(x-d/2)/c}^t V dt. \quad (7.17)$$

Substituting the expression for V , and integrating the above equation gives

$$\frac{w}{d} = \frac{1}{2\mu} \frac{V_0}{c} \ln \frac{1 + \mu + 2\mu ct/d}{1 + 2\mu x/d}, \quad (7.18)$$

where x should satisfy the inequality: $d/2 \leq x \leq d/2 + ct$. Due to symmetry of the deflection of the beam about the impacted area, the expression for the deflection is given only for one side in Eq. (7.18). Setting $x = d/2$ in Eq. (7.18) gives the displacement of the rigid mass

$$\frac{w_0}{d} = \frac{1}{2\mu} \frac{V_0}{c} \ln \left(1 + \frac{2\mu}{1 + \mu} \frac{ct}{d} \right). \quad (7.19)$$

This quantity is easily measured in experiments, and thus can be used to make a comparison between the present analytical solutions and test results.

7.2.2.3 Strain and critical impact velocity

Differentiating the transverse deflection w with respect to x gives the slope of the beam/string

$$\frac{\partial w}{\partial x} = \frac{V_0}{c} \frac{1}{1 + 2\mu x/d}. \quad (7.20)$$

Under moderately large deflection, the axial tensile strain of the beam/string can be defined as

$$\varepsilon = \frac{1}{2} \left(\frac{\partial w}{\partial x} \right)^2 = \frac{1}{2} \left(\frac{V_0}{c} \right)^2 \left(\frac{1}{1 + 2\mu x/d} \right)^2. \quad (7.21)$$

It appears that the plastic tension strain decreases with the distance away from the impacted zone. The maximum value is located at the edge of the impacted zone, i.e. $x = d/2$,

$$\varepsilon_{\max} = \frac{1}{2} \left(\frac{V_0}{c} \right)^2 \frac{1}{(1 + \mu)^2}. \quad (7.22)$$

As discussed earlier on, a beam under rigid mass impact probably fails by either shear plugging or tensile necking. In the present formulation, a through-thickness shear is not considered and thus the beam/string tends to fail by tensile tearing. The constant critical plastic strain $\bar{\varepsilon}_f$ is often used as a fracture criterion to predict necking failure of the beam. Setting the maximum tensile strain equal to the fracture strain, i.e. $\varepsilon_{\max} = \bar{\varepsilon}_f$, yields the critical impact velocity

$$\frac{V_{\text{cr}}}{c} = (1 + \mu) \sqrt{2\bar{\varepsilon}_f}. \quad (7.23)$$

7.2.2.4 Energy dissipation

The initial kinetic energy, E_0 , of the projectile is

$$E_0 = \frac{1}{2} M_0 V_0^2. \quad (7.24)$$

Immediately after impact, both the impacted zone of the beam and the rigid projectile have a common velocity, V_0^* . The corresponding kinetic energy of the system, E_0^* , is given by

$$E_0^* = \frac{1}{2} (M_0 + md) (V_0^*)^2 = \frac{E_0}{1 + \mu}. \quad (7.25)$$

This kinetic energy will be gradually dissipated in the target beam in the form of plastic deformation. Compared E_0^* with E_0 , it can be seen that some of the kinetic energy of the rigid mass has been lost upon impact

$$\Delta E_0 = E_0 - E_0^* = \frac{\mu}{1 + \mu} E_0. \quad (7.26)$$

The loss of the kinetic energy is attributed to a complex local plastic deformation under the rigid mass. This phenomenon cannot be described using an one-dimensional beam model.

As the stress waves propagate along the beam from the impacted zone, the transverse velocity of the beam and rigid mass gradually decreases. At a given time t , the total kinetic energy of the system becomes

$$E = \frac{1}{2} (M_0 + md + 2mct) V^2 = \frac{E_0}{1 + \mu + 2\mu tc/d}. \quad (7.27)$$

The loss of the kinetic energy of the system during the stress wave propagation is given by

$$\Delta E = E_0 \left(\frac{1}{1 + \mu} - \frac{1}{1 + \mu + 2\mu tc/d} \right). \quad (7.28)$$

For a rigid-plastic material, the loss of the kinetic energy is completely dissipated in the form of the plastic compression of the impacted zone. In reality, some lateral plastic deformation must be present due to the property of plastic incompressibility of materials.

For a rigid-plastic string, the loss of the kinetic energy is completely converted to the plastic tension energy, defined by

$$W = \int_{-ct}^{ct} 2bh\sigma_0 \varepsilon dx. \quad (7.29)$$

Substituting the expression for the tension strain into the above equation, by integration one gets

$$W = E_0 \left(\frac{1}{1 + \mu} - \frac{1}{1 + \mu + 2\mu tc/d} \right), \quad (7.30)$$

which is exactly equal to the loss of the kinetic energy, ΔE . Therefore, not only the linear momentum but also the energy are conserved during the wave propagation process for a rigid-perfectly plastic beam/string.

7.2.2.5 Range of applicability

The present solution is applicable to a plastic string, in which axial stretching is only an effective response to impact loading. The beam case is more complicated since shearing, bending, and axial stretching may participate subsequently or simultaneously in the impact response. Immediately after impact, local shearing through the target thickness is predominant. If the impact velocity is sufficiently high, the beam would be sheared off in this phase,

which is the subject of Chapter 7.5. As transverse disturbances (transverse stress waves) travel away from the impacted zone, local shearing will give way to bending deformation. Axial stretching would become equally important as, or even exceed bending response as the transverse deflection increases. Alternatively, at a relatively low impact velocity the beam would stop deformation before entering into the phase of axial stretching. Hence, it is necessary to determine the range of applicability of the present solution to the beam case.

Suppose that the beam is subjected to the combined action of axial stretching and bending. The neutral axis is located at the distance ζh from the bottom surface where $0 < \zeta < 1$, see Fig. 7-5.

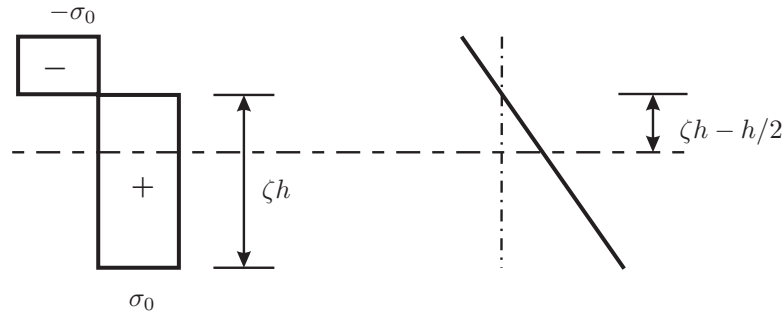


Fig. 7-5: Schematic representation of stress distribution along the thickness and the neutral axis.

The bending moment M_b acting on the section is given by

$$M_b = \sigma_0 2b (h - \zeta h) \zeta h. \tag{7.31}$$

Setting $\zeta = 1/2$ in the above expression, i.e. the neutral axis is located at the center of the cross-section, gives the pure plastic bending moment

$$M_{b,0} = \sigma_0 b h^2 / 2. \tag{7.32}$$

The axial tensile force acting on the cross-section is

$$N = \sigma_0 2b [h - 2(h - \zeta h)]. \tag{7.33}$$

Combining Eqs. (7.31) with (7.33) and eliminating ζ gives the yield locus

$$\frac{M_b}{M_{b,0}} + \left(\frac{N}{N_0}\right)^2 = 1. \quad (7.34)$$

Assume that the cross-section remains plane and thus the membrane strain rate at the central axis has the following relation with the bending curvature rate

$$\dot{\varepsilon} = \dot{\kappa} \left(\zeta h - \frac{h}{2} \right). \quad (7.35)$$

By eliminating ζ , we obtain

$$\frac{\dot{\varepsilon}}{\dot{\kappa}} = \frac{h}{2} \frac{N}{N_0}. \quad (7.36)$$

Assume that the uniform distribution of the transient transverse velocity field is still valid for the beam under the combined action of bending and axial stretching. Thus, the transient deflection of the beam is also given by Eq. (7.18). Differentiating the deflection twice with respect to the spatial coordinate yields the bending curvature κ

$$\kappa = -\frac{\partial^2 w}{\partial x^2} = \frac{V_0}{c} \frac{2\mu}{d} \left(\frac{1}{1 + \mu + 2\mu x/d} \right)^2. \quad (7.37)$$

Similarly to the plastic string case, the material element at the stress wave front is suddenly stretched and at the same time bent. The acquired bending strain and the axial stretching strain keep constant in the rest of the impact process. Hence, we have

$$\frac{\varepsilon}{\kappa} = \frac{\dot{\varepsilon}}{\dot{\kappa}} = \frac{h}{2} \frac{N}{N_0} \quad (7.38)$$

Substituting the expressions for ε and κ , we have

$$\frac{V_0}{c} \frac{d}{4\mu} = \frac{h}{2} \frac{N}{N_0}. \quad (7.39)$$

Setting $N = N_0$ in the above equation gives a critical velocity at which transition takes

place from the combined to pure membrane response

$$\frac{V_0}{c} = 2\mu\frac{h}{d}. \quad (7.40)$$

This critical velocity is actually the lower bound of the range of applicability of the present solution to the beam case since $N \leq N_0$. For $d = 2h$ and $\mu = 0.1$, the low bound impact velocity is about $V_0 = 50$ m/s for 2024-T351 aluminum alloy. This condition includes all the input variables. By contrast, Jones [133] and Yu & Stronge [128] gave, respectively, the constant critical deflection $w_0 = h/2$ and $w_0 = h$, at which the impact response of a beam changes from the combined action to the pure axial stretching.

At a very high impact velocity, indentation of the impacted zone and local through-thickness shearing becomes important and a beam would be perforated before entering into the phase of axial stretching. Such a problem is the subject of Chapter 7.5.

7.2.3 Round-nosed projectile

Besides the mass and impact velocity, the nose shape of the projectile also has an effect on the impact response of a target. The preceding theoretical analysis for the flat-nosed mass was recently extended by Wierzbicki and Teng [130] to the case with the round-nosed projectile.

In the flat-nosed case, the whole impacted zone immediately acquires the common velocity with the projectile and acts as a rigid body. By contrast, the impacted zone of the beam/string gradually wraps around the round-nosed projectile as the transverse momentum transfers from the projectile to the impacted zone, see Fig. 7-6. The transverse plastic stress waves are entrapped in the impacted zone in this wrapping phase. The reason behind it will be explained in the following.

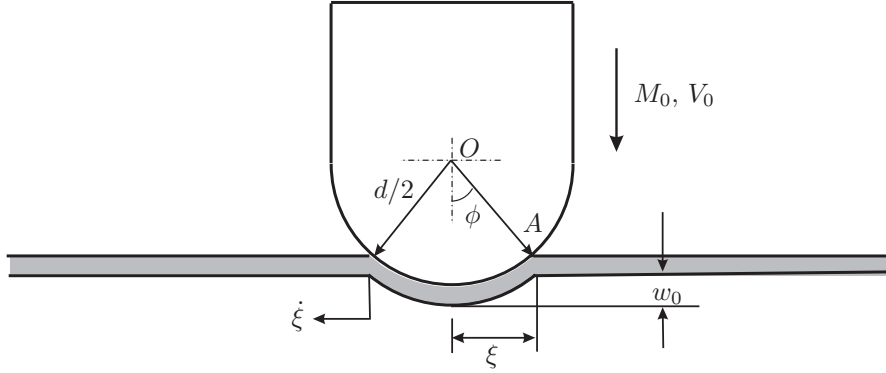


Fig. 7-6: Wrapping of the beam-string around the round nose of the projectile in the supersonic phase.

The axial coordinate ξ of the point A at which the beam loses contact with the projectile is given by

$$\xi = \frac{d}{2} \sin \phi, \quad (7.41)$$

where d is the diameter of the projectile, and ϕ is the contact angle. Differentiating ξ with respect to time gives the traveling velocity of the contact point A :

$$\dot{\xi} = \frac{d}{2} \cos \phi \dot{\phi}. \quad (7.42)$$

The transverse displacement w_0 of the projectile in the wrap-around zone is

$$w_0 = \frac{d}{2} (1 - \cos \phi). \quad (7.43)$$

Differentiating the above equation with respect to time t gives the velocity of the projectile in the wrapping phase

$$V = \frac{d}{2} \sin \phi \dot{\phi}. \quad (7.44)$$

Eliminating $\dot{\phi}$ between Eqs. (7.42) and (7.44) yields

$$\frac{\dot{\xi}}{V} = \frac{1}{\tan \phi}. \quad (7.45)$$

Initially $V(t=0) = V_0$ and $\phi = 0$, hence, $\dot{\xi} \rightarrow \infty$, which indicates the contact point A

travels at a “supersonic” velocity $\dot{\xi} > c$ in the initial phase. Hence, no information on deformation is able to propagate ahead of the contact point and the beam/string must wrap up around the lateral surface of the round nose.

As the velocity V of the projectile decreases and the contact angle ϕ increases, the traveling velocity $\dot{\xi}$ may decrease to the sonic value, i.e. $\dot{\xi} = c$. The entrapped transverse stress wave will escape from the impacted zone and propagate to far fields. Another possible situation is that the beam/string would break during the wrapping phase. As the impacted zone wraps around the projectile, the beam/string is stretched. The axial plastic strain at the contact point A is given by

$$\varepsilon = \sqrt{1 + \tan^2 \phi} - 1 \approx \frac{1}{2} \tan^2 \phi \quad x \leq \frac{d}{2} \sin \phi_1. \quad (7.46)$$

If the plastic tensile strain reaches the fracture strain of the beam/string $\bar{\varepsilon}_f$, the beam/string will be torn apart before the escape of the stress wave. This condition gives the critical contact angle ϕ_f

$$\phi_f = \tan^{-1} \sqrt{2\bar{\varepsilon}_f}. \quad (7.47)$$

The common velocity of the projectile and the wrapped zone can be determined using the principle of linear momentum conservation

$$\frac{V}{V_0} = \frac{M_0}{M_0 + 2m\xi} = \frac{1}{1 + \mu \sin \phi}. \quad (7.48)$$

The above solution is valid until the velocity $\dot{\xi}$ decreases to the sonic value c or the contact angle reaches the critical value for fracture ϕ_f , whichever takes place first, see Fig. 7-7. At a larger mass ratio μ , it is more likely that the stress wave would escape from the wrapped zone, i.e. Eq. (7.48) would intersect with the curve $V = c \tan \phi$ before fracture.

The wrapping phase terminates at $\dot{\xi} = c$. The corresponding wrapping angle ϕ_1 can be obtained by combining Eqs. (7.45) and (7.48), which is given by the following transcendental equation

$$c \tan \phi_1 = \frac{V_0}{1 + \mu \sin \phi_1}. \quad (7.49)$$

For small ϕ , $\tan \phi \approx \sin \phi \approx \phi$. The above equation becomes a quadratic equation in ϕ_1 ,

which has the solution

$$\phi_1 = \frac{-1 + \sqrt{1 + 4\mu V_0/c}}{2\mu}. \quad (7.50)$$

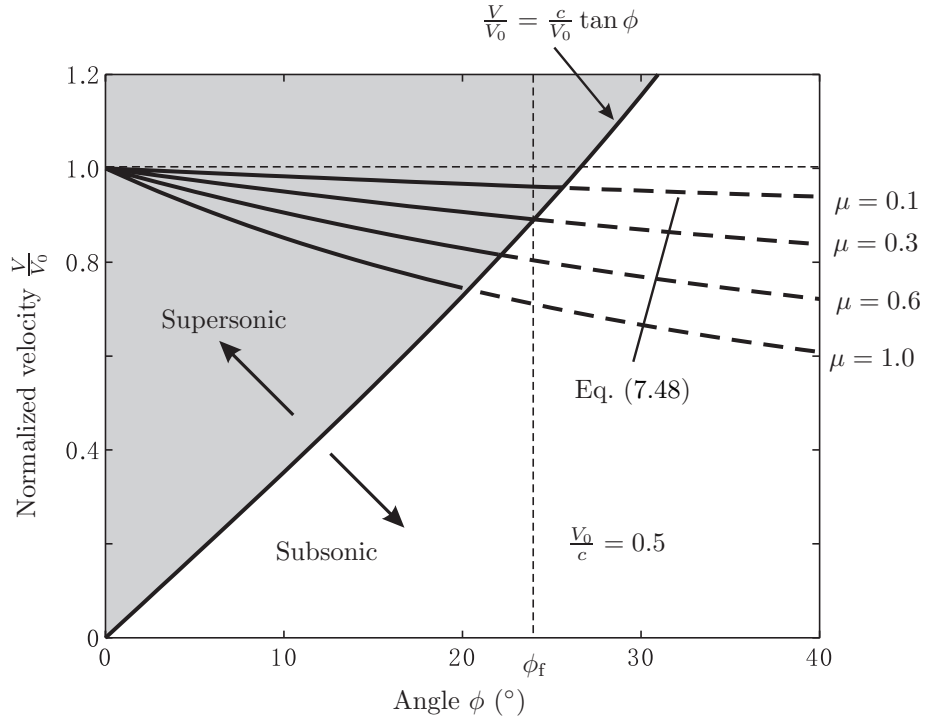


Fig. 7-7: Transient velocity of the projectile vs. contact angle in the supersonic phase. The solution represented by the shaded area is bounded by fracture angle or by the boundary with the subsonic region, whichever occurs first.

Combining Eqs. (7.44) and (7.48) gives

$$\frac{V_0}{1 + \mu \sin \phi} = \frac{d}{2} \sin \phi \frac{d\phi}{dt}. \quad (7.51)$$

Integration of the above equation from 0 to ϕ_1 give the duration of the supersonic phase t_1 .

$$\frac{V_0 t_1}{d} = \frac{1}{2} - \frac{1}{2} \cos \phi_1 + \frac{1}{4} \mu \phi_1 - \frac{1}{8} \mu \sin 2\phi_1 \approx \frac{1}{4} \phi_1^2. \quad (7.52)$$

In the next phase, the transverse stress wave will travel away from the wrapping zone to far fields with the constant speed c . Similarly to the case with the flat-nosed projectile,

the transverse velocity is uniformly distributed in the deformed region of the beam/string. The principle of momentum conservation gives the transient transverse velocity

$$\frac{V}{V_0} = \frac{M_0}{M_0 + md \sin \phi_1 + 2mc(t - t_1)} = \frac{1}{1 + \mu \sin \phi_1 + 2\mu(t - t_1)/d}. \quad (7.53)$$

The deformation of the beam-string at x is expressed as

$$w = \int_{\frac{x-d/2 \sin \phi_1}{c} + t_1}^t V dt. \quad (7.54)$$

Substituting the expression for V and integrating the above equation gives

$$\frac{w}{d} = \frac{1}{2\mu} \frac{V_0}{c} \ln \frac{1 + \mu \sin \phi_1 + 2\mu c(t - t_1)/d}{1 + 2\mu x/d}. \quad (7.55)$$

Similarly, the axial tensile strain is

$$\varepsilon = \frac{1}{2} \left(\frac{\partial w}{\partial x} \right)^2 = \frac{1}{2} \left(\frac{V_0}{c} \right)^2 \left(\frac{1}{1 + 2\mu x/d} \right)^2 \quad x \geq \frac{d}{2} \sin \phi_1. \quad (7.56)$$

Figure 7-8 shows the distribution of plastic tensile strain along the beam. It can be easily seen that the maximum tensile strain occurs at the point A , i.e. $x = d/2 \sin \phi_1$. The critical impact velocity to tear apart the beam/string is given by

$$\frac{V_{\text{cr}}}{c} = \sqrt{2\varepsilon_f} \left(1 + \mu \sqrt{\frac{2\varepsilon_f}{1 + 2\varepsilon_f}} \right). \quad (7.57)$$

By comparing Eqs. (7.23) with (7.57), we can clearly see that the critical velocity for the round-nosed projectile is smaller than that for the flat-nosed one. It is not consistent with experimental results by Børvik et al. [56] and numerical results presented in Chapter 3.2.5. The sharp corners of the flat-nosed projectile would induce stress concentration and make crack formation easier. It seems that only numerical methods would be able to take this local factor into account.

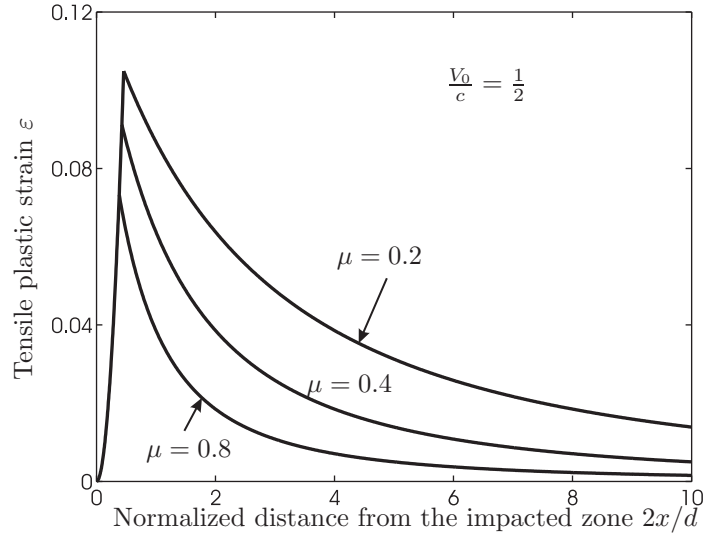


Fig. 7-8: Distribution of plastic tensile strain at various mass ratios.

7.2.4 Comparison with finite element solutions

Several simplifying assumptions were introduced in the development of the present closed-form solution. Since no experimental results are available currently in the literature, finite element solutions are developed here to verify the accuracy of the theoretical predictions.

Consider a 2024-T351 aluminum alloy plane-strain fixed-fixed beam of the length of $l = 1.0$ m and $h = 10$ mm impacted by a rigid, flat-nosed (round-nosed) projectile with the breadth (diameter) $d = 20$ mm. The mass and impact velocity of the mass were varied to investigate their effects on the impact response. Fifty elements (CPE4R) were used through the beam thickness. The JC's material constitutive model was defined and no fracture locus was assigned in the simulation.

Plots of transient transverse velocity are shown in Figs. 7-9 for the flat-nosed case with the impact velocity $V_0/c = 0.5$ and the mass ratio $\mu = 0.05$. In the theoretical analysis, only the plastic stress wave with the constant speed is considered corresponding to the simplified rigid-perfectly plastic material. By contrast, in the finite element calculation, elastic transverse stress waves are also generated preceding the plastic stress wave since the elastic-plastic, strain-hardening material model was used. The elastic stress waves, which travel at a much higher speed than the plastic waves, also carry transverse momentum. This

leads to the oscillation of the transverse velocity field ahead of the plastically deforming region. The finite element solutions predict the ear-like transient transverse velocity field at the later phase of the impact process, which is largely different from the uniform distribution assumed in the theoretical model. The reason behind it is not clear to the author.

Figure 7-10 shows the comparison of the time history of the displacement of the projectile in a wide range of the mass ratio. Figures 7-11 and 7-12 show the transient deflection profiles of the beam under impact by the flat-nosed and round-nosed projectiles, respectively. It can be concluded by comparison that the theoretical predictions have rather good agreements with the finite element solutions. The differences between them become large at the end of the impact process, probably due to effects of unloading stress waves or boundary conditions. These factors, neglected in the theoretical model, are taken into account in the finite element modeling.

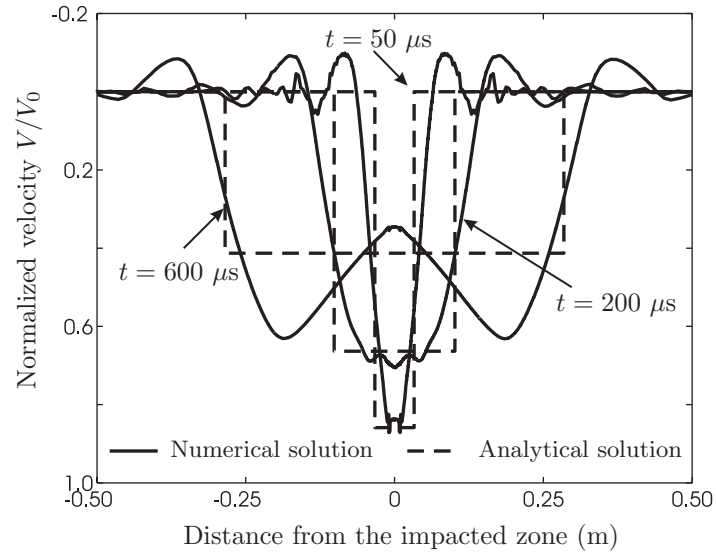


Fig. 7-9: Comparison of transient transverse velocity profiles of the beam impacted by the flat-nosed projectile with $\mu = 0.05$ and $V_0 = 229$ m/s.

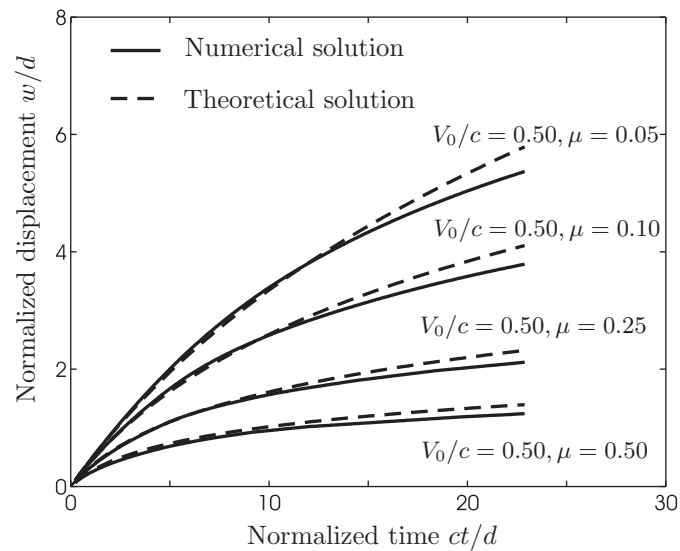


Fig. 7-10: Displacement of the flat-nosed rigid mass vs. time at various combination of the impact velocity and the mass ratio.

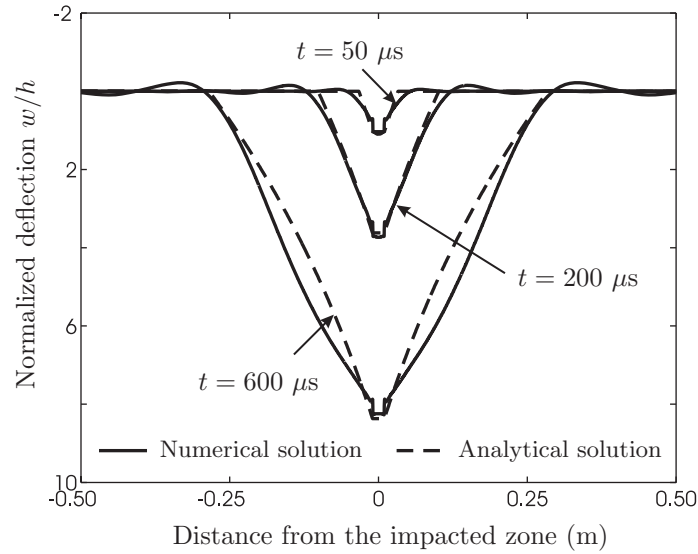


Fig. 7-11: Comparison of transient transverse deflection profiles of the beam impacted by the flat-nosed projectile with $\mu = 0.05$ and $V_0 = 229$ m/s.

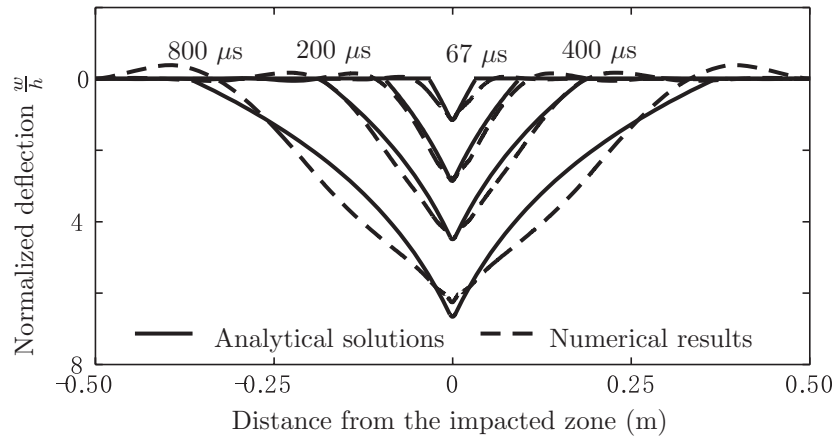


Fig. 7-12: Comparison of the transient deformation profiles of the 2024-T351 aluminum alloy beam impacted by the round-nosed projectile with $\mu = 0.1$ and $V_0 = 200$ m/s.

7.2.5 Discussions

In this section, a theoretical model of a long, plastic beam impacted by a rigid mass was developed. The closed-form solutions were obtained for the deflection, strain, and critical velocity of the target beam. Comparison with the finite element simulations were made showing good agreements. Without much difficulty, the present formulation can be extended to the axisymmetric case, e.g. cylindrical projectile impact on a circular plate.

Note, that the present formulation satisfies the condition of kinematic and dynamic continuity as well as global equilibrium, expressed via the principle of conservation of linear momentum and energy. However, local equilibrium may be violated. For example, the boundary condition at $x = d/2$, i.e. Eq. (7.8), becomes invalid in the later phase of the impact process. Eq. (7.8) states that the inertial force of the projectile is balanced by the vertical component of the plastic axial tensile force at the edge of the impacted zone. The inertial force of the projectile decreases with time while the plastic resistance is constant during the impact process. This discrepancy may lead to large difference between the closed-form solution and the finite element results.

Response of a real beam is always dominated by shearing and bending before entering into the phase of axial stretching. During this process, a large part of transverse momenta are transferred from the projectile to the target. However, these momenta are not taken into account in the present model. In a real beam, the tensile strain gradually increase with the deflection. In the present formulation, the struck beam/string immediately acquires the maximum plastic tensile strain at the edge of the impacted zone. Thus, the present formulation is able to predict the ballistic limit but not the residual velocity of the projectile.

Note, that the critical velocity predicted by the present model may be a little overestimated since only the contribution from axial stretching is considered. In actuality, damage also accumulates in the initial phase due to shearing and bending. At the same time, the sharp corners of the flat-nosed projectile would induce stress concentration and crack initiation. It is difficult to include these effects into an one-dimensional theoretical model and at the same time keeps its simplicity.

7.3 Single impact of beam-to-beam

7.3.1 Introduction

In the September 11th attack, the wings of the airplanes broke into numerous pieces while the exterior columns of the Twin Towers were either torn apart or cut through. This motivates us to develop a theoretical model of the single impact of beam-to-beam, in which the struck and striking beams represent the exterior column and the airplane wing, respectively. Compared with rigid mass-to-beam/plate impact, the coupling of the impact response of two deforming and fracturing bodies renders the problem more difficult and at the same time interesting. However, such a problem was little studied theoretically in the literature. Yu and his coworkers [137, 138] formulated the problem that a cantilever beam is impacted at its tip by a moving free-free beam. This theoretical model can be considered to be a combination of two basic models (i): a cantilever beam under rigid mass impact at its tip first formulated by Parkes [139] and (ii): a free-free beam loading at its mid-point by a pulse of force proposed by Lee and Symonds [140]. The same problem was also studied by Ruan et al. [141] using the modal approximate technique. Yang et al. [142, 143] extended the solutions to other impact configurations of a cantilever beam struck by a hinged beam and a clamped beam struck by a free-free beam, respectively. In all these theoretical models, attention was focused on plastic bending response and energy partitioning between two impacting beams, and fracture was not taken into account. Hence, these solutions obtained apply to the lower end of the spectrum of the impact velocity.

In contrast to the theoretical analyses presented in the literature, this section reports a closed-form solution of large plastic deformation and fracture response of two impacting beams. The impact velocity is assumed to be high enough so that the response of both beams is controlled by inertia force and wave propagation. The momentum conservation approach first formulated for rigid mass-to-beam impact is extended to the present case. Of interest is the determination of transient velocity and deflection profiles, maximum slopes, and the critical impact velocity to fracture.

7.3.2 Problem formulation

Consider a right angle impact of two plastic beams of rectangular, solid, cross-sections made of different materials. The width and thickness of two impacting beams are denoted respectively by $2b_i$ and h_i . Hereinafter, the subscript $i = 1$ denotes the struck beam and $i = 2$ the striking beam. The mechanical properties of two impacting beams are defined by the mass density ρ_i and the average plastic flow stress σ_i . From the above parameters, one can uniquely define the mass density per unit length of the beams $m_i = 2\rho_i b_i h_i$. The impact configuration is shown in Fig. 7-13, which also uniquely defines the coordinate system (x_1, x_2) . For convenience, the origin of the axial coordinate is defined at the edge of the impacted zone. Due to symmetry of the impact response about the impacted zone, the expressions for solution variables will be given only for the positive side of the axial coordinate in the following derivation.

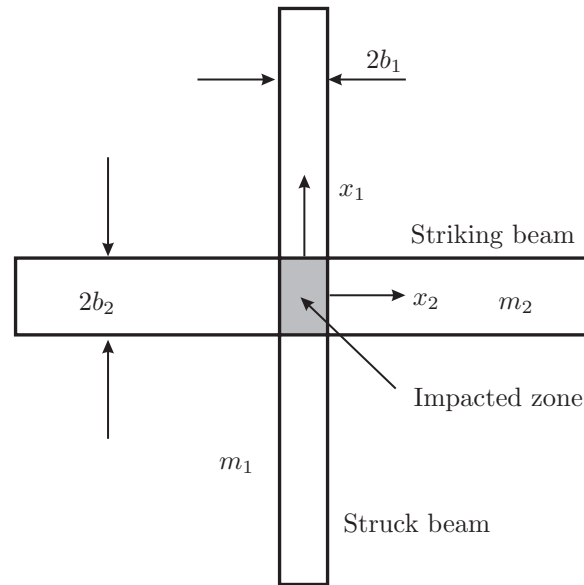


Fig. 7-13: Mechanical and geometrical parameters of the striking and struck beams.

The geometry of the beam is arbitrary provided that two inequalities are satisfied $b_1/h_2 \gg 1$ and $b_2/h_1 \gg 1$. Both inequalities ensure that the moderately large deflection theory of the beam with predominantly membrane action is valid. Otherwise the problem becomes three-dimensional and can only be treated by means of numerical methods.

Both beams undergo large plastic deformation such that axial stretching dominates over bending and local shearing. The problem is formulated by following the same procedure for rigid mass-to-beam impact given in the preceding section. In the absence of external forcing terms and bending moment, the force equilibrium equation of the beam/string in the transverse direction is

$$(N_i w_i')' = m_i \ddot{w}_i \quad i = 1, 2 \quad (7.58)$$

where w_i is the transverse deflection of the beam, and $N_i = 2\sigma_i b_i h_i$ is the axial tensile force. Eq. (7.58) can be reduced to the familiar wave equation for each of the beams.

$$c_i^2 w_i'' = \ddot{w}_i \quad (7.59)$$

where c_i is the transverse stress wave speed, defined by

$$c_i = \sqrt{\frac{N_i}{m_i}} = \sqrt{\frac{\sigma_i}{\rho_i}}. \quad (7.60)$$

Figure 7-14 shows the original and deformed configurations of both beams. Immediately upon impact, two shock waves are generated for each beam due to the discontinuity of the initial velocity field in the impacted zone. As the shock waves propagate along both sides of the beams, the initially stationary struck beam gradually acquires the transverse momentum while the velocity field of the striking beam becomes nonuniform. Both beams undergo plastic deformation. It is assumed that the material elements at the stress wave front acts as a plastic traveling extensional hinge, and all the plastic deformation concentrates at the wave front and keeps constant since then. Hence, the deformed region behind the wave fronts will be subjected to a rigid body motion. Note, that this assumption was initially introduced for the case of rigid mass-to-beam impact. From this assumption, we can qualitatively determine the transverse velocity field. A typical description of the transient velocity fields at a certain time for both beams is illustrated in Fig. 7-15. Physically, the central part of the struck beam translate with a uniform velocity and the remaining part of the struck beam ahead of the wave fronts is still at rest. The striking beam can also be divided into two parts moving at different velocities.

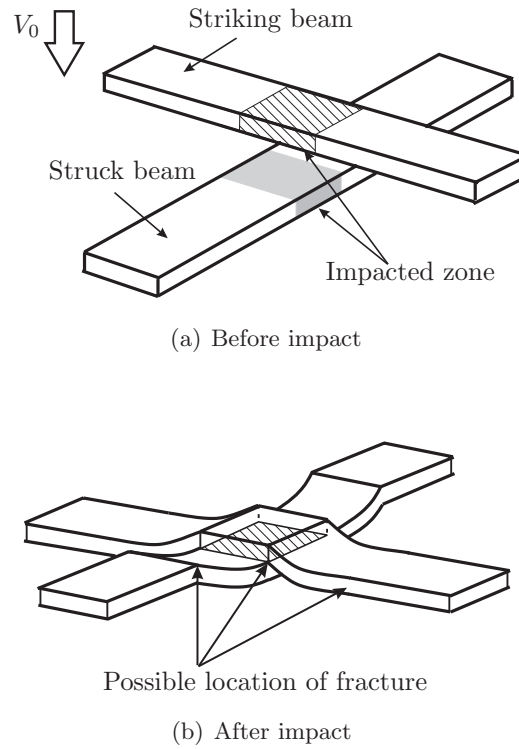


Fig. 7-14: Schematic representation of plastic deformation patterns of both beams.

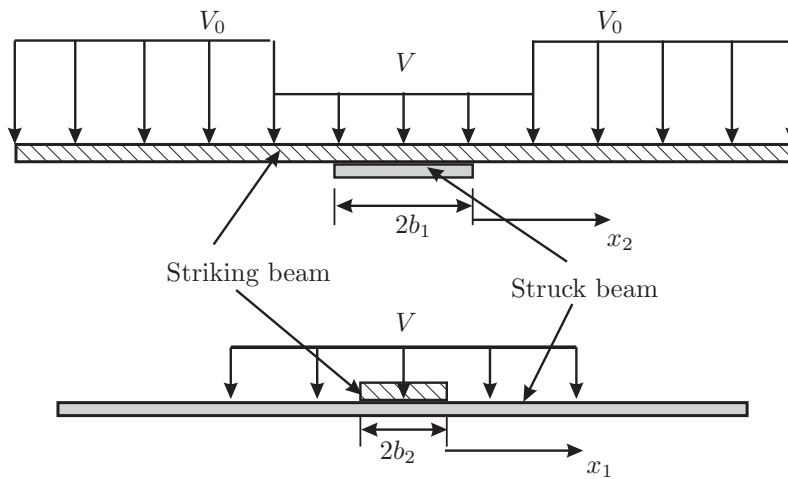


Fig. 7-15: Transient velocity profiles for both beams at a certain time after impact.

The force equilibrium for the impacted zone prescribes one boundary condition of the beams at $x_i = 0$, see free body diagrams illustrated in Fig. 7-16,

$$\begin{cases} 2N_1w'_1 = -P + 2m_1b_2\ddot{w}_1 & \text{at } x_1 = 0 \\ 2N_2w'_2 = +P + 2m_2b_1\ddot{w}_2 & \text{at } x_2 = 0 \end{cases} \quad (7.61)$$

where P is the interaction force between the beams. Another boundary condition is located at the wave front, i.e. $w_i(\xi_i, t) = 0$ at $\xi_i = c_it$.

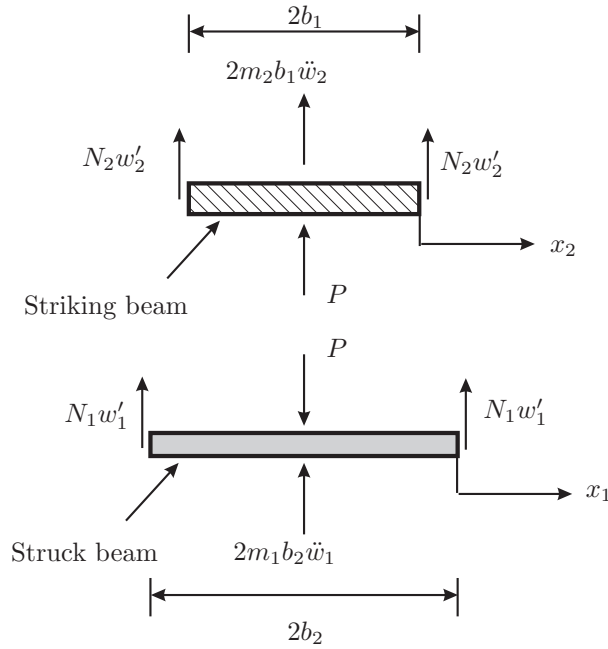


Fig. 7-16: Free body diagram for the impacted zone.

The problem is also subject to the following initial conditions:

$$\begin{cases} w_i(x_i, 0) = 0 \\ \dot{w}_1(x_1, 0^-) = 0 \\ \dot{w}_2(x_2, 0^-) = V_0 \end{cases} \quad (7.62)$$

It is assumed that the striking beam maintains contact with the struck beam during the whole impact process. So, both the striking and struck beams have a common displacement,

velocity and acceleration at the impacted zone,

$$w_1 = w_2, \quad \dot{w}_1 = \dot{w}_2, \quad \ddot{w}_1 = \ddot{w}_2. \quad (7.63)$$

Further, since the transverse velocity is uniform in the deformed region for both beams, it can be inferred that both the striking and struck beams have a common velocity not only at the impacted zone but also in the deformed region, see Fig. 7-15.

The solutions have to satisfy both kinematic and dynamic continuity conditions at the moving boundary, $\xi_i = c_i t$, which require, respectively,

$$\dot{w}_i] + c_i w_i'] = 0 \quad \text{at} \quad x_i = c_i t. \quad (7.64)$$

and

$$N_i w_i'] + m_i c_i \dot{w}_i] = 0 \quad \text{at} \quad x_i = c_i t, \quad (7.65)$$

where the velocity jump at the wave front of the struck beam is

$$\dot{w}_1] = \dot{w}_1|_{\xi_1^+} - \dot{w}_1|_{\xi_1^-} = 0 - \dot{w}_1, \quad (7.66)$$

and the velocity jump at the wave front for the striking beam is

$$\dot{w}_2] = \dot{w}_2|_{\xi_2^+} - \dot{w}_2|_{\xi_2^-} = V_0 - \dot{w}_2. \quad (7.67)$$

Considering that the transverse velocity and acceleration of the deformed regions are constant in space and vary in time, integration of Eq. (7.58) with respect to x from $x_i = 0$ to $\xi_i = c_i t$ yields

$$N_i w_i']_{x_i=0}^{\xi_i=c_i t} = m_i \ddot{w}_i c_i t. \quad (7.68)$$

Substituting the boundary conditions at $x_i = 0$ and the dynamic continuity conditions at $\xi_i = c_i t$, one obtains, for the struck beam,

$$-m_1 c_1 \dot{w}_1 + \frac{P}{2} - m_1 b_2 \ddot{w}_1 = m_1 \dot{w}_1 c_1 t, \quad (7.69)$$

and for the striking beam,

$$m_2 c_2 (V_0 - \dot{w}_2) - \frac{P}{2} - m_2 b_1 \ddot{w}_2 = m_2 \ddot{w}_2 c_2 t. \quad (7.70)$$

Eliminating the interaction force P between Eqs. (7.69) and (7.70), the governing equation becomes

$$m_1 (b_2 + c_1 t) \ddot{w}_1 + m_2 (b_1 + c_2 t) \ddot{w}_2 + m_1 c_1 \dot{w}_1 + m_2 c_2 \dot{w}_2 - m_2 c_2 V_0 = 0. \quad (7.71)$$

Using the contact condition, Eq. (7.63), the governing equation is further reduced to

$$(m_1 b_2 + m_1 c_1 t + m_2 b_1 + m_2 c_2 t) \dot{V} + (m_1 c_1 + m_2 c_2) V = m_2 c_2 V_0, \quad (7.72)$$

where $\dot{V} = \ddot{w}_1 = \ddot{w}_2$ and $V = \dot{w}_1 = \dot{w}_2$. The above equation furnishes an initial value problem for the common velocity V . The initial value of the common velocity V_0^* is determined from the conservation of transverse momentum in the impacted zone immediately upon impact:

$$V_0^* = \frac{m_2 b_1}{m_1 b_2 + m_2 b_1} V_0 \quad \text{at} \quad t = 0. \quad (7.73)$$

The equation of motion can also be derived using the principle of linear momentum conservation:

$$2m_2 (b_1 + c_2 t) (V_0 - V) = 2m_1 (b_2 + c_1 t) V \quad (7.74)$$

where the term in the left hand side represents the loss of the momentum of the striking beam, and the term in the right hand side represents the gain of the momentum of the struck beam. Differentiating the above equation with respect to time t , one can obtain the same equation as (7.72). The latter approach is strikingly simple and thus will be used in the analysis of multiple impact of beam-to-beam.

7.3.3 Solutions for velocity and deformation

Eq. (7.74) gives the transverse velocity of the deformed region as a function of time t

$$\frac{V}{V_0} = \frac{1}{1 + \frac{m_1}{m_2} \left(\frac{b_2 + c_1 t}{b_1 + c_2 t} \right)}. \quad (7.75)$$

Introducing a mass parameter α , a velocity parameter β and a time parameter τ , it is convenient to re-arrange the solution in the dimensionless form

$$\frac{V}{V_0} = \beta + \frac{\alpha - \beta}{1 + t/\tau}. \quad (7.76)$$

where

$$\left\{ \begin{array}{l} \alpha = \frac{m_2 b_1}{m_1 b_2 + m_2 b_1}, \quad 0 < \alpha < 1 \\ \beta = \frac{m_2 c_2}{m_1 c_1 + m_2 c_2}, \quad 0 < \beta < 1 \\ \tau = \frac{m_1 b_2 + m_2 b_1}{m_1 c_1 + m_2 c_2} \end{array} \right. . \quad (7.77)$$

The mass parameter α represents the mass ratio of both beams in the impacted zone, and the velocity parameter β can be understood as the wave speed ratio weighted by the mass per unit length of the beams. The second term in the right hand side of Eq. (7.76) can be either negative or positive, depending on the relative values between α and β . In terms of the mass parameter α , Eq. (7.73) can be rewritten in a simpler form

$$V_0^* = \alpha V_0. \quad (7.78)$$

Depending on the relative value of α and β , three types of the velocity history of the velocity may develop, see Fig. 7-17. It appears that for $\alpha > \beta$ ($b_1 c_1 > b_2 c_2$) the common velocity V acquires the maximum value immediately upon impact, then gradually decreases, while for $\alpha < \beta$, the common velocity V eventually increases with time. Both cases approach an asymptote β as $t \rightarrow \infty$. The third case with $\alpha = \beta$ ($b_1 c_1 = b_2 c_2$) is also interesting because the common velocity is constant not only in space but also in time. Note, that the transverse velocity always decreases with time in rigid mass impact.

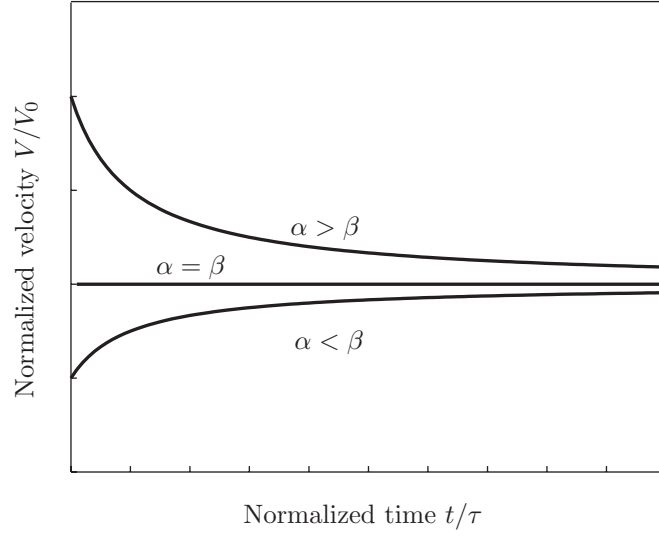


Fig. 7-17: Time history of the transverse velocity in the deformed region at various relative values of α and β .

For the struck beam, a point located at a distance x_1 starts to deform only after time $t = x_1/c_1$. The transverse deflection w_1 of the struck beam is given by

$$w_1 = \int_{x_1/c_1}^t V dt. \quad (7.79)$$

Substituting the expression for V , one obtains the deflection of the struck beam

$$\frac{w_1}{V_0\tau} = \beta \left(\frac{t}{\tau} - \frac{x_1}{\tau c_1} \right) + (\alpha - \beta) \ln \frac{1 + t/\tau}{1 + x_1/(\tau c_1)}. \quad (7.80)$$

For the striking beam, a point located at a distance x_2 from the impacted zone moves with the initial velocity V_0 before the wave front arrives at $t = x_2/c_2$. Thus, the transverse deformation of the striking beam w_2 is defined by

$$w_2 = \int_0^{x_2/c_2} V_0 dt + \int_{x_2/c_2}^t V dt. \quad (7.81)$$

Integrating the above equation yields the transverse deformation of the striking beam

$$\frac{w_2}{V_0\tau} = \frac{x_2}{\tau c_2} + \beta \left(\frac{t}{\tau} - \frac{x_2}{\tau c_2} \right) + (\alpha - \beta) \ln \frac{1 + t/\tau}{1 + x_2/(\tau c_2)}. \quad (7.82)$$

The first term in the right hand side of the above equation represents the rigid body translation of the beam before the wave front arrives, which is different from the expression for the deflection of the struck beam. The deflection w_0 in the impacted zone, which is the same for the striking and struck beams, is determined by setting $x_1 = 0$ in Eq. (7.80) or $x_2 = 0$ in Eq. (7.82):

$$\frac{w_0}{V_0\tau} = \beta\frac{t}{\tau} + (\alpha - \beta)\ln\left(1 + \frac{t}{\tau}\right). \quad (7.83)$$

Plots of transient deflection profiles of the struck beam for three different relative values of α and β are shown in Fig. 7-18. When $\alpha = \beta$, the logarithmic term in Eq. (7.80) disappears, and only the linear term is left. Correspondingly, the deflection profile of the beam is a straight line. When $\alpha > \beta$, the logarithmic term is always positive and contributes to the deflection magnitude of the beam, and vice versa. This logarithmic term also has an effect on the slope of the beam, which will be shown later on. Similarly, there are three types of deflection profiles for the striking beam, see Fig. 7-19. As opposed to the struck beam, the part in front of the wave front moves like a rigid body with the velocity V_0 .

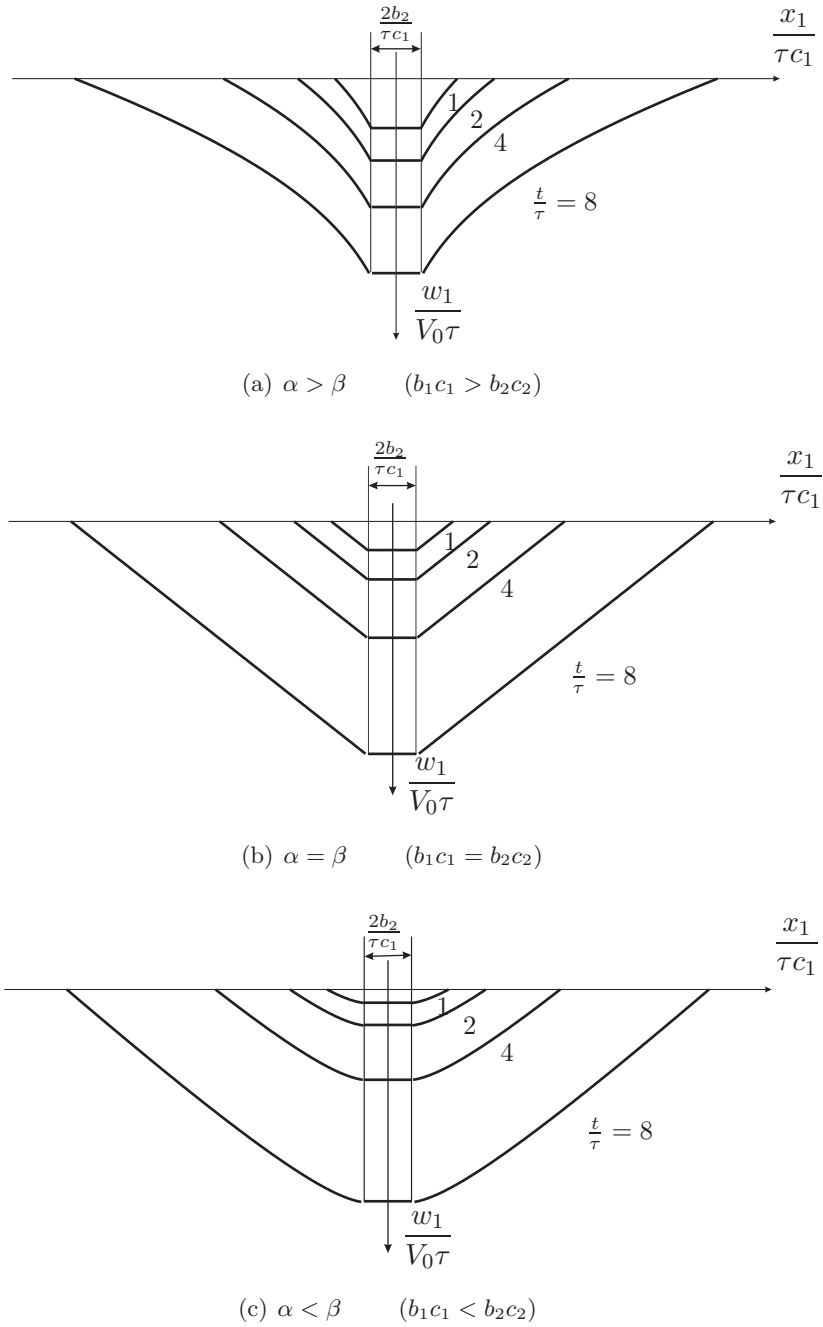


Fig. 7-18: Transient deflection profiles of the struck beam for various values of α and β .

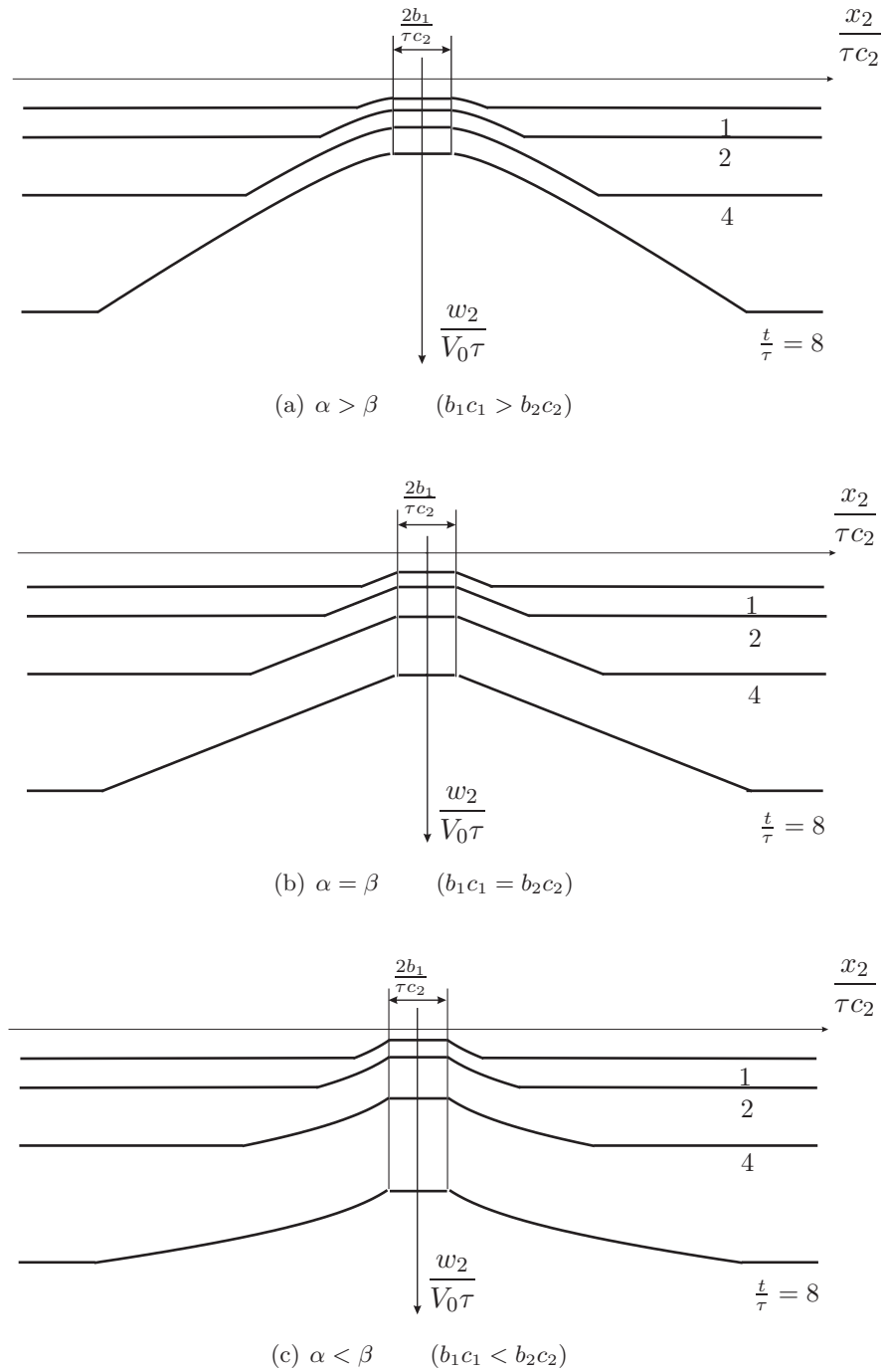


Fig. 7-19: Transient deflection profiles of the striking beam for various values of α and β .

7.3.4 Tensile strains and critical velocity to fracture

The failure mechanism and failure mode are complicated in the case of beam-to-beam impact. As demonstrated by preliminary numerical investigations, either of the beams may fail by shear plugging or tensile necking during the impact process, depending on various combinations of input variables. Here, it is assumed that both beams will fail due to tensile necking. This assumption restricts the applicability of the following solutions, but still a class of beams satisfying the solutions is very broad.

Under moderately large deformation, the plastic tensile strain is given by, respectively, for the struck and striking beams

$$\begin{cases} \varepsilon_1 &= \frac{1}{2} \left(\frac{V_0}{c_1} \right)^2 \left[\beta + (\alpha - \beta) \frac{1}{1 + x_1/(\tau c_1)} \right]^2 \\ \varepsilon_2 &= \frac{1}{2} \left(\frac{V_0}{c_2} \right)^2 \left[(1 - \beta) - (\alpha - \beta) \frac{1}{1 + x_2/(\tau c_2)} \right]^2 \end{cases} \quad (7.84)$$

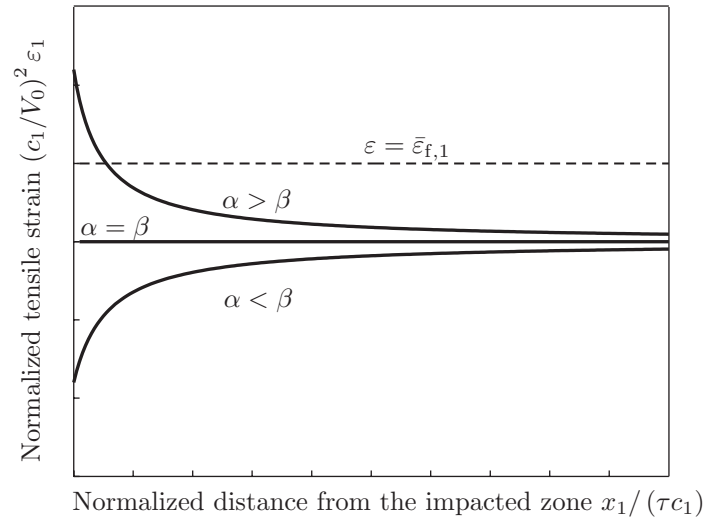
Corresponding to the deformation profiles, the plastic tensile strains also have three types of distribution along each beam, see Fig. 7-20. It transpires that for the struck beam, the maximum tensile strain occurs at $x_1 = 0$ at $\alpha > \beta$, while it occurs somewhere far from the impacted zone at $\alpha < \beta$. Different from the response of the struck beam, the plastic tensile strain in the striking beam gradually increases at $\alpha > \beta$. All the curves approach an asymptote for large x_i , which corresponds to the limiting case $\alpha = \beta$. As shown earlier on, the deflection profile is the straight line at $\alpha = \beta$, which indicates that the tensile strain is the same everywhere in the deformed region. Note, that in rigid mass impact, the maximum tensile strain always occurs at the edge of the impacted zone and thus the beam always fails at the impacted zone. By contrast, in beam-to-beam impact it is possible that the beams would break somewhere far from the impacted zone. Or say, the fracture is delayed.

Setting the maximum tensile strain equal to the fracture strain $\bar{\varepsilon}_{f,i}$, we obtain the critical impact velocities, for the struck beam,

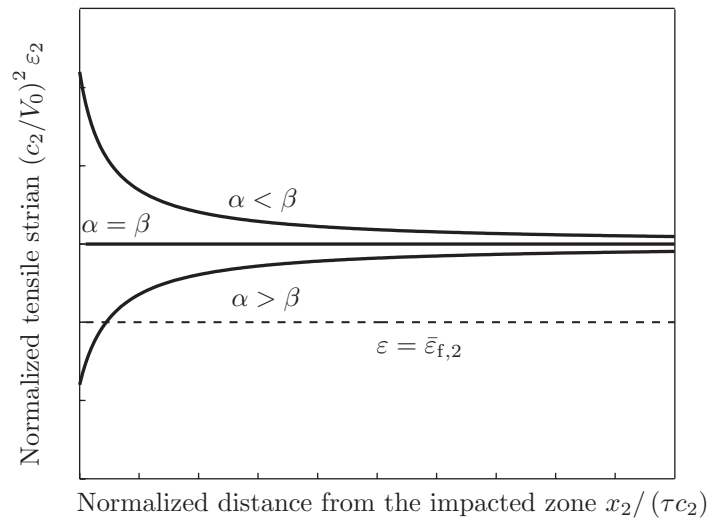
$$\frac{V_{cr,1}}{c_1 \sqrt{2\bar{\varepsilon}_{f,1}}} = \min \left\{ \frac{1}{\alpha}, \frac{1}{\beta} \right\}, \quad (7.85)$$

and for the striking beam,

$$\frac{V_{cr,2}}{c_2 \sqrt{2\bar{\epsilon}_{f,2}}} = \min \left\{ \frac{1}{1-\alpha}, \frac{1}{1-\beta} \right\}. \quad (7.86)$$



(a) Struck beam



(b) Striking beam

Fig. 7-20: Plastic tensile strain variation along the beams for various values of α and β .

7.3.5 Location and time of fracture

At an impact velocity higher than the critical velocity, both/either of the beams will break. The fracture location and the fracture time can be determined by setting the maximum tensile strain equal to the fracture strain in Eq. (7.84). Since the response of both beams depends on the relative values of α and β , it is convenient to separately solve the problem for two cases with $\alpha > \beta$ and $\alpha < \beta$.

7.3.5.1 The struck beam at $\alpha > \beta$

As shown in Fig. 7-21, the tensile strain gradually decreases from the impacted zone to far fields at $\alpha > \beta$. Hence, the struck beam will fracture at $x_1 = 0$ immediately upon impact ($t = 0$), if the impact velocity V_0 is larger than the critical velocity $V_{cr,1}$ given in Eq. (7.85).

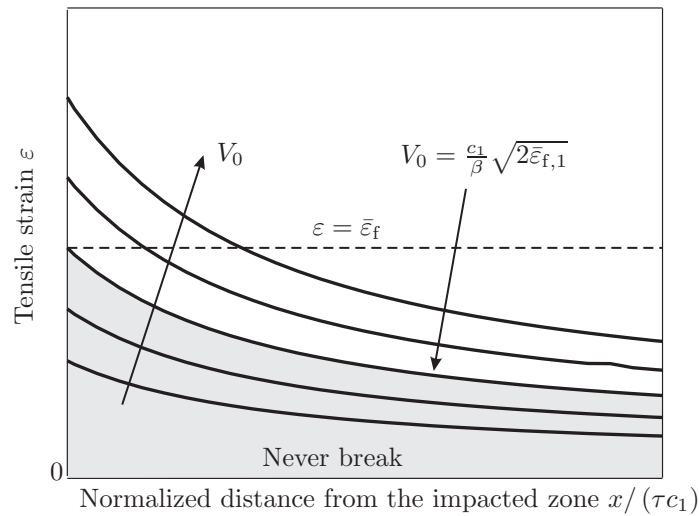


Fig. 7-21: Tensile strains versus distance for the struck beam with $\alpha > \beta$ under various impact velocities.

7.3.5.2 The struck beam at $\alpha < \beta$

At $\alpha < \beta$, the tensile strain of the struck beam gradually increases from the impacted zone, see Fig. 7-22. It is possible that the struck beam will break somewhere away from the

impacted zone in this case. If the impact velocity is in the range of

$$V_{cr,1} = \frac{c_1}{\beta} \sqrt{2\bar{\epsilon}_{f,1}} < V_0 < \frac{c_1}{\alpha} \sqrt{2\bar{\epsilon}_{f,1}} \quad (\alpha < \beta), \quad (7.87)$$

the fracture location and time are given by

$$\frac{x_{cr,1}}{\tau c_1} = \frac{t_{cr,1}}{\tau} = \frac{\sqrt{2\bar{\epsilon}_{f,1}} - \alpha V_0 / c_1}{\beta V_0 / c_1 - \sqrt{2\bar{\epsilon}_{f,1}}}. \quad (7.88)$$

The above expression is derived from Eq. (7.84) by setting $\epsilon_1 = \bar{\epsilon}_{f,1}$ to solve x_1 . As the impact velocity V_0 increases, the fracture location will approach the impacted zone. If

$$V_0 > \frac{c_1}{\alpha} \sqrt{2\bar{\epsilon}_{f,1}}, \quad (7.89)$$

the struck beam would fail in the impacted zone immediately upon impact.

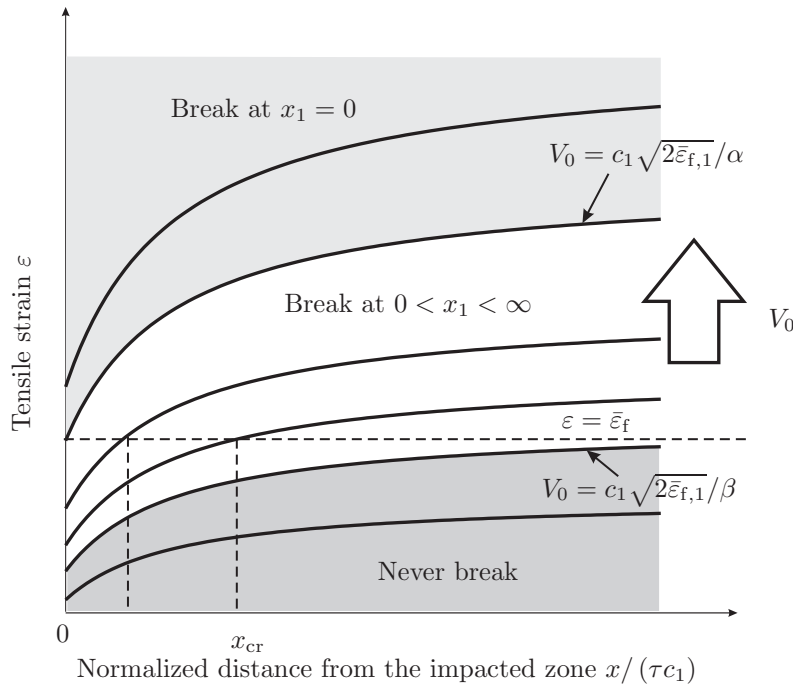


Fig. 7-22: Fracture location for the struck beam with $\alpha < \beta$.

The plastic tensile strains as a function of the distance from the impacted zone at various

impact velocities are shown in Fig. 7-22. The lower shaded area indicates that the fracture will never happen, if the impact velocity is lower than the critical velocity. The middle blank area indicates that the fracture location moves from far field to the impacted zone as the impact velocity increases from $V_0 = c_1\sqrt{2\bar{\varepsilon}_{f,1}}/\beta$ to $V_0 = c_1\sqrt{2\bar{\varepsilon}_{f,1}}/\alpha$.

7.3.5.3 The striking beam at $\alpha > \beta$

If $\alpha > \beta$, the tensile strain of the striking beam increases with the distance from the impacted zone, see Fig. 7-20, which is similar to the case of the struck beam with $\alpha < \beta$. The fracture location and time are given by

$$\frac{x_{cr,2}}{\tau c_2} = \frac{t_{cr,2}}{\tau} = \frac{\sqrt{2\bar{\varepsilon}_{f,2}} - (1 - \alpha) V_0/c_2}{(1 - \beta) V_0/c_2 - \sqrt{2\bar{\varepsilon}_{f,2}}} \quad (7.90)$$

for the impact velocity in the range

$$V_{cr,2} = \frac{c_2}{1 - \beta} \sqrt{2\bar{\varepsilon}_{f,2}} < V_0 < \frac{c_2}{1 - \alpha} \sqrt{2\bar{\varepsilon}_{f,2}} \quad (\alpha > \beta). \quad (7.91)$$

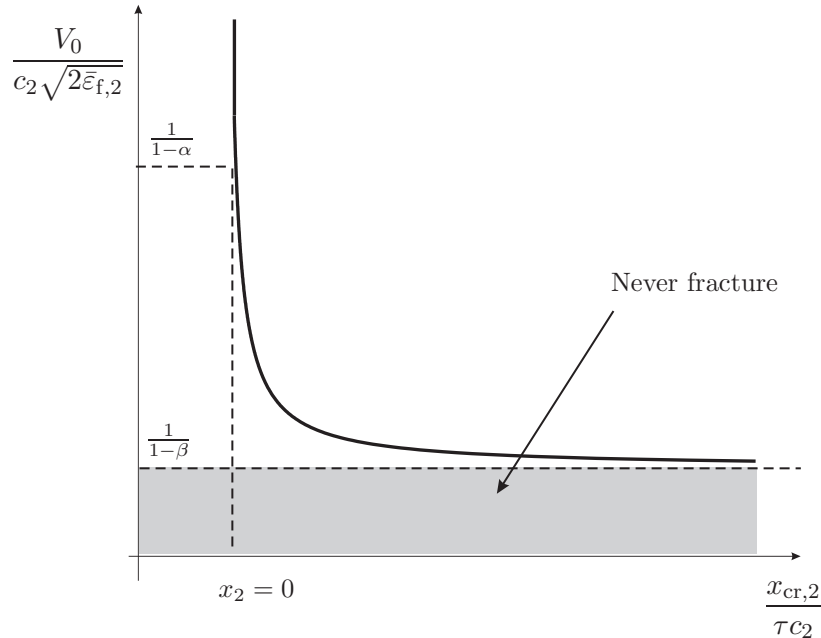


Fig. 7-23: Fracture location as a function of the impact velocity for the striking beam at $\alpha < \beta$.

Similarly, the striking beam will break in the impacted zone immediately upon impact at $\alpha > \beta$, if it is satisfied that

$$V_0 > \frac{c_2}{1 - \alpha} \sqrt{2\bar{\varepsilon}_{f,2}}. \quad (7.92)$$

An alternative way of looking at the relation between the fracture location and the impact velocity is shown in Fig. 7-23.

7.3.5.4 The striking beam at $\alpha < \beta$

At $\alpha < \beta$, the maximum tensile strain is located at $x_2 = 0$. Therefore, the striking beam will always fracture in the impacted zone immediately upon impact, if $V_0 > V_{cr,2}$. This case is similar to that of the struck beam with $\alpha > \beta$.

7.3.6 Fracture scenarios

In rigid mass-to-beam impact, there is only one possible fracture scenario. The target beam breaks in the impacted zone or keeps intact. By contrast, there are five possible fracture scenarios in the single impact event of beam-to-beam, which are summarized in the following.

7.3.6.1 Case 1: Both beams fracture immediately upon impact

From Eq. (7.84), the plastic tensile strains of both beams at $t = 0$ are

$$\begin{cases} \varepsilon_1|_{t=0} = \frac{1}{2}\alpha^2 \left(\frac{V_0}{c_1}\right)^2 \\ \varepsilon_2|_{t=0} = \frac{1}{2}(1 - \alpha)^2 \left(\frac{V_0}{c_2}\right)^2 \end{cases}. \quad (7.93)$$

If both the struck and striking beams break in the impacted zone immediately upon impact, the generated plastic tensile strains must be larger than their respective critical values $\bar{\varepsilon}_{f,i}$.

In other words, the impact velocity V_0 must be given by

$$V_0 > \max \left\{ \frac{c_1 \sqrt{2\bar{\varepsilon}_{f,1}}}{\alpha}, \frac{c_2 \sqrt{2\bar{\varepsilon}_{f,2}}}{1 - \alpha} \right\}. \quad (7.94)$$

7.3.6.2 Case 2: The striking beam breaks at $t = 0$; and the struck beam keeps intact

In this case, the strain of the struck beam at $x_1 = 0$, $\varepsilon_1|_{t=0}$, must be smaller than $\bar{\varepsilon}_{f,1}$; and the strain of the striking beam at $x_2 = 0$, $\varepsilon_2|_{t=0}$, must be larger than $\bar{\varepsilon}_{f,2}$. The corresponding range of the impact velocity V_0 is given by

$$\frac{c_2\sqrt{2\bar{\varepsilon}_{f,2}}}{1-\alpha} < V_0 < \frac{c_1\sqrt{2\bar{\varepsilon}_{f,1}}}{\alpha}. \quad (7.95)$$

It can be observed from the above equation that there is an implicit, necessary condition:

$$\frac{c_2\sqrt{2\bar{\varepsilon}_{f,2}}}{1-\alpha} < \frac{c_1\sqrt{2\bar{\varepsilon}_{f,1}}}{\alpha}. \quad (7.96)$$

Hence, if the above condition is not satisfied, this fracture scenario will never happen.

7.3.6.3 Case 3: The struck beam breaks at $t = 0$; and the striking beam keeps intact

Similarly, for this case, the range of the impact velocity is given by

$$\frac{c_1\sqrt{2\bar{\varepsilon}_{f,1}}}{\alpha} < V_0 < \frac{c_2\sqrt{2\bar{\varepsilon}_{f,2}}}{1-\alpha}. \quad (7.97)$$

The implicit, necessary condition is given by

$$\frac{c_1\sqrt{2\bar{\varepsilon}_{f,1}}}{\alpha} < \frac{c_2\sqrt{2\bar{\varepsilon}_{f,2}}}{1-\alpha}. \quad (7.98)$$

7.3.6.4 Case 4: The striking beam breaks after some time; and the struck beam keeps intact

The striking beam will break after some time, which means that the tensile strain in the striking beam gradually increases with time and distance from the impacted zone. As shown in Fig. 7-20(b), this corresponds to the case $\alpha > \beta$, at which the range of the impact velocity has been already given in Eq. (7.91). The struck beam will keep intact. Hence, the strain of the struck beam at $x_1 = 0$, $\varepsilon_1|_{t=0}$, must be smaller than $\bar{\varepsilon}_{f,1}$. Combining these conditions

give the range of the impact velocity for Case 4

$$\frac{c_2\sqrt{2\bar{\epsilon}_{f,2}}}{1-\beta} < V_0 < \min\left\{\frac{c_1\sqrt{2\bar{\epsilon}_{f,1}}}{\alpha}, \frac{c_2\sqrt{2\bar{\epsilon}_{f,2}}}{1-\alpha}\right\} \quad (\alpha > \beta). \quad (7.99)$$

7.3.6.5 Case 5: The struck beam breaks after some time; and the striking beam keeps intact

Similarly, we can obtain the condition for Case 5,

$$\frac{c_1\sqrt{2\bar{\epsilon}_{f,1}}}{\beta} < V_0 < \min\left\{\frac{c_1\sqrt{2\bar{\epsilon}_{f,1}}}{\alpha}, \frac{c_2\sqrt{2\bar{\epsilon}_{f,2}}}{1-\alpha}\right\} \quad (\alpha < \beta). \quad (7.100)$$

The five cases discussed above are illustrated in Fig. 7-24.

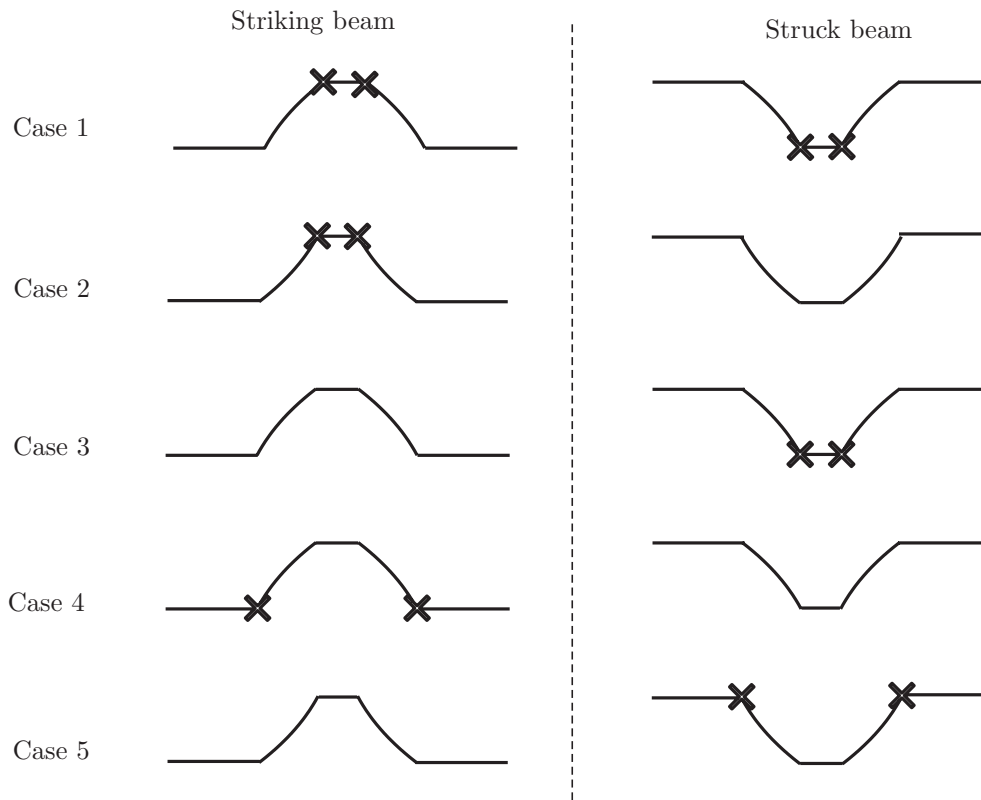


Fig. 7-24: Five fracture scenarios (The symbol \times denotes fracture location).

7.3.7 Deflection after fracture

If one beam breaks, the other intact beam will continue to deform as the stress waves continue to propagate down the beam to far fields. Although the deformation of the beam continuously increases, the beam will never fracture, which is shown next. Considering that there are five possible fracture scenarios, we will take only two typical cases as examples.

First, consider the case that the striking beam breaks immediately upon impact and the struck beam keeps intact, where the range of the impact velocity is given in Eq. (7.95). The acquired momentum of the struck beam is conserved after impact

$$2m_1b_2V_0^* = m_1(2b_2 + 2c_1t)V. \quad (7.101)$$

So the velocity V at a certain time t is given by

$$\frac{V}{V_0} = \frac{\alpha}{1 + c_1t/b_2} = \frac{\alpha(1 - \alpha)}{(1 - \alpha) + (1 - \beta)t/\tau}. \quad (7.102)$$

Substituting the expression for V into Eq. (7.79), one obtains the deflection w_1 of the struck beam

$$\frac{w_1}{V_0\tau} = \frac{\alpha b_2}{c_1\tau} \ln \frac{b_2 + c_1t}{b_2 + x_1} = \frac{\alpha(1 - \alpha)}{1 - \beta} \ln \frac{(1 - \alpha) + (1 - \beta)t/\tau}{(1 - \alpha) + (1 - \beta)x_1/(\tau c_1)}. \quad (7.103)$$

Plots of deflection profiles of the struck beam are shown in Fig. 7-25. It appears that the deflection of the struck beam in the case of the striking beam with fracture is always smaller than that without fracture.

From the deformation shape given in Eq. (7.103), one can calculate the tensile strain in the struck beam

$$\varepsilon_1 = \frac{1}{2}\alpha^2 \left(\frac{V_0}{c_1}\right)^2 \left(\frac{b_2}{b_2 + x_1}\right)^2. \quad (7.104)$$

It can be observed that the tensile strain reaches the maximum value at $x_1 = 0$ ($t = 0$), then gradually decreases. Hence, if the struck beam does not break immediately upon impact, the beam will never break for this case.

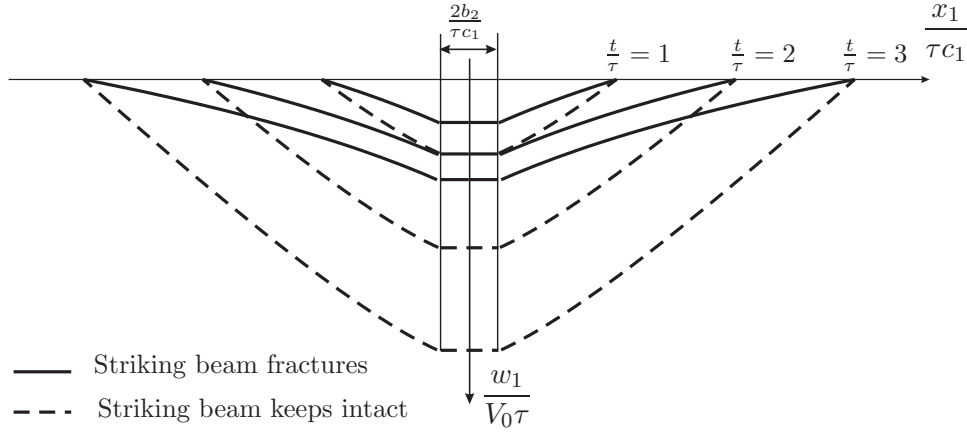


Fig. 7-25: Plots of deflection profiles of the struck beam after fracture of the striking beam.

Consider another case that the struck beam breaks immediately upon impact and the striking beam keeps intact. The corresponding impact condition is given in Eq. (7.97). The deflection of the striking beam can be calculated in a similar procedure shown above. The conservation of momentum for the striking beam after impact is expressed as

$$2m_2b_1V_0^* + 2m_2c_2tV_0 = 2m_2(b_1 + c_2t)V. \quad (7.105)$$

where the second term in the left hand side represents the initial momentum of the striking beam before the arrival of the wave front. From the above equation, one gets the velocity

$$\frac{V}{V_0} = \frac{\alpha + c_2t/b_1}{1 + c_2t/b_1} = \frac{\alpha^2 + \beta t/\tau}{\alpha + \beta t/\tau}. \quad (7.106)$$

It can be seen that the velocity V in the deformed part gradually increases due to the momentum transfer from the part moving with the initial impact velocity V_0 . Substituting the expression for the velocity into Eq. (7.79), one arrives at the deflection of the striking beam

$$\frac{w_2}{V_0\tau} = \frac{t}{\tau} - (1 - \alpha) \frac{\alpha}{\beta} \ln \frac{\alpha + \beta t/\tau}{\alpha + \beta x_2/(\tau c_2)}. \quad (7.107)$$

The plastic tensile strain of this striking beam is given by

$$\varepsilon_2 = \frac{1}{2} (1 - \alpha)^2 \left(\frac{V_0}{c_2} \right)^2 \left(\frac{b_1}{b_1 + x_2} \right)^2 = \frac{1}{2} (1 - \alpha)^2 \left(1 + \frac{\beta x_2}{\alpha \tau c_2} \right)^{-2}. \quad (7.108)$$

Similarly to the above case, the tensile strain reaches the maximum value at $x_2 = 0$, or say immediately upon impact $t = 0$, and then decreases with the distance from the impacted zone. It is seen from Fig. 7-26 that the tensile strain in the case of the struck beam with fracture is always larger than that without fracture. Hence, the same conclusion can be drawn for this case that the beam will never break, after the other beam breaks.

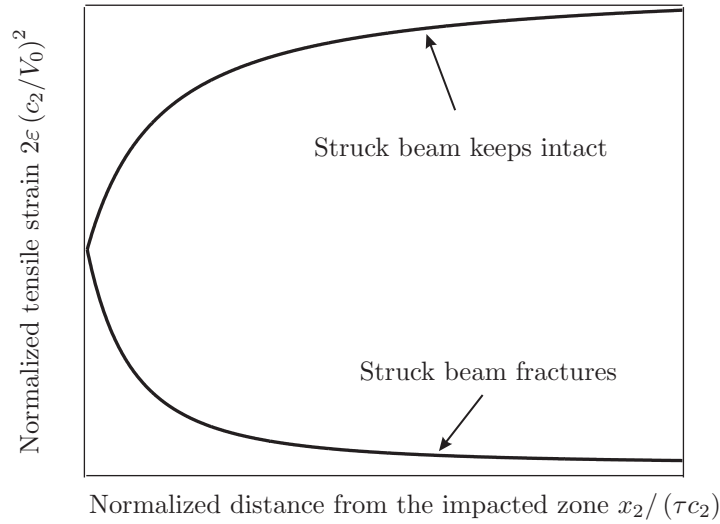


Fig. 7-26: Comparison of tensile strain in the striking beam for the case of the struck beam with and without fracture ($\alpha > \beta$).

7.3.8 Comparison with finite element solutions

To verify the present theoretical model, finite element calculation was performed using ABAQUS/Explicit. Two impacting beams considered have the same geometrical size: the length $l = 1.0$ m, the width $2b_1 = 2b_2 = 10$ mm, and the thickness $h_1 = h_2 = 2$ mm. The impact velocity is $V_0 = 240$ m/s. It is assumed that the striking and struck beam is made of 2024-T351 aluminum and Weldox 460 E steel, respectively. The JC's material models were defined for both materials and no fracture loci were implemented. Since of interest is the deflection of both beams, an one-dimensional beam element model (B31) was built instead of an expensive three-dimensional solid element model.

Figures 7-27 and 7-28 show plots of transient transverse deflections profiles of both beams. It appears that the present closed-form solutions agree very well with the numerical

results. Due to the neglect of elastic deformation and reflected stress waves from far-fields boundaries in the theoretical model, the difference between the two solutions becomes large at the end of the impact process.

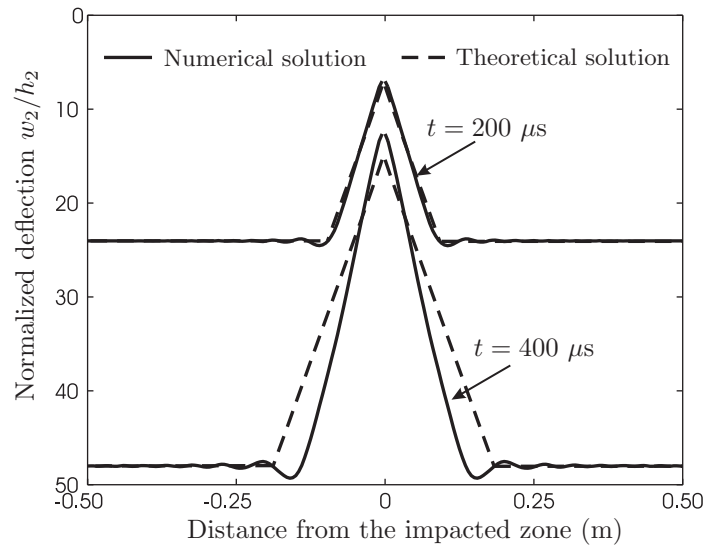


Fig. 7-27: Comparison of transient deflection profiles of the striking beam at $V_0 = 240$ m/s.

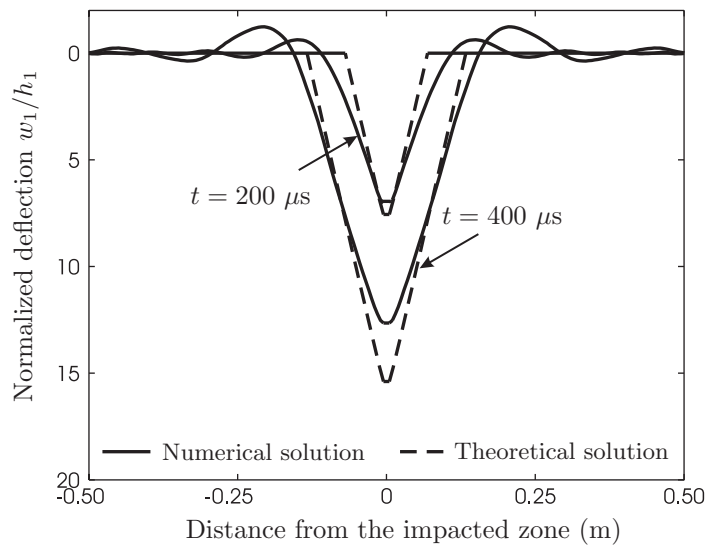


Fig. 7-28: Comparison of transient deflection profiles of the struck beam at $V_0 = 240$ m/s.

7.3.9 Discussion

The problem of high velocity impact between two beams has been formulated. The closed-form solutions are obtained for the transverse velocity, the deflection profile, and the tensile strain, respectively. It is found that there are three types of the transverse velocity history, the deflection profile, and the tensile strain distribution, depending on the relative values of the mass ratio and the wave speed ratio. By assuming the failure mode of tensile necking, the critical impact velocities have been obtained for the striking and struck beams, respectively. Five fracture scenarios are identified and the corresponding conditions are determined.

It is assumed in the present problem formulation that axial stretching dominates over bending and shearing and thus the theoretical solutions apply to the case with a high impact velocity. Tensile tearing is assumed to determine the critical impact velocities to fracture the striking and struck beams. As demonstrated in Chapter 3.2, shear plugging is another possible failure mode in high velocity impact. This is not considered in the present theoretical model. Shear plugging often competes with tensile tearing, which makes the problem more complicated. A theoretical model accounting for these factors is developed in Chapter 7.5.

7.4 Multiple impact of beam-to-beam

7.4.1 Introduction

In this section, the momentum conservation approach, first formulated for rigid mass-to-beam impact and the single impact of beam-to-beam, is extended to a multiple impact event. Let us assume that a deforming and fracturing beam is impacted sequentially by arbitrary number identical beams. The striking beams represent the structural components of the airplane wing; and the stationary struck beam the exterior column of the Twin Towers. However, the present analysis is rather general and is applicable to any beams of solid section made of same or different materials. It is for the first time in the literature that this type of problem is investigated.

Similarly to the single impact problem of beam-to-beam, the present theoretical model applies to a restricted range of geometrical parameters and impact velocities for which the beams can indeed be treated as a string. Consequently, the bending phase of the response which is relevant for the deflection less than one thickness is neglected. Attention is focused on the plastic deformation and failure response of the struck beam. Of interest is a determination of the transient velocity, the deflection profile, the tensile strain, and the critical impact velocity to fracture the struck beam.

A preliminary numerical study indicates that many failure scenarios could develop depending on geometrical size and material properties of two impacting beams for the single impact of beam-to-beam. Both beams may fail by either tensile tearing or shear plugging, or one beam is sheared off or torn apart while the other keeps intact. It is also possible that both beams continue plastic deformation without fracture. The failure patterns may be still more complicated in the multiple impact event. Here, it is assumed that all the striking beams immediately fail upon impact while the struck beam keeps deforming until fracture occurs. This assumption further restricts the applicability of our solution. Still a class of beams satisfying the solution is very broad.

Two situations may develop later. The remainder of the striking beams could stick to the struck beam and move with it. Alternatively, the broken piece will slide off the impacted zone and will no longer interfere with the struck beam. Both cases will be considered in

this section. For simplicity, the latter case will be taken as an example to present the formulation of the problem.

7.4.2 Double impact

Consider first a stationary plastic beam subjected to double normal impact by two identical plastic beams moving with the velocity V_0 and separated by the time interval t_0 , Fig. 7-29. This problem still allows us to develop a closed-form solution and will provide a starting point for the formulation of the multiple impact event with arbitrary number striking beams.

Since all the striking beams are assumed to be identical, we can use the same notations here as those in the single impact of beam-to-beam. For example, the width and thickness of the impacting beams are denoted by $2b_2$ and h_2 for all the striking beams, and $2b_1$ and h_1 for the struck beam. The mechanical properties of the beam are defined by the mass density ρ_2 and the average plastic flow stress σ_2 for all the striking beams, ρ_1 and σ_1 for the struck beam, respectively. Figure 7-13 can be referred to for the definition of the impact configuration.

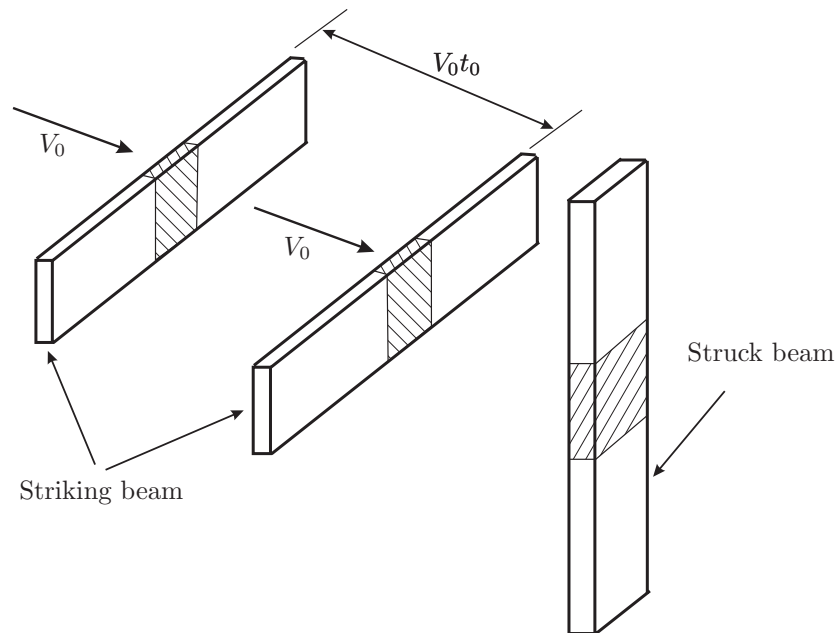


Fig. 7-29: Schematic representation of double impact of beam-to-beam.

7.4.2.1 Problem formulation

Immediately upon the first impact, two shock waves are generated in the impacted zone due to the discontinuity of the transverse velocity field. As the transverse stress waves propagate along both sides of the struck beam, a material element at the stress wave front is instantly stretched, rotated, and imparted a transverse momentum. The plastically deformed region behind the stress wave front undergoes a rigid body motion. This response is the same as the single impact of beam-to-beam and has been studied in Chapter 7.3. After time $t = t_0$, the target beam is impacted by the second striking beam. Similarly, two new stress waves are generated in the impacted zone. However, different from the first stress waves, the second stress waves travel in the already deformed region moving at a certain transverse velocity. Hence, the second impact is an entirely new initial-boundary value problem. A material element at the second wave front is stretched and rotated again, and acquires a new transverse momentum. It is assumed that the deformed region behind the second wave fronts also translates like a rigid body. Thus, the whole deformed region behind the first wave fronts can be divided into two parts, each of which undergoes rigid body motions but with different transverse velocities denoted by $V_{1,1}$ and $V_{1,2}$, respectively, where the first subscript 1 denotes the struck beam and the second subscripts $j = 1, 2$ denotes the impact number. Both velocities are constant in space and vary with time. A typical profile of the velocity field after the second impact for the struck beam and the striking beams is shown in Fig. 7-30.

Correspondingly, the governing wave equation for the struck beam can be easily written, for each part, as

$$\begin{cases} (N_1 w_1')' = m_1 \dot{V}_{1,2} & 0 \leq x_1 \leq \xi_{1,2} \\ (N_1 w_1')' = m_1 \dot{V}_{1,1} & \xi_{1,2} \leq x_1 \leq \xi_{1,1} \end{cases}, \quad (7.109)$$

where $\xi_{1,1} = c_1 t$ and $\xi_{1,2} = c_1 (t - t_0)$ are the location of the first and second wave fronts, respectively. The governing equations are subject to the kinematic and dynamic continuity conditions at the wave fronts. Both conditions can be expanded, at the first wave fronts as

$$\begin{cases} (0 - V_{1,1}) + c_1 (0 - w_1'|_{x=\xi_{1,1}^-}) = 0 \\ N_1 (0 - w_1'|_{x=\xi_{1,1}^-}) + m_1 c_1 (0 - V_{1,1}) = 0 \end{cases} \quad \text{at} \quad x_1 = \xi_{1,1} \quad (7.110)$$

where zero initial conditions ahead of the first wave front are used. Similarly, the continuity conditions at the second wave front are specified by

$$\begin{cases} (V_{1,2} - V_{1,1}) + c_1 \left(w_1' |_{x_1=\xi_{1,2}^-} - w_1' |_{x_1=\xi_{1,2}^+} \right) = 0 \\ N_1 \left(w_1' |_{x_1=\xi_{1,2}^-} - w_1' |_{x_1=\xi_{1,2}^+} \right) + m_1 c_1 (V_{1,2} - V_{1,1}) = 0 \end{cases} \quad \text{at} \quad x_1 = \xi_{1,2}. \quad (7.111)$$

As mentioned above, several cases may develop after the second impact. For simplicity, the case that no parts of the striking beams would remain in the contact with the struck beam after the impact is considered here, which gives the following boundary condition at $x_1 = 0$

$$2N_1 w_1' = 2m_1 b_2 \dot{V}_1, \quad (7.112)$$

where only the mass of the struck beam in the impacted zone contributes to the inertia force. It is not necessary to introduce interaction force between the struck beam and striking beams in the above equation, because no more momentum transfers among the beams after the fracture of the striking beams. Without difficulty, one can derive boundary conditions for the other case where the remainder of the striking beam moves with the struck beam.

Since the transverse velocity is uniform in each deformed part, Eq. (7.109) can be integrated with respect to x_1 , which gives for each part

$$\begin{cases} N_1 w_1' |_{x_1=\xi_{1,2}^-} - N_1 w_1' |_{x_1=0} = m_1 \dot{V}_{1,2} (c_1 t - c_1 t_0) & 0 \leq x_1 \leq \xi_{1,2} \\ N_1 w_1' |_{x_1=\xi_{1,1}^-} - N_1 w_1' |_{x_1=\xi_{1,2}^+} = m_1 \dot{V}_{1,1} c_1 t_0 & \xi_{1,2} \leq x_1 \leq \xi_{1,1} \end{cases} \quad (7.113)$$

Substituting the corresponding boundary and dynamic continuity conditions, and combining the above equations together gives the governing equation for the struck beam with respect to the transverse velocities

$$[b_2 + c_1 (t - t_0)] \dot{V}_{1,2} + c_1 t_0 \dot{V}_{1,1} + c_1 V_{1,2} = 0. \quad (7.114)$$

Similarly to the case of rigid mass impact and the single impact of beam-to-beam, the above governing equation can also be directly obtained from the principle of conservation of linear

momenta by differentiating the following equation with respect to time t

$$2m_1 [b_2 + c_1 (t - t_0)] V_{1,2} + 2m_1 c_1 t_0 V_{1,1} = I, \tag{7.115}$$

where I is a constant denoting the total momentum of the struck beam supplied by the striking beams during the double impact process.

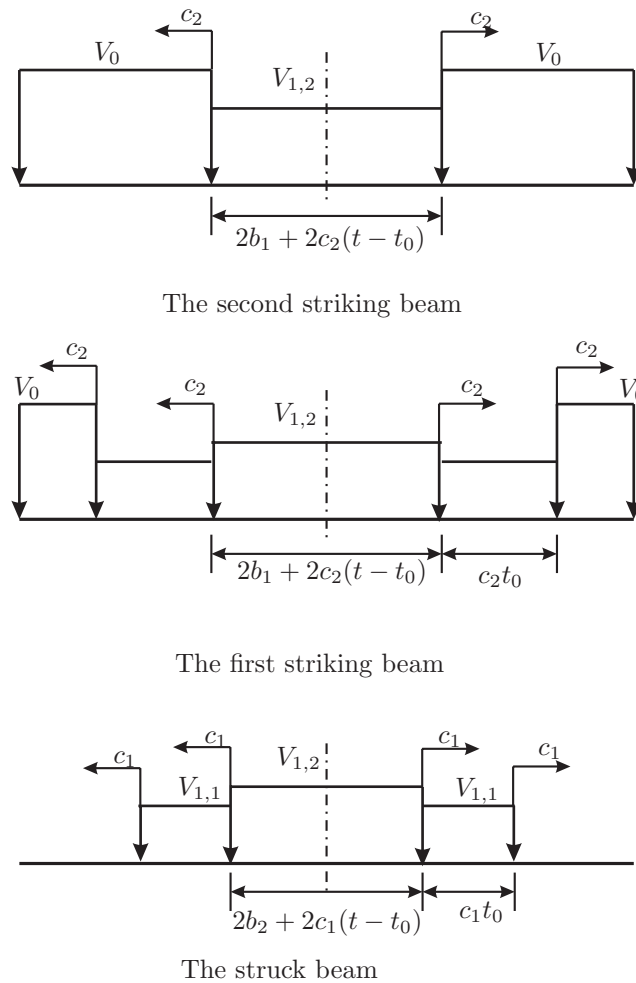


Fig. 7-30: Transient velocity field in three beams after the second impact.

Note, that the momenta transferred from the striking beam are slightly underestimated, since only the momenta in the impacted zone are taken into account. When both struck beams are sheared off, some momenta of both striking beams away from the impacted

zone is transferred to the struck beam. Finite element simulations of the single impact of beam-to-beam indicate that the failure duration is of the order of $100 \mu\text{s}$, and thus the underestimation of the momenta imparted by the striking beams would not be significant. Estimate can be given on the amount of momentum loss during the fracture process. Assuming the duration of the shear fracture process, t_f , is

$$t_f = \frac{h_2}{3V_0} \quad (7.116)$$

where the coefficient $1/3$ in the expression for the duration of fracture comes from the property that shear crack travels at a speed approximately equal three times higher than the impact velocity [59], also see Chapter 4. The neglected momentum in the first impact is approximately given by

$$\Delta I_s = \rho_2 2b_2 h_2 2t_f c_2 (V_0 - V_{1,1}^*). \quad (7.117)$$

where $V_{1,1}^*$ is the instantaneous velocity of the striking beam at the impacted zone immediately upon impact, and c_2 is the speed of the transverse stress wave of the striking beams. The considered momentum transferred from the first striking beam to the struck beam, I_s , is

$$I_s = \rho_2 2b_2 h_2 2b (V_0 - V_{1,1}^*). \quad (7.118)$$

The ratio of the neglected momentum to the considered momentum is

$$\frac{\Delta I_s}{I_s} = \frac{1}{3} \frac{h_2}{b_1} \frac{c_2}{V_0}. \quad (7.119)$$

In order for the problem to be one dimensional rather than three dimensional, we have already assumed that $h_2 \ll b_1$. Therefore, the term ΔI_s can be indeed disregarded as long as the impact velocity V_0 is of the same order as the transverse plastic stress wave speed c_2 .

7.4.2.2 Assumptions

It can be observed that from the global equilibrium and the conditions of the kinematic and dynamic continuity, only one equation is found for the two unknown velocities $V_{1,1}(t)$ and

$V_{1,2}(t)$. Therefore, an additional condition is needed to solve the problem.

As stated earlier, the slope $w'_1|_{x_1=\xi_{1,1}^+}$ is generated when the first wave arrives at $x_1 = \xi_{1,1}$. Since then, the slope of the beam does not change with time until the second shock wave arrives there. Hence, $\Delta w'_{1,2} = w'_1|_{x_1=\xi_{1,2}^-} - w'_1|_{x_1=\xi_{1,2}^+}$ is the increment of the slope at $x_1 = \xi_{1,2}$ due to the second shock wave. The kinematic and dynamic continuity conditions at the second wave front, $x_1 = \xi_{1,2}$, Eq. (7.111), can be recast in the incremental form

$$\begin{cases} \Delta V_{1,2} + c_1 \Delta w'_{1,2} = 0 \\ N_1 \Delta w'_{1,2} + m_1 c_1 \Delta V_2 = 0 \end{cases} \quad (7.120)$$

where $\Delta V_{1,2} = V_{1,2} - V_{1,1}$.

Now, we introduce an assumption that the incremental parts, $\Delta V_{1,2}$ and $\Delta w'_{1,2}$, satisfy the governing wave equation at $0 \leq x_1 \leq \xi_{1,2}$,

$$(N_1 \Delta w'_{1,2})' = m_1 \Delta \dot{V}_{1,2} \quad 0 \leq x_1 \leq \xi_{1,2} \quad (7.121)$$

where $\Delta \dot{V}_{1,2} = \dot{V}_{1,2} - \dot{V}_{1,1}$. Then, the governing wave equation, Eq. (7.109), with regard to the velocity $V_{1,1}$ can be extended from the region between the two wave fronts, $\xi_{1,2} \leq x_1 \leq \xi_{1,1}$, to the whole deformed region, $0 \leq x_1 \leq \xi_{1,1}$,

$$(N_1 w'_{1,1})' = m_1 \dot{V}_{1,1} \quad 0 \leq x_1 \leq \xi_{1,1}, \quad (7.122)$$

where the deflection $w_{1,1}$ is generated due to the transverse velocity $V_{1,1}$. The above equation indicates that the first shock wave will continue to propagate to far fields after the second impact as if the second impact never happened. In fact, both shock waves propagate with the common wave speed in the same direction. It is impossible that the second shock wave would interfere or overtake the first one, and vice versa. Also note, that the governing wave equation is a homogeneous partial differential equation such that the superposition of the solutions is applicable.

Based on the assumption, there are two governing Eqs. (7.121) and (7.122) with regard to $\Delta V_{1,2}$ and $V_{1,1}$, respectively, both of which satisfy the continuity conditions at the corresponding wave fronts, Eqs. (7.110) and (7.120). As shown in the preceding section, if the

transverse velocity satisfies the governing equation and the continuity conditions, the transverse momentum is conserved during the wave propagation process. As shown in Fig. 7-31, the transverse velocity field in the struck beam after the second impact is decomposed into two parts. Each part represents a shock wave propagating with the wave speed, c , and the transverse momentum is conserved for each part. It is convenient to derive the transverse velocity at any time from the principle of linear momentum conservation.

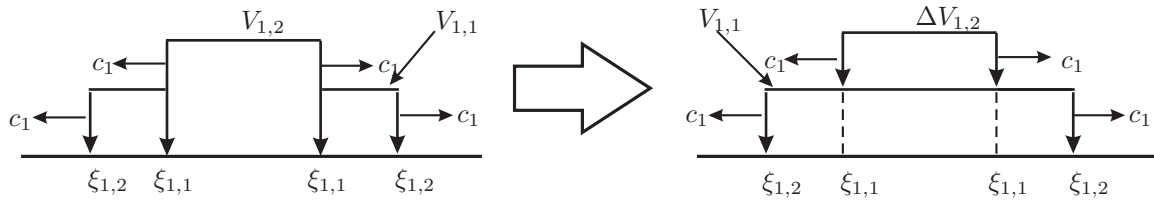


Fig. 7-31: Velocity field of the struck beam after decomposition.

7.4.2.3 Velocity history

The solution to the velocity and deformation before the second impact is the same as the single impact case, which has been presented in Chapter 7.3. Immediately upon the first impact, the velocity is

$$V_{1,1}^* = \frac{2m_2b_1}{2m_2b_1 + 2m_1b_2}V_0 = \alpha V_0, \tag{7.123}$$

where the velocity with the superscript $*$ represents the instantaneous velocity upon impact. At a time before the second impact, the principle of linear momentum conservation gives

$$2m_1(b_2 + c_1t)V_{1,1} = 2m_1b_2V_{1,1}^*. \tag{7.124}$$

Note, that there is no more momentum transfer between the striking beam and the struck beam after the impact. From the above equation, one obtains the velocity $V_{1,1}$

$$\frac{V_{1,1}(t)}{V_0} = \frac{\alpha}{1 + \eta t/t_0} \tag{7.125}$$

where the dimensionless parameter η is defined by

$$\eta = \frac{c_1 t_0}{b_2} = \frac{1 - \beta t_0}{1 - \alpha \tau}, \quad (7.126)$$

and the parameter η is related to the wave speed ratio, β , and the time parameter, τ , both of which are first introduced in the single impact case. Using the parameters β and τ , one can make a comparison between the double impact and the single impact. Just before the second impact, $t = t_0$, the velocity $V_{1,1}$ becomes

$$\frac{V_{1,1}(t_0)}{V_0} = \frac{\alpha}{1 + \eta} = \theta. \quad (7.127)$$

For convenience, a new dimensionless parameter θ is defined in the above equation.

Now solve the velocity field of the struck beam after the second impact. Immediately upon the second impact, the velocity $V_{1,2}^*$ can be obtained from the momentum conservation in the impacted zone

$$(2m_2 b_1 + 2m_1 b_2) V_{1,2}^* = 2m_2 b_1 V_0 + 2m_1 b_2 V_{1,1}(t_0), \quad (7.128)$$

where the first term on the right hand side represents the momentum provided by the second striking beam, and the second term denotes the existing momentum of the struck beam in the impacted zone. Using the dimensionless parameters α and η , it is convenient to write $V_{1,2}^*$ as

$$\frac{V_{1,2}^*}{V_0} = \alpha \left(1 + \frac{1 - \alpha}{1 + \eta} \right). \quad (7.129)$$

From the momentum conservation for the incremental part as shown in Fig. 7-31, one gets the velocity increment $\Delta V_{1,2}(t)$

$$\frac{\Delta V_{1,2}}{\Delta V_{1,2}^*} = \frac{m_1 2b_2}{m_1 [2b_2 + 2c_1(t - t_0)]} = \frac{1}{1 + \eta(t/t_0 - 1)}, \quad (7.130)$$

where $\Delta V_{1,2}^*$ is the initial value of the incremental part, given by

$$\Delta V_{1,2}^* = V_{1,2}^* - V_{1,1}(t_0) = \alpha V_0 (1 - \theta). \quad (7.131)$$

As stated earlier, the variation of the velocity $V_{1,1}$ with time is independent of the second impact, i.e. the expression for the velocity $V_{1,1}$ after the second impact is the same as Eq. (7.125). The velocity $V_{1,2}$ is obtained by adding $V_{1,1}$ and $\Delta V_{1,2}$ together

$$\frac{V_{1,2}}{V_0} = \alpha \left[\frac{1}{1 + \eta t/t_0} + \frac{1 - \theta}{1 + \eta (t/t_0 - 1)} \right]. \quad (7.132)$$

Plots of the velocity variation with time for specific values of α and η are shown in Fig. 7-32.

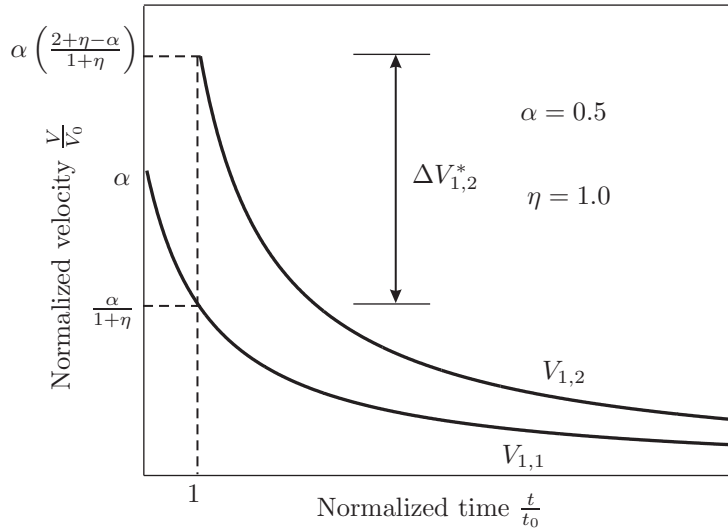


Fig. 7-32: Velocity variation with time for $V_{1,1}$ and $V_{1,2}$ in the double impact case.

7.4.2.4 Deflection and plastic strain

The transverse deflection of the beams is calculated by integrating the transverse velocity with respect to time. For the struck beam, a point located at a distance x_1 from the impacted zone acquires displacement only after time $t = x_1/c_1$. The transverse velocity at this point changes from $V_{1,1}$ to $V_{1,2}$ at $t = t_0 + x_1/c_1$. Hence, the transverse deflection of the struck beam after the second impact can be expressed as

$$\begin{cases} w_1 = \int_{x_1/c_1}^{t_0 + x_1/c_1} V_{1,1} dt + \int_{t_0 + x_1/c_1}^t V_{1,2} dt & 0 \leq x_1 \leq \xi_{1,2} \\ w_1 = \int_{x_1/c_1}^t V_{1,1} dt & \xi_{1,2} \leq x_1 \leq \xi_{1,1} \end{cases} \quad (7.133)$$

Substituting the expressions for the velocities, and integrating Eq. (7.133), one obtains the transverse deflection of the struck beam,

$$\left\{ \begin{array}{l} \frac{w_1}{b_2} = \frac{\alpha V_0}{c_1} \ln \left(\frac{1 + \eta t/t_0}{1 + x_1/b_2} \right) + \frac{\alpha V_0}{c_1} (1 - \theta) \ln \left(\frac{1 - \eta + \eta t/t_0}{1 + x_1/b_2} \right) \quad 0 \leq x_1 \leq \xi_{1,2} \\ \frac{w_1}{b_2} = \frac{\alpha V_0}{c_1} \ln \left(\frac{1 + \eta t/t_0}{1 + x_1/b_2} \right) \quad \xi_{1,2} \leq x_1 \leq \xi_{1,1} \end{array} \right. \quad (7.134)$$

The first term on the right hand side of Eq. (7.134) represents the deflection due to the velocity $V_{1,1}$, and the second term denotes the deflection due to the velocity increment $\Delta V_{1,2}$. Plots of instantaneous deflection profiles of the struck beam are shown in Fig. 7-33.

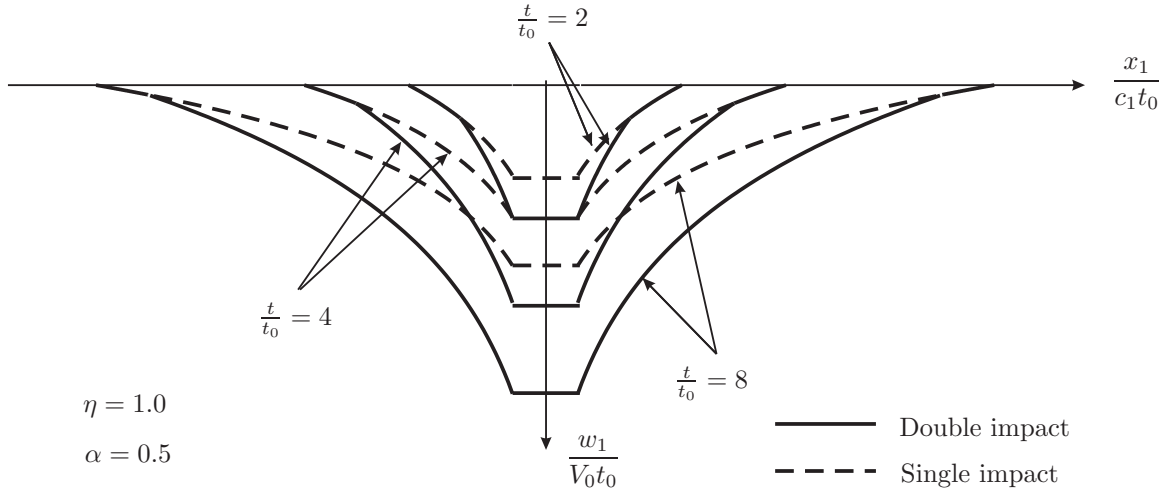


Fig. 7-33: Deflection profiles of the struck beam after the second impact and comparison with of the single impact event.

From the moderately large deflection theory, the axial tensile strain in the struck beam is given by

$$\varepsilon_1 = \frac{1}{2} \left(\frac{\partial w_1}{\partial x_1} \right)^2 = \left\{ \begin{array}{l} \frac{1}{2} \left(\frac{\alpha V_0}{c_1} \right)^2 (2 - \theta)^2 \left(1 + \frac{x_1}{b_2} \right)^{-2} \quad 0 \leq x_1 \leq \xi_{1,2} \\ \frac{1}{2} \left(\frac{\alpha V_0}{c_1} \right)^2 \left(1 + \frac{x_1}{b_2} \right)^{-2} \quad \xi_{1,2} \leq x_1 \leq \xi_{1,1} \end{array} \right. \quad (7.135)$$

Plots of the tensile strain variation along the beam for different values of η are shown in Fig. 7-34. It is seen that there is a jump of the tensile strain at the second wave front,

i.e. $x_1 = \xi_{1,2}$. At $\xi_{1,2} \leq x_1 \leq \xi_{1,1}$, the tensile strain is the same as that in the case of the single impact. The maximum tensile strain $\varepsilon_{1,\max}$ always takes place at the impact point, i.e. $x_1 = 0$,

$$\varepsilon_{1,\max} = \frac{1}{2} \left(\frac{\alpha V_0}{c_1} \right)^2 (2 - \theta)^2. \quad (7.136)$$

When the time interval t_0 goes infinity, $\eta \rightarrow \infty$, the maximum tensile strain approaches an asymptote

$$\varepsilon_{1,\max} = 2^2 \cdot \frac{1}{2} \left(\frac{\alpha V_0}{c_1} \right)^2 \quad \eta \rightarrow \infty, \quad (7.137)$$

which means that the double impact becomes two separate, single impact. When the time interval t_0 goes zero, the maximum tensile strain approaches another asymptotic value,

$$\varepsilon_{1,\max} = \frac{1}{2} \left(\frac{\alpha V_0}{c_1} \right)^2 (2 - \alpha)^2 \quad \eta \rightarrow 0. \quad (7.138)$$

The ratio of the maximum strain corresponding to $\eta \rightarrow 0$ and $\eta \rightarrow \infty$ is equal to $(1 - \frac{\alpha}{2})^2$ and is seen to depend only on the mass ratio parameter α .

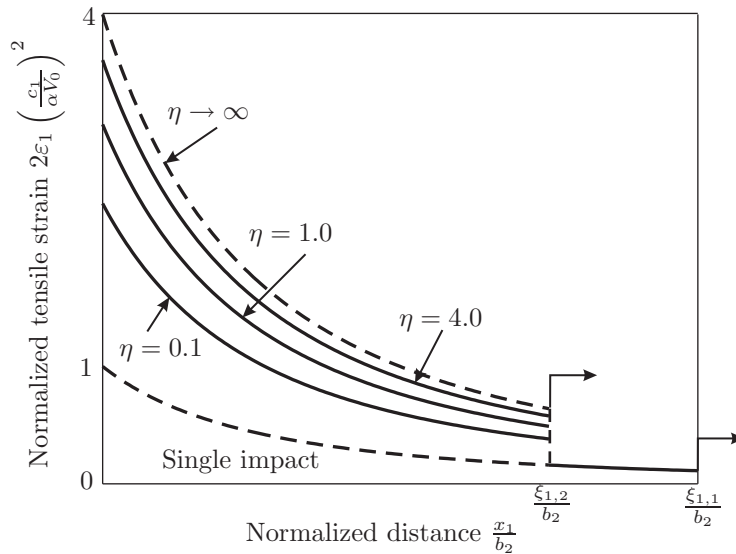


Fig. 7-34: Strain variation along the struck beam for different values of η .

7.4.2.5 Kinetic energy and plastic energy

Immediately upon impact, the struck beam acquires the kinetic energy

$$E_0 = \frac{1}{2} 2m_1 b_2 (V_{1,1}^*)^2 = m_1 b_2 (\alpha V_0)^2. \quad (7.139)$$

At time $t < t_0$ before the second impact, the kinetic energy of the struck beam becomes

$$E_1(t) = \frac{1}{2} (2m_1 b_2 + 2m_1 c_1 t) V_{1,1}^2 = \frac{E_0}{1 + c_1 t / b_2}, \quad t < t_0. \quad (7.140)$$

Upon the second impact, the newly acquired kinetic energy is

$$\Delta E = \frac{1}{2} (2m_1 b_2) [(V_2^*)^2 - V_{1,1}^2(t_0)] = E_0 \left[1 + 2 \frac{1 - \alpha}{1 + \eta} + \frac{\alpha^2 - 2\alpha}{(1 + \eta)^2} \right]. \quad (7.141)$$

At a time, t , after the second impact, the total kinetic energy of the struck beam becomes

$$\begin{aligned} E_2(t) &= \frac{1}{2} [2m_1 b_2 + 2m_1 c_1 (t - t_0)] V_{1,2}^2(t) + \frac{1}{2} (2m_1 c_1 t_0) V_{1,1}^2(t) \\ &= E_0 \left[\frac{3 - 2\theta}{1 + \eta t / t_0} + \frac{(1 - \theta)^2}{1 + \eta (t / t_0 - 1)} \right]. \end{aligned} \quad (7.142)$$

The loss of the kinetic energy during the wave propagation is absorbed by plastic membrane deformation

$$\begin{aligned} W(t) &= E_0 + \Delta E - E_2 \\ &= E_0 \left[1 + (1 - \theta)^2 + 2 \frac{1 - \theta}{1 + \eta} - \frac{3 - 2\theta}{1 + \eta t / t_0} - \frac{(1 - \theta)^2}{1 + \eta (t / t_0 - 1)} \right]. \end{aligned} \quad (7.143)$$

For a rigid-perfectly plastic string, the loss of the kinetic energy is completely converted to the axial stretching energy. For a plastic beam, some of the kinetic energy is dissipated through plastic bending action, besides plastic axial stretching.

7.4.2.6 Critical impact velocities

A beam under high velocity impact would fail by either tensile tearing or shear plugging. Here, it is assumed that the struck beam fails by tensile tearing. A constant critical plastic strain, $\bar{\varepsilon}_{1,f}$, is used to predict fracture of the struck beam, due to its simplicity.

By setting the maximum plastic strain equal to the fracture strain, one can estimate the critical impact velocity of the striking beam, $V_{1,cr}$, to fracture the struck beam,

$$\frac{V_{1,cr}}{c_1} = \frac{\sqrt{2\bar{\varepsilon}_{1,f}}}{\alpha(2-\theta)} = \sqrt{2\bar{\varepsilon}_{1,f}} \frac{(1-\alpha) + (1-\beta)t_0/\tau}{\alpha[(2-\alpha)(1-\alpha) + 2(1-\beta)t_0/\tau]}. \quad (7.144)$$

The component of the bending strain is not taken into account in the estimation of the critical impact velocity in the above equation.

It can be shown that the critical velocity always decreases as the time interval increases, no matter whether $\alpha > \beta$ or $\alpha < \beta$, see Fig. 7-35. When the time interval t_0 goes infinity, the critical velocity becomes half of that in the single impact,

$$\frac{V_{1,cr}}{c_1} = \frac{1}{2} \frac{\sqrt{2\bar{\varepsilon}_{1,f}}}{\alpha}. \quad (7.145)$$

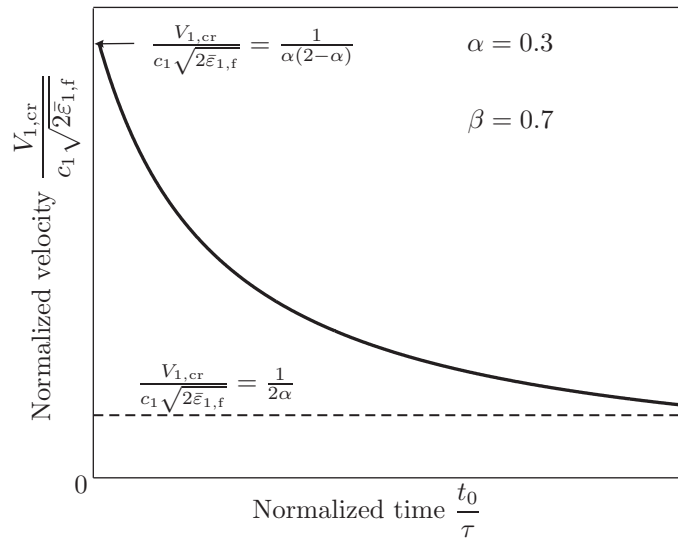


Fig. 7-35: Critical velocity variation with time interval in the double impact case.

In the preceding, the critical impact velocity is determined by differentiating the deflection to obtain the strain. In the following, we will show an alternative way to determine the critical impact velocity.

Considering that the transverse velocity is a function of time, independent of the spatial coordinate, the deflection slope of the beam can be calculated by differentiating Eq. (7.133) with respect to x_1 ,

$$\frac{\partial w_1}{\partial x_1} = -\frac{1}{c_1} \left[V_{1,1} \left(\frac{x_1}{c_1} \right) - V_{1,1} \left(t_0 + \frac{x_1}{c_1} \right) + V_{1,2} \left(t_0 + \frac{x_1}{c_1} \right) \right] \quad 0 \leq x_1 \leq \xi_{1,2}. \quad (7.146)$$

where the Leibniz's differential rule has been used. Specifically, the slope at edge of the the impacted zone, i.e. at $x_1 = 0$, is given by

$$\left. \frac{\partial w_1}{\partial x_1} \right|_{x_1=0} = -\frac{1}{c_1} [V_{1,1}(0) - V_{1,1}(t_0) + V_{1,2}(t_0)] = -\frac{1}{c_1} [V_{1,1}^* - V_{1,1}(t_0) + V_{1,2}^*]. \quad (7.147)$$

Three instantaneous velocities, $V_{1,1}^*$, $V_{1,1}(t_0)$, and $V_{1,2}^*$, are involved to determine the slope at $x_1 = 0$, which have been given in Eqs. (7.123), (7.127), and (7.129), respectively. Note, that these velocities are exactly obtained from the principle of linear momentum conservation without introducing any additional assumptions, hence the slope at $x_1 = 0$ is exactly determined. Substituting the expressions for these velocities into Eq. (7.147), the same critical velocity as Eq. (7.144) can be obtained after similar algebra. This method is more convenient, and thus will be used in the following cases.

7.4.2.7 Double impact by two identical rigid masses

Consider another case that both striking beams break immediately upon impact, the remainder of the striking beams sticks to the struck beam in the impacted zone and moves with it, Fig. 7-36. In fact, this case is equivalent to the double impact event of a plastic beam by two identical rigid projectiles with the mass $M_0 = 2m_2b_1$. The problem can be completely solved in the same procedure as described in the preceding sections. For simplicity, only the critical impact velocity to fracture the struck beam will be given next.

The simple method based on the Leibniz's differential rule will be used, in which only three instantaneous velocities $V_{1,1}^*$, $V_{1,1}(t_0)$, and $V_{1,2}^*$, are involved to determine the tensile

strain at $x_1 = 0$, Eq. (7.147). These velocities can be exactly solved from the principle of momentum conservation.

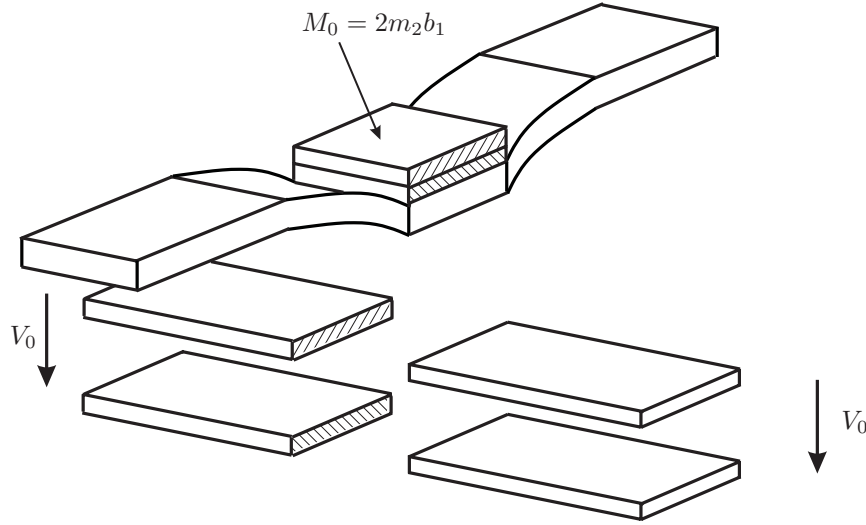


Fig. 7-36: Schematic of deformation and fracture of the beams in the double impact case.

Let us assume that the masses of the remainder of two striking beams or two rigid bodies contribute to the transverse momentum in the struck beam during the whole wave propagation process. After the first impact, the momentum conservation in the struck beam gives

$$[2m_1(b_2 + c_1t) + 2m_2b_1] V_{1,1} = (2m_1b_2 + 2m_2b_1) V_{1,1}^*. \quad (7.148)$$

From the above equation, one can express the velocity $V_{1,1}(t)$ in terms of the mass ratio, α , and the time parameter, η ,

$$\frac{V_{1,1}(t)}{V_0} = \frac{\alpha}{1 + (1 - \alpha)\eta t/t_0}. \quad (7.149)$$

Particularly, the velocity $V_{1,1}$ at $t = t_0$ is given by

$$\frac{V_{1,1}(t_0)}{V_0} = \frac{\alpha}{1 + (1 - \alpha)\eta}. \quad (7.150)$$

Upon the second impact at $t = t_0$, the momentum conservation can be expressed as

$$(4m_2b_1 + 2m_1b_2) V_{1,2}^* = 2m_2b_1V_0 + (2m_1b_2 + 2m_2b_1) V_{1,1}(t_0). \quad (7.151)$$

which yields the velocity $V_{1,2}^*$

$$\frac{V_{1,2}^*}{V_0} = \frac{\alpha}{1 + \alpha} \left(1 + \frac{1}{1 + (1 - \alpha)\eta} \right). \quad (7.152)$$

Substituting the expressions for $V_{1,1}^*$, $V_{1,1}(t_0)$, and $V_{1,2}^*$ into Eq. (7.147), one can determine the slope and further the tensile strain at $x = 0$:

$$\varepsilon_{1,\max} = \frac{1}{2} \left(\frac{\partial w_1}{\partial x_1} \right)^2 = \frac{1}{2} \left(\frac{V_0}{c_1} \right)^2 \left(\frac{\alpha}{1 + \alpha} \right)^2 \left(2 + \alpha - \frac{\alpha}{1 + (1 - \alpha)\eta} \right)^2. \quad (7.153)$$

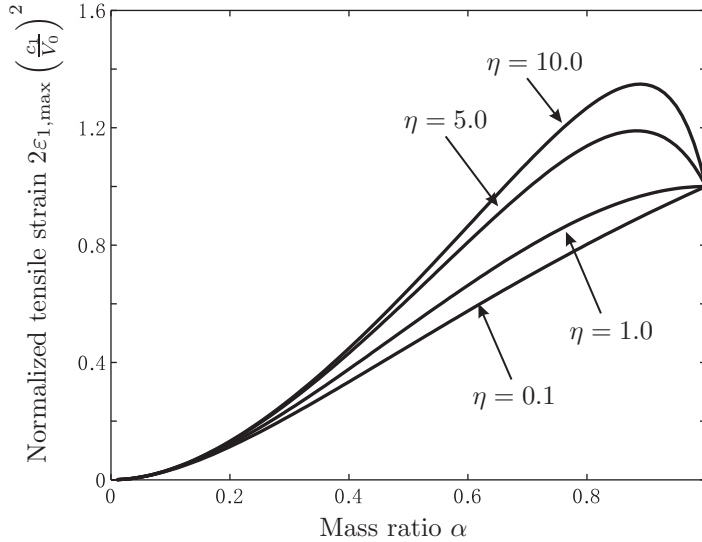


Fig. 7-37: Maximum tensile strains versus mass ratios for different values of η in the case of double rigid mass impact.

Plots of the maximum tensile strain versus the mass ratio α at various values of η are shown in Fig. 7-37. It appears that the maximum tensile strain does not increase monotonically with the mass ratio for the time parameter η falling in a certain range, which is different from the single impact event of a plastic beam by a rigid mass. The condition

under which the extreme value of the maximum tensile strain exists can be found by setting the differential of the maximum tensile strain with respect to the mass ratio equal to zero,

$$\frac{\partial \varepsilon_{1,\max}}{\partial \alpha} = 0, \quad (7.154)$$

which after arrangement gives

$$\eta^2 \alpha^4 - 2\eta \alpha^3 - (\eta^2 + 2\eta) \alpha^2 - (2\eta^2 + 2\eta) \alpha + 2(\eta + 1)^2 = 0. \quad (7.155)$$

With the value of η given, the above polynomial equation in α can be solved numerically, Fig. 7-38. The root of the equation determines the location of the extreme value in Fig. 7-37. If $\eta = 1.0$, the extreme value of the maximum tensile strain occurs at $\alpha = 1.0$. If $\eta < 1$, there is no extreme values of $\varepsilon_{1,\max}$; and the tensile strain always increases monotonically with the mass ratio. The extreme value usually occurs at $\alpha \approx 0.90$ under the condition of $\eta > 1$. In the case of the single rigid mass impact, a heavy impacting body is always easy to break the struck beam, as shown by Wierzbicki and Hoo Fatt [12]. However, in the case of the double rigid mass impact, there is an optimal mass ratio as a function of the time interval, with which the struck beam is the easiest to fracture.

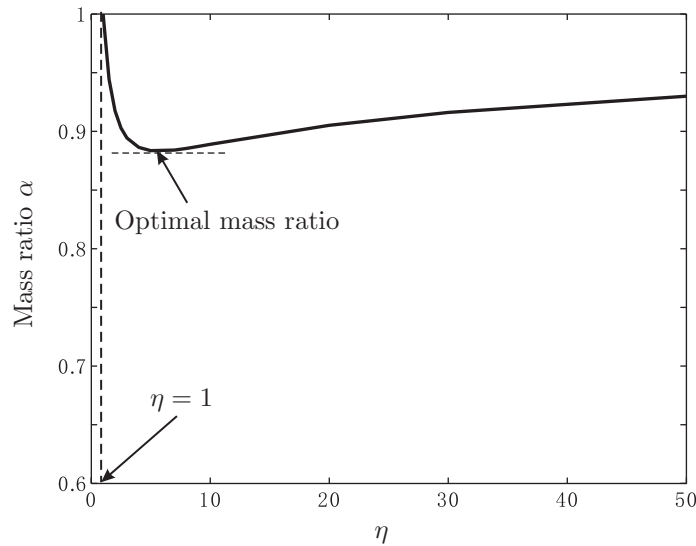


Fig. 7-38: Critical mass ratio α determining the extreme value of the maximum tensile strain.

Setting $\varepsilon_{1,\max} = \bar{\varepsilon}_{1,f}$ in Eq. (7.153), one can determine the critical impact velocity to fracture the struck beam,

$$\frac{V_{1,\text{cr}}}{c} = \sqrt{2\bar{\varepsilon}_{1,f}} \frac{1+\alpha}{\alpha} \left(2 + \alpha - \frac{\alpha}{1+(1-\alpha)\eta} \right)^{-1}. \quad (7.156)$$

Plots of the critical impact velocity versus the time interval are shown in Fig. 7-40.

7.4.2.8 Double impact by two intact striking beams

In the preceding sections, the cases that both striking beams undergo fracture immediately upon impact have been solved. Now, consider the third case that both striking beams deform plastically and never fracture during the impact process. The striking beams will always contact with the struck beam.

Assume that the maximum slope in the struck beam occurs at $x_1 = 0$ after the second impact. The expression for the slope at the impact point is the same as Eq. (7.147), while the expressions for two instantaneous velocities, $V_{1,1}(t_0)$ and $V_{1,2}^*$, will be different.

From the analysis of the single impact of beam-to-beam presented in Chapter 7.3, the velocity $V_{1,1}(t_0)$ is given by

$$\frac{V_{1,1}(t_0)}{V_0} = \beta + \frac{\alpha - \beta}{1 + t_0/\tau}. \quad (7.157)$$

The transverse momentum is conserved in the impacted zone immediately upon the second impact, i.e. $t = t_0$,

$$2m_2b_1V_0 + (2m_2b_1 + 2m_1b_2)V_{1,1}(t_0) = (4m_2b_1 + 2m_1b_2)V_{1,2}^*. \quad (7.158)$$

which gives the velocity $V_{1,2}^*$

$$\frac{V_{1,2}^*}{V_0} = \frac{\alpha}{1+\alpha} + \frac{1}{1+\alpha} \frac{V_{1,1}(t_0)}{V_0} \quad (7.159)$$

Substituting the expressions for $V_{1,1}^*$, $V_{1,1}(t_0)$ and $V_{1,2}^*$ into Eq. (7.147), and setting $\varepsilon_{1,\max} = \bar{\varepsilon}_{1,f}$, one can obtain the critical velocity $V_{1,\text{cr}}$ to break the struck beam in the case of both

striking beams without fracture

$$\frac{V_{1,cr}}{c_1} = \sqrt{2\bar{\epsilon}_{1,f}} \frac{1 + \alpha}{\alpha} \frac{1 + t_0/\tau}{2 + (2 + \alpha - \beta) t_0/\tau} \tag{7.160}$$

Plots of the critical velocity variation with the time interval are shown in Fig. 7-39. There are three cases depending on relative values of α and β . For the case of $\alpha = \beta$, the critical velocity is constant and independent of the time interval. For the case of $\alpha > \beta$, the critical velocity decreases with the time interval, and vice versa. If the time interval t_0 goes infinity, the critical velocity approaches an asymptote,

$$\frac{V_{1,cr}}{c_1} = \sqrt{2\bar{\epsilon}_{1,f}} \frac{1 + \alpha}{\alpha} \frac{1}{2 + \alpha - \beta}. \tag{7.161}$$

Figure 7-40 illustrates comparison of the critical velocity to fracture the struck beam among the three cases. It can be seen that the critical impact velocities always decrease with the time interval for the three cases. The struck beam is the most prone to fracture in the case where both striking beams break immediately upon impact and no parts remain in contact with the struck beam.

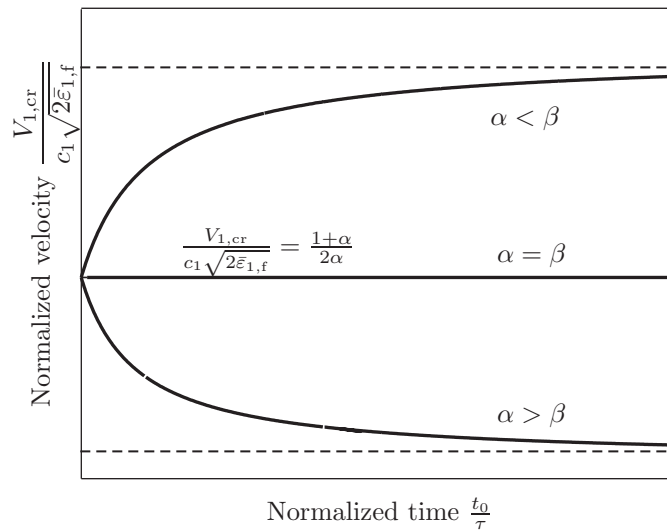


Fig. 7-39: Critical velocity variation with time interval for different values of α and β .

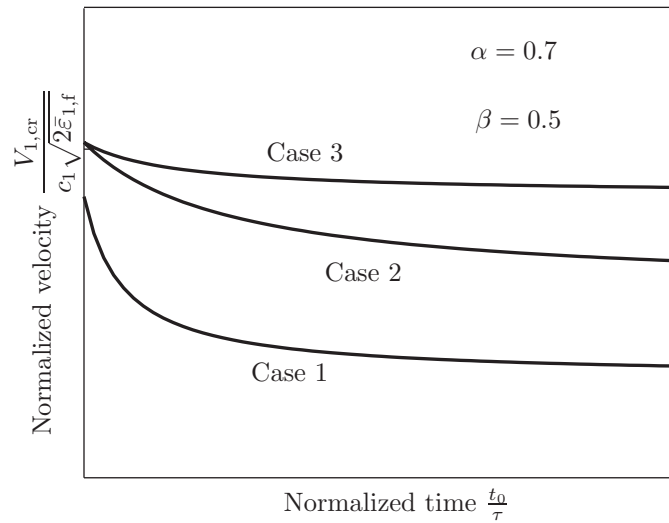


Fig. 7-40: Comparison of the critical velocity to fracture the struck beam among three cases, Case 1: both striking beams fracture upon impact and no parts of the striking beams remain in contact with the struck beam; Case 2: both striking beams fracture upon impact and the remainder of the striking beam at the contact area moves with the striking beam, or this case can be thought as double impact by a rigid mass; Case 3: both striking beams keep intact during the impact process.

7.4.3 Multiple impact

7.4.3.1 Problem formulation

Consider a stationary beam subjected to multiple impact by n identical beams moving with the velocity, V_0 , the time interval, t_0 , and the total spacing, $L = (n - 1) V_0 t_0$, Fig. 7-41. Because totally $n + 1$ beams are involved during the impact process, there are many possible fracture scenarios leading to complicated transverse velocity field for every beam. Here, two simple cases will be investigated. The first case is that all the striking beams break immediately upon impact; and no parts of the striking beams still rest on the struck beam after the impact (Case 1). The second is that all of the striking beams break immediately upon impact; and the remainder of the striking beams moves with the struck beam, as shown in Fig. 7-36 (Case 2). Case 2 can also be considered as the multiple impact by identical rigid bodies with the mass $M_0 = 2m_2b_1$. In both cases, attention is focused on the response of the struck beam. For simplicity, Case 1 will be taken as an example to present the problem formulation and the solution procedure.

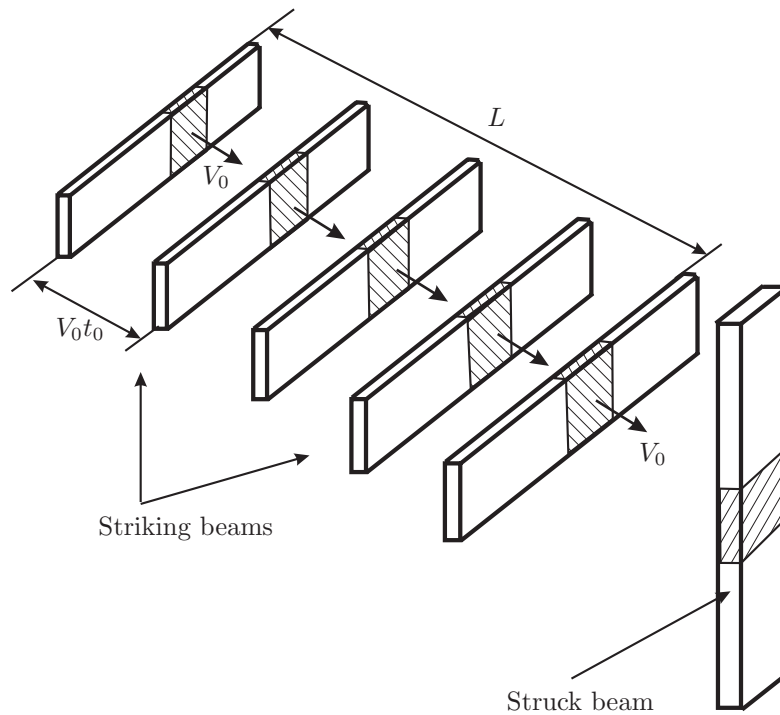


Fig. 7-41: Schematic of multiple impact of beam-to-beam.

After each impact, two new shock waves are generated in the impacted zone and propagate to far fields along both sides of the struck beam. An additional plastic deformation in the struck beam is instantaneously generated at the new wave front. The region behind the new wave front is subjected to a rigid body motion again. Hence, similarly to the case of the double impact, the velocity and acceleration between two wave fronts are constant in space and vary with time. A typical transverse velocity field in the struck beam after the n_{th} impact is shown in Fig. 7-42.

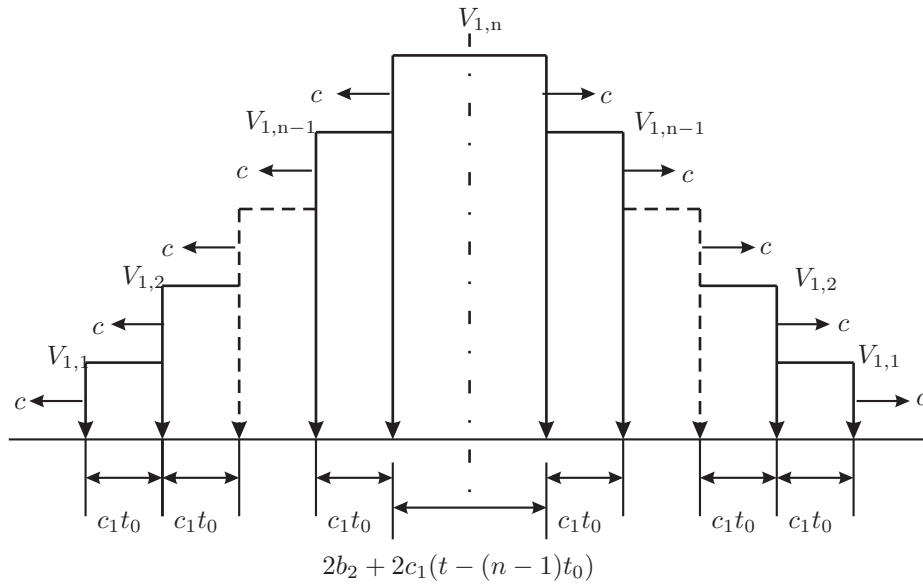


Fig. 7-42: Schematic of the velocity field in the multiple impact case.

Following the procedure for the double impact event, it can also be shown that from the global equilibrium, the kinematic and dynamic continuity conditions, there is only one governing equation for the problem of the multiple impact, which is related to n unknown velocities after the n_{th} impact. Hence, the problem cannot be solved without introducing additional conditions or assumptions.

Let us look at the kinematic and dynamic continuity conditions at the j_{th} wave front, which are given by

$$\begin{cases} (V_{1,j} - V_{1,j-1}) + c_1 (w'_1|_{x_1=\xi_{1,j}^-} - w'_1|_{x_1=\xi_{1,j}^+}) = 0 \\ N_1 (w'_1|_{x_1=\xi_{1,j}^-} - w'_1|_{x_1=\xi_{1,j}^+}) + m_1 c_1 (V_{1,j} - V_{1,j-1}) = 0 \end{cases} \quad (7.162)$$

where $\xi_{1,j} = c_1(t - jt_0)$ is the location of the j th wave front. Both conditions can be recast in the incremental form

$$\begin{cases} \Delta V_{1,j} + c_1(\Delta w'_{1,j}) = 0 \\ N_1(\Delta w'_{1,j}) + m_1 c_1 \Delta V_{1,j} = 0 \end{cases} \quad (7.163)$$

where $\Delta V_{1,j} = V_{1,j} - V_{1,j-1}$ is the velocity increment; and $\Delta w'_{1,j}$ is the slope jump at the j th wave front. Eq. (7.163) indicates that the increment of the plastic slope is proportional to the velocity increment. Similarly to the case of the double impact, it is assumed that the velocity increment $\Delta V_{1,j}$ and the corresponding plastic slope increment $\Delta w'_{1,j}$ satisfy the governing wave equation,

$$(N_1 \Delta w'_{1,j})' = m_1 \Delta \dot{V}_{1,j} \quad \xi_{1,j-1} \leq x_1 \leq \xi_{1,j}. \quad (7.164)$$

It can be shown that the transverse momentum is conserved with regard to the velocity increment $\Delta V_{1,j}$, if the governing equation, the kinematic and dynamic continuity conditions are satisfied. The velocity field in Fig. 7-42 can be decomposed into n parts, Fig. 7-43. Every part represents a shock wave propagating with the same wave speed c_1 . The transverse momentum for every part is conserved during the shock wave propagation process. Thus, the problem becomes amenable.

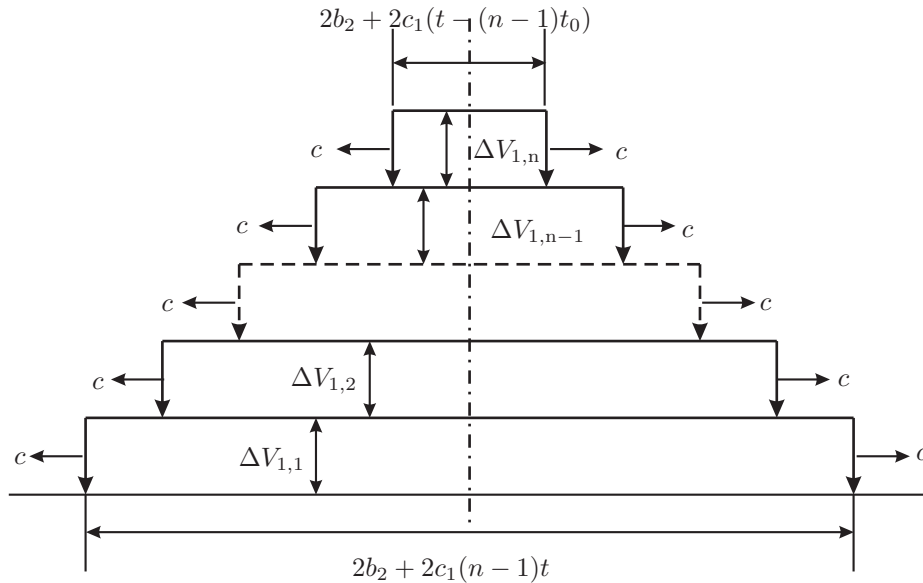


Fig. 7-43: Decomposition of the velocity field in the multiple impact case

7.4.3.2 Velocity history

To develop the solution procedure, assume that the velocity field after the j_{th} impact has been determined. Then the solution process for the next impact corresponding to the $(j + 1)_{\text{th}}$ impact is typical and can be applied repetitively until the n_{th} impact is completed.

At $t = jt_0$, the struck beam is impacted by the $(j + 1)_{\text{th}}$ striking beam. The transverse momentum is conserved in the impacted zone upon impact, given by

$$m_2 2b_1 V_0 + m_1 2b_2 V_{1,j}(jt_0) = (m_2 2b_1 + m_1 2b_2) V_{1,j+1}^*, \quad (7.165)$$

where the subscript j represents the j_{th} impact; $V_{1,j+1}^*$ is the instantaneous velocity in the impacted zone just upon the $(j + 1)_{\text{th}}$ impact; and $V_{1,j}(jt_0)$ is the velocity of the struck beam at $t = jt_0$ after the j_{th} impact. From the above equation, it is convenient to express $V_{1,j+1}^*$, in terms of the mass ratio, as

$$V_{1,j+1}^* = \alpha V_0 + (1 - \alpha) V_{1,j}(jt_0). \quad (7.166)$$

The transverse velocity increment due to the $(j + 1)_{\text{th}}$ impact is defined by

$$\Delta V_{1,j+1}(t) = V_{1,j+1}(t) - V_{1,j}(t), \quad t \geq jt_0. \quad (7.167)$$

As assumed earlier, the transverse momentum is conserved for this velocity increment as the $(j + 1)_{\text{th}}$ shock wave propagates away from the impacted zone. Hence, $\Delta V_{1,j+1}$ at a time, t , is given by

$$\frac{\Delta V_{1,j+1}(t)}{\Delta V_{1,j+1}^*(jt_0)} = \frac{m_1 2b_2}{m_1 2b_2 + m_1 2c_1(t - jt_0)} = \frac{1}{1 + \eta(t/t_0 - j)}, \quad t \geq jt_0. \quad (7.168)$$

where $\Delta V_{1,j+1}^*$ is the velocity increment immediately upon impact, i.e. at $t = jt_0$,

$$\Delta V_{1,j+1}^* = V_{1,j+1}^* - V_{1,j}(jt_0) = \alpha [V_0 - V_{1,j}(jt_0)]. \quad (7.169)$$

The total velocity $V_{1,j+1}$ at the region near the impacted zone is a summation of all of the

velocity increments,

$$V_{1,j+1}(t) = V_{1,j}(t) + \Delta V_{1,j+1}(t) = \sum_{k=1}^{j+1} \Delta V_{1,k}(t) \quad (7.170)$$

where $\Delta V_{1,1}(t) = V_{1,1}(t)$. Particularly, at $t = jt_0$, the velocity $V_{1,j}(jt_0)$ is given by

$$\begin{aligned} V_{1,j}(jt_0) &= \sum_{k=1}^j \Delta V_{1,k}(jt_0) \\ &= \frac{\Delta V_{1,1}^*}{1+j\eta} + \frac{\Delta V_{1,2}^*}{1+(j-1)\eta} + \dots + \frac{\Delta V_{1,j}^*}{1+\eta} \end{aligned} \quad (7.171)$$

where Eq. (7.168) has been used.

Based on the above solution process, it is easy to develop a calculation routine to determine the velocity of the struck beam at any time. Plots of the velocity versus time for specific values of α and η are shown in Fig. 7-44.

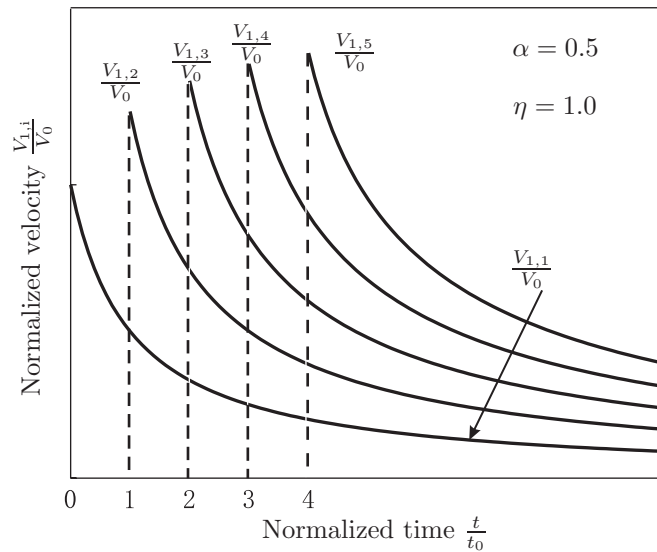


Fig. 7-44: Temporal variation of the velocities of the struck beam in the multiple impact case.

7.4.3.3 Deflection

The deflection of the struck beam at a distance x from the impacted zone after the n_{th} impact is given by

$$w_1 = \int_{x_1/c_1}^{t_0+x_1/c_1} V_{1,1}dt + \int_{t_0+x_1/c_1}^{2t_0+x_1/c_1} V_{1,2}dt + \dots + \int_{(n-1)t_0+x_1/c_1}^t V_{1,n}dt \quad 0 \leq x_1 \leq c_1 [t - (n-1)t_0]. \tag{7.172}$$

Similar expressions can be given for the deflection in other regions. Specially, the displacement at the impacted zone, i.e. at $x_1 = 0$, is

$$w_0 = \int_0^t \Delta V_{1,1}dt + \int_{t_0}^t \Delta V_{1,2}dt + \dots + \int_{(n-1)t_0}^t \Delta V_{1,n}dt. \tag{7.173}$$

Figure 7-45 shows comparison of the displacement history of the impacted zone among three cases.

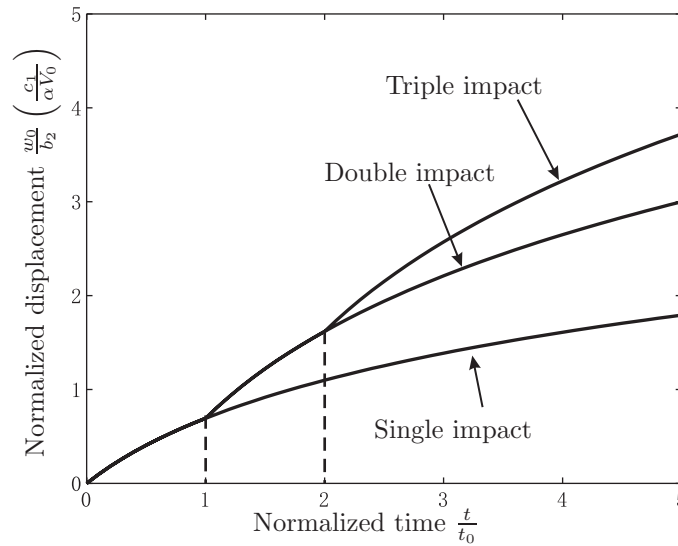


Fig. 7-45: Comparison of the displacement at $x_1 = 0$ among three cases.

7.4.3.4 Tensile strain and critical impact velocity

In this section, the simple method based on the Leibniz’s differential rule will be used to derive the tensile strain at the impact point and further the critical impact velocity to break the struck beam. From Eq. (7.172), differentiating the deflection with the spatial coordinate

x , the slope of the beam at $x = 0$ after the n_{th} impact is given by

$$\begin{aligned} \left. \frac{\partial w_1}{\partial x_1} \right|_{t=(n-1)t_0} &= -\frac{1}{c_1} [V_{1,1}(0) - V_{1,1}(t_0) + V_{1,2}(t_0) - V_{1,2}(2t_0) + \cdots + V_{1,n}((n-1)t_0)] \\ &= -\frac{1}{c_1} [V_{1,1}^* - V_{1,1}(t_0) + V_{1,2}^* - V_{1,2}(2t_0) + \cdots + V_{1,n}^*]. \end{aligned} \quad (7.174)$$

From Eq. (7.169), the above equation can be rewritten as

$$\left. \frac{\partial w_1}{\partial x_1} \right|_{t=(n-1)t_0} = -\frac{1}{c_1} [\Delta V_{1,1}^* + \Delta V_{1,2}^* + \cdots + \Delta V_{1,n}^*] = -\frac{1}{c_1} \sum_{j=1}^n \Delta V_{1,j}^*, \quad (7.175)$$

where $\Delta V_{1,1}^* = V_{1,1}^*$. The above equation indicates that the plastic slope of the struck beam at $x_1 = 0$ is proportional to the summation of all the velocity increments upon impact. This equation will be used to derive a recursion formula for the plastic slope later on.

Substituting the expression, Eq. (7.169), for every term in the right hand side of the above equation, one gets

$$\left. \frac{\partial w_1}{\partial x_1} \right|_{t=(n-1)t_0} = -n \frac{\alpha V_0}{c_1} + \frac{\alpha}{c_1} [V_{1,1}(t_0) + V_{1,2}(2t_0) + \cdots + V_{1,n-1}((n-1)t_0)]. \quad (7.176)$$

From Eq. (7.171), the above equation can be expanded as

$$\begin{aligned} \left. \frac{\partial w_1}{\partial x_1} \right|_{t=(n-1)t_0} &= -n \frac{\alpha V_0}{c_1} + \frac{\alpha}{c_1} \left[\left(\frac{\Delta V_{1,1}^*}{1+\eta} \right) + \left(\frac{\Delta V_{1,1}^*}{1+2\eta} + \frac{\Delta V_{1,2}^*}{1+\eta} \right) + \cdots \right. \\ &\quad \left. + \left(\frac{\Delta V_{1,1}^*}{1+(n-1)\eta} + \frac{\Delta V_{1,2}^*}{1+(n-2)\eta} + \cdots + \frac{\Delta V_{1,n-1}^*}{1+\eta} \right) \right]. \end{aligned} \quad (7.177)$$

Further, collecting common terms in the above equation, one obtains

$$\begin{aligned} \left. \frac{\partial w_1}{\partial x_1} \right|_{t=(n-1)t_0} &= -n \frac{\alpha V_0}{c_1} + \frac{\alpha}{1+\eta} \cdot \frac{1}{c_1} (\Delta V_{1,1}^* + \Delta V_{1,2}^* + \cdots + \Delta V_{1,n-1}^*) \\ &+ \frac{\alpha}{1+2\eta} \cdot \frac{1}{c_1} (\Delta V_{1,1}^* + \Delta V_{1,2}^* + \cdots + \Delta V_{1,n-2}^*) + \cdots + \frac{\alpha}{1+(n-1)\eta} \cdot \frac{1}{c_1} (\Delta V_{1,1}^*). \end{aligned} \quad (7.178)$$

As indicated in Eq. (7.175), the above equation can be rearranged as

$$\begin{aligned} \left. \frac{\partial w_1}{\partial x_1} \right|_{t=(n-1)t_0} &= -n \frac{\alpha V_0}{c_1} + \frac{\alpha}{1+\eta} \cdot \left. \frac{\partial w_1}{\partial x_1} \right|_{t=(n-2)t_0} + \\ &\quad \frac{\alpha}{1+2\eta} \cdot \left. \frac{\partial w_1}{\partial x_1} \right|_{t=(n-3)t_0} + \cdots + \frac{\alpha}{1+(n-1)\eta} \cdot \left. \frac{\partial w_1}{\partial x_1} \right|_{t=0}. \end{aligned} \quad (7.179)$$

For simplicity, introduce a dimensionless parameter γ_j to denote the slope at $x_1 = 0$ after the j th impact,

$$\gamma_j = - \left. \frac{\partial w_1}{\partial x_1} \right|_{t=(j-1)t_0} \frac{c_1}{\alpha V_0}. \quad (7.180)$$

In terms of the definition of γ_j , Eq. (7.179) becomes a recursion formula for the plastic slope

$$\gamma_n = n - \frac{\alpha}{1+\eta} \gamma_{n-1} - \frac{\alpha}{1+2\eta} \gamma_{n-2} - \cdots - \frac{\alpha}{1+(n-1)\eta} \gamma_1 \quad (7.181)$$

where $\gamma_1 = 1$. For the case of $\eta > 2$, an approximate closed-form solution for γ_n can be obtained by neglecting high order terms with regard to η

$$\gamma_n = n - \alpha \sum_{j=1}^{n-1} \frac{n-j}{1+j\eta}. \quad (7.182)$$

A short computational routine is developed to calculate the plastic slope with the dimensionless parameters given.

In terms of the dimensionless slope γ_n , the tensile strain in the struck beam after the n th impact is given by

$$\varepsilon_{1,n} = \frac{1}{2} \left(\frac{\alpha V_0}{c_1} \right)^2 \gamma_n^2. \quad (7.183)$$

It is interesting to discuss two limiting cases: $\eta \rightarrow \infty$ and $\eta \rightarrow 0$, which are helpful to understand the general case derived in the preceding. If the time interval η goes infinity, the transverse velocity in the struck beam becomes infinitesimal until the next impact. That is, the velocity $V_{1,j}(jt_0)$ in Eq. (7.176) can be neglected. The tensile strain approaches an asymptote

$$\varepsilon_{1,n} = \frac{1}{2} \left(\frac{\alpha V_0}{c_1} \right)^2 n^2 \quad \eta \rightarrow \infty. \quad (7.184)$$

On the other hand, if the time interval becomes infinitesimal, no shock waves have

sufficient time to propagate away from the impact area until the whole impact process is finished. In this case, the momentum conservation in the impacted zone after the j_{th} impact is expressed as

$$2m_2b_1V_0 + 2m_1b_2V_{1,j}^* = (2m_2b_1 + 2m_1b_2)V_{1,j+1}^* \quad (7.185)$$

where the velocity in the impacted zone before the next impact is still $V_{1,j}^*$. The velocity $V_{1,j+1}^*$ is given by

$$V_{1,j+1}^* = \alpha V_0 + (1 - \alpha)V_{1,j}^*. \quad (7.186)$$

A recursion formula with respect to the difference in the velocities can be obtained from the above equation,

$$V_{1,j+1}^* - V_{1,j}^* = (1 - \alpha)(V_{1,j}^* - V_{1,j-1}^*). \quad (7.187)$$

This recursion formula gives the closed-form solution for $V_{1,j}^*$

$$\frac{V_{1,j}^*}{V_0} = 1 - (1 - \alpha)^j. \quad (7.188)$$

Note, that in this case,

$$\Delta V_{1,j}^* = V_{1,j}^* - V_{1,j-1}^*. \quad (7.189)$$

Substituting the above expression into Eq. (7.175), the slope of the struck beam after the n_{th} impact depends only on the velocity upon the last impact,

$$\left. \frac{\partial w_1}{\partial x_1} \right|_{t=(n-1)t_0} = -\frac{1}{c_1} [V_{1,1}^* + V_{1,2}^* - V_{1,1}^* + \cdots + V_{1,n}^* - V_{1,n-1}^*] = -\frac{V_{1,n}^*}{c_1}. \quad (7.190)$$

Hence, the tensile strain becomes

$$\varepsilon_{1,n} = \frac{1}{2} \left(\frac{V_0}{c_1} \right)^2 [1 - (1 - \alpha)^n]^2 \quad \eta \rightarrow 0. \quad (7.191)$$

As shown in Figs. 7-46 and 7-47, the final tensile strain increases with the mass ratio and the time interval.

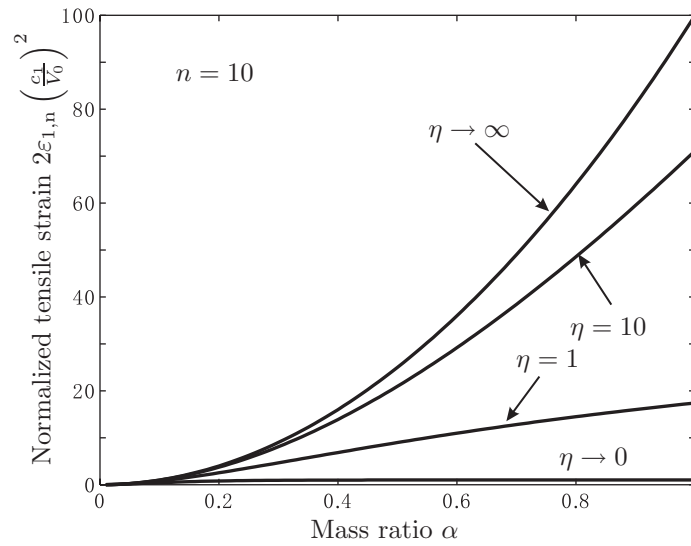


Fig. 7-46: Tensile strains versus mass ratios for different time intervals for Case 1.

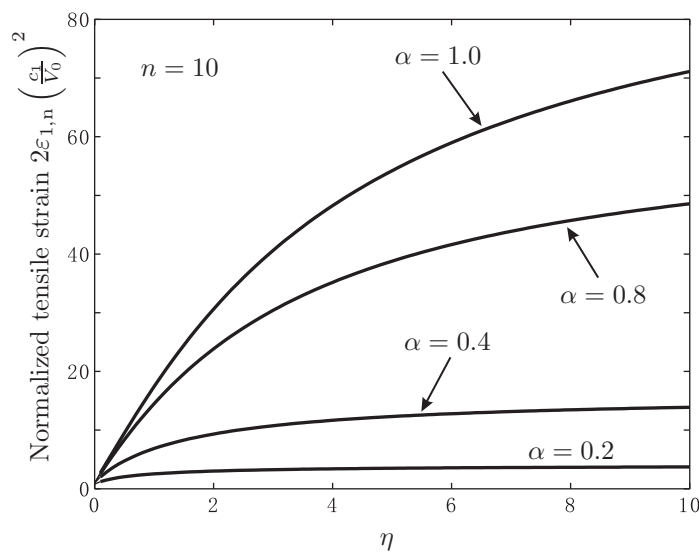


Fig. 7-47: Tensile strain versus time intervals for different mass ratios for Case 1.

Similarly to the double impact case, it is assumed that the struck beam fails by tensile tearing, and the struck beam does not have any damage before the final impact. Hence, the critical velocity to fracture the struck beam is given by setting $\varepsilon_{1,n} = \bar{\varepsilon}_{1,f}$ in Eq. (7.183),

$$\frac{V_{1,cr}}{c_1} = \frac{\sqrt{2\bar{\varepsilon}_{1,f}}}{\alpha\gamma_n}. \quad (7.192)$$

Alternatively, with the impact velocity V_0 given, one can determine the critical impact number n_{cr} to fracture the struck beam, as shown in Fig. 7-48. The discrete points are calculated at specific values of α and η . These points are fitted with two smooth solid curves for two cases.

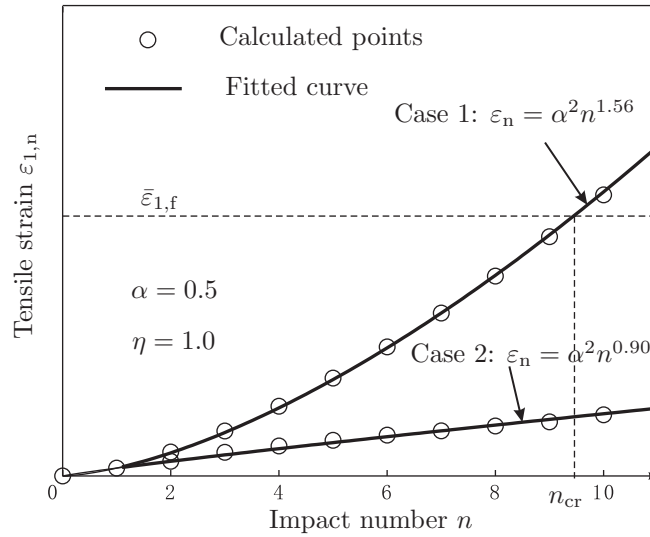


Fig. 7-48: Tensile strain versus impact number.

7.4.3.5 Multiple rigid mass impact

In the preceding section, the case that no parts of the striking beams remain in contact with the struck beam after the impact was formulated and solved. Here it is assumed that all the striking beams break immediately upon impact, and the remainder of the striking beams in the impacted zone sticks to the struck beam and moves with it. Similarly, this case is equivalent to the case of the struck beam impacted multiply by the identical rigid masses with the mass $M_0 = 2m_2b_1$.

The problem is solved in the same procedure as that in the preceding case. Assume that we have solved the velocity field after the j_{th} impact. Now, we want to determine the velocity after the $(j+1)_{\text{th}}$ impact. The momentum conservation upon the $(j+1)_{\text{th}}$ impact in the impacted zone is expressed as

$$2m_2b_1V_0 + (j \cdot 2m_2b_1 + 2m_1b_2) V_{1,j}(jt_0) = [(j+1) \cdot 2m_2b_1 + 2m_1b_2] V_{1,j+1}^*, \quad (7.193)$$

which gives the instantaneous velocity, $V_{1,j+1}^*$,

$$\frac{V_{1,j+1}^*}{V_0} = \frac{\alpha}{j\alpha + 1} + \left(1 - \frac{\alpha}{j\alpha + 1}\right) \frac{V_{1,j}(jt_0)}{V_0}. \quad (7.194)$$

Based on the assumption, the transverse momentum is conserved at any time with regard to the velocity increment $\Delta V_{1,j+1}$,

$$[2m_1b_2 + (j+1)2m_2b_1] \Delta V_{1,j+1}^* = [2m_1b_2 + (j+1)2m_2b_1 + 2m_1c_1(t - jt_0)] \Delta V_{1,j+1}(t), \quad (7.195)$$

where $\Delta V_{1,j+1}^*$ is the velocity increment upon the $(j+1)_{\text{th}}$ impact, defined by

$$\frac{\Delta V_{1,j+1}^*}{V_0} = \frac{V_{1,j+1}^*}{V_0} - \frac{V_{1,j}(jt_0)}{V_0} = \frac{\alpha}{j\alpha + 1} \left(1 - \frac{V_{1,j}(jt_0)}{V_0}\right). \quad (7.196)$$

In terms of α and η , $\Delta V_{1,j+1}(t)$ can be expressed as

$$\frac{\Delta V_{1,j+1}(t)}{\Delta V_{1,j+1}^*} = \frac{j\alpha + 1}{j\alpha + 1 + (1 - \alpha)\eta(t/t_0 - j)}. \quad (7.197)$$

Particularly, at $t = (j + 1) t_0$,

$$\frac{\Delta V_{1,j+1}((j+1)t_0)}{\Delta V_{1,j+1}^*} = \frac{j\alpha + 1}{j\alpha + 1 + (1 - \alpha)\eta}. \quad (7.198)$$

With every velocity increment known, one can obtain the velocity $V_{1,j}(t)$ from Eq. (7.170), and further the slope at $x = 0$ can be obtained from Eq. (7.175). As opposed to the preceding case, no recursion formula was found. A short computational routine was developed to calculate the tensile strain with the mass ratio, α , the time parameter, η , and the impact number, n , given. Numerical results for specific cases are shown in Figs. 7-49 and 7-50, and compared to Case 1. It appears that the tensile strains in Case 1 are much larger than those in Case 2. Similarly to the double impact case, the tensile strain does not increase monotonically with the mass ratio, Fig. 7-49.

Two limiting cases are also investigated as follows. First, if the time interval t_0 goes infinity, the velocity in the struck beam becomes infinitesimal until the next impact. Hence, in this case,

$$\Delta V_{1,j}^* = V_{1,j}^*. \quad (7.199)$$

The total mass in the impacted zone in the struck beam increases by $2m_2b_1$ after every impact. After the j th impact, the velocity $V_{1,j}^*$ is obtained from the momentum conservation,

$$\frac{\Delta V_{1,j}^*}{V_0} = \frac{V_{1,j}^*}{V_0} = \frac{2m_2b_1}{j \cdot 2m_2b_1 + 2m_1b_2} = \frac{\alpha}{(j-1)\alpha + 1}. \quad (7.200)$$

Substituting the expression for every velocity into Eq. (7.175), one can obtain the slope at $x_1 = 0$, and further the tensile strain in the struck beam after the n th impact

$$\varepsilon_{1,n} = \frac{1}{2} \left(\frac{V_0}{c} \right)^2 \left[\sum_{j=1}^n \frac{\alpha}{1 + (j-1)\alpha} \right]^2 \quad \eta \rightarrow \infty. \quad (7.201)$$

As shown in Fig. 7-50, the tensile strain approaches to an asymptotic value as the time interval increases.

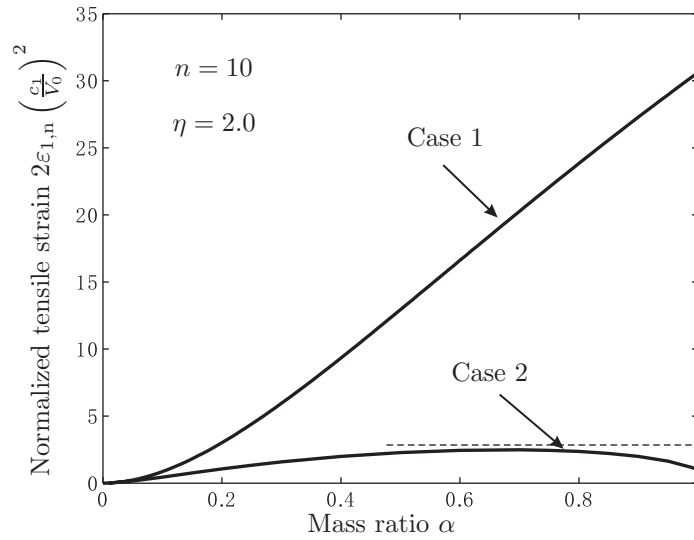


Fig. 7-49: Comparison of tensile strains versus mass ratio between Case 1 and Case 2.

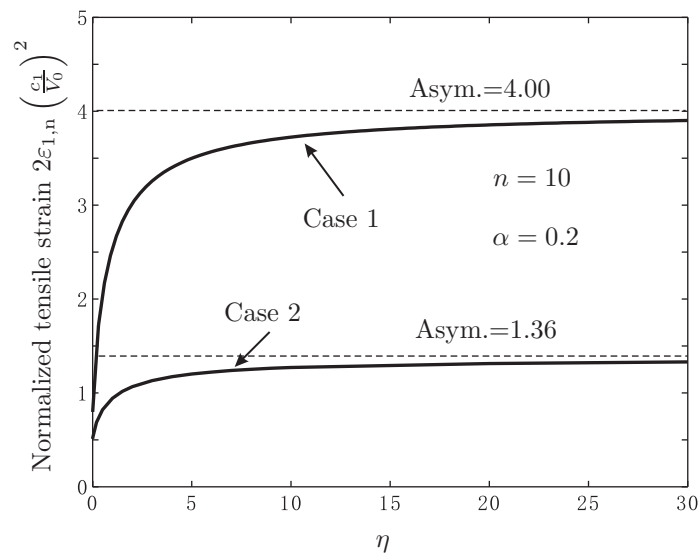


Fig. 7-50: Comparison of tensile strains versus time interval between Case 1 and Case 2.

Now consider another limiting case that the time interval t_0 becomes infinitesimal. No shock waves propagate away from the impacted zone until the whole impact process is finished. Similar to the limiting case with $\eta \rightarrow 0$ in Case 1, the slope after the n_{th} impact depends only on the velocity upon the last impact, $V_{1,n}^*$. $V_{1,n}^*$ can be obtained from the momentum conservation

$$\frac{V_{1,n}^*}{V_0} = \frac{n \cdot 2m_2b_1}{n \cdot 2m_2b_1 + 2m_1b_2} = \frac{n\alpha}{(n-1)\alpha + 1}. \tag{7.202}$$

Hence, the tensile strain $\varepsilon_{1,n}$ after the n_{th} impact is given by

$$\varepsilon_{1,n} = \frac{1}{2} \left(\frac{V_0}{c} \right)^2 \left(\frac{n\alpha}{(n-1)\alpha + 1} \right)^2 \quad \eta \rightarrow 0. \tag{7.203}$$

Figure 7-51 shows the relations between the tensile strain and the mass ratio for different values of η . The critical mass ratio α corresponding to the extreme value of the tensile strain increases with the time interval η , and approaches unity as η becomes infinity.

Note, that no assumptions are introduced in the asymptotic analysis. Good agreements between the asymptotic analysis and the general solutions for large values of η verify the correctness of the additional assumption introduced in Section 7.4.3.1.

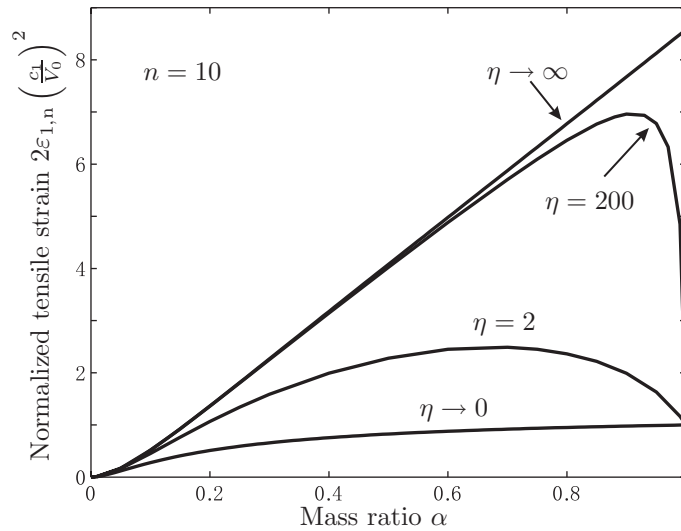


Fig. 7-51: Tensile strains versus mass ratios for different values of η for Case 2.

7.4.4 Partial conclusions

The problem of multiple impact of beam-to-beam was formulated based on the rigid-plastic beam/string model. In the case of the double impact, the closed-form solutions were obtained for the deflection profile, the transverse velocity, and the tensile strain. By assuming the failure mode of tensile necking, the critical impact velocity to fracture the struck beam was predicted. In the case of the multiple impact, a recursion formula with respect to the impact number was found to calculate the tensile strain. A computational routine was composed to solve the critical impact velocity to fracture the struck beam with the impact number given, and to determine the critical impact number with the impact velocity given. Asymptotic analyses were performed for two limiting cases that the time interval goes either infinity or is kept infinitesimal.

It was assumed that all the striking beams fail by shear plugging immediately upon impact. In reality, the striking beams may fail by other modes or keep intact. If all the possible failure modes are taken into account at the same time, the problem may become intractable theoretically and can only be treated in a numerical way.

7.5 Dynamic shear plugging

7.5.1 Introduction

In general, a metallic beam/plate impacted by a heavy, flat-nosed projectile traveling at a sub-ordnance velocity fails by shear plugging. Due to lateral constraints, the material in the impacted zone of the target beneath the projectile moves forwards, and acquires a common velocity with the projectile. When indentation reaches a certain depth, two cracks are induced by the sharp corners of the flat-nosed mass, and rapidly grow ahead of the projectile. Finally, the impacted zone is sheared off from the surrounding material and ejected as a plug. At the same time, a portion of transverse momentum of the projectile is transferred to the surrounding region leading to global deformation of the target.

Many theoretical perforation models that emphasize various mechanisms have been proposed in the literature. Comprehensive reviews on this subject were given by Anderson & Bodner [43] and Corbett et al. [44]. Based on both principles of momentum and energy conservation, Retch and Ipson [144] developed an expression for the residual velocity of a projectile provided that the ballistic limit of a target was known. Friction between the projectile and the target was taken into account by Woodward and Morton [145] in the problem formulation. Woodward [146] also introduced an improved solution that considers the combined bending-membrane response of a target. A two-stage perforation model including indentation and shear sliding was built by Averbuch [147]. In the subsequent paper, Averbuch and Bodner [148] added an intermediate stage, in which inertia force, compressive resistance, and shear resistance act simultaneously on the impacted zone. A five-stage plugging model coupled with global structural response was suggested by Liss et al. [149], which is capable of predicting the residual velocity of the projectile and the deflection profile of the target as well as the force acting on the projectile. This model was further extended to the case of a deformable projectile by Liss and Goldsmith [150]. The problem of a membrane perforated by a rigid projectile was studied by Wierzbicki and Hoo Fatt [11], and a closed-form solution for the ballistic limit was given. A theoretical model considering simultaneously bending, stretching, and shearing was developed by Liu and Stronge [151] in which the velocity field of a target was derived from the Tresca yield

surface. Jones et al. [152] investigated theoretically the perforation response of a finite plate by accounting for the influence of the transverse shear force, the radial and circumferential bending moments, and the radial and circumferential membrane forces in governing equations. Recently, Chen and Li [153] proposed a coupled shear-bending solution for a circular plate struck by a rigid mass and gave an explicit expression for the ballistic limit.

Due to complexity of the problem, most of the theoretical models mentioned above have to resort to numerical procedures to solve equations of motion of the plug and of deflection of the target, which are usually represented by a system of ordinary differential equations (ODEs). A question was raised by Anderson & Bodner [43] and Zukas [154] whether it is worthwhile to develop such complicated theoretical models. They argued that it would not take many efforts to model the perforation process using finite element codes or other numerical codes on high performance personal computers available to date. The accuracy of numerical simulations would depend on the success in developing adequate criteria for initiation and propagation of cracks. However, we believe that simple analytical solutions are still complementary to numerical simulations for complicated problems, as they help identify dimensionless groups of parameters and are suitable for making a parametric study. Such a solution is developed in the present research.

An assumption is implied in most of theoretical analysis that the plug is completely separated from the surrounding material when the head of the projectile arrives at the distal surface of the target. Such a simplification is tempting and it was uniformly accepted, because it is difficult to track down the crack growth in perforation experiments. Perforation experiments performed recently by Børvik et al. [56] indicate that the cracks propagate ahead of the projectile, i.e. the plug is completely formed even when the head of the projectile is still inside the target. This phenomenon is taken into account in the present problem formulation.

In many theoretical solutions presented in the literature, both shear force and bending moment in the ligament were assumed to be constant, which results in a conclusion that the size of the plastically deformed region of a target is fixed during the whole perforation process, e.g. Chen and Li [153]. In reality, as the cracks propagate through the target thickness, the resistance in the ligament decreases, and the plastic bending hinges travel to

far-fields. In the present solution, the shear force is variable, which gives a more accurate result.

Earlier theoretical solutions made use of some empirical data. For example, an elementary fracture criterion with $k = 1$, defined in Eq. (7.207), was used to predict the formation of a plug [152, 153], which supposes that the whole impacted area is sheared off only when the projectile head reaches the distal surface of the target. An average width of a shear zone was assumed in Averbuch and Bodner's three-stage model [148]. By contrast, these empirical parameters can be determined explicitly from the present solution.

As demonstrated in Chapter 4 by the detailed numerical simulations of the perforation process, local plastic indentation and crack growth are two of the most important mechanisms for a thin or intermediately thick plate/beam under rigid projectile impact. A simple analytical expression relating the indentation depth to the crack length has been developed. The objective of the present section is to apply this expression to construct a new dynamic perforation model. The whole process is divided into two stages. In the first stage, plastic indentation is the main mechanism, and a shock wave approach is used to solve the response in the impacted zone. In the second stage, crack growth is dominant, and the problem is formulated based on force equilibrium. Closed-form expressions for instantaneous velocities, residual velocities, plastic energy, shear zone width, and crack propagation speeds are obtained. A coupled shear-tension model that takes into account global deformation of the target is also developed, which improves the prediction of ballistic limits. Comparisons of the present solutions with both virtual and real experiments are made showing rather good correlations.

7.5.2 Critical indentation depth

Before formulating the problem, let us introduce an important variable: critical indentation depth u_{cr} . This parameter is defined as the relative displacement between the projectile head and the proximal surface of the target when the cracks reach the distal surface, see Fig. 4-1. The critical indentation depth can be obtained by setting the crack length equal

to the target thickness, i.e. $a = h$, in Eq. (4.1),

$$\frac{u_{\text{cr}}}{h} = \frac{K^{-\frac{1}{\lambda}} V_0}{(1 + \mu) c}, \quad (7.204)$$

By combining Eqs. (4.1) and (7.204), the relationship between the crack length and the indentation depth can be recast in a simpler form:

$$\frac{a}{h} = \left(\frac{u}{u_{\text{cr}}} \right)^\lambda. \quad (7.205)$$

Introducing a dimensionless factor, k ,

$$k = \frac{K^{-\frac{1}{\lambda}} V_0}{1 + \mu c}, \quad (7.206)$$

the critical indentation depth can be rewritten as

$$u_{\text{cr}} = kh. \quad (7.207)$$

This expression with a constant value of k was proposed first by Jones [155] to predict transverse shear failure of a beam under explosive loading. Here, an explicit expression for k is given as a function of the mass ratio, the impact velocity, and the material properties of a target, Eq. (7.206). This is a major improvement over the elementary fracture criterion, in which k is an empirical data. Usually, the crack propagates much faster than the projectile, and thus $k < 1$. Jouri and Jones [156] performed a series of low-velocity impact experiments on double-shear specimens and found that $k = 0.2 \sim 0.4$ depending on the thickness of specimens and the ductility of materials. A limited number of numerical simulations of high velocity impact indicate that k ranges from 0.2 to 0.5 [59]. $k = 1$ is commonly used in the literature, e.g. Jones et al. [152], Chen and Li [153], mainly because of the resulting simplification. As a consequence, the energy dissipated in shear cracking would be overestimated.

7.5.3 Perforation analysis for a circular plate

As observed from numerical simulations of shear plugging [59, 55], two cracks usually initiate near the sharp corners of the flat-nosed projectile, and grow along an almost straight path through the thickness of the target. In the case of a circular plate, a circumferential crack is formed. The ejected plug retrieved from tests was found to be slightly lighter than the mass within the impacted zone [100]. Hence, it is reasonably assumed that the whole impacted zone is sheared off from the target as a plug during the perforation process.

In high velocity impact, the perforation duration is very short (roughly $10 - 100 \mu\text{s}$), and thus there is not much time to transfer the transverse momentum from the projectile to the surrounding material of the target. The global deflection of the target is usually small compared with the target thickness. As a first approximation, only localized shear deformation in a narrow region is taken into account in the present formulation. The coupled shear-tension solution accounting for the global deformation of a target will be presented later on.

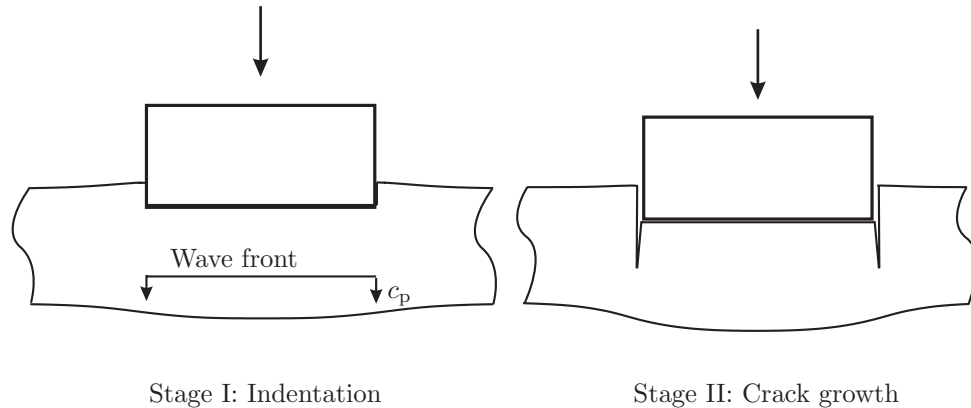


Fig. 7-52: Schematic representation of two stages: indentation and crack growth.

Two main mechanisms are involved in high velocity perforation: indentation of the impacted zone and crack growth forming a plug. In the present paper, the whole failure process is divided into two separated but interconnected stages: (i) dominant indentation accompanied with very slow crack growth, and (ii) rapid crack growth of a varying speed, see Fig. 7-52. The present model is much simpler than Averbuch and Bodner's three-stage model [148] and Liss et al.'s five-stage model [149]. In the first stage, the impacted zone

of the target beneath the projectile is accelerated by the projectile until the the whole impacted zone acquires a common velocity with the projectile. In the second stage, the cracks initiating in the first stage rapidly grow through the target thickness, and the impacted zone is separated from the surrounding material. This stage will end when the cracks reach the distal surface of the target, i.e. a plug is completely formed. Since the crack propagation speed is much higher than the impact velocity, the projectile head is still inside the target at the end of the second stage. It is assumed that the projectile will slide off from the target without friction in the remainder of the perforation process.

7.5.3.1 Stage I: indentation

Immediately upon impact, a plastic shock wave is generated at the impact interface. The wave propagates through the target thickness. The compressive stress behind the wave front decelerates the projectile, and simultaneously pushes the material in the impacted zone to move forwards. Compared with the axial compressive stress, lateral shear force acting on the impacted zone can be neglected. Hence, the indentation of the impacted zone by the projectile can be simplified as a stationary, free body impacted by a rigid moving projectile, as shown in Fig. 7-53. This computational model corresponds to either an inverse Taylor test in which a plastic projectile impacts against a rigid wall [61], or a dynamic compression test that a specimen placed on a rigid anvil is struck by a rigid projectile [157].

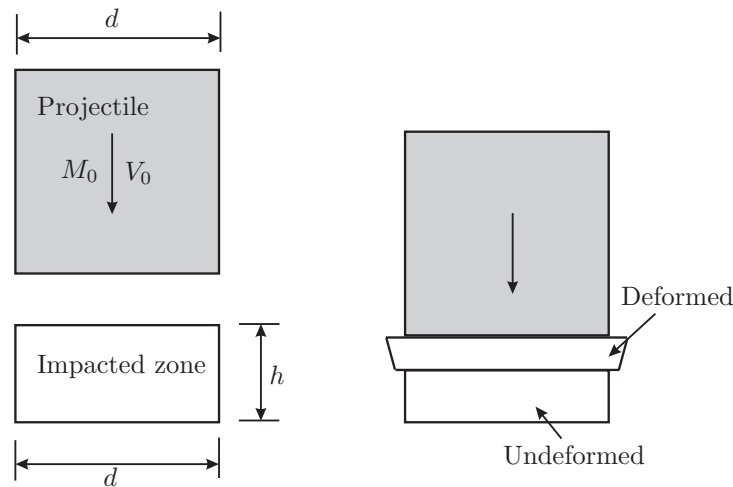


Fig. 7-53: Schematic representation of a free, stationary plastic body struck by a rigid projectile.

It is assumed that the plastic shock wave propagates at a constant velocity c_p . Behind the wave front, the deformed region of the plug moves as a rigid body with the projectile. Ahead of the wave front, the undeformed region of the plug is still at rest. Across the wave front, the compressive plastic stress jumps from σ_0 to 0. Hence, for both the deformed region and the projectile, the equation of motion is given by

$$\frac{d}{dt} \left[\left(M_0 + \rho \frac{\pi}{4} d^2 c_p t \right) V \right] = 0. \quad (7.208)$$

The stage of indentation ends when the plastic shock wave reaches the distal surface of the plug. The duration of this stage is

$$t_1 = \frac{h}{c_p} \quad (7.209)$$

Integrating Eq. (7.208) with respect to time gives the transient velocity of the projectile

$$\frac{V}{V_0} = \frac{1}{1 + \mu c_p t / h}, \quad (7.210)$$

where the initial condition has been used: $V = V_0$ at $t = 0$. At $t = t_1$, the whole plug acquires the common velocity, V_0^* , with the projectile,

$$\frac{V_0^*}{V_0} = \frac{1}{1 + \mu}. \quad (7.211)$$

Note, that V_0^* can be obtained directly from the principle of momentum conservation without resorting to the shock wave approach.

Integrating the velocity of the projectile with respect to time gives the indentation depth of the target, u ,

$$\frac{u}{h} = \frac{1}{\mu} \frac{V_0}{c_p} \ln \left(1 + \mu \frac{c_p t}{h} \right). \quad (7.212)$$

Setting $t = t_1$ in the above equation yields the indentation depth at the end of the first stage, u_1 ,

$$\frac{u_1}{h} = \frac{\ln(1 + \mu)}{\mu} \frac{V_0}{c_p}. \quad (7.213)$$

The indentation is due to the compressive plastic wave, hence u_1 can be thought of as the shortening of the plug. The linear relation between the shortening of the plug and the

initial impact velocity indicated by Eq. (7.213) is consistent with the experimental results by Børvik et al. [100]. Eq. (7.213) provides one possibility of estimating the plastic shock wave speed from tests by measuring the shortening of a recovered plug. Since Eq. (4.1) governs the relationship between the indentation depth and the crack length over the whole process, the crack length at the end of the first stage, a_1 , is given by

$$\frac{a_1}{h} = \left(\frac{u_1}{u_{cr}} \right)^\lambda = \left[\frac{1 + \mu}{\mu} \ln(1 + \mu) \frac{c}{c_p} \right]^\lambda. \quad (7.214)$$

Note, that the plastic shock wave speed is an order of magnitude higher than the initial impact velocity and the transverse plastic stress wave, c . For example, the shock wave speed of 2024 aluminum alloy ranges from 5,300 to 7,700 m/s as an increasing function of pressure [158], while the impact velocity is of the same order of magnitude as the transverse plastic stress wave, i.e. $V_0 \sim c$, and $c = 457.6$ m/s. Therefore, a_1 can be neglected compared with the response in the second stage.

7.5.3.2 Stage II: crack propagation

At the end of the first stage, the whole plug acquires the common velocity, V_0^* , with the projectile. In the second stage, the plug moves as a rigid body with the projectile, and the cracks initiating in the first stage rapidly grow ahead of the projectile. The shear force exerted by the surrounding material decelerates both the plug and projectile until the cracks reach the distal surface of the target. Finally, both the plug and projectile will exit at a residual velocity.

The inertia force of the projectile-plug system is balanced by shear force acting on the ligament, i.e.

$$M_0 (1 + \mu) \frac{d^2 u}{dt^2} = -k_1 (h - a), \quad (7.215)$$

where k_1 is the shear force per unit length, for a circular plate,

$$k_1 = \pi d \tau_0, \quad (7.216)$$

where $\tau_0 = \sigma_0 / \sqrt{3}$ is the plastic shear flow stress from the von-Mises yield criterion. Most

of theoretical solutions in the literature do not account for the fact that the shear resistance decreases with the crack growth. Note, $V = du/dt$, and thus Eq. (7.215) can be recast as

$$M_0 (1 + \mu) V dV = -k_1 h \left(1 - \frac{a}{h}\right) du. \quad (7.217)$$

Substituting the expression for a/h given in Eq. (4.1) and integrating the above equation yields the transient velocity of the projectile as a function of the indentation depth

$$\left(\frac{V}{c}\right)^2 = \left(\frac{V_0^*}{c}\right)^2 - \frac{8}{\sqrt{3}} \frac{h}{d} \frac{\mu}{1 + \mu} \left(\frac{u}{h} - \frac{1}{1 + \lambda} \frac{u a}{h} - \frac{u_1}{h} + \frac{1}{1 + \lambda} \frac{u_1 a_1}{h}\right), \quad (7.218)$$

where the initial condition of the second stage has been used: $V = V_0^*$ and $u = u_1$. The residual velocity of the projectile, V_r , is obtained by setting $a = h$ and $u = u_{cr}$ in the above equation

$$\left(\frac{V_r}{c}\right)^2 = \left(\frac{V_0^*}{c}\right)^2 - \frac{8}{\sqrt{3}} \frac{\mu}{1 + \mu} \frac{\lambda}{1 + \lambda} \frac{u_{cr}}{d} + \frac{8}{\sqrt{3}} \frac{\mu}{1 + \mu} \frac{u_1}{d} \left(1 - \frac{1}{1 + \lambda} \frac{a_1}{h}\right). \quad (7.219)$$

By neglecting the contribution of the first stage, the residual velocity is approximated as

$$\left(\frac{V_r}{c}\right)^2 \approx \left(\frac{V_0^*}{c}\right)^2 - \frac{8}{\sqrt{3}} \frac{\mu}{1 + \mu} \frac{\lambda}{1 + \lambda} \frac{u_{cr}}{d}. \quad (7.220)$$

Setting $V_r = 0$ in Eq. (7.220) yields the ballistic limit of the target

$$\frac{V_{bl}}{c} = \frac{8}{\sqrt{3}} \frac{\lambda}{\lambda + 1} \frac{h}{d} \frac{\mu}{K^{1/\lambda}}. \quad (7.221)$$

This predicted ballistic limit is expressed in terms of all the input parameters of the problem. However, the value of V_{bl} is underestimated because the transverse momentum transferred to the surrounding material is neglected. An improved solution considering the global deformation of the target will be given later on.

The physical time in the second stage can be related to the indentation depth by

$$\begin{aligned} t &= \int_0^u \frac{1}{V} du \\ &= \int_0^u \left[(V_0^*)^2 - \frac{8}{\sqrt{3}} \frac{h}{d} \frac{\mu}{1+\mu} \left(\frac{u}{h} - \frac{1}{1+\lambda} \frac{u}{h} \left(\frac{u}{u_{cr}} \right)^\lambda \right) c^2 \right]^{-1/2} du, \end{aligned} \quad (7.222)$$

which can be integrated using numerical methods. Setting the upper limit of the above integral $u = u_{cr}$ gives the time duration of the second stage

$$t_2 = \int_0^{u_{cr}} \left[(V_0^*)^2 - \frac{8}{\sqrt{3}} \frac{h}{d} \frac{\mu}{1+\mu} \left(\frac{u}{h} - \frac{1}{1+\lambda} \frac{u}{h} \left(\frac{u}{u_{cr}} \right)^\lambda \right) c^2 \right]^{-1/2} du. \quad (7.223)$$

The time duration, t_2 , can also be quickly estimated by assuming the uniform deceleration of the projectile in the second stage

$$t_2 = \frac{2u_{cr}}{V_0^* + V_r}. \quad (7.224)$$

The duration of the whole perforation process is given by

$$t_f = t_1 + t_2 + \frac{h - u_{cr}}{V_r}, \quad (7.225)$$

where the third term in the right hand side represents the duration that the projectile passes through the rest of the target thickness after the plug is completely formed. For a thin or intermediately thick plate, the third component may be larger than the sum of t_1 and t_2 . The perforation time is recorded in some tests, e.g. Børvik et al. [100], and thus it can be used to make a comparison with the present solution.

The loss of the kinetic energy of the plug-projectile system in the second stage is

$$\begin{aligned} \Delta E_2 &= \frac{1}{2} M_0 (1 + \mu) (V_0^*)^2 - \frac{1}{2} M_0 (1 + \mu) (V_r)^2 \\ &= \frac{8}{\sqrt{3}} \frac{h}{d} \frac{c}{V_0} \frac{\lambda}{1 + \lambda} \frac{\mu}{1 + \mu} \frac{E_0}{K^{1/\lambda}}. \end{aligned} \quad (7.226)$$

The lost kinetic energy is dissipated in the form of shear cracking and the plastic deformation of the target. The loss of the kinetic energy in the first stage is given in Eq. (7.28).

7.5.3.3 Crack propagation speed

Differentiating Eq. (7.205) with respect to time gives the instantaneous crack propagation speed, v ,

$$\frac{v}{V} = \lambda \left(\frac{u}{u_{\text{cr}}} \right)^{\lambda-1} \frac{h}{u_{\text{cr}}} \quad (7.227)$$

where $v = da/dt$. Substituting the expression for the instantaneous projectile velocity V , one obtains the crack propagation speed as a function of the indentation depth, u ,

$$\frac{v}{c} = \lambda \left(\frac{u}{u_{\text{cr}}} \right)^{\lambda-1} \frac{h}{u_{\text{cr}}} \sqrt{\left(\frac{V_0^*}{c} \right)^2 - \frac{8}{\sqrt{3}} \frac{\mu}{1+\mu} \frac{u}{d} \left[1 - \frac{1}{1+\lambda} \left(\frac{u}{u_{\text{cr}}} \right)^\lambda \right]}. \quad (7.228)$$

The history of the crack propagation speed for a specific case is shown in Fig. 7-54. It appears that the heavier the projectile and the higher the impact velocity, the faster is the crack propagation speed. Due to the decrease in the shear resistance, the process of the crack propagation is accelerated. The maximum value of the crack growth speed occurs at the end of the process, and is given by

$$\frac{v_{\text{max}}}{c} = \frac{V_r}{c} \frac{\lambda h}{u_{\text{cr}}} = \frac{\lambda h}{u_{\text{cr}}} \sqrt{\left(\frac{V_0^*}{c} \right)^2 - \frac{8}{\sqrt{3}} \frac{\mu}{1+\mu} \frac{\lambda}{1+\lambda} \frac{u_{\text{cr}}}{d}}. \quad (7.229)$$

As can be seen from Fig. 7-54, the crack propagation speed ($\sim 2,000$ m/s) is one order of magnitude higher than the impact velocity of the projectile (~ 200 m/s), and is lower than the elastic Rayleigh wave speed given in Eq. (4.6).

The average crack propagation speed can be approximately expressed as

$$\frac{\bar{v}}{c} = \frac{h}{ct_2} = \frac{V_0^* + V_r}{2c} \frac{h}{u_{\text{cr}}}. \quad (7.230)$$

A plot of the average crack propagation speed vs. the target thickness for a specific case is shown in Fig. 7-55. It is seen that the average crack propagation speed decreases with the increasing target thickness.

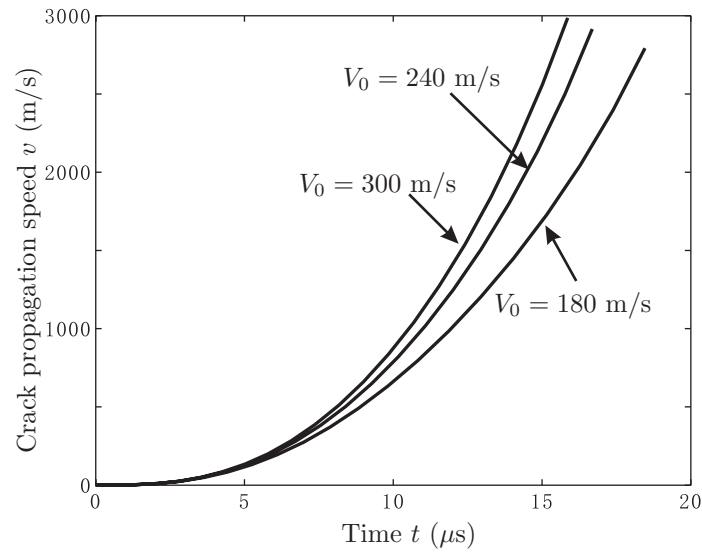
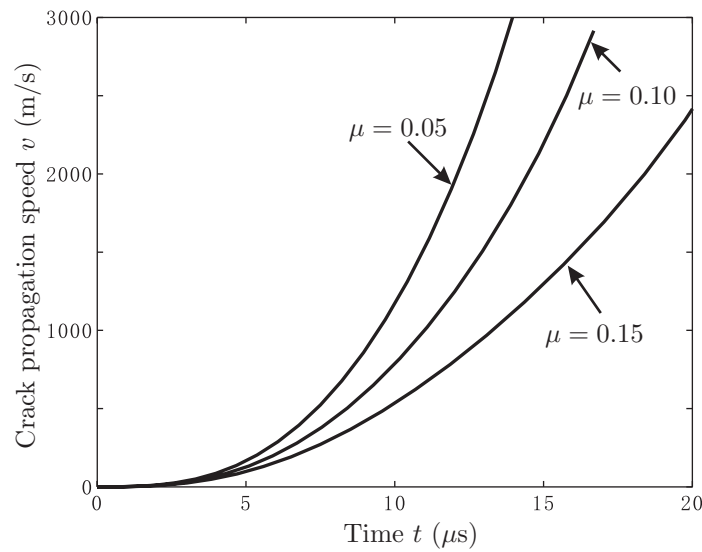
(a) $\mu = 0.1$ for different impact velocities.(b) $V_0 = 240$ m/s for different mass ratios.

Fig. 7-54: Time history of the instantaneous crack propagation speed of a 2024-T351 aluminum alloy circular plate. Other parameters are used: $c = 457.6$ m/s, $h = 10$ mm, $d = 20$ mm, $K = 10$ and $\lambda = 4$.

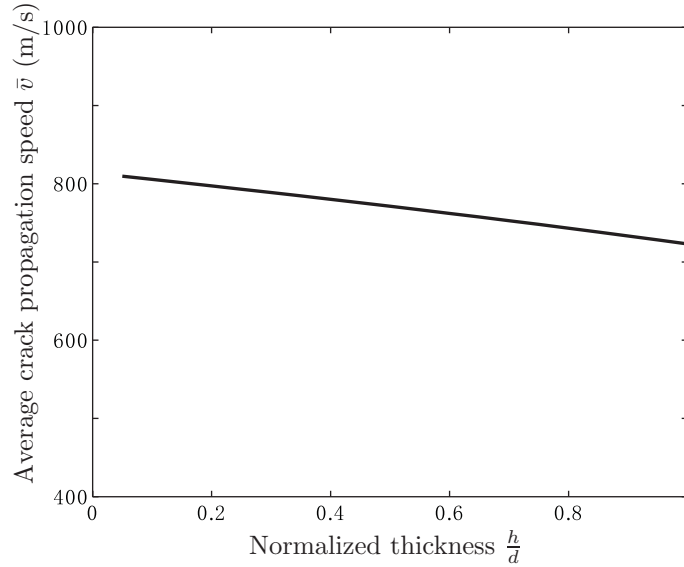


Fig. 7-55: Average crack propagation speed vs. target thickness for a 2024-T351 aluminum alloy circular plate. Other parameters are used: $c = 457.6$ m/s, $V_0 = 240$ m/s, $\mu = 0.1$, and $d = 20$ mm.

7.5.3.4 Shear zone width

As the impacted zone is indented, the surrounding materials of the target rotate due to shearing, and the plastically deformed region grows with indentation, see Fig. 7-56. This kind of plastic deformation is verified by an etched cross-section of a post-perforation aluminum plate (Fig. 1 in Ref. [145]). The plastically deformed region is the widest at the distal surface and the narrowest at the proximal surface, which is different from quasi-static punch tests where the widest deformed region is located in the center through the target thickness [159]. Note, that in quasi-static punch tests the target is supported by rigid anvils while in high velocity perforation the target is supported by its own inertial force. The plastically deformed region is usually called the shear zone since shearing is dominant.

The average width of the shear zone as an empirical data was introduced by Averbuch and Bodner [148] in their three-stage model. By contrast, the width of the shear zone can be determined analytically from the present solution. Following the blanking model

proposed by Zhou and Wierzbicki [159] for quasi-static punch tests, it is assumed that the shear zone consists of numerous parallel material elements with unknown length from the proximal surface to the distal surface, and each material element is subjected to uniform shear deformation. The element grows with the indentation depth, and simultaneously rotates around its center due to shearing. A typical material element located in front of the crack tip is shown in Fig. 7-57. When the propagating crack arrives at this element, the element is about to break. At this time, both the size and rotation angle of the element reach their maximum values. The maximum rotation angle, θ_f , is related to shear fracture strain, γ_f ,

$$\gamma_f = \tan \theta_f = \frac{u}{e} \quad (7.231)$$

where e is the final width of the considered element. Substituting Eq. (4.1) gives the final width of the shear zone as a function of position represented by the crack length a

$$e(a) = \left(\frac{a}{h}\right)^{\frac{1}{\lambda}} \frac{u_{cr}}{\gamma_f} = \left(\frac{a}{h}\right)^{\frac{1}{\lambda}} e_{max} \quad (7.232)$$

where $e_{max} = u_{cr}/\gamma_f$ is the maximum value of the width of the shear zone located at the distal surface.

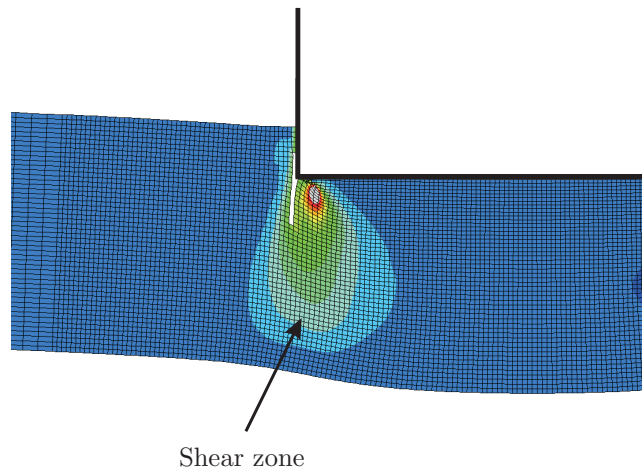


Fig. 7-56: Plastic shear strain contour showing plastically deformed zone around a crack.

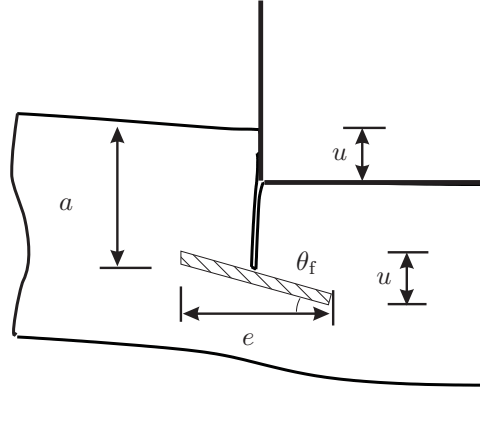


Fig. 7-57: Schematic representation of a shear element in the shear zone.

Alternatively, the average width of the shear zone, \bar{e} , can be calculated by assuming that the loss of the kinetic energy is completely dissipated in shear plastic deformation,

$$\Delta E_2 = \pi dh \bar{e} \tau_0 \gamma_f, \quad (7.233)$$

where $\pi dh \bar{e}$ represents the volume of the shear zone. Substituting the expression for ΔE_2 into the above equation, one obtains the average value of the shear zone width

$$\frac{\bar{e}}{h} = \frac{1}{\gamma_f} \frac{V_0}{c} \frac{1}{1 + \mu} \frac{\lambda}{1 + \lambda} K^{-1/\lambda}. \quad (7.234)$$

The present result that explicitly accounts for the impact velocity and mass of the projectile, and the material properties of the target in the expression for the size of the shear zone is a major improvement over Li and Jones's solution [77], in which a constant value, $\bar{e} = 0.866h$, was given. This value is much larger than that predicted by Eq. (7.234), e.g. $\bar{e} = 0.41h$ for $\gamma_f = 1$, $K = 10$, $\lambda = 4$, $\mu = 0.1$, and $V_0 \approx c$. Woodward and Morton [145] presented a photo of an etched post-test aluminum specimen clearly showing plastic slip lines around the impacted area. A rough estimation gives the average width of the shear zone about one-third of the target thickness. This experimental data is much closer to the present prediction than the theoretical value given by Li and Jones [77].

7.5.4 Perforation analysis for a beam

In the preceding section, the case of a circular plate perforated by a cylindrical projectile was investigated. Now consider a beam impacted by a rigid, flat-nosed, high velocity projectile. Due to various expressions for the shear force per unit length, results for a beam are slightly different from those for a circular plate.

The problem can be formulated in a similar way as presented for the case of a circular plate. Some important results are summarized in the following. First, the shear force per unit length in a beam is given by

$$k_1 = 4b\tau_0. \quad (7.235)$$

The instantaneous velocity of the projectile is

$$\left(\frac{V}{c}\right)^2 = \left(\frac{V_0^*}{c}\right)^2 - \frac{4}{\sqrt{3}} \frac{h}{d} \frac{\mu}{1+\mu} \left(\frac{u}{h} - \frac{1}{1+\lambda} \frac{u}{h} \frac{a}{h}\right). \quad (7.236)$$

Setting $a = h$ and $u = u_{\text{cr}}$ in the above equation, one obtains the residual velocity of the projectile

$$\left(\frac{V_r}{c}\right)^2 = \left(\frac{V_0^*}{c}\right)^2 - \frac{4}{\sqrt{3}} \frac{\mu}{1+\mu} \frac{\lambda}{\lambda+1} \frac{u_{\text{cr}}}{d}. \quad (7.237)$$

By comparing Eqs. (7.237) with (7.220), it can be seen that the residual velocity of the projectile in the case of a beam is higher than that in the case of a circular plate, if both targets are of the same material, aspect ratio, mass ratio, and impact velocity. This result gives a clear explanation of the difference in the residual velocity history between the beam and the circular plate as shown in Fig. 4-11.

The time duration of the second stage, t_2 , is

$$t_2 = \int_0^{u_{\text{cr}}} \left[(V_0^*)^2 - \frac{4}{\sqrt{3}} \frac{h}{d} \frac{\mu}{1+\mu} \left(\frac{u}{h} - \frac{1}{1+\lambda} \frac{u}{h} \left(\frac{u}{u_{\text{cr}}} \right)^\lambda \right) c^2 \right]^{-1/2} du, \quad (7.238)$$

which is smaller than the value given by Eq. (7.223) provided that the beam and the circular plate are under the same impact conditions. This finding is also consistent with the numerical results presented in Fig. 4-11.

The loss of the kinetic energy of the system in the second stage is

$$\Delta E_2 = \frac{4}{\sqrt{3}} \frac{h}{d} \frac{c}{V_0} \frac{\mu}{1+\mu} \frac{\lambda}{1+\lambda} \frac{E_0}{K^{1/\lambda}}, \quad (7.239)$$

which is half of the corresponding value in the case of a circular plate. However, the average width of the shear zone is the same in both cases.

The instantaneous crack propagation speed for a beam is given by

$$\frac{v}{c} = \lambda \left(\frac{u}{u_{\text{cr}}} \right)^{\lambda-1} \frac{h}{u_{\text{cr}}} \sqrt{\left(\frac{V_0^*}{c} \right)^2 - \frac{4}{\sqrt{3}} \frac{\mu}{1+\mu} \frac{u}{d} \left[1 - \frac{1}{1+\lambda} \left(\frac{u}{u_{\text{cr}}} \right)^\lambda \right]}, \quad (7.240)$$

which predicts that crack propagation is slower in a circular plate than in a beam.

7.5.5 Coupled shear-tension analysis

In the preceding solutions, only localized shear deformation is taken into account in the second stage, and the transverse momentum transferred to the surrounding material is neglected. Hence, the predicted residual velocity of the projectile is underestimated, specially for the case of the initial impact velocity near the ballistic limit of the target.

For either a thin or intermediately thick beam/plate impacted by a projectile at an impact velocity near the ballistic limit, the maximum deflection of the target is larger than or close to the thickness of the target, as observed from the experimental results by Børvik et al. [100], Liss and Goldsmith [150]. Jones [133] proved that when the maximum transverse deflection of a rigid-perfectly plastic beam exceeds one-half of the beam thickness, axial stretching response becomes dominant over bending response. Hence, it is necessary to introduce membrane response for the case with the initial impact velocity near the ballistic limit. Here, a coupled shear-tension solution that accounts for the global deformation of the target is developed. By comparison, most of coupled solutions presented in the literature considered both shear and bending response at the same time, e.g. Jones et al. [152], Chen and Li [153], but not shear/membrane response.

7.5.5.1 Circular plate

In the following, we focus on the response of the projectile-target system in the second stage. The solution for the first stage is the same as the preceding, which provides the initial conditions of the second stage.

Since axial stretching is dominant and bending response is negligible, a beam/plate can be simplified as a string/membrane. Immediately upon impact, transverse disturbances (transverse plastic stress waves) are generated and propagate away from the impacted zone with the constant speed c defined by Eq. (7.4). Note, that this transverse plastic stress wave propagating along the radial direction in the second stage is different from the plastic shock wave c_p through the target thickness in the first stage. The momentum conservation approach, used in the preceding sections for the global membrane response of an impacted beam/string, is extended to the present coupled problem with through-thickness crack propagation. This coupled shear-tension procedure was first developed by Wierzbicki and Hoo Fatt [11] to predict the ballistic limit of a membrane under rigid mass impact. The theoretical solutions were compared with experiments by Calder and Goldsmith [160] showing good correlation. As opposed to the analysis by Wierzbicki and Hoo Fatt [11] in which a constant shear resistance was assumed in the ligament, here, the shear force decreases as the cracks grow through the target thickness. Similarly to the preceding sections, the uniform distribution of the transverse velocity field is assumed in the surrounding material, and the velocity suffers a jump from the impacted zone to the surrounding material, see Fig. 7-58. This type of velocity field is different from the triangular form commonly adopted in the coupled shear-bending solution, e.g. Chen and Li [153].

Applying transverse momentum equilibrium to the projectile-plug system and the surrounding materials of the target, respectively, gives

$$\left\{ \begin{array}{l} \frac{d}{dt} [M_0 (1 + \mu) \dot{w}_p] = -k_1 h \left(1 - \frac{a}{h}\right) \\ \frac{d}{dt} \left\{ \rho \pi h \left[\left(ct + \varsigma + \frac{d}{2}\right)^2 - \frac{d^2}{4} \right] \dot{w}_t \right\} = k_1 h \left(1 - \frac{a}{h}\right) \end{array} \right. , \quad (7.241)$$

where the terms on the left hand side represent the rate of change of the transverse momentum in the projectile-plug system and in the surrounding material, respectively; the terms

on the right hand side represent the shear force in the ligament; t is the time measured from the beginning of the second phase; w_p is the displacement of the plug; w_t is the maximum deflection of the target at $r = d/2$; \dot{w}_p is the velocity of the projectile-plug; \dot{w}_t is the transverse velocity of the surrounding material, which is constant in space and varies with time; and ζ is the initial length of the bending response. The reason for introducing the initial length ζ in the formulation is as follows.

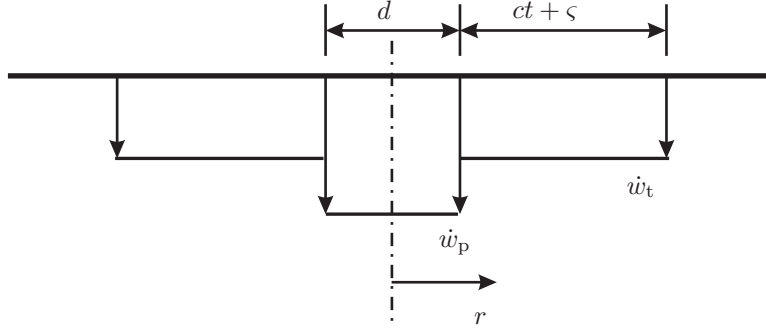


Fig. 7-58: Schematic of a transient velocity profile in a target.

As the transverse momentum is transferred to the impacted zone in the first stage, plastic shear force is generated in the ligament. When the entire impacted zone acquires a common velocity with the projectile, the whole ligament through the target thickness becomes fully plastic. Hence, before entering into the second stage, the surrounding materials are already subjected to the plastic shear force. The bending response of the surrounding material is dominant. The plastic bending hinges travel to far fields as the plastic shear force increases, see Fig. 7-59. At the end of the first stage, the moment equilibrium with respect to the far-field plastic hinge gives

$$\bar{M}_b \pi d + \bar{M}_b \pi (2\zeta + d) = k_1 h \zeta, \tag{7.242}$$

where the contribution of the inertia force of the target is neglected; and $\bar{M}_b = \frac{1}{4} \sigma_0 h^2$ is the fully plastic bending moment per unit length. Solving the above equation yields the

position of the far-field plastic bending hinge

$$\frac{\varsigma}{h} = \frac{1}{2/\sqrt{3} - h/d}, \quad (7.243)$$

where ς is smaller than the target thickness. Mathematically, if the initial length, ς , was set to zero in Eq. (7.241), an unrealistic numerical result that $\dot{w}_t > \dot{w}_p$, i.e. the velocity of the target would be higher than that of the plug, would occur.

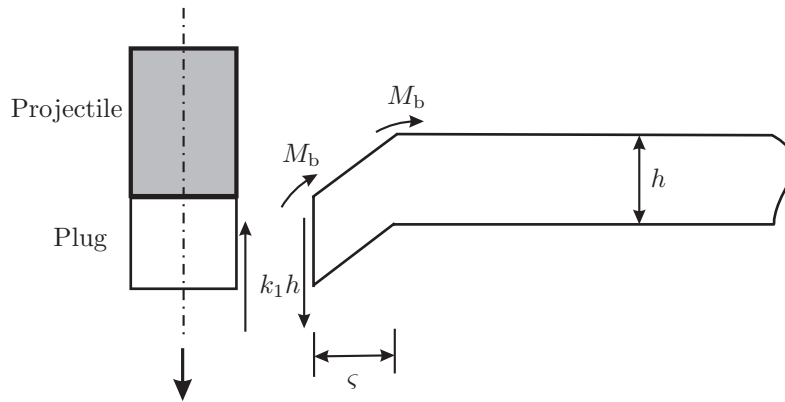


Fig. 7-59: Schematic of the initial length and the bending response.

It can be observed that Eq. (7.243) imposes a restriction condition for the present formulation, i.e. $h/d < 2/\sqrt{3}$. For the case of the aspect ratio larger than this critical value, shear or coupled shear-bending response could be dominant, and a target could be sheared off before entering into the axial stretching phase.

As the deflection increases, the membrane response becomes dominant in the second stage. The plastic hinges continue to travel to far fields with the constant speed, c . By contrast, in the coupled shear-bending solution developed by Jones [133] for the beam case and by Chen and Li [153] for the circular plate case, the plastic bending hinge immediately reaches a certain location and is fixed during the whole impact process. This is a consequence of constant shear resistance and bending moment in the ligament assumed in their formulation.

By means of Eq. (7.205), the crack length is related to both w_p and w_t :

$$\frac{a}{h} = \left(\frac{u}{u_{cr}} \right)^\lambda = \left(\frac{w_p - w_t}{u_{cr}} \right)^\lambda, \quad (7.244)$$

where $u = w_p - w_t$. Thus, Eq. (7.241) furnishes a system of two second-order ordinary differential equations (ODEs) in w_p and w_t , which can be rewritten equivalently as a system of four first-order ODEs:

$$\begin{cases} \dot{I}_p = -k_1 h \left(1 - \frac{a}{h}\right) \\ \dot{w}_p = \frac{I_p}{M_0 (1 + \mu)} \\ \dot{I}_t = k_1 h \left(1 - \frac{a}{h}\right) \\ \dot{w}_t = \frac{I_t}{\rho \pi h \left[\left(ct + \varsigma + \frac{d}{2}\right)^2 - \frac{d^2}{4} \right]} \end{cases}, \quad (7.245)$$

where I_p is the transverse momentum in the projectile-plug system; I_t is the transverse momentum in the surrounding material. The problem is subject to the following initial conditions at $t = 0$

$$I_p = M_0 V_0, \quad w_p = 0, \quad I_t = 0, \quad w_t = 0, \quad (7.246)$$

where the contribution of both the transverse momentum and the deflection in the bending phase (Stage I) to the surrounding material is neglected. The present formulation is much simpler than most of theoretical analyses presented in the literature, where except for the transverse momentum equilibrium, both the angular momentum equilibrium and the energy conservation are involved.

Using the Runge-Kutta finite difference method implemented in the ODE Toolbox of Matlab, a computational routine was developed to solve the above system of ODEs. When the difference between w_p and w_t reaches the critical indentation depth u_{cr} , the routine stops the calculation and outputs the residual velocity of the projectile.

Note, the present shear-tension solution is applied to the case of a thin or intermediately thick plate. For a target whose thickness is comparable to the diameter of the projectile, the bending response is always dominant, and thus it must be taken into account instead

of the axial stretching. Such a coupled shear-bending model with traveling plastic hinges can also be formulated. Corresponding to three unknowns: w_p , w_t , and the location of the plastic bending hinge, a system of three ODEs can be built from transverse momentum equilibrium for the projectile-plug system, angular momentum equilibrium for the target, the energy conservation including the effect of the circumferential bending moment. The problem is more complicated and beyond the scope of the present paper.

7.5.5.2 Beam

The case of a beam can be formulated in the same way as the preceding. The transverse momentum equilibrium gives a system of four first-order ODEs:

$$\left\{ \begin{array}{l} \dot{I}_p = -k_1 h \left(1 - \frac{a}{h}\right) \\ \dot{w}_p = \frac{I_p}{M_0 (1 + \mu)} \\ \dot{I}_t = k_1 h \left(1 - \frac{a}{h}\right) \\ \dot{w}_t = \frac{I_t}{2\rho b h (ct + \varsigma)} \end{array} \right. , \quad (7.247)$$

which are subject to the same initial conditions as Eq. (7.246). Similarly, the initial length is given by

$$\varsigma = \frac{4\bar{M}_b b}{2\tau_0 h b} = \frac{\sqrt{3}}{2} h. \quad (7.248)$$

The present initial length is one third of the value given by Jones [133] where the inertial force was considered in moment equilibrium.

7.5.6 Validation of the analytical solution

7.5.6.1 Experiments on 2024 aluminum alloy plates

Comparison with virtual tests

In Chapter 4.5, a comprehensive parametric study on beams/plates struck by various rigid, flat-nosed projectiles was performed using ABAQUS/Explicit. The constants in Eq. (4.1) $K = 10$ and $\lambda = 4$ for 2024-T351 aluminum alloy were obtained by fitting the

curve of crack growth. With these two material constants known, Eq. (7.218) can be used to predict the transient velocity of the projectile during the perforation process. Figure 7-60 shows a comparison of the velocity history of the projectile for a specific case between the present theoretical prediction and the finite element solution given in Chapter 4.5. The agreement is excellent.

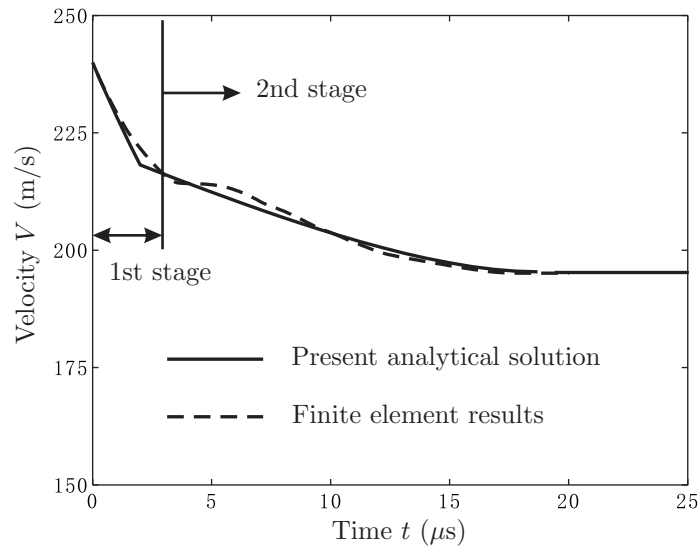


Fig. 7-60: Comparison of the velocity history of the projectile impacting against a circular plate made of 2024-T351 aluminum alloy. The parameters are used: $h = 10$ mm, $d = 20$ mm, $c = 457.6$ m/s, $c_p = 5,000$ m/s, $\rho = 2,700$ kg/m³, $V_0 = 240$ m/s and $\mu = 0.1$.

Comparison with Liss and Goldsmith's tests

Liss and Goldsmith [150] conducted perforation experiments on 2024-O aluminum alloy circular plates. Two material constants $K = 10$ and $\lambda = 4$ for 2024-T351 aluminum alloy are tentatively used here to predict the residual velocity of the 2024-O aluminum alloy plate, see Fig. 7-61. Note, that 2024-T351 is much stronger than 2024-O, but both have approximately the same fracture elongation [161]. It appears that the predicted residual velocities correlate rather well with the experimental results, except that the ballistic limit of the plate of $h = 6.4$ mm is underestimated.

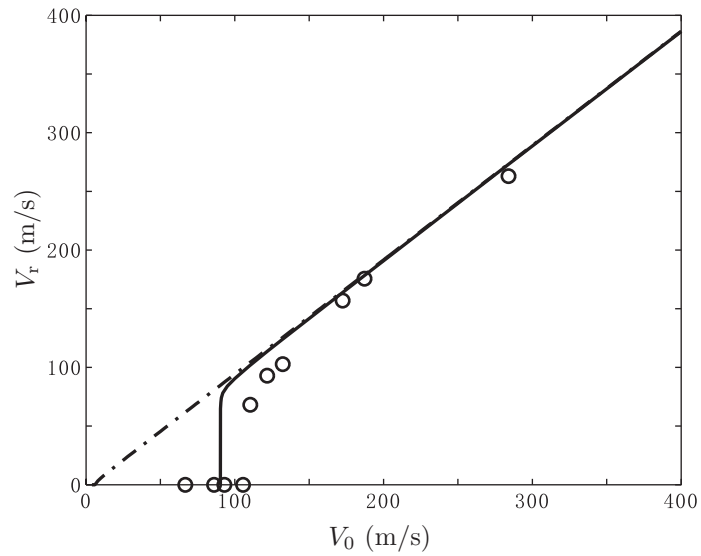
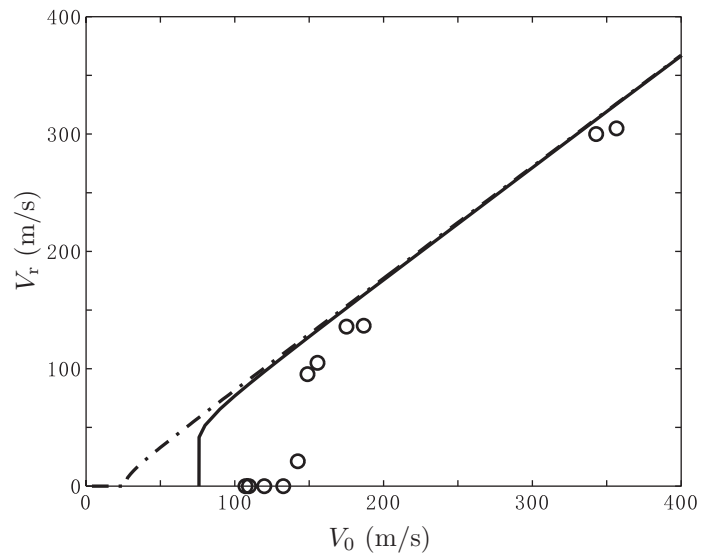
(a) $h = 3.2$ mm(b) $h = 6.4$ mm

Fig. 7-61: Residual velocity vs. impact velocity. The circular points denote Liss and Goldsmith's experimental results [149]. The solid curve represents the coupled shear-tension solution. The dash-dot curve represents the pure shear solution.

7.5.6.2 Experiments on Weldox 460 E steel plates

Børvik et al. [100] performed a series of perforation tests on Weldox 460 E steel plates and provided the abundant experimental results, which allow us to verify the present theoretical solutions.

Shock wave speed

The shock wave is usually related to the impact problem in the range of the ordnance velocity or hypervelocity. A question is naturally raised: are there any shock waves generated in the case with a sub-ordnance impact velocity? To answer this question, three material points of the impacted zone were selected to track the time history of pressure and equivalent stresses for the case of the plate of $h = 10$ mm impacted by the rigid mass moving at $V_0 = 241.5$ m/s, see Fig. 7-62. It appears that the pressure is much higher than the corresponding equivalent stress in the initial phase ($t < 3 \mu\text{s}$). The shock wave travels through the target thickness. Hence, it is reasonable to use the shock wave approach to formulate and solve the response of the impacted zone in the Stage I.

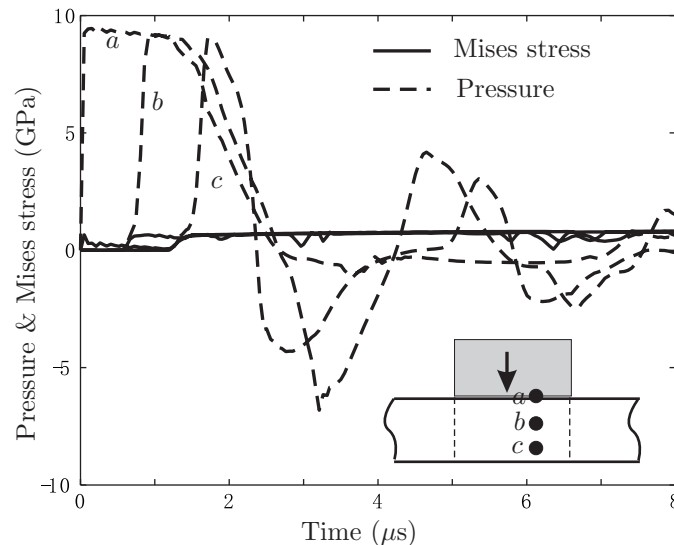


Fig. 7-62: Time history of pressure and equivalent stress of three material points of the impacted area for the case of a Weldox 460 E steel circular plate of $h = 10$ mm impacted by a rigid cylinder moving at $V_0 = 241.5$ m/s.

The plastic shock wave speed can be estimated from the recovered plugs using Eq. (7.213). As shown in Fig. 7-63, the shock wave speed for Weldox 460 E steel under high velocity impact ranges from 2,500 to 6,000 m/s depending on the impact velocity and the target thickness. The shock wave speed is the same order of magnitude as the elastic wave speed (5,172 m/s), but much higher than the transverse plastic stress wave speed ($c = 321$ m/s). At such a high speed, the shock wave immediately arrives at the distal surface of the target. The duration of the first stage is approximately $2.5 \sim 8.0 \mu\text{s}$, and the shortening of the plug is about $5\% \sim 6\%$ of the plate thickness in most cases. Hence, it is reasonable to assume that the impacted zone immediately acquires a common velocity V_0^* with the projectile. The contribution of the first stage to crack growth can be neglected.

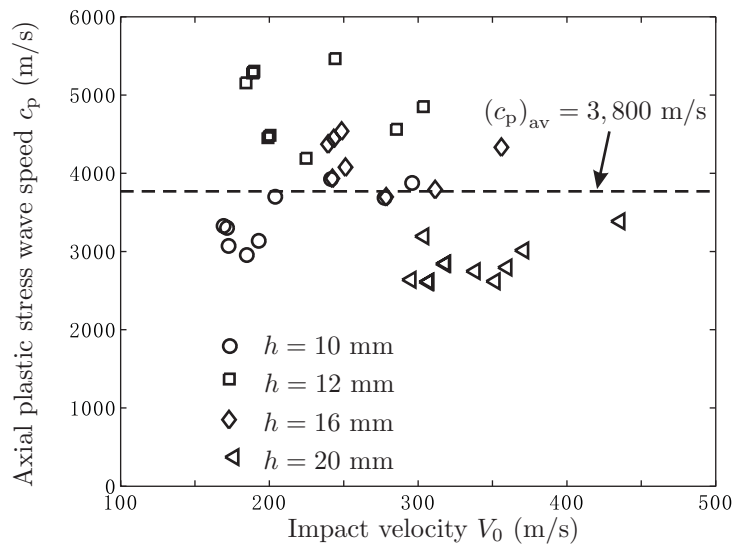


Fig. 7-63: Axial shock wave speed vs. impact velocity for plates with various thicknesses. The shock wave speeds are calculated based on data provided by Børvik et al. [100].

Determination of K and λ

A straightforward way to determine two constants, K and λ , for a specific material is curve-fitting of the relation between the crack length and the indentation depth, if these data are recorded in perforation experiments. Alternatively, K and λ can be obtained by combining the present theoretical analysis and perforation tests. Combining Eqs. (7.204) with (7.220) gives K and λ as a function of the critical indentation depth and the residual

velocity, respectively,

$$\frac{\lambda}{1+\lambda} = \frac{\sqrt{3}}{8} \frac{1+\mu}{\mu} \frac{d}{u_{cr}} \left[\left(\frac{V_0^*}{c} \right)^2 - \left(\frac{V_r}{c} \right)^2 \right], \quad (7.249)$$

and

$$K = \left[(1+\mu) \frac{u_{cr}}{h} \frac{c}{V_0} \right]^{-\lambda}. \quad (7.250)$$

Table 7.1: Comparison of the residual velocity between the experimental and numerical results.

	Thickness	Impact velocity	Experimental	Numerical
	h (mm)	V_0 (m/s)	V_r (m/s)	V_r (m/s)
Case 1	12	224.7	120.43	117.79
Case 2	10	241.5	169.73	164.34
Case 3	10	277.5	201.65	206.0

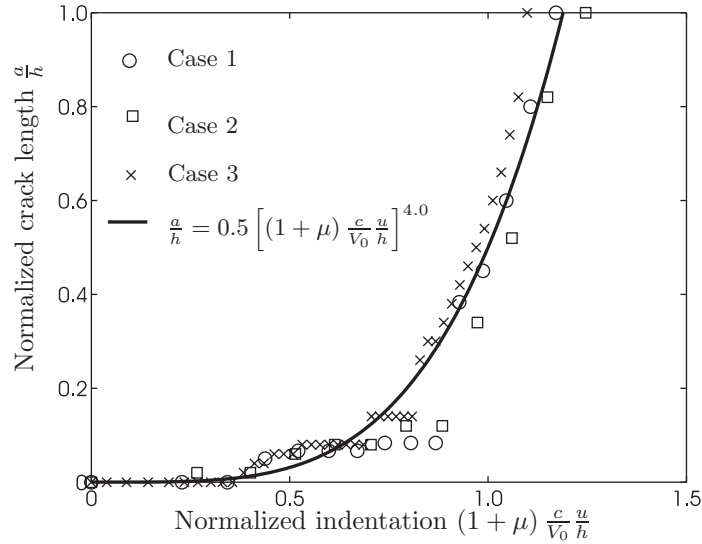


Fig. 7-64: Crack length vs. indentation depth for three cases in Børvik et al.'s tests.

Here, three cases were simulated using ABAQUS/Explicit to determine K and λ for Weldox 460 E steel. The finite element modeling was presented in Chapter 5.3. The calculated residual velocities are listed in Table 7.1. It is seen that all the numerical predictions are quite close to the corresponding experimental values. Plots of the crack length vs. the

indentation depth obtained from the numerical simulations are shown in Fig. 7-64. Curve-fitting gives two constants: $K = 0.5$ and $\lambda = 4.0$ for Weldox 460 E steel. Note, $K = 10.0$ and $\lambda = 4.0$ for 2024-T351 aluminum alloy, which is less ductile than Weldox 460 E steel.

Residual velocities

With the two material constants known, Eq. (7.220) can be used to predict the residual velocity of the projectile. Figure 7-65 shows comparisons between the experimental and predicted results. The target thickness ranges from 6 mm to 20 mm. Due to large difference in the measured residual velocity between the projectile and the plug, the experimental residual velocity is defined in an average sense

$$V_r = \frac{M_0 V_{r,pr} + M_{pl} V_{r,pl}}{M_0 + M_{pl}}, \quad (7.251)$$

where M_{pl} is the mass of the plug, $V_{r,pr}$ and $V_{r,pl}$ are the residual velocities of the projectile and the plug, respectively. It appears that the pure shear solution neglecting the global deformation of the target gives a rather good prediction for the impact velocity higher than 200 m/s. At such a high velocity, the impact duration is so short that the transverse momentum transferred to the surrounding material can be neglected. Most of the kinetic energy is dissipated in the form of plastic shear deformation and plastic compression in the impacted zone. The prediction of the pure shear solution becomes poor as the impact velocities approach the ballistic limits. At a relatively low impact velocity, the maximum deflection of the target is comparable to its thickness, and a rather large portion of the kinetic energy is dissipated in the surrounding material in the form of axial stretching and bending. Instead, the coupled shear-tension solutions accounting for the global deformation of the target correlate well with the experimental results.

It should be mentioned that for a thick plate, indentation response in the Stage I becomes important. In the last two cases of $h/d = 0.8$ and $h/d = 1.0$, this factor is taken into account, i.e. Eq. (7.219) was used to calculate the residual velocities. The theoretical predictions agree well with the experimental results. At the same time, shear and bending response would be dominant instead of axial stretching for a thick plate. The coupled shear-tension solution is not suitable for this kind of targets.

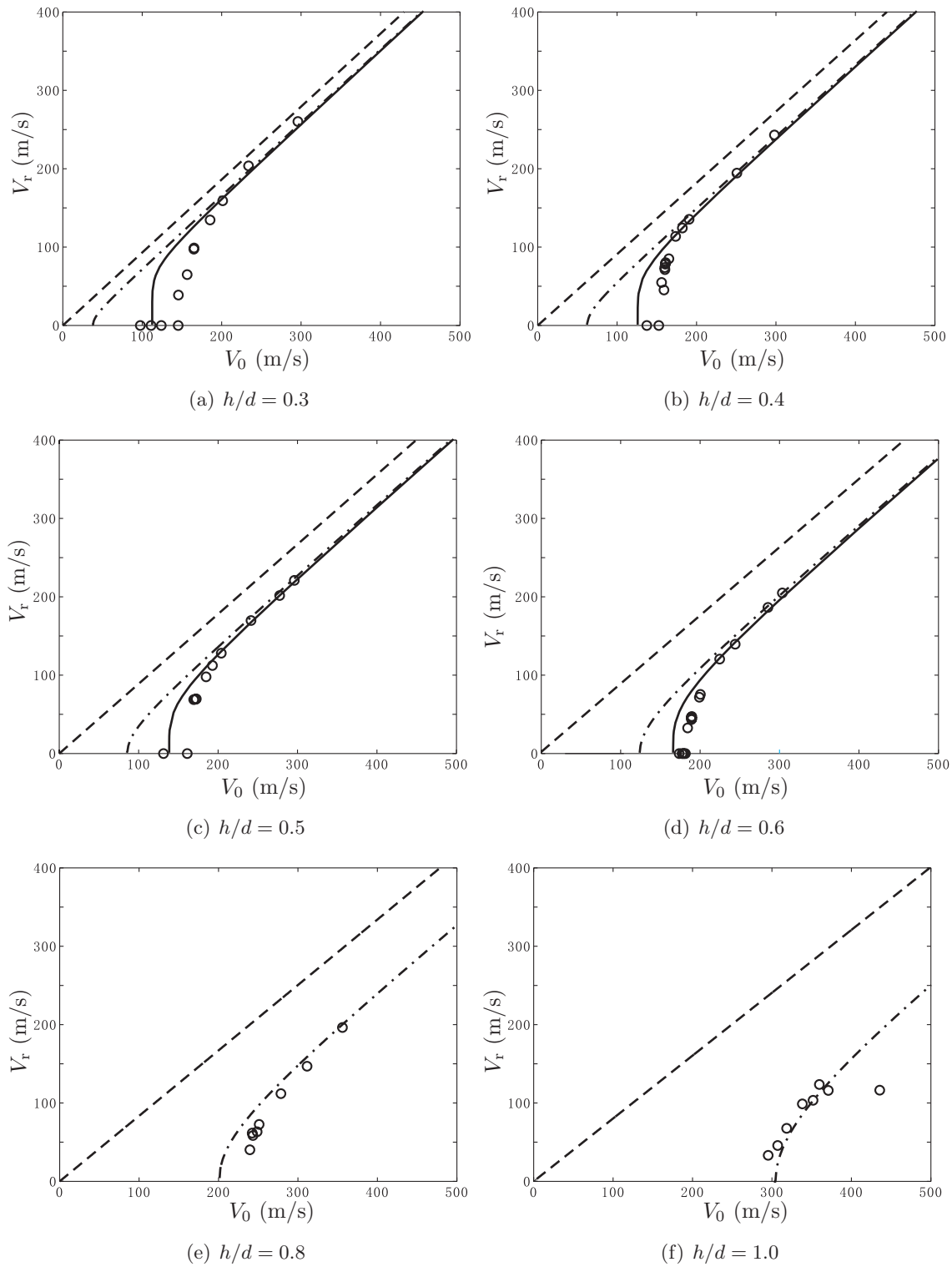


Fig. 7-65: Residual velocity vs. impact velocity for the Weldox steel target. The circular points denote Børvik et al.'s experimental results [100]. The solid curves represents the coupled shear-tension solution. The dash-dot curves represent the pure shear solution. The dash line represents $V_r = V_0 / (1 + \mu)$.

7.5.7 Transition from tensile tearing to shear plugging

The perforation energy dissipated during the whole process can be defined by the difference between the initial kinetic energy of the projectile and the residual kinetic energy of the projectile-plug system

$$W = \frac{1}{2}M_0V_0^2 - \frac{1}{2}M_0(1 + \mu)V_r^2. \quad (7.252)$$

Figure 7-66 shows the relation between the perforation energy and the initial impact velocity. It appears that the dissipated energy decreases from the ballistic limit to a minimum value, and then monotonically increases with the initial impact velocity. This phenomenon was noticed first by Goldsmith and Finnegan [50] from experimental results. The local drop of the dissipated energy, which is evident for a thin target, can be captured by the present coupled shear-tension solution.

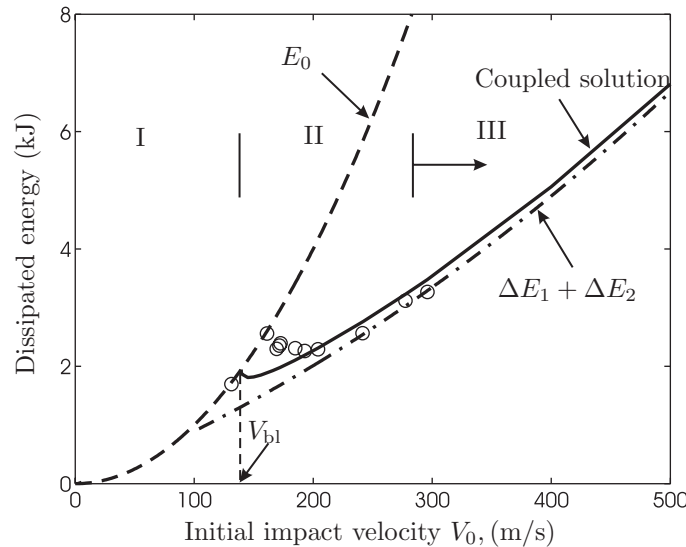


Fig. 7-66: Dissipated energy vs. initial impact velocity for a specific case with $h = 10$ mm. The circular points represent the experimental results by Børvik et al. [100].

Three ranges can be distinguished in Fig. 7-66. If the initial impact velocity is lower than the corresponding ballistic limit (Range I: $V_0 < 150$ m/s), the whole kinetic energy of the projectile, represented by the dash curve, is absorbed by the plate in the form of axial stretching, bending, or partial crack growth. For the initial impact velocity higher

than 300 m/s (Range III), the closed-form analysis neglecting the global deformation of the target does not much differ from the coupled solution, where most of the kinetic energy is dissipated in the form of through-thickness crack growth and indentation in the impacted zone. In the intermediate range, a small proportion of the kinetic energy is converted to the deformation energy in the surrounding material.

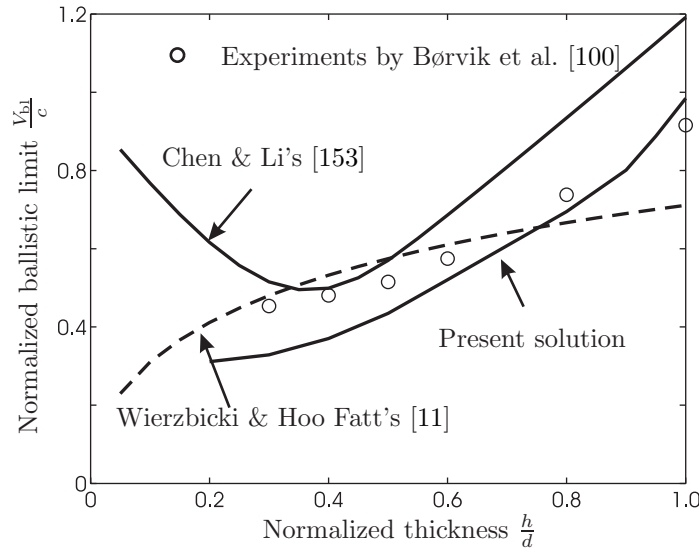


Fig. 7-67: Comparison of the ballistic limit among various analytical solutions and experimental results. For a thin target of $h/d < 0.7$, the coupled shear-tension solutions were used. For a thick target of $h/d > 0.8$, the pure shear solution with the indentation depth considered was used to calculate the ballistic limits.

7.5.8 Comparison with previous analytical solutions

Wierzbicki and Hoo Fatt [11] gave a closed-form solution for the ballistic limit of a circular membrane perforated by a rigid, cylindrical projectile:

$$\frac{V_{bl}}{c} = \frac{4}{\sqrt{3}} \left(\sqrt{\mu(1+\mu)} - \mu \right). \tag{7.253}$$

This solution is quite simple and depends only on the mass ratio and the transverse plastic stress wave speed. Recently, Chen and Li [153] developed a coupled shear-bending solution

in which the ballistic limit is given by

$$\frac{V_{bl}}{c} = \sqrt{\frac{8}{\sqrt{3}} \frac{h}{d} k (1 + \mu) (\mu + \psi)} \quad (7.254)$$

where ψ is a coefficient as a function of the location of the plastic bending hinge, and $k = 1$ was used as an empirical data in their calculation.

Both theoretical solutions are compared with the present solutions and the experiments by Børvik et al. [100]. Figure 7-67 shows comparison of the ballistic limit as a function of the target thickness. It can be observed that both of the above solutions over-predict the ballistic limits of the targets. Note, that Wierzbicki and Hoo Fatt's solution was formulated for a membrane, i.e. bending response is neglected. In Chen and Li's solution, both $k = 1$ and the constant plastic shear force probably lead to the overestimation of the ballistic limits.

7.5.9 Concluding remarks

Based on the newly developed relationship between the indentation and the crack length, a two-stage shear plugging model with the advancing crack is proposed for both the beam and the circular plate. The closed-form solutions for the instantaneous velocity, the residual velocity, the plastic energy, the width of the shear zone, and the crack propagation speed are obtained. A coupled shear-tension model taking into account the global deformation of the target is also developed, which improves the prediction of the ballistic limit. Comparisons with the virtual and real experiments presented in the open literature are made showing rather good agreement, which validates the accuracy of the present solutions. The good correlations further verify that Eq. (4.1) is quite general and capable of predicting the perforation response in a wide range of the impact velocity and the target thickness.

It should be pointed out that shear plugging is not the unique failure mode for a target struck by a rigid, flat-nosed projectile. For example, besides shear plugging, a circular plate may fail by either discing or petalling depending on various combinations of parameters such as the impact velocity and mass of a projectile, the thickness of a target, etc. No simple conditions for the transition of the failure modes have been developed in the literature. In

Chapter 4.5, the present author gave the ranges of the impact velocity and the mass ratio for a beam impacted by a flat-nosed projectile, in which shear plugging is favorable.

Chapter 8

Conclusions and Recommendations

8.1 Summary of results

Fracture modes and fracture mechanisms of high velocity impact problems were investigated numerically and theoretically. A number of macroscopic fracture modes were successfully recreated for the first time in the literature. Attention was focused on crack formation and propagation, which is difficultly captured using currently available instruments. The applicability of the newly developed Bao-Wierzbicki's fracture criterion was convincingly demonstrated. Deficiencies of the existing fracture loci were pointed out. Four theoretical models were developed and closed-form solutions were obtained. Comparison with virtual and real experiments was made showing very good agreements.

Qualitative analysis of failure modes

The deformation and failure response of a long, plane-strain beam impacted by a rigid, flat-/round-nosed projectile was studied numerically in a wide range of impact velocities using the BW's fracture criterion. Three distinct failure modes were identified including fragmentation, shear plugging, and tensile tearing. The corresponding failure mechanisms were revealed by tracking down the time history of the effective plastic strain and the stress triaxiality of critical points at crack pathes. Effects of material ductility are highlighted by introducing two metals: 2024-T351 aluminum alloy and Weldox 460 E steel. It was found that tensile tearing is a favorable failure mode for both materials at a velocity near

the ballistic limit. The steel beam tends to break by tensile tearing while the aluminum beam fails by shear plugging at an impact velocity well above the ballistic limit. At an intermediately high impact velocity, the target fails by a mixed mode of shear plugging and tensile tearing. The numerical findings are consistent with experimental observations published in the open literature.

The failure process and failure mechanism of a three-dimensional solid cylinder fired against a rigid wall in the Taylor test was studied. The cylinder is predominated by compression for which ductile fracture could not be easily predicted. Three fracture modes observed in experiments were successfully recreated for the first time in the literature: confined fracture inside the cylinder, petalling of the front surface, and shear cracking on the lateral surface. Petalling would more likely take place in a more ductile projectile moving at a high velocity while shear cracking in a less ductile material. Confined fracture is a common failure mode for both materials, which occurs in a wide range of the impact velocity. The research provides an insight into the mechanics and mechanism of ductile fracture in the Taylor test.

Adiabatic shear banding and subsequent fracture

A recently performed dynamic compression test on an axisymmetric hat specimen was simulated. The formation and propagation of adiabatic shear bands and subsequent cracks were successfully captured and the corresponding mechanisms were explored. In contrast to the analyses published in the literature, fracture was clearly distinguished from adiabatic shear banding in this research. Cracking is thought of as a final, catastrophic failure mode. The adiabatic shear banding was automatically resolved using a very fine mesh model with the minimum element edge length of $10\ \mu\text{m}$ while the prediction of cracking was achieved by implementing the BW's fracture locus. The experimentally observed hot spots that periodically occur in a propagating shear band were convincingly recreated using conventional finite element procedures. Most importantly, it was found that these hot spots act as the initiation sites of the crack. Thus, the formation of the crack within the shear band resembles a linkage of small cracks rather than the growth of a single major crack. Comparison with the experimental results was made showing very good agreements, which

prove the accuracy of the present numerical studies.

Properties of through-thickness crack growth

An analytical expression controlling through-thickness crack propagation for a beam/plate under impact by a flat-nosed projectile was proposed. An extensive parametric study was performed to verify this expression in a wide range of impact velocities, projectile weight, target thickness, etc. It was found the maximum value of crack propagation speeds in ductile shear plugging reaches half of the Rayleigh wave speed (~ 3000 m/s).

Applicability of the BW's fracture criterion

The successful recreation of a number of failure modes clearly demonstrates the applicability of the BW's ductile fracture locus to high velocity impact problems. The effectiveness of the BW's fracture model was further examined by comparing the predicted failure response of three types of problems using two other fracture criteria: the JC's fracture locus and the constant critical plastic strain. Since the JC's fracture model and the critical fracture strain were calibrated from tensile tests alone, they do not represent real fracture characteristics of a material dominated by compression. This deficiency leads to the unrealistic failure patterns that a number of elements were artificially eroded in the critical region. By contrast, the BW's fracture criterion predicted distinct crack pathes and macroscopic fracture modes.

Mesh size effects

High strain gradient and strain softening were identified as two critical factors leading to mesh size sensitivity. Mesh size effects were studied through two typical problems: a circular plate struck by a flat-nosed rigid cylindrical mass and a hat specimen under dynamic compression. It was found that crack growth and residual velocities at high impact velocities are not much dependent on element size. However, the prediction of ballistic limit and the evolution of adiabatic shear bands is quite sensitive to the mesh size.

Four benchmark analytical solutions

Motivated by the September 11th attack, three theoretical models were developed using

the momentum conservation approach. These three models include rigid mass-to-beam impact, the single impact of beam-to-beam, and the multiple impact of beam-to-beam. The corresponding solutions are applicable to large deformation problems, in which axial stretching dominates over shearing and bending. Closed-form solutions were developed for transient velocities, deflection, plastic strain, and critical impact velocities to fracture the impacting bodies. Comparison with finite element solutions are made showing very good correlations. In rigid mass-to-beam impact, the range of applicability of the theoretical solution was determined. In the single impact of beam-to-beam, five fracture scenarios were identified and the corresponding conditions were specified. In the multiple impact, a recursion formula for plastic tensile strain was derived.

Based on the analytical expression controlling through-thickness crack growth, a two-stage shear plugging model with advancing cracks was built for beams and circular plates. Closed-form solutions for the instantaneous velocity, the residual velocity, the crack propagation speed, etc. were derived. The explicit expressions for the shear zone width and the critical indentation depth, which were taken as empirical data in the literature, were also determined explicitly. A coupled shear-tension model taking into account the global deformation of a target was also formulated, which improves the prediction of the ballistic limit. The theoretical solutions agree well with virtual and real experiments published in the literature, which further verify that the crack growth curve is quite general and capable of predicting the perforation response in a wide range of the impact velocity and the target thickness.

8.2 Suggestions for future studies

- Ductile fracture criteria are usually calibrated from monotonically loaded tests. However, a structural component may have a complex loading history before fracture. For example, in the initial phase of the impact process, compression is dominant in the impacted zone of a target beneath a projectile, where cracks are often generated. As transverse deflection increases, shear, bending, and axial stretching becomes important leading to crack formation in the impacted zone, see Fig. 3-7. The Bao-

Wierzbicki's fracture locus assumes that the increase in the effective plastic strain would not contribute to the damage accumulation in the compression dominated phase. However, preliminary strain reversal tests performed by Wierzbicki and Bao [5], in which a notched, axisymmetric specimen was first compressed to a certain level of plastic strain and then stretched to fracture, reveal that the final fracture strain of the specimens clearly depends on the magnitude of the first compressive deformation. Therefore, it is necessary to incorporate effects of loading histories into a ductile fracture criterion for practical applications.

- Solid elements were used in the present thesis to model growth of cracks and evolution of adiabatic shear bands through the target thickness. However, such a finite element model is not affordable for failure analysis of a large structure such as a colliding car or a grounding ship, for which large shell elements have to be adopted. A preliminary study indicates that numerical results are strongly sensitive to element size of shell models. At the same time, it is impossible for a shell model to capture through-thickness crack growth, adiabatic shear banding evolution, or spallation. These types of localized damage would significantly reduce the load carrying capability of a component, or even a whole structure. It would be very interesting if effects of mesh size and localized damage could be taken into account in large shell element analysis. In such a way, a large shell element model would be able to predict a failure process.
- The BW's fracture criterion was essentially developed for the prediction of crack formation rather than crack propagation. Crack growth was thought of as a series of crack formation for each failed element. Although it has been shown that this approximation is able to make a reasonable prediction of the failure process, it is still attractive to develop a ductile fracture criterion for crack propagation.
- As shown in Chapter 5.3, the formation and evolution of adiabatic shear bands and the prediction of ballistic limits is quite sensitive to mesh size. An effective approach to remedy this deficiency should be derived.
- The crack growth curve, Eq. (4.1), was developed in Chapter 4 using curve-fitting the numerical results. It would be desirable to theoretically determine this expression or

relate two coefficients K and λ of Eq. (4.1) to fracture properties of a material.

- Experimental investigation, numerical simulation, and theoretical analysis is complementary to each other. The present thesis focused on the latter two methods. Experiments should be conducted to corroborate the obtained theoretical and numerical solutions. In particular, an advanced experimental instrument need to be developed to track down crack propagation and to capture deformation and temperature fields in the vicinity of a propagating crack tip.

Appendix A

Choice of Parameters in Finite Element Modeling

This appendix summarizes the rationale for the choice of important technical parameters in finite element modeling of the problems considered in the present thesis.

- **Time step**

In ABAQUS/Explicit, the central-difference time integration rule is used to solve governing differential equations. This integration operator is conditionally stable. The stable time increment can be manually defined or automatically determined by the code. In this thesis, the latter was adopted. The stable time increment is proportional to the element size. In the case of adiabatic shear banding of the hat specimen (Chapter 3.4) where the minimum element edge length is about $10\ \mu\text{m}$, the typical value of the time increment is about $10^{-10} \sim 10^{-11}$ s. The total increment number is of the order of 10^5 for the impact duration $100\ \mu\text{s}$. It was noted that the nodal displacements increase without much oscillation and the total energy almost keeps constant. These results indicate that the obtained solutions are stable.

- **Elements**

Only first-order elements with reduced integration are available in ABAQUS/Explicit. These first-order elements are essentially constant strain elements. Hence, they can be used to approximately model discontinuities in the gradient field of solution variables, which are

common in dynamic plasticity problems such as adiabatic shear banding.

- **Hourglass control**

Reduced integration decrease CPU time and storage requirements but introduces a zero-energy deformation mode called “hourglassing”. To suppress excessive deformation due to hourglassing, an additional artificial stiffness is added to the elements. ABAQUS/Explicit provides four options to control hourglassing. In this thesis, the integral viscoelastic approach, which is the default option in ABAQUS/Explicit, was chosen. No excessive deformations were observed in all the numerical simulations and thus this approach is quite effective. However, in a preliminary numerical simulation of the single impact of beam-to-beam using three-dimensional solid elements, where both beams are deformable and breakable, none of the four hourglass control options work well. This problem need to be further investigated.

- **Adaptive meshing**

In Chapter 3.4, adaptive meshing was used to maintain the high-quality elements of the gauge section of the hat specimen throughout the analysis of adiabatic shear banding and subsequent fracture. There are two major control parameters: the frequency and the intensity of adaptive meshing. ABAQUS/Explicit suggests adaptive meshing every 5-100 time increments. The author found adaptive meshing should be performed every time increment for the present problem. Otherwise, the calculation would be terminated prematurely due to excessive distortion of elements. In an adaptive meshing increment, a new, smoother mesh is generated by relocating elemental nodes. This process is called sweeping in ABAQUS/Explicit. The number of sweeps was set to two in the present modeling. There are three basic mesh smoothing methods: volume smoothing, Laplacian smoothing, and equipotential smoothing. The first one is the default option and it works well for the present problem.

- **Contact modeling**

The momentum and energy of a projectile is transferred to a target through contact. ABAQUS/Explicit provides two algorithms for modeling contact events: general contact algorithm and contact pair algorithm. The latter was adopted since all the problems considered in the present thesis involve a deformable surface of targets and a rigid surface of

projectiles, which contact with each other during the impact process. For two deformable contact surfaces such as long rod penetration into a thick plate, the general contact algorithm is a more suitable option.

A contact surface can be defined based on either nodes or elements. Considering that elements in contact with the projectile may fail, a node-based contact surface should be defined in contact pairs instead of an element-based contact surface.

ABAQUS/Explicit offers two contact constraint methods: kinematic and penalty algorithms. The kinematic algorithm is a more stringent enforcement and was used in this thesis. However, a preliminary study indicates that the penalty algorithm is more effective for impact problems associated with two deformable bodies.

ABAQUS/Explicit accounts for three possible relative motions between two contact surfaces: finite, small, and infinitesimal sliding. The first one, which is the most general, was defined.

Bibliography

- [1] FEMA. World Trade Center building performance study: data collection, preliminary observations, and recommendations. Technical Report Federal Emergency Management Agency 403, New York, May 2002. <http://www.fema.gov/library/wtcstudy.shtm>.
- [2] Columbia Accident Investigation Board. Columbia. Technical report, 2003. <http://www.caib.us>.
- [3] A. J. Rosakis and G. Ravichandran. Dynamic failure mechanics. *International Journal of Solids and Structures*, 37:331–348, 2000.
- [4] Y. Bao and T. Wierzbicki. On fracture locus in the equivalent strain and stress triaxiality space. *International Journal of Mechanical Sciences*, 46(1):81–98, 2004.
- [5] T. Wierzbicki and Y. Bao. Bridgman revisited: On the history effects on ductile fracture. *Journal of the Mechanics and Physics of Solids*, 2004. submitted.
- [6] M. E. Backman and W. Goldsmith. The mechanics of penetration of projectiles into targets. *International Journal of Engineering Sciences*, 16:1–99, 1978.
- [7] J. A. Zukas. Penetration and perforation of solids. In J. A. Zukas, T. Nicholas, H. F. Swift, L. B. Greszczuk, and D. R. Curran, editors, *Impact Dynamics*, pages 155–214. John Wiley & Sons, Inc., 1982.
- [8] W. Goldsmith. Non-ideal projectile impact on targets. *International Journal of Impact Engineering*, 22(2-3):95–395, 1999.

- [9] F. F. Abraham. Very large scale simulations of materials failure. *Philosophical Transactions of the Royal Society of London. A*, 360:367–382, 2002.
- [10] A. Needleman. Computational mechanics at the mesoscale. *Acta Materialia*, 48:105–124, 2000.
- [11] T. Wierzbicki and M. S. Hoo Fatt. Deformation and perforation of a circular membrane due to rigid projectile impact. In T. L. Geers and Y. S. Shin, editors, *Dynamic Response of Structures to High Energy Excitation*, pages 73–83. AMSE, 1991.
- [12] T. Wierzbicki and M. S. Hoo Fatt. Impact response of a string-on-plastic foundation. *International Journal of Impact Engineering*, 12(1):21–36, 1992.
- [13] A. Pandolfi, P. R. Guduru, M. Ortiz, and A. J. Rosakis. Three dimensional cohesive-element analysis and experiments of dynamic fracture in c300 steel. *International Journal of Solids and Structures*, 37:3733–3760, 2000.
- [14] A. Needleman. An analysis of tensile decohesion along an interface. *Journal of the Mechanics and Physics of Solids*, 38:289–324, 1990.
- [15] A. Needleman. Numerical modeling of crack growth under dynamic loading conditions. *Computational Mechanics*, 19:463–469, 1997.
- [16] X.-P. Xu and A. Needleman. Numerical simulations of dynamic crack-growth along an interface. *International Journal of Fracture*, 74:289–324, 1996.
- [17] G. T. Camacho and M. Ortiz. Computational modeling of impact damage in brittle materials. *International Journal of Solids and Structures*, 33:2899–2938, 1996.
- [18] N. Chandra and C. Shet. A micromechanistic perspective of cohesive zone approach in modeling fracture. *Computer Modeling in Engineering and Sciences*, 5(1):21–33, 2004.
- [19] A. Pandolfi, P. Krysl, and M. Ortiz. Finite element simulation of ring expansion and fragmentation: the capturing of length and time scales through cohesive models of fracture. *International Journal of Fracture*, 95:279–297, 1999.

- [20] V. Tvergaard. Crack growth predictions by cohesive zone model for ductile fracture. *Journal of the Mechanics and Physics of Solids*, 49:2191–2207, 2001.
- [21] V. Tvergaard. Predictions of mixed mode interface crack growth using a cohesive zone model for ductile fracture. *Journal of the Mechanics and Physics of Solids*, 52:925–940, 2004.
- [22] F. A. McClintock. A criterion for ductile fracture by the growth of holes. *Journal of Applied Mechanics*, 35:363–371, 1968.
- [23] J. R. Rice and D. M. Tracey. On the ductile enlargement of voids in triaxial stress fields. *Journal of the Mechanics and Physics of Solids*, 17:201–217, 1969.
- [24] A. L. Gurson. *Plastic flow and fracture behavior of ductile materials incorporating void nucleation, growth and interaction*. Ph.d. thesis, Brown University, 1975.
- [25] V. Tvergaard. Influence of voids on shear band instabilities under plane strain conditions. *International Journal of Fracture*, 17:389–407, 1981.
- [26] V. Tvergaard and A. Needleman. Analysis of the cup-cone fracture in a round tensile bar. *Acta Metallurgy*, 32:157–169, 1984.
- [27] M. J. Worswick and R. J. Pick. Void growth and coalescence during high-velocity impact. *Mechanics of Materials*, 19:293–309, 1995.
- [28] F. L. Addessio, J. N. Johnson, and P. J. Maudlin. The effect of void growth on Taylor cylinder impact experiments. *Journal of Applied Physics*, 73(11):7288–7297, 1993.
- [29] M. Zhou and R. J. Clifton. Dynamic ductile rupture under conditions of plane strain. *International Journal of Impact Engineering*, 19(3):189–206, 1997.
- [30] J. W. Hancock and A. C. Mackenzie. On the mechanisms of ductile failure in high strength steels subjected to multi-axial stress-states. *Journal of the Mechanics and Physics of Solids*, 24:147–169, 1976.
- [31] M. G. Cockcroft and D. J. Latham. Ductility and the workability of metals. *Journal of In*, 96:33–39, 1968.

- [32] Y. Bao, Y.-W. Lee, and T. Wierzbicki. Evaluation and calibration of seven fracture models. *International Journal of Mechanical Sciences*, 2004. submitted.
- [33] A. S. Wifi, A. Abdel-Hamid, and N. El-Abbasi. Computer-aided evaluation of workability in bulk forming processes. *Journal of Materials Processing Technology*, 77:285–293, 1998.
- [34] K. Komori. Effect of ductile fracture criteria on chevron crack formation and evolution in drawing. *International Journal of Mechanical Sciences*, 45:141–160, 2003.
- [35] Y. Bao and T. Wierzbicki. A comparative study on various ductile crack formation criteria. *Journal of Engineering Materials and Technology*, 126(3):314–324, 2004. In press.
- [36] P. W. Bridgman. *Studies in Large Plastic Flow and Fracture*. Harvard University Press, 1964.
- [37] G. R. Johnson and W. H. Cook. Fracture characteristics of three metals subjected to various strains, strain rates, temperatures and pressures. *Engineering Fracture Mechanics*, 21(1):31–48, 1985.
- [38] G. R. Johnson and T. J. Holmquist. Test data and computational strength and fracture model constants for 23 materials subjected to large strain, high-strain rates, and high temperatures. Technical Report LA-11463-MS, Los Alamos National Laboratory, 1989.
- [39] T. Nicholas and A. M. Rajendran. Material characterization at high strain rates. In J. A. Zukas, editor, *High Velocity Impact Dynamics*, pages 127–296. John Wiley & Sons, Inc., New York, 1990.
- [40] T. Børvik, O. S. Hopperstad, T. Berstad, and M. L. Langseth. A computational model of viscoplasticity and ductile damage for impact and penetration. *European Journal of Mechanics: A/Solids*, 20:685–712, 2001.

- [41] A. H. Clausen, T. Børvik, O. S. Hopperstad, and A. Benallal. Flow and fracture characteristics of aluminum alloy AA5083-H116 as function of strain rate, temperature and triaxiality. *Materials Science and Engineering A*, 364:260–272, 2004.
- [42] Y. Bai and B. Dodd. *Adiabatic Shear Localization: Occurrence, Theories and Applications*. Pergamon Press, New York, 1992.
- [43] C. E. Anderson and S. R. Bodner. Ballistic impact: The status of analytical and numerical modelling. *International Journal of Impact Engineering*, 7(1):9–35, 1988.
- [44] G. G. Corbett, S. R. Reid, and W. Johnson. Impact loading of plates and shells by free-flying projectiles: A review. *International Journal of Impact Engineering*, 18(2):141–230, 1996.
- [45] W. Johnson. *Impact Strength of Materials*. Arnold, London, 1972.
- [46] J. A. Zukas, T. Nicholas, H. F. Swift, L. B. Greszczuk, and D. R. Curran, editors. *Impact Dynamics*. John Wiley & Sons, Inc., New York, 1982.
- [47] J. A. Zukas, editor. *High Velocity Impact Dynamics*. John Wiley & Sons, Inc., New York, 1990.
- [48] R. L. Woodward. Material failure at high strain rates. In J. A. Zukas, editor, *High Velocity Impact Dynamics*, pages 65–125. John Wiley & Sons, Inc., New York, 1990.
- [49] T. Wierzbicki and X. Teng. Simulation of spalling. In *Topics on Analytical Dynamics and Applied Mechanics*, SMAC-Stanford Symposium in honor of Professor Thomas R. Kane. Stanford University, 2004.
- [50] W. Goldsmith and S. A. Finnegan. Penetration and perforation process in metal targets at and above ballistic velocities. *International Journal of Mechanical Sciences*, 13:843–866, 1971.
- [51] R. S. J. Corran, P. J. Shadbolt, and C. Ruiz. Impact loading of plates—An experimental investigation. *International Journal of Impact Engineering*, 1(1):3–22, 1983.

- [52] N. Levy and W. Goldsmith. Normal impact and perforation of thin plates by hemispherically-tipped projectiles –II. Experimental results. *International Journal of Impact Engineering*, 2(4):299–324, 1984.
- [53] N. Jones and C. Jones. Inelastic failure of fully clamped beams and circular plates under impact loading. *Journal of Mechanical Engineering Science*, 216:133–149, 2002.
- [54] W. Q. Shen, N. O. Rieve, and B. Baharun. A study on the failure of circular plates struck by masses. Part 1: Experimental results. *International Journal of Impact Engineering*, 27:399–412, 2002.
- [55] T. Børvik, O. S. Hopperstad, T. Berstad, and M. Langseth. Perforation of 12 mm thick steel plates by 20 mm diameter projectiles with flat, hemispherical and conical noses part II: Numerical simulations. *International Journal of Impact Engineering*, 27(1):37–64, 2002.
- [56] T. Børvik, M. Langseth, O. S. Hopperstad, and K. A. Malo. Perforation of 12 mm thick steel plates by 20 mm diameter projectiles with flat, hemispherical and conical noses: Part I: Experimental study. *International Journal of Impact Engineering*, 27(1):19–35, 2002.
- [57] ABAQUS. User’s Manuals Ver.6.4, 2001. Hibbitt, Karlsson and Sorensen Inc.
- [58] Y. Bai, Y. Bao, and T. Wierzbicki. Fracture of prismatic aluminum tubes under reverse straining. In *International Symposium on Crashworthiness of Light-Weight Automotive Structures*, Trondheim, Norway, June 2004.
- [59] X. Teng and T. Wierzbicki. Numerical study on crack propagation in high velocity perforation. *Computers and Structures*, 2004. Accepted for publication.
- [60] X. Teng and T. Wierzbicki. Effects of fracture criteria on high velocity perforation of thin beams. *International Journal of Computational Methods*, 1(1):171–200, 2004.
- [61] G. I. Taylor. The use of flat-ended projectiles for determining dynamic yield stress. I. Theoretical considerations. *Proceedings of the Royal Society of London. Series A, Mathematical and Physical Sciences*, 194(1308):289–299, 1948.

- [62] G. R. Johnson and T. J. Holmquist. Evaluation of cylinder-impact test data for constitutive model constants. *Journal of Applied Physics*, 64(8):3901–3910, 1988.
- [63] I. Rohr, H. Nahme, and K. Thoma. A modified Taylor-test in combination with numerical simulations—a new approach for the determination of model parameters under dynamic loads. *Journal De Physique IV France*, 110:513–518, 2003.
- [64] S. Walley. Bibliographies on dynamic topics, 2003.
- [65] H. Couque. On the use of the symmetric Taylor test to evaluate dynamic ductile compression fracture properties of metals. In *Proceedings of the 5th International Conference on Structures Under Shock and Impact*, pages 579–589. Computational Mechanics Inc, Billerica, MA, USA, 1998.
- [66] R. L. Woodward, R. G. O’Donnell, and C. J. Flockhart. Failure mechanisms in impacting penetrators. *Journal of Materials Science*, 27:6411–6416, 1992.
- [67] D. E. Grady and M. E. Kipp. Fragmentation of solids under dynamic loading. In T. Wierzbicki and N. Jones, editors, *Structural Failure*, chapter 1, pages 1–40. John Wiley & Sons, New York, 1989.
- [68] R. P. Papirno, J. F. Mescall, and A. M. Hansen. Beyond the Taylor test to fracture. In *Designing for extremes: Environment, loading, and structural behavior*, Proceedings of the Army Symposium on Solid Mechanics, pages 367–385, Watertown, MA, September 1980. Army Materials and Mechanics Research Center.
- [69] T. W. Wright. *The Physics and Mathematics of Adiabatic Shear Bands*. Cambridge University Press, New York, 2002.
- [70] A. Marchand and J. Duffy. An experimental study of the formation process of adiabatic shear bands in a structural steel. *Journal of the Mechanics and Physics of Solids*, 36(3):251–283, 1988.
- [71] M. Zhou, A.J. Rosakis, and G. Ravichandran. Dynamically propagating shear bands in impact-loaded prenotched plates—I. Experimental investigations of temperature sig-

- natures and propagation speed. *Journal of the Mechanics and Physics of Solids*, 44(6):981–1006, 1996.
- [72] P. R. Guduru, G. Ravichandran, and A. J. Rosakis. Observations of transient temperature vortical microstructures in solids during adiabatic shear banding. *Physical Review E*, 64(3):036128, 2001.
- [73] P. R. Guduru, A. J. Rosakis, and G. Ravichandran. Dynamic shear bands: an investigation using high speed optical and infrared diagnostics. *Mechanics of Materials*, 33:371–402, 2001.
- [74] M. Zhou, G. Ravichandran, and A. J. Rosakis. Dynamically propagating shear bands in impact-loaded prenotched plates—II. Numerical simulations. *Journal of the Mechanics and Physics of Solids*, 44(6):1007–1032, 1996.
- [75] T. Lodygowski and P. Perzyna. Numerical modelling of localized fracture of inelastic solids in dynamic loading processes. *International Journal for Numerical Methods in Engineering*, 40:4137–4158, 1997.
- [76] C. Mason and M. I. Worswick. Adiabatic shear in annealed and shock-hardened iron and in quenched and tempered 4340 steel. *International Journal of Fracture*, 111:29–51, 2001.
- [77] Q. M. Li and N. Jones. Formation of a shear localization in structural elements under transverse dynamic loads. *International Journal of Solids and Structures*, 37:6683–6704, 2000.
- [78] S. Li, W-K. Liu, D. Qian, P. R. Guduru, and A. J. Rosakis. Dynamic shear band propagation and micro-structure of adiabatic shear band. *Computational Methods in Applied Mechanics and Engineering*, 191:73–92, 2001.
- [79] S. Li, W. K. Liu, A. J. Rosakis, T. Belytschko, and W. Hao. Mesh-free Galerkin simulations of dynamic shear band propagation and failure mode transition. *International Journal of Solids and Structures*, 39:1213–1240, 2002.

- [80] J. F. Kalthoff and S. Winkler. Failure mode transition at high rates of shear loading. In C. Y. Chiem, H.-D. Kunze, and L. W. Meyer, editors, *Impact Loading and Dynamic Behaviour of Materials*, volume 1, pages 185–195. Informationsgesellschaft, Verl, 1988.
- [81] A. Needleman and V. Tvergaard. Analysis of a brittle-ductile transition under dynamic shear loading. *International Journal of Solids and Structures*, 32(17/18):2571–2590, 1995.
- [82] H. Couque. A hydrodynamic hat specimen to investigate pressure and strain rate dependence on adiabatic shear band formation. *Journal de Physique IV France*, 110:423–428, 2003.
- [83] H. Couque. Dynamic compression failure of two metals at 0.5 and 1.5 GPa. In N. Jones and C. A. Brebbia, editors, *Proceedings of the Computational Ballistics II Conference*, Cordoba, Spain, 2005. WIT Press.
- [84] C. K. Dharan and F. E. Hauser. Determination of stress-strain characteristics at very high strain rates. *Experimental Mechanics*, 10:370, 1970.
- [85] L. W. Meyer and S. Manwaring. Critical adiabatic shear strength of low alloyed steel under compressive loading. In *Metallurgical Applications of Shock-Wave and High-Strain-Rate Phenomena*, pages 657–674. Marcel Dekker Inc., 1986.
- [86] T. W. Wright and J. W. Walter. On stress collapse in adiabatic shear bands. *Journal of the Mechanics and Physics of Solids*, 35(6):701–720, 1987.
- [87] S. P. Timothy and I. M. Hutchings. Initiation and growth of microfractures along adiabatic shear bands in Ti-6Al-4V. *Materials Science and Technology*, 1:526–530, 1985.
- [88] R. C. Batra and N. V. Nechitailo. Analysis of failure modes in impulsively loaded pre-notched steel plates. *International Journal of Plasticity*, 13:291–308, 1997.
- [89] T. W. Wright and G. Ravichandran. Canonical aspects of adiabatic shear bands. *International Journal of Plasticity*, 13(4):309–325, 1997.

- [90] C-S. Yueh and C-I. Weng. Linear stability analysis of plane Couette flow with viscous heating. *Physics of Fluids*, 8(7):1802–1813, 1996.
- [91] A. Molinari and Y. M. Leroy. Structures in shear zones due to thermal effects. *Comptes Rendus de l'Académie des sciences. Série II*, 313:7–13, 1991.
- [92] R. G. O'Donnell and R. L. Woodward. Instability during high strain rate compression of 2024-T351 aluminum. *Journal of Material Science*, 23:3578–3587, 1988.
- [93] M. N. Raftenberg. A shear banding model for penetration calculations. *International Journal of Impact Engineering*, 25:123–146, 2001.
- [94] T. Børvik, J. R. Leinum, J. K. Solberg, O. S. Hopperstad, and M. Langseth. Observations on shear plug formation in weldox 460 e steel plates impacted by blunt-nosed projectiles. *International Journal of Impact Engineering*, 25:553–572, 2001.
- [95] S. Dey. *High-strength steel plates subjected to projectile impact*. PhD thesis, Norwegian University of Science and Technology, 2004.
- [96] D. R. Ambur, N. Jaunky, R. E. Lawson, and N. R. Knight. Numerical simulations for high-energy impact of thin plates. *International Journal of Impact Engineering*, 25:683–702, 2001.
- [97] J. Guo, G. Shi, Y. Wang, and C. Lu. Efficient modeling of panel-like structures in perforation simulations. *Computers and Structures*, 81:1–8, 2003.
- [98] F. A. McClintock and A. H. Slocum. Predicting fully plastic mode II crack growth from an asymmetric defect. *International Journal of Fracture*, 27(1):49–62, 1985.
- [99] D. J. Bammann, M. L. Chiesa, M. F. Horstemeyer, and L. I. Weingarten. Failure in ductile materials using finite element methods. In N. Jones and T. Wierzbicki, editors, *Structural Crashworthiness and Failure*, chapter 1, pages 1–54. Elsevier Science Publisher Ltd, 1993.
- [100] T. Børvik, O. S. Hopperstad, M. Langseth, and K. A. Malo. Effects of target thickness in blunt projectile penetration of Weldox 460 E steel plates. *International Journal of Impact Engineering*, 28(4):413–464, 2003.

- [101] A. J. Rosakis. Intersonic shear cracks and fault ruptures. *Advances in physics*, 51(4):1189–1257, 2002.
- [102] L. B. Freund. *Dynamic Fracture Mechanics*. Cambridge University Press, New York, 1990.
- [103] T. Nicholas and R. F. Recht. Introduction to impact phenomena. In J. A. Zukas, editor, *High Velocity Impact Dynamics*, pages 1–64. John Wiley & Sons, Inc., 1990.
- [104] G. R. Johnson and W. H. Cook. A constitutive model and data for metals subjected to large strains, high strain rates and high temperatures. In *Proceedings of the seventh international symposium on ballistics*, pages 541–547, Hague, Netherlands, 1983.
- [105] T. Børvik, O. S. Hopperstad, and T. Berstad. On the influence of stress triaxiality and strain rate on the behaviour of a structural steel. Part II: Numerical study. *European Journal of Mechanics A/Solids*, 22:15–23, 2003.
- [106] O. S. Hopperstad, T. Børvik, M. Langseth, K. Labibes, and C. Albertini. On the influence of stress triaxiality and strain rate on the behaviour of a structural steel. Part I: Experiments. *European Journal of Mechanics A/Solids*, 22:1–13, 2003.
- [107] T. Børvik, O. S. Hopperstad, T. Berstad, and M. Langseth. Numerical simulation of plugging failure in ballistic penetration. *International Journal of Solids and Structures*, 38(34-35):6241–6264, 2001.
- [108] G. R. Johnson, J. M. Hoegfeldt, U. S. Lindholm, and A. Nagy. Response of various metals to large torsional strains over a large range of strain rates—Part 2: Less ductile metals. *Journal of Engineering Materials and Technology*, 105:48–55, 1983.
- [109] U. S. Lindholm and G. R. Johnson. Strain-rate effects in metals at large shear strains. In J. Mescall and Volker Weiss, editors, *Material Behavior under High Stress and Ultrahigh Loading Rates*, pages 61–79. Plenum Press, New York, 1982.
- [110] D. R. Lesuer. Experimental investigations of material models for Ti-6Al-4V titanium and 2024-T3 aluminum. Technical Report DOT/FAA/AR-00/25, Lawrence Livermore National Laboratory, 2000.

- [111] A. Needleman. Material rate dependence and mesh sensitivity in localization problems. *Computer Methods in Applied Mechanics and Engineering*, 67:69–85, 1988.
- [112] A. Needleman and V. Tvergaard. Mesh effects in the analysis of dynamic ductile crack growth. *Engineering Fracture Mechanics*, 47(1):75–91, 1994.
- [113] J. A. Zukas and D. R. Scheffler. Practical aspects of numerical simulations of dynamic events: effects of meshing. *International Journal of Impact Engineering*, 24:925–945, 2000.
- [114] Z. P. Bažant. Mechanics of distributed cracking. *Applied Mechanics Review*, 39(5):675–705, 1986.
- [115] H. E. Read and G. A. Hegemier. Strain softening of rock, soil and concrete—a review article. *Mechanics of Materials*, 3:271–294, 1984.
- [116] D. Lasry and T. Belytschko. Localization limiters in transient problems. *International Journal of Solids and Structures*, 24(6):581–597, 1988.
- [117] P. Perzyna. Localized fracture phenomena in plastic flow process under dynamic loading. Annual Review Meeting of the Projects Conducted at ICL, MIT, 2003.
- [118] P. Redanz, N. A. Fleck, and R. M. McMeeking. Failure of a porous solid from a deep notch. *International Journal of Fracture*, 88:187–203, 1997.
- [119] B. S. Holmes, S. W. Kirkpatrick, J. W. Simons, J. H. Giovanola, and L. Seaman. Modeling the process of failure in structure. In N. Jones and T. Wierzbicki, editors, *Structural Crashworthiness and Failure*, pages 55–91. Elsevier Applied Science, 1993.
- [120] J. H. Giovanola and S. W. Kirkpatrick. Using the local approach to evaluate scaling effects in ductile fracture. *International Journal of Fracture*, 92:101–116, 1998.
- [121] Lee Y.-W, T. Wierzbicki, and Y. Bao. Effect of mesh size on initiation and propagation of crack in flat tensile specimens. *Mechanics of Materials*, 2004. Submitted for publication.

- [122] V. Tvergaard and A. Needleman. Effects of nonlocal damage in porous plastic solids. *International Journal of Solids and Structures*, 32(8/9):1063–1077, 1995.
- [123] A. K. Kamel, M. J. Worswick, and D. Nandlall. Effect of nonlocal damage treatment on dynamic fracture prediction. In H. S. Levine, editor, *Structures under Extreme Loading Conditions*, volume PVP-Vol. 361, pages 195–201, 1998.
- [124] B. C. Simonsen and R. Törnqvist. Experimental and numerical modelling of ductile crack propagation in large-scale shell structures. *Marine Structures*, 17(1):1–27, 2004.
- [125] F. A. McClintock. Plasticity aspects of fracture. In H. Liebowitz, editor, *Fracture: An Advanced Treatise*, volume III. Academic Press, New York, 1971.
- [126] J. F. Mescall. Computer simulation of penetration. In G. C. Sih, editor, *Recent Advances in Engineering Science*, Proceedings of the 14th annual meeting of the society of engineering science, pages 81–93, Pennsylvania, November 1977. Lehigh University Publication.
- [127] R. Fields. Federal building and fire safety investigation of the world trade center disaster, project # 3: Analysis of structural steel, June 2004.
- [128] T. X. Yu and W. J. Stronge. Large deflections of a rigid-plastic beam-on-foundation from impact. *International Journal of Impact Engineering*, 9(1):115–126, 1990.
- [129] M. S. Hoo Fatt and T. Wierzbicki. Impact damage of long plastic cylinders. In *Proceedings of the First International Offshore and Polar Engineering Conference*, pages 172–182, Edinburgh, United Kingdom, 1991.
- [130] T. Wierzbicki and X. Teng. How the airplane wing cut through the exterior columns of the World Trade Center. *International Journal of Impact Engineering*, 28:601–625, 2003.
- [131] J. H. Liu and N. Jones. Experimental investigation of clamped beams struck transversely by a mass. *International Journal of Impact Engineering*, 6(4):303–335, 1987.

- [132] J. Yu and N. Jones. Further experimental investigations on the failure of clamped beams under impact loads. *International Journal of Solids and Structures*, 27(9):1113–1137, 1991.
- [133] N. Jones. *Structural Impact*. Cambridge University Press, Cambridge, UK, 1997.
- [134] J. H. Liu and N. Jones. Dynamic response of a rigid plastic clamped beam struck by a mass at any point on the span. *International Journal of Solids and Structures*, 24(3):251–270, 1988.
- [135] M. Mihailescu-Suliciu, I. Sulicio, T. Wierzbicki, and M.S. Hoo Fatt. Transient response of an impulsively loaded plastic string on a plastic foundation. *Quarterly of Applied Mathematics*, LIV(2):327–343, June 1996.
- [136] M. Mihailescu-Suliciu and T. Wierzbicki. Wave solution for an impulsively loaded rigid-plastic circular membrane. *Archives of Mechanics*, 54(5-6):737–759, 2002.
- [137] T. X. Yu, J. L. Yang, and S. R. Reid. Deformable body impact: Dynamic plastic behavior of a moving free-free beam striking the tip of a cantilever beam. *International Journal of Solids and Structures*, 38:261–287, 2001.
- [138] T. X. Yu and H. H. Ruan. Modelling of beam-on-beam collisions. *Key Engineering Materials*, 233(2):1–12, 2003.
- [139] E. W. Parkes. The permanent deformation of a cantilever struck transversely at its tip. *Proceedings of the Royal Society of London. Series A, Mathematical and Physical Sciences*, 228:462–476, 1955.
- [140] E. H. Lee and P. S. Symonds. Large plastic deformation of beams under transverse impact. *Journal of Applied Mechanics*, 19:308–314, 1952.
- [141] H. H. Ruan, T. X. Yu, and Y. L. Hua. Plastic modal approximations in analyzing beam-on-beam collisions. *International Journal of Solids and Structures*, 40(12):2937–2956, 2003.

- [142] J. L. Yang and T. X. Yu. Dynamic plastic behavior of a free rotating hinged beam striking a cantilever beam. *Mechanics of Structure and Machines*, 29:393–411, 2001.
- [143] J. L. Yang, X. H. Liu, and S. R. Reid. Dynamic plastic behavior of a free-free beam striking the mid-span of a clamped beam with shear and membrane effects considered. *International Journal of Mechanical Sciences*, 45:915–940, 2003.
- [144] R. F. Recht and T. W. Ipson. Ballistic perforation dynamics. *Journal of Applied Mechanics*, 30:384–390, 1963.
- [145] R. L. Woodward and M. E. Morton. Penetration of targets by flat-ended projectiles. *International Journal of Mechanical Sciences*, 18:119–127, 1976.
- [146] R. L. Woodward. A structural model for thin plate perforation by normal impact of blunt projectile. *International Journal of Impact Engineering*, 6(2):129–140, 1987.
- [147] J. Awerbuch. A mechanics approach to projectile penetration. *Israel Journal of Technology*, 8(4):375–383, 1970.
- [148] J. Awerbuch and S. R. Bodner. Analysis of the mechanics of perforation of projectile in metallic plates. *International Journal of Solids and Structures*, 10:671–684, 1974.
- [149] J. Liss, W. Goldsmith, and J. M. Kelly. A phenomenological penetration model of plates. *International Journal of Impact Engineering*, 1(4):321–341, 1983.
- [150] J. Liss and W. Goldsmith. Plate perforation phenomena due to normal impact by blunt cylinders. *International Journal of Impact Engineering*, 2(1):37–64, 1984.
- [151] D. Liu and W. J. Stronge. Perforation of rigid-plastic plate by blunt missile. *International Journal of Impact Engineering*, 16(5/6):739–758, 1995.
- [152] N. Jones, S.-B. Kim, and Q. M. Li. Response and failure of ductile circular plates struck by a mass. *Journal of Pressure Vessel Technology*, 119:332–342, 1997.
- [153] X. W. Chen and Q. M. Li. Shear plugging and perforation of ductile circular plates struck by a blunt projectile. *International Journal of Impact Engineering*, 28:513–536, 2003.

- [154] J. A. Zukas. Survey of computer codes for impact simulation. In J. A. Zukas, editor, *High Velocity Impact Dynamics*, pages 593–714. John Wiley & Sons, Inc., New York, 1990.
- [155] N. Jones. Plastic failure of ductile beams loaded dynamically. *Journal of Engineering for Industry*, 98(1):131–136, 1976.
- [156] W. S. Jouri and N. Jones. The impact behavior of aluminum alloy and mild steel double-shear specimens. *International Journal of Mechanical Sciences*, 30(3/4):153–172, 1988.
- [157] E. H. Lee and H. Wolf. Plastic-wave propagation effects in high-speed testing. *Journal of Applied Mechanics*, 18:379–386, 1951.
- [158] M. A. Meyers. *Dynamic Behavior of Materials*. John Wiley & Sons, Inc., New York, 1994.
- [159] Q. Zhou and T. Wierzbicki. A tension zone model of blanking and tearing of ductile metal plates. *International Journal of Mechanical Sciences*, 38(3):303–324, 1996.
- [160] C. A. Calder and W. Goldsmith. Plastic deformation and perforation of thin plates resulting from projectile impact. *International Journal of Solids and Structures*, 7(7):863–881, 1971.
- [161] ASM Aerospace Specification Metals, Inc., 2003. <http://www.aerospacemetals.com>.